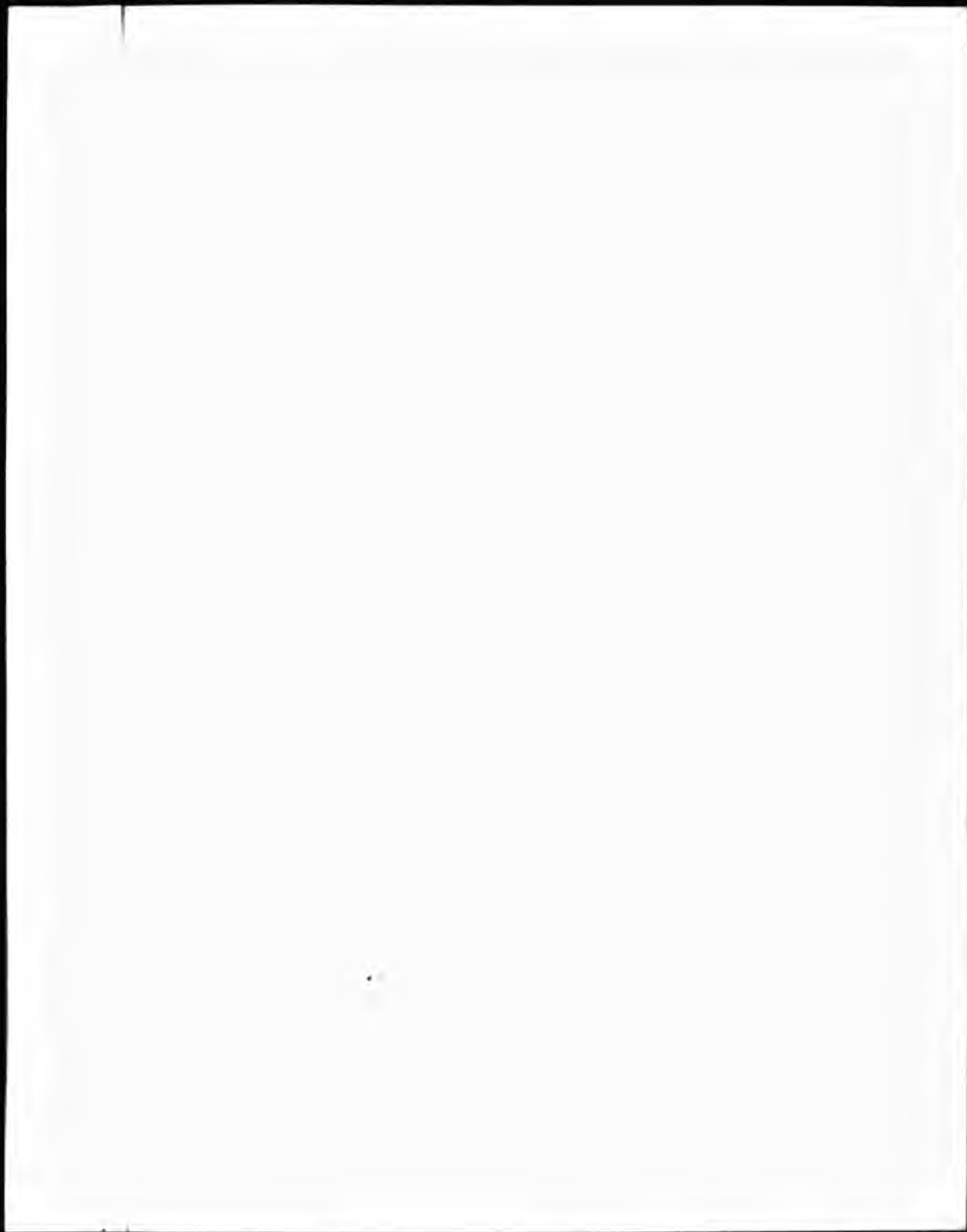


This PDF was created from the British Library's microfilm copy of the original thesis. As such the images are greyscale and no colour was captured.

Due to the scanning process, an area greater than the page area is recorded and extraneous details can be captured.

This is the best available copy

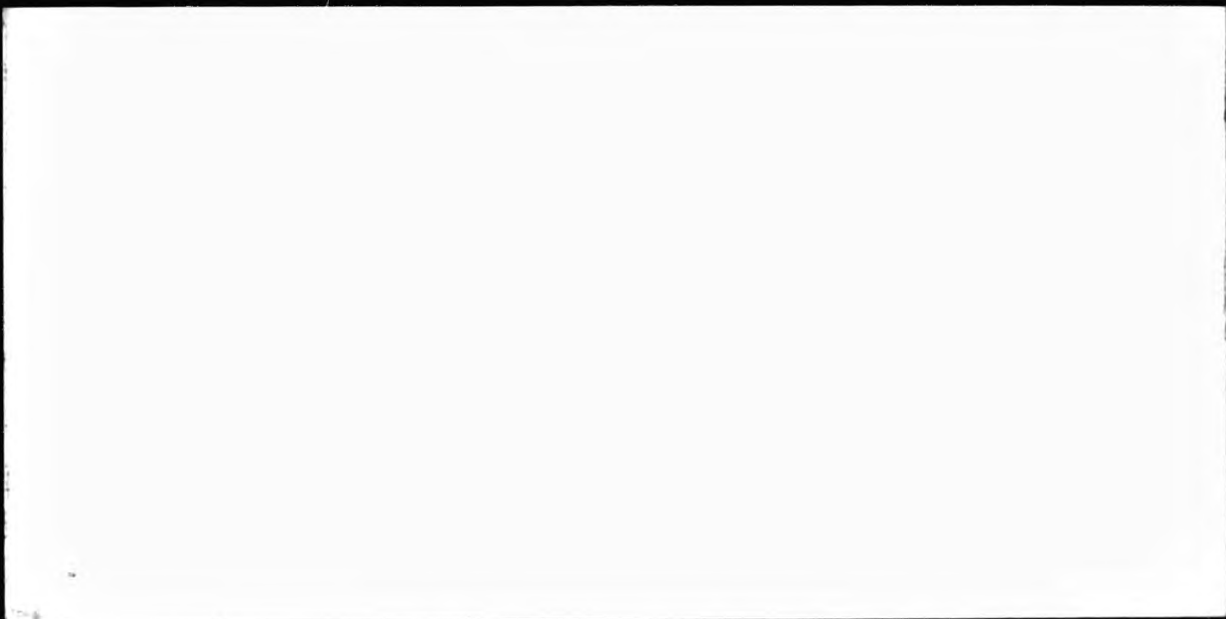


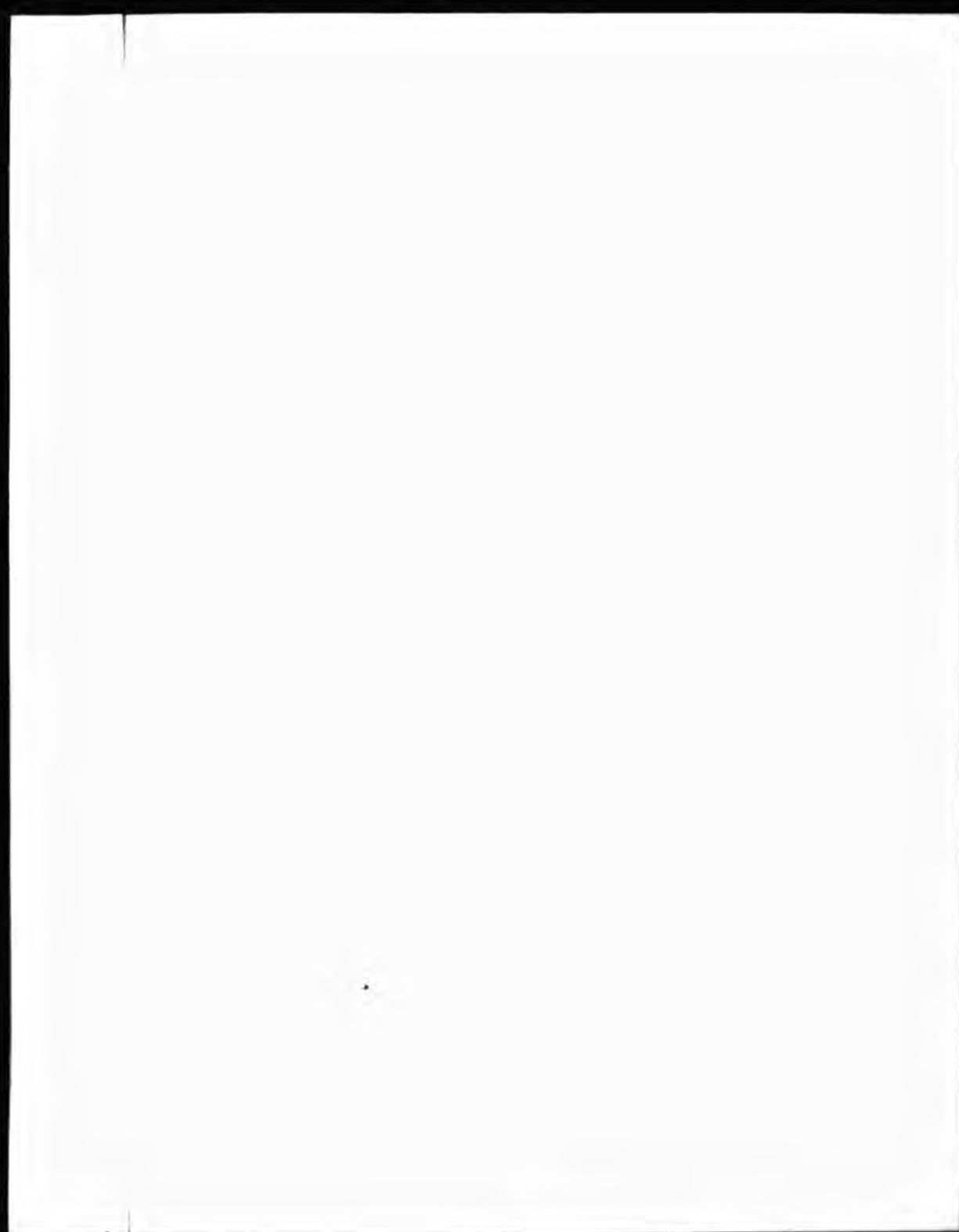


DX



89312





THE BRITISH LIBRARY DOCUMENT SUPPLY CENTRE

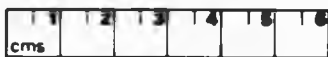
TITLE HYDROGEN EMBRITTLEMENT OF AN Al-4.5Zn-2.5Mg ALLOY

AUTHOR EDWARD JOHN BORAN

INSTITUTION and DATE CITY OF LONDON POLYTECHNIC.
..... C N A A 1989

Attention is drawn to the fact that the copyright of this thesis rests with its author.

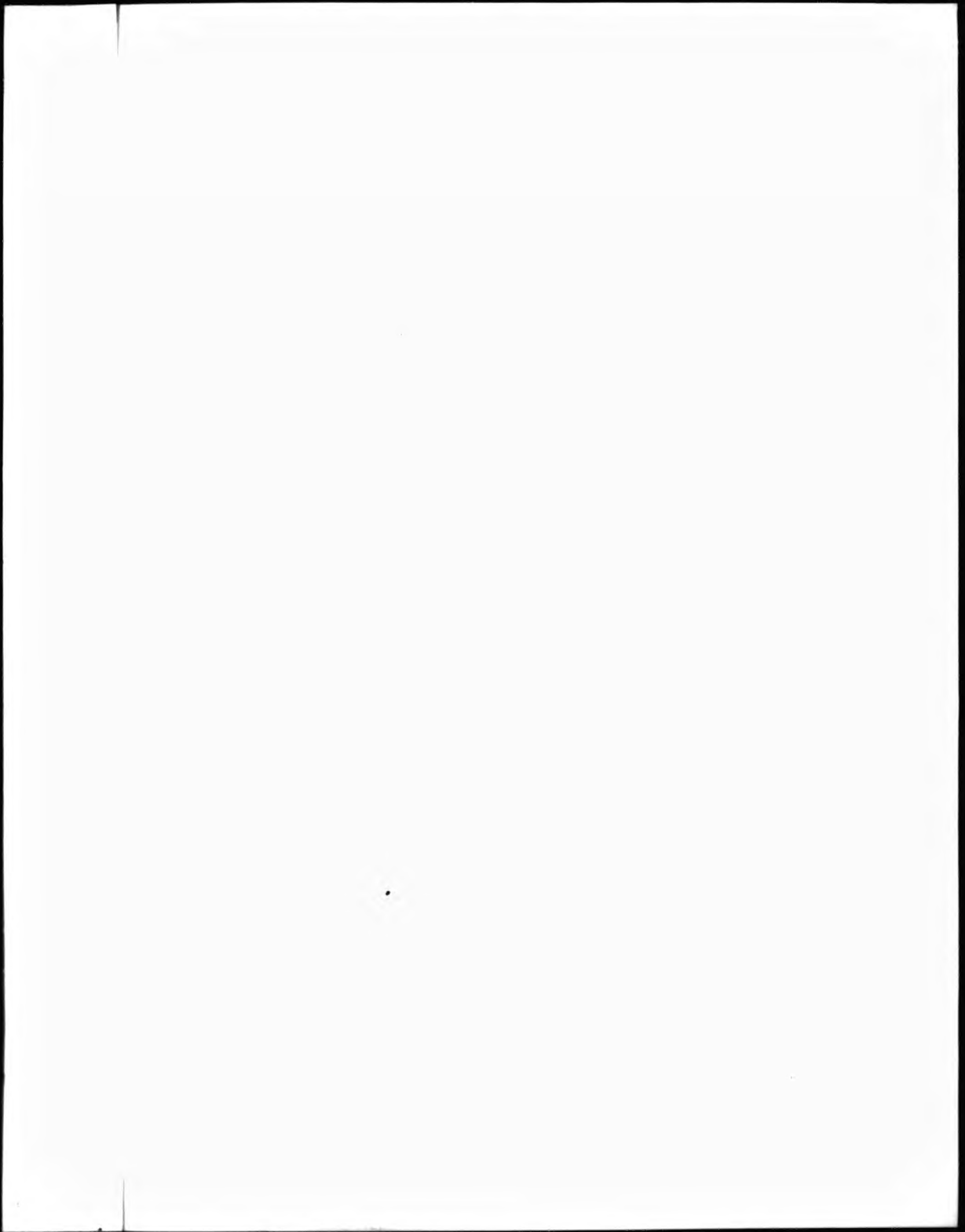
This copy of the thesis has been supplied on condition that anyone who consults it is understood to recognise that its copyright rests with its author and that no information derived from it may be published without the author's prior written consent.



THE BRITISH LIBRARY
DOCUMENT SUPPLY CENTRE
Boston Spa, Wecharby
West Yorkshire
United Kingdom

REDUCTION X 21

CAM. 1



HYDROGEN EMBRITTLEMENT OF AN Al-4.5Zn-2.5Mg ALLOY

by

EDWARD JOHN BORAN BSc MIM CEng

This thesis is submitted in partial fulfilment of the requirements of the Council for National Academic Awards for the Degree of Doctor of Philosophy.

Sponsoring Establishment:

DEPARTMENT OF METALLURGY AND MATERIALS ENGINEERING
CITY OF LONDON POLYTECHNIC.

Collaborating Establishment:

ALCAN INTERNATIONAL LTD
BANBURY.

November 1989

ACKNOWLEDGEMENTS

I would like to thank the following for their encouragement, help and advice during the preparation of this thesis.

Firstly, I would like to thank my Father and Mother for their encouragement. Thanks are due to the staff at Alcan Atlantic Region Laboratories, Banbury, for their assistance in giving me access to experimental facilities and for their many helpful discussions. I would like to thank, in particular, Dr G M Scamans, Dr C D S Tuck and Dr N J H Holroyd. Thanks are also due to the academic and technical staff at the City of London Polytechnic, Department of Metallurgy and Materials Engineering, and, in particular, to Dr C A May and Professor L L Shreir for their many helpful discussions and to Mr A Mandal, Mr P Cook and Mr A Curtis for their technical assistance.

I would like to thank Ms J Hilliard, Ms S Christian, Mrs J Elliot and Mrs M Evans for their assistance in typing various parts of the text.

Finally, I would like to thank my friend and colleague Dr P Lydon for his helpful advice and for proof reading the text and to my friends, Mr D Morley, Ms P Singer, Ms H Matheson and my companion, Sue Garnham for their encouragement in completing the thesis.

HYDROGEN EMBRITTLEMENT OF AN Al-4.5Zn-2.5Mg ALLOY

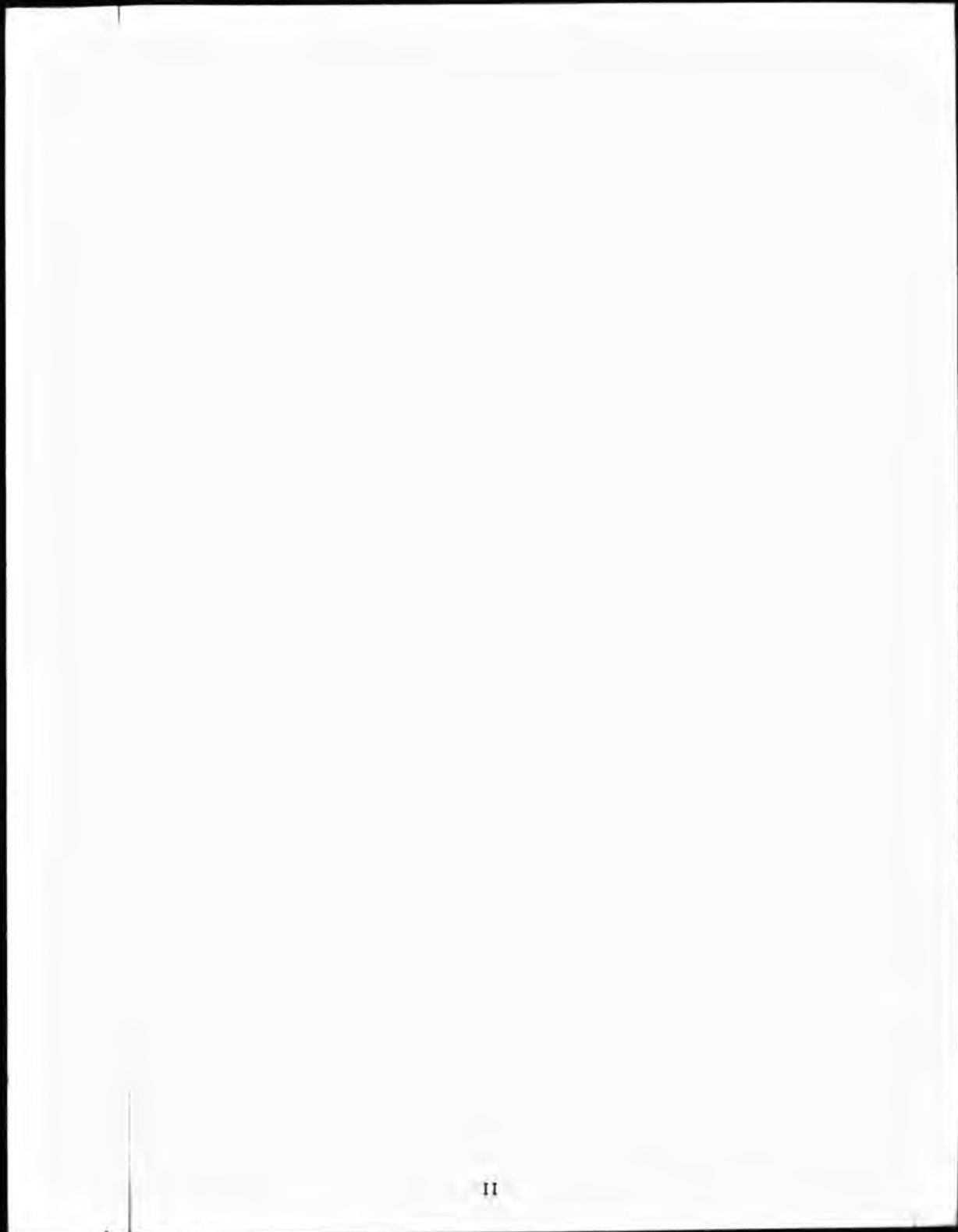
By E J BORAN

ABSTRACT

Experimental results are presented here for a 7017-T651 AlZnMg alloy where stress corrosion crack growth data on compact tension and double cantilever beam specimens has been obtained in distilled water, water saturated air vapour and aqueous chloride environments over a range of temperatures. The results, including fracture surface examination, are interpreted as indicating that a hydrogen embrittlement mechanism is operative whereby hydrogen, generated by a corrosion reaction, embrittles the alloy. Activation energy determinations have been made for stress corrosion crack growth at the free corrosion potential, and the activation energy results have been interpreted as indicating that the same process is rate controlling during both region I and region II crack growth.

Hydrogen diffusion in AlZnMg has been investigated by electrochemical permeation and gas chromatography techniques. It was found that the sensitivity of the electrochemical permeation technique is not sufficient to detect a permeation transient due to hydrogen. However, the diffusion coefficient for hydrogen in AlZnMg was determined by gas chromatography over a range of temperatures. A critique is made of previous reported measurements of hydrogen diffusion in an AlZnMg alloy by electrochemical permeation. The average diffusion rate of hydrogen in AlZnMg alloy material using gas chromatography on hollow cylindrical specimens was determined.

Finally, the surface reactions between polished AlZnMg alloy surfaces and distilled water, water saturated air vapour and aqueous chloride solutions have been investigated to determine the rate of hydrogen production and the morphology of the reaction products. It was shown that the reaction of water saturated air vapour with the commercial AlZnMg alloy surface did not exhibit specificity with respect to grain boundary attack, unlike the specificity shown by high purity versions of these alloys. The contribution of these studies to the understanding of stress corrosion crack growth by a hydrogen embrittlement mechanism is discussed.



CONTENTS

	<u>Page No.</u>
ABSTRACT	I
CONTENTS	III
1.0 INTRODUCTION	1
2.0 REVIEW OF THE LITERATURE	7
2.1 Physical metallurgy of Al-Zn-Mg alloys	7
2.1.1 Compositions and mechanical properties	7
2.1.2 Age hardening	11
2.1.3 Grain boundary precipitation	15
2.1.4 Processing and heat treatments	18
2.1.5 The role of alloying elements	22
2.2 Stress corrosion cracking	27
2.2.1 The corrosion of aluminium	27
2.2.2 Stress corrosion cracking mechanisms - a general review	30
2.2.3 Anodic dissolution mechanisms	30
2.2.4 Hydrogen embrittlement mechanisms	34
2.3 Review of the stress corrosion cracking of high strength aluminium alloys, with particular reference to Al-Zn-Mg alloys - anodic dissolution mechanisms	43
2.3.1 A summary of experimental observations of SCC in Al-Zn-Mg alloys	43
2.3.1.1 Mechanical aspects	44
2.3.1.2 Environmental aspects	46
2.3.1.3 Metallurgical aspects	56
2.3.2 Electrochemical Mechanisms	59
2.3.3 Mechanical aspects of crack growth mechanisms	70

	<u>Page No.</u>
2.4 Review of the stress corrosion cracking of high strength aluminium alloys, with particular reference to Al-Zn-Mg alloys - hydrogen embrittlement mechanisms	73
2.4.1 Environmental aspects	73
2.4.1.1 Crack growth in gaseous environments	73
2.4.1.2 Crack growth in aqueous solutions	80
2.4.1.3 Effect of pH	82
2.4.1.4 Effect of electrochemical potential	84
2.4.1.5 Effect of poisons and catalysts for the hydrogen recombination reaction	88
2.4.2 The role of heat treatment and its effect on grain boundary segregation in the hydrogen embrittlement of Al-Zn-Mg alloys	93
2.4.3 Microstructural aspects of hydrogen embrittlement in Al-Zn-Mg alloys - the crack path	99
2.4.4 Slow strain rate testing of Al-Zn-Mg alloys	103
2.4.5 Mode III (torsional) and Mode I (tensile) testing of pre-cracked specimens	107
2.5 Hydrogen diffusion	110
2.5.1 Introduction	110
2.5.2 Sources of hydrogen	110
2.5.3 Metals and hydrogen	111
2.5.4 Mode of distribution and form of hydrogen in aluminium	113
2.5.4.1 Lattice hydrogen	113
2.5.4.2 Hydrogen in traps	114
2.5.5 Hydrogen evolution reaction on aluminium and on aluminium alloys	121
2.5.6 Water saturated air vapour reaction on aluminium and aluminium alloys	123

	<u>Page No.</u>
2.5.7 Diffusion and permeation of hydrogen	129
2.5.7.1 Adsorption of hydrogen	129
2.5.7.2 Solution of hydrogen	131
2.5.7.3 Diffusion of hydrogen	133
2.5.7.4 Permeation of hydrogen	140
2.5.8 Promoters and inhibitors	142
2.5.9 The determination of hydrogen diffusion coefficients	144
3.0 EXPERIMENTAL PROCEDURE	147
3.1 Materials	147
3.2 Specimen preparation	148
3.2.1 Compact tension specimens	148
3.2.2 Double cantilever beam specimens	151
3.2.3 Hydrogen diffusion experiment specimens	153
3.3 Equipment and procedure	155
3.3.1 Fatigue pre-cracking	155
3.3.2 Constant load compact tension specimen machine	156
3.3.3 Compact tension specimen crack growth monitoring	156
3.3.4 Double cantilever beam specimen, constant displacement loading	164
3.3.5 Electrochemical hydrogen permeation experimental procedure	171
3.3.5.1 Introduction	171
3.3.5.2 Solutions	172
3.3.5.3 The permeation cell	172
3.3.5.4 Specimen preparation	176
3.3.5.5 Analysis of the permeation transient	177

	<u>Page No.</u>
3.3.6 Hydrogen diffusion experiments with environmental charging and gas chromatography analysis	182
3.3.7 Hydrogen evolution rate experimental procedure	185
3.4 Environments	185
3.5 Microscopy	187
3.5.1 Optical microscopy	187
3.5.2 Scanning electron microscopy (SEM)	187
3.5.3 Transmission electron microscopy (TEM) and scanning transmission electron microscopy (STEM)	188
4.0 RESULTS	189
4.1 The influence of environment on stress corrosion crack growth in compact tension specimens	189
4.1.1 The influence of temperature	189
4.1.2 Stress corrosion crack growth activation energy determinations in distilled water WSAV and 3%NaCl for compact tension specimens.	226
4.2 The influence of test conditions on stress corrosion crack growth	231
4.2.1 The effect of blanking-off compact tension specimen sides	232
4.2.2 The influence of pre-exposure and electrochemical pre-charging	238
4.2.3 Anomalous crack growth rates at 70 °C in water and WSAV	244
4.3 The influence of environment on stress corrosion crack growth in double cantilever beam specimens	250
4.3.1 The influence of temperature	253
4.3.2 Stress corrosion crack growth in DCB specimens from fatigue pre-cracked starter cracks	262

	<u>Page No.</u>
4.3.3 Stress corrosion crack growth in 3%NaCl in DCB specimens from fatigue pre-cracked starter cracks and with regular solution replacement and DCB specimen cleaning	265
4.3.4 Stress corrosion crack growth in laboratory air	267
4.3.5 Stress corrosion crack growth activation energy determinations in distilled water, WSAV and 3%NaCl for double cantilever beam specimens.	273
4.4 Hydrogen diffusion experiments	281
4.4.1 Electrochemical hydrogen permeation experiments on EN8 steel - proving the technique	281
4.4.2 Electrochemical hydrogen permeation experiments on Al-Zn-Mg coupons	289
4.4.2.1 Analysis of theoretical hydrogen diffusion current levels from hydrogen diffusion coefficients and hydrogen solubilities reported for Al-Zn-Mg alloys	303
4.4.3 Gas chromatography hydrogen diffusion experiments using cylindrical geometry specimens	312
4.4.3.1 Solution of the diffusion equation for cylindrical geometry	312
4.4.3.2 Results of the hydrogen diffusion experiments using cylindrical geometry specimens and gas chromatography analysis	318
4.5 Surface reactions on Al-Zn-Mg alloys in water, WSAV and 3% sodium chloride	332
4.5.1 Hydrogen production rates of Al-Zn-Mg alloys in water, WSAV and 3% sodium chloride	334
4.5.2 WSAV reaction and examination on Al-Zn-Mg alloy surfaces	341
5.0 DISCUSSION	366
5.1 Summary of results	366
5.2 Discussion of CT and DCB crack growth rate experiments	375
5.3 Anomalous crack growth rates at 70 C in water and WSAV	382

	<u>Page No.</u>
5.4 Activation energy experiments on crack growth rates in CT and DCB geometry specimens	388
5.5 Stress corrosion crack propagation in Al-Zn-Mg alloys	393
6.0 CONCLUSIONS	401
7.0 RECOMMENDATIONS FOR FURTHER WORK	404
REFERENCES	406
APPENDIX A Chart recorder traces of hydrogen permeation current versus time for permeation experiments performed on Al-Zn-Mg alloy coupons	A1

1.0 INTRODUCTION

Aluminium is one of the so called "light" metals which along with magnesium and titanium have gained in technological importance, in particular since 1950, when world aluminium production surpassed copper production.

The relative densities of these three metals range from 1.7 (magnesium) to 4.5 (titanium) which contrasts with relative densities of 7.9 and 8.9 respectively for the older structural metals iron and copper.

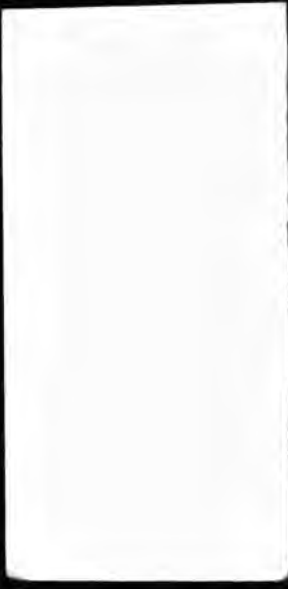
The property of lightness, or more specifically strength:weight ratio have led to the association of light metals with transportation applications, particularly in aerospace, land-based military vehicles and cryogenic applications, which has provided a stimulus for the development of large numbers of different alloys during the last forty years. In addition to this aspect of weight saving, the light metals possess other properties of considerable technological importance, e.g. the high corrosion resistance and electrical and thermal conductivities of aluminium, the machinability of magnesium and the extreme corrosion resistance of titanium.

Alloys based upon aluminium-zinc-magnesium form the so called high strength group of aluminium based alloys. These alloys are precipitation hardened and some versions of the alloy are readily weldable. Importantly, these alloys do not suffer a loss of strength on welding like many other heat treated alloys as

natural ageing after welding results in a significant recovery of strength. Commercial weldable alloys in plate form can have a yield stress in excess of 500 MNm⁻².

The AlZnMg alloys are referenced here by the American National Standard Alloy and Temper Designation System for Aluminium (ANSI H35.1). The 7000 range of alloys refer to the AlZnMg and AlZnMgCu alloys. The third and fourth digits serve to identify the different aluminium alloys in the group. The second digit indicates variants in an alloy type e.g. the designation 7475 represents a slight composition change from 7075. An "X" prefixed in the alloy designation (e.g. X7991) denotes an experimental alloy.

Temper designations follow the alloy designation and are based on a sequence of different treatments to produce the different tempers. The basic temper designations consist of letters that follow a hyphen after the alloy designation, e.g. F (as fabricated), O (annealed), H (strain hardened), W (solution heat-treated) and finally the most important temper for the 7000 series of alloys, T, which designates a thermally treated alloy where thermal treatment produces a stable temper other than F, O or H etc. Temper designations are then further subdivided by up to three digits as defined in ANSI H 35.1. The T6 and T7 tempers are important here in that they designate alloys which have been solution treated and artificially aged and alloys which have been



solution treated and artificially aged beyond their point of maximum strength (overaged) respectively.

The 7017 alloy specifically is used for high strength weldable armour applications on vehicles (e.g. the Scorpion tank) and other applications requiring protection against ballistic projectiles. In applications where a high ballistic performance is required AlZnMg alloys are used because the areal density (weight per unit area), which is the governing criterion, is significantly less than that of steel armour. In addition, there is a requirement to protect against spalling or back damage and against fragmentation attack. Clearly there is also a requirement in the fabrication of military vehicles for good weldability. The inert gas TIG and MIG methods are most frequently used when AlZnMg alloys require to be fabricated by welding. However, ballistic performance and weldability are not the subjects of concern here and they will not be dealt with further.

A major problem, however, is the susceptibility of AlZnMg alloys to attack by stress corrosion which can in some instances lead to catastrophic failure of the component if the crack growth is not detected in time for remedial action. Stress corrosion cracking has been a major problem in the development of these alloys for commercial service. The literature on the various aspects of stress corrosion, which is reviewed in Section 2.0, and in particular the literature on the mechanism by which stress

corrosion crack growth proceeds has been contentious for many years. The T73 temper for alloy 7075, introduced in 1960, was the first aluminium temper specifically developed to provide high resistance to stress corrosion cracking. The initial use of the alloy was for hydraulic fittings, where 7075-T73 could replace 2014-T6 (AlCuMg) on an equal strength basis. By 1962, 7075-T73 was replacing higher strength alloys such as 7075-T6 and 7079-T6 in more critical aerospace applications such as landing gear and hydraulic cylinders. These higher strength alloys in the T6 temper were susceptible to stress corrosion. By 1964 the replacement alloy was being used for major structural components such as fuselage frames, spars and bulkheads. 7075-T73 alloy is still in use today for applications where resistance to stress corrosion is critical, however its use is associated with a decrease in the strength level available to the designer. The yield stress of the alloy is 420 MNm⁻² compared with 500 MNm⁻² for the T6 temper.

The excellent service record of AlZnMgCu permitted development of alloys and tempers with an intermediate resistance to SCC, beginning with 7175-T736 in 1968. These newer alloys were used in applications where some reduction in resistance to stress corrosion could be tolerated in favour of higher strength or toughness.

Early proposals concerning the mechanism by which stress corrosion cracking took place were based upon considerations of anodic dissolution. The literature on these mechanisms is

reviewed in Section 2.3. As stress corrosion in these alloys is primarily intergranular, anodic dissolution mechanisms proposed were based upon dissolution of anodic phases or regions of the grain boundary and the precipitate free zone adjacent to the grain boundary. Dix⁴² in 1940, made the first proposal based upon the grain boundary precipitate being anodic to the aluminium matrix. Dissolution of the grain boundary precipitate would leave the grain boundary weakened and susceptible to tearing in the presence of stress. Various developments in proposed mechanisms of anodic dissolution are reviewed in Section 2.3.2.

Mechanisms for stress corrosion based upon considerations of hydrogen embrittlement are reviewed in Section 2.4. Early suggestions that a hydrogen embrittlement mechanism may be responsible for stress corrosion crack growth in AlZnMg alloys include those of Gest and Troiano⁸⁶ in 1972 and Montgrain and Swann¹⁰⁰ in 1974. These proposals were based upon observations including the diffusion of hydrogen in AlZnMg alloys and reversible embrittlement effects and on observations of microscopically brittle fracture with no evidence of tearing or plastic deformation of the fracture surface. Whilst a large amount of the current literature favours a hydrogen embrittlement mechanism, the exact mechanism is still contested with a number of papers in the literature, including for example Peel and Poole⁵⁰ and Ford⁷¹, proposing an anodic dissolution mechanism.

A discussion of the literature on hydrogen diffusion in AlZnMg alloys can be viewed to a certain extent in isolation from its role in stress corrosion cracking by a hydrogen embrittlement mechanism. It is thought that such an approach is useful and is adopted here for the review of the literature on hydrogen diffusion which is presented in Section 2.5.

2.0 REVIEW OF THE LITERATURE

2.1 PHYSICAL METALLURGY OF Al-Zn-Mg ALLOYS

2.1.1 Compositions and mechanical properties

All the commercial alloys in the AlZnMg group contain more zinc than magnesium, high Zn+Mg levels produce the best strength and the best response to heat treatment, along with the greatest susceptibility to stress corrosion. Low Zn+Mg levels produce the best weldability and the least quench sensitivity. The alloys are mainly used in the wrought form because of their limited castability. The 7017 alloy is a medium strength, weldable alloy with a typical ultimate tensile strength of 485 MNm⁻², a 0.2% proof stress of 435 MNm⁻² and a longitudinal elongation of 11% when heat treated to its highest strength condition (T651). In this alloy the Zn:Mg ratio is 2 and the composition is nominally Zn 5%, Mg 2.5%.

Most commercial alloys have a Zn:Mg ratio of 2 - 4 with copper being the other major alloying addition. Copper reduces stress corrosion susceptibility at the expense of weldability where additions drastically increase cracking in the heat affected zone by increasing the hot shortness of the alloy. A typical copper containing alloy is 7475 with a nominal composition of Zn 5.7% Mg 2.25% Cu 1.5%, i.e. with a Zn:Mg ratio of 2.5. The 7475 alloy has a UTS of 530 MNm⁻², a 0.2% proof stress of 460 MNm⁻² and a longitudinal elongation of 9% in the same peak aged condition, T651. Two other mechanical properties are important when considering these alloys and their end uses, namely fracture

toughness and fatigue endurance. The original versions of these alloys contained high levels of impurity elements, especially iron and silicon. In 7075 alloys these levels are Fe 0.5%, Si 0.4% giving a fracture toughness of $22 \text{ MNm}^{-3/2}$. This low fracture toughness is due to coarse and intermediate sized second phase particles (1-10 μm and 0.03 - 0.5 μm respectively) which fracture easily when stressed at low levels and leave voids which act as stress raisers, particularly in the case of coarse particles. These second phase particles are either insoluble, Al₇Cu₂Fe₂, Mg₂Si₂, or (Fe, Mn) Al₆ or relatively soluble, CuAl₂. Intermediate sized particles such as Al₂Mg₂Cr are formed during homogenisation of the ingot. These generally contain the alloying additions Cr, Mn or Zr and these dispersoids initiate micro voids at the particle - matrix interface thus promoting transgranular fracture. The precipitates are however important in suppressing recrystallisation and grain growth which would otherwise promote intergranular fracture.

7475 is a tougher version of 7075 in which the iron and silicon levels have been restricted to 0.15% and 0.10% respectively. The manganese level has also been reduced from 0.30% to 0.06%, resulting in a fracture toughness of $33 \text{ MNm}^{-3/2}$ in the T6512 condition and $36 \text{ MNm}^{-3/2}$ in the T7351 condition.

In plate form the fracture toughness, along with other mechanical properties, is directional due to the pancake shape of the grains which are elongated and flattened in the rolling direction with many oval shaped grain boundaries exposed in the short transverse

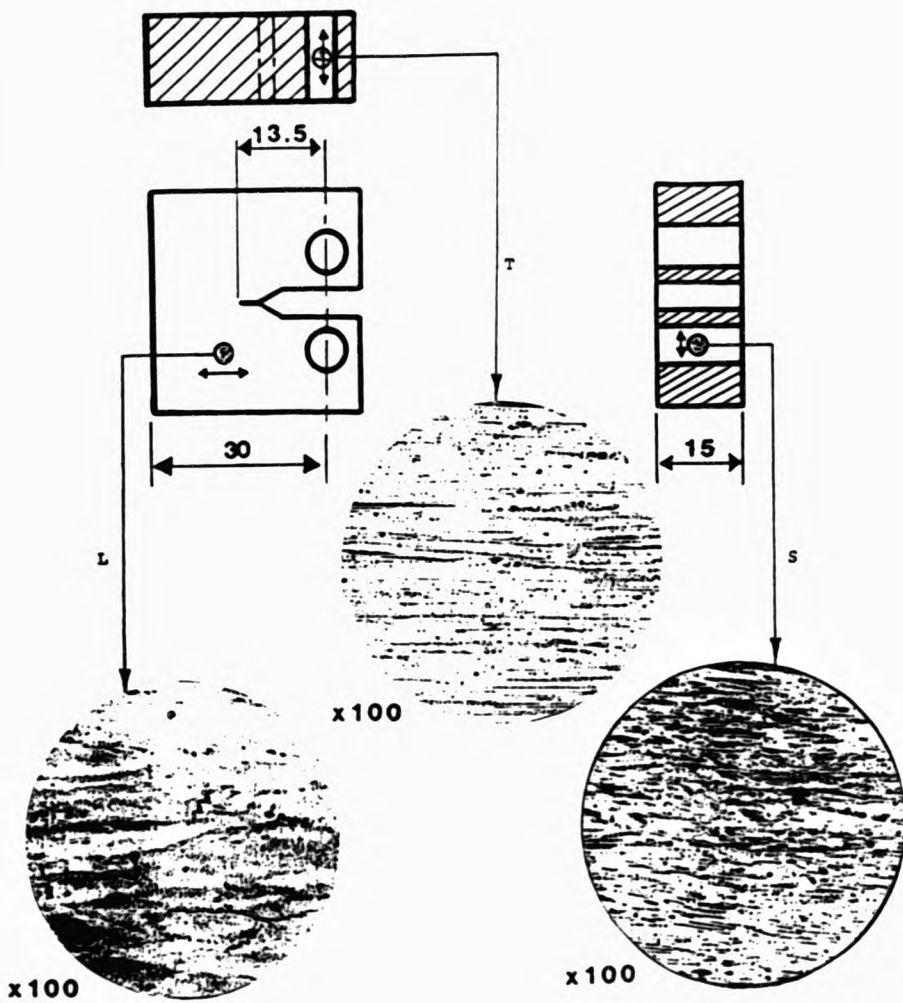
direction (Fig. 1). In a high purity 7075 type alloy with a 0.2% chromium addition, the fracture toughness, K_{1C} , shows the following relationship³. (Table 1).

Direction (Stress axis - crack growth)	K_{1C} (MNm ^{-3/2})	Yield stress (MNm ^{-3/2})
Long-Transverse	44	445
Transverse-Longitudinal	41	430
Short Transverse-Longitudinal	31	410

Table 1 The variation in fracture toughness with test direction for a high purity 7075 type alloy with 0.2% Cr.

The fatigue endurance of all aluminium alloys at low values of cyclic stress intensity, ΔK , is remarkably similar, but low in comparison with other alloy systems. The cyclic stress intensity being a more dominant factor in determining fatigue endurance than alloy composition and microstructure. Whilst aluminium alloys, in common with other non-ferrous alloys, do not have a fatigue limit, no alloy development has been reported that has a higher cyclic stress intensity limit, ΔK_o , than 2MNm^{-3/2}.

At high values of ΔK aluminium alloys show marked variations in fatigue crack growth rate, the alloys with higher fracture toughness showing lower fatigue crack growth rates. For instance, alloy 7475 -T6 has a fatigue crack growth of 7×10^{-6} m/cycle at a



- L Longitudinal or rolling direction
- T Transverse or width direction
- S Short transverse or thickness direction

Fig 1 Optical Micrograph of the Grain Structure of 7017-T651 Rolled Plate.

ΔK of $40 \text{ MNm}^{-3/2}$ at 20 Hz in laboratory air, whilst 7075 -T6 has a fatigue crack growth rate of $2 \times 10^{-5} \text{ m/cycle}$ under the same conditions.

2.1.2 Age hardening

The 7000 series are precipitation hardening alloys. The precipitation of Guinier-Preston (GP) zones and platelets leads to a difference in microstructure between the matrix and the grain boundary which is thought to be important in the stress corrosion cracking (SCC) and corrosion fatigue of these alloys. The different heat treatments given at the solution treatment and ageing stages also result in different stress corrosion (SC) susceptibilities, so these processes will be dealt with in some detail.

The primary strengthening constituents in 7000 series alloys are zinc and magnesium which have equilibrium solid solubilities of 70% and 17.4% respectively at 450 °C and of 2% each at 20 °C.

The maximum strength commercial temper for these alloys is T651 which involves the following treatment:

- o Hot rolled
- o Solution treated at 400 - 500 °C
- o Cold water quenched
- o Controlled stretch (typically 1-2%)
- o 48 hours at room temperature for zone development
- o Aged at 90 °C for 8 hours and 150 °C for 8 hours

This temper also corresponds to the maximum stress corrosion susceptibility. The T6 temper denotes solution heat treatment and artificial ageing and the T7 temper denotes solution heat treatment followed by overageing which results in a lower tensile strength and higher stress corrosion resistance. Tensile strength is reduced by 15 - 20% in the commercial T7351 temper; -51 after the temper designation indicates a controlled stretch after quenching of the alloy.

The super saturated solid solution formed after solution heat treatment of a 7017 type alloy is aluminium with a vacancy and dislocation concentration governed by the thermomechanical history, together with intermetallics formed by impurities and alloying additions. The solution heat treatment temperature is below the recrystallisation temperature and little or no recrystallisation takes place. A temperature of 450^o C is an adequate solution treatment temperature for most AlZnMg alloys (Fig 2). During solution heat treatment clustering takes place of zinc and magnesium due to their rejection from the aluminium lattice. The repulsions originate from steric effects, valency effects and the effect of interaction with vacancies. Magnesium and zinc are repelled by the lattice towards vacancies and dislocations, while magnesium has an affinity towards zinc^{6,7}.

Quenching in water yields a disordered super saturated solid solution with vacancies, screw dislocations⁸ and dislocation loops. At temperatures below the GP zone solvus, which is a function of composition and vacancy concentration, the solid

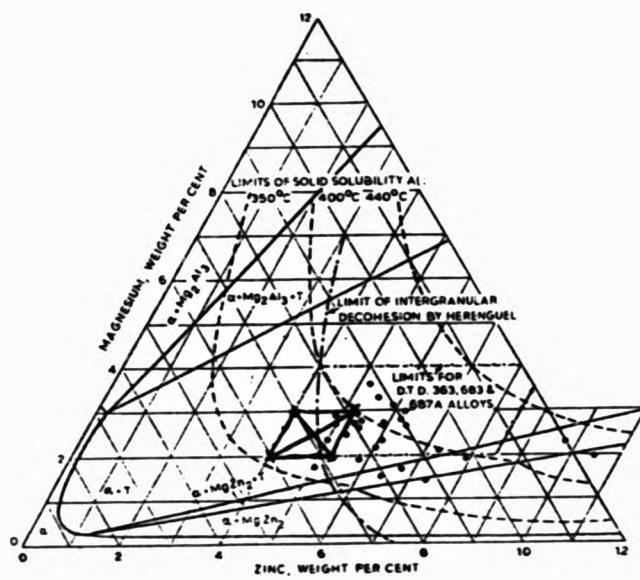


Fig 2. Al-Zn-Mg phase diagram, the 200°C section showing the solid solubility curves at 350°C, 400°C and 440°C. (from J. Inst., Metals, April 1958, p338).

solution decomposes by the formation of GP zones. The decomposition of the solid solution follows the following sequence.

- (a) Clusters (b) GP zones (c) GP compounds (η') 160 °C
 (d) $MgZn_2$ (η) 200 °C (e) $Mg_{32}(Al,Zn)_{49}(T)$

The T phase which forms above 200 °C plays little part in the strengthening of the alloy because of its large equilibrium size and small degree of dispersion. After quenching, ageing at 120 °C allows vacancies and solute atoms to diffuse forming more clusters which act as zone nuclei. After 30 minutes at 120 °C GP zone formation can be detected. These zones are spherical and 30-50 Å diameter, they are coherent with the parent lattice but produce appreciable elastic strains. GP zone density is usually very high, $10^{15} - 10^{18} \text{ cm}^{-3}$, and therefore very finely dispersed. GP zone density is primarily dependent upon the frozen-in vacancy concentration which is a function of;

- 1 The trace element concentration which reacts preferentially with vacancies to reduce the zone nucleation rate.
- 2 The solution heat treatment temperature which increases the excess vacancy concentration.
- 3 The quench rate, increasing quench rates increase the excess vacancy concentration.

Growth of the GP zones depends upon temperature and time, being a diffusion and growth phenomena. At ageing temperatures above the GP zone solvus the GP zones redissolve into the matrix. Ageing for different times at a constant temperature results in a proportion of GP zones that have reached the critical size for heterogeneous nucleation of the GP compound η' ($MgZn$)⁹. This is nucleated in the form of platelets about 200×50 Å with growth on the (111) matrix planes. Maximum hardness is reached on forming 50% zone and 50% platelets. Full coherency is not maintained with the parent lattice and no coherency strain effects can be detected. Heterogeneous nucleation of η' can take place on intermetallic compounds, grain boundaries and dislocations. Grain boundaries and dislocations act as sinks for vacancies and solute atoms and consequently generate GP zones and η' platelets faster than in the bulk α phase. η' platelets grow along the grain boundary and join up to form discrete grain boundary particles. Platelets in the matrix also grow whilst GP zones disappear and the equilibrium $MgZn$ (η)² phase is formed with a hexagonal structure very close to that of η' $MgZn$ ² and has a low misfit with the parent lattice and a lath morphology with preferential growth on the (110) matrix planes. If the tempering temperature is raised above 200 °C other phase fields of the ternary system can be intersected and the $MgZn$ forms the ternary compound Mg (Al,Zn)^{32 49} (T), which results in considerable softening of the matrix.

2.1.3 Grain boundary precipitation

The grain boundary precipitation processes are thought to be important in the SC susceptibility of these alloys. Grain

boundaries consist of a thin disordered layer 2-4 atoms thick with regions of good and bad fit of atoms on periodic sites. In regions of bad fit there is a high density of grain boundary ledges, steps and lattice dislocations. Enhanced solute diffusion proceeds through these channels of misfit. Preferential nucleation of the second phase occurs at the grain boundary because the free energy barrier is lower and growth is faster due to enhanced solute diffusion. This results in a coarser grain boundary precipitate than the matrix precipitate formed by the same heat treatment.

Another important feature of the grain boundary is the development of a precipitate free zone (PFZ). This arises because the boundary acts as a vacancy sink, the depletion of vacancies preventing subsequent nucleation of large numbers of clusters and GP zones. PFZ formation may also be due to solute denudation of areas around the grain boundary by competitive growth of grain boundary precipitates.

The distribution of vacancies near a grain boundary can take the form shown schematically in Figure 3. A critical concentration of vacancies, C_1 , is needed before nucleation of the precipitate can occur at T_1 . The resultant PFZ width is W_1 . For higher solution heat treatment temperatures, or faster quench rates, (Curve B), both of which increase the excess vacancy concentration, and for lower ageing temperatures (T_2), the zones are narrower, (W_2). The latter effect of lower ageing temperatures has been attributed to

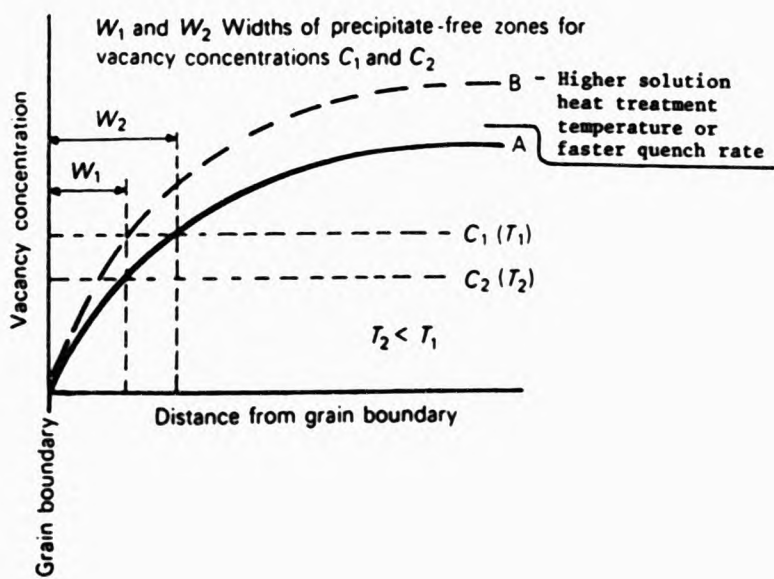


Fig 3. Representation of profiles of vacancy concentration adjacent to a grain boundary in an as quenched alloy. (from Taylor, J.L., J. Inst. Metals 92, p301, 1963-4).

a higher concentration of solute (as diffusion rates to the grain boundary are reduced) which allows smaller nuclei to be stable, thereby reducing the critical vacancy concentration required for nucleation to occur (C_2 in Fig.3).

Solute denudation of the PFZ and the relative enhancement of Mg and Zn concentration in the region just adjacent to the PFZ gives rise to solute profiles across the matrix - PFZ - grain boundary structure that are fundamental to the stress corrosion cracking behaviour of this alloy, irrespective of whether anodic dissolution or hydrogen embrittlement is responsible for crack growth. The role of the PFZ in stress corrosion of AlZnMg alloys will be examined in greater detail in the Sections on stress corrosion (2.3 and 2.4).

2.1.4 Processing and heat treatments

The normal production route for this alloy in plate form is direct chill (DC) casting which is preferred as the faster cooling rates promote the formation of finer dendrite arms which reduce microsegregation in the interdendritic spaces. Faster cooling rates also result in smaller intermetallic compounds and a smaller final grain size.

The ingots are homogenized to reduce segregation and remove non equilibrium low melting point eutectics. Homogenization is particularly important for the higher strength alloys as it serves to precipitate and redistribute the submicron intermetallic compounds of the transition metals such as $MnAl_6$, $Al_{12}Mg_2Cr$ and

ZrAl₃. These intermetallics are used to control grain structure but they also have an effect on the subsequent ageing response of the alloy. The intermetallics may super-saturate during the relatively fast cooling of ingots and homogenization promotes precipitation of uniform dispersions of the compounds in order to control grain structure. This is achieved by regulation of the rate of heating, where a relatively slow rate of 75 C hr⁻¹ is required to promote nucleation and growth of a fine and uniform dispersion of the compounds. The intermetallics are nucleated on η₂- (MgZn)₂ precipitates which subsequently dissolve during homogenization.

Production of plate through hot rolling breaks down the cast structure. The uniformity of working is achieved by increasing the reduction for each pass.

Wrought aluminium products exhibit to varying degrees a thin pancake grain elongated in the longitudinal and transverse directions and flattened in the short transverse direction. In AlZnMg alloys, stress corrosion cracking is nearly always intergranular, with the lowest energy path lying normal to the short transverse direction, and with the applied load normal to the crack growth direction. SCC tests in the longitudinal and transverse direction show much lower crack growth rates. An equiaxed structure shows an as great (or greater) susceptibility to SCC as a wrought structure, with any stressed face of a structure giving cause for concern. A wrought grain structure is

preferred, therefore, which restricts concern to one axis of a component. Alignment of the short transverse direction with the stress axis at a surface is avoided.

Solution treatment is carried out commercially in air furnaces except for clad plate where stricter control of temperature is required to prevent alloying elements diffusing to the cladding and reducing corrosion resistance. In this case solution treatment is in mixed nitrate salt baths. Solution treatment temperatures are 400 - 430 C for 7017 type AlZnMg alloys and care is taken not to prolong solution treatment or carry it out at unnecessarily high temperatures to prevent the formation of coarse recrystallised grain structures. Particular care is taken with forgings and extrusions where differential working can lead to grain growth in localised regions.

Cold water quenching is normally applied to AlZnMg plate but this leads to residual stresses which are compressive at the surface and tensile in the core and may approach the yield stress in higher strength alloys. For plate, residual stresses are relieved by a 2.5% stretch in the case of the 7017-T651 alloy and heat treatment.

The alternative to stress relief by stretching is slower cooling rates on quenching or quench interruption. Whether this treatment can be applied depends upon the quench sensitivity of the alloy. The critical temperature region is 250 - 300 C, where during slow cooling there is a tendency for solute elements to precipitate out

as coarse particles, reducing the level of supersaturation and subsequent response of the alloy to age hardening. This behaviour is more pronounced in highly alloyed products and is aggravated by heterogeneous nucleation on submicron intermetallic compounds produced during homogenization. Quench sensitivity is more pronounced in the 7010, 7475 and 7075 copper containing alloys than in the 7017, 7020 type weldable alloys and slow quenching can be employed in these low-copper containing alloys.

Commercial ageing of 7017 alloy is by a two stage age of 8 hours at 90 °C followed by 8 hours at 150 °C after a period of 48 hours at room temperature for GP zone development. This ageing treatment is equivalent in terms of response to 24 hours at 120 °C. The time the alloy is held at room temperature may be critical for slowly quenched or quench interrupted alloys because of the lower supersaturation of vacancies which alters precipitation kinetics, and sufficient time is required for the nucleation and growth of GP zones.

Double ageing treatments in which a period of up to 10 hours at a higher temperature of 160 - 170 °C follows a T6 temper ageing treatment of 120 °C for 24 hours, have been shown to be beneficial to the stress corrosion behaviour of these alloys. This slightly overaged temper is designated T73 and results in a 15% reduction in tensile strength. A single stage ageing treatment at 160 - 170 °C results in the formation of η' (MgZn)₂ or η (MgZn)₂ and a significant reduction in SCC at the cost of a reduction in 0.2%

proof stress from 500 MNm^{-2} to 370 MNm^{-2} , whereas the T73 temper shows a smaller reduction in 0.2% proof stress to 430 MNm^{-2} , but still with a substantial reduction in SC susceptibility. This reduction is apparent principally in plateau velocities where for example 7075-T651 has a plateau velocity of $2 \times 10^{-8} \text{ ms}^{-1}$ in 3.5% NaCl at 23°C , and 7075-T73 has a plateau velocity of $4 \times 10^{-10} \text{ ms}^{-1}$ in the same environment. Generally improvements in SC susceptibility have been to plateau velocities rather than in threshold stress intensities needed to initiate stress corrosion crack growth.

The precipitate formed in double ageing treatments is still η' (MgZn_2) or η (MgZn_2), but this is nucleated on pre-existing GP zones resulting in a finer precipitate dispersion. During the second ageing treatment the smaller GP zones redissolve.

2.1.5 The role of alloying elements

Commercial alloys can contain Si, Fe, Mn, Cr, V, Zr, Mn, Ag, Cu, Ti and B as alloying additions or impurities.

Iron and silicon are the two common impurities in aluminium. Both these elements have a pronounced effect upon fracture toughness due to the presence of FeAl_3 and MgSi_2 needles which initiate voids in the surrounding matrix and result in low fracture toughness values as previously reported (see Section 2.1.1). This effect is particularly pronounced in cast products where the needle structure is not broken up by homogenization and working.

Both elements have little effect upon strength on ageing unless the silicon content is very high and the Zn:Mg ratio is close to 2:1 when magnesium depletion occurs due to Mg₂Si formation. This produces a decrease in strength, and especially ductility. Silicon has no reported effect on quench sensitivity whereas iron increases it slightly. Principally because of their effect on fracture toughness, the levels of these elements are reduced to Fe-0.12% and Si-0.10% in 7475, the fracture tough version of 7075 and Fe-0.15%, Si-0.10% in 7010 a similar fracture tough aerospace alloy. The alloy under investigation here is 7017 which contains Fe-0.45% and Si- 0.35%; approximately the same levels as found in 7075. 7017 is used in defence type applications where the fracture toughness requirements are lower than those in aerospace applications.

Cr, Mn and Zr have all been reported as grain refiners in AlZnMg alloys. Zr, Cr and Mn have the effect of both strengthening the alloy and reducing its SC sensitivity. All three elements have a low solubility in the α solid solution and a slow rate of diffusion during homogenization. Manganese and chromium also have a large effect in increasing the quenching sensitivity of these alloys due to heterogeneous nucleation on the submicron intermetallics formed.

Zr, Cr and Mn when dissolved in α aluminium raise the recrystallisation temperature from 280 - 330 °C to the solution treatment temperature range of 400 - 430 °C.

These additions, with the exception of chromium, pin down vacancies and thus reduce the effect of the vacancy depleted zone adjacent to grain boundaries and therefore decrease PFZ widths. Chromium creates further PFZ, especially around any coarse $MgZn_2$ precipitates. Chromium solubility is 0.015% in aluminium at 300 °C and it forms $CrZn_{17}$ and the compounds Al_7Cr and $Al_{12}Mg_2Cr$. Because of its low solubility, chromium readily precipitates on dislocations and grain boundaries before zone formation takes place, aiding heterogeneous precipitation. $Al_{11}Cr$ is not redissolved during homogenization, but for optimum properties must be finely dispersed.

Zirconium compounds are the most effective of the transition metal intermetallics used as grain refiners. Zirconium forms a compound $ZrAl_3$ which is smaller, at around 20 nm, when compared with 0.05 - 0.5 μm for the chromium and manganese based intermetallics. Zirconium also has the least effect on quench sensitivity. The smaller $ZrAl_3$ particles promote a tougher microstructure and like chromium and manganese intermetallics, are used to control grain size. The tougher microstructure partially derives from fine unrecrystallised grains which favour a high energy absorbing, transcrystalline mode of fracture. However, such particles tend to initiate microvoids by decohesion at the interface with the matrix which may lead to the formation of sheets of voids, subsequently developing into cracks. In the aerospace alloys Mn, Cr and Zr are all employed as grain refiners as shown (Table 2).

Alloy	Nominal composition (%)		
	Mn	Cr	Zr
7075	0.30	0.24	-
7475	0.06	0.21	-
7010	0.30	0.05	0.14

Table 2. Nominal alloy compositions of grain refining additions used in aerospace type AlZnMg alloys.

The 7017 type defence application alloys have a nominal composition Mn-0.30%, Cr - 0.15%, Zr - 0.15%. It should be noted that the more recently developed alloys, 7010 and 7017, employ zirconium as a grain refiner.

Copper has multiple effects on the precipitation hardening of these alloys resulting from zone interactions. Its solubility in aluminium at 250 °C is 0.15% and it forms Mg_2Cu and $MgCu$. It can form different GP zones, θ' and θ'' , in Al-Cu alloys. A 0.5% Cu addition is sufficient to influence the transformation kinetics. The general effect is to increase the rate of hardening giving a higher peak hardness with one quarter of the zone density and an increased spherical zone size of 80 Å. Manganese additions retard this effect as copper goes into solid solution in manganese. This improves SC resistance but increases the general corrosion rate of the alloy. Copper has a rapid diffusion rate during homogenization and increases quench sensitivity as a result of its effect in stimulating precipitation.

Copper has a significant effect on the weldability of AlZnMg alloys. High zinc contents make the alloy hot short with a tendency to crack in the weld. Copper forms a low melting point quaternary eutectic $\text{Al} + \text{CuMgAl}_2 + \text{MgZnAl}_3 + \text{MgZn}_2$ at 475°C which heals cracks in the weld itself, but drastically increases cracking in the heat affected zone. 475°C is the upper temperature limit for homogenization temperatures for quaternary AlZnMgCu alloys. High strength ternary alloys can be homogenized at 530°C and medium strength alloys can be safely homogenized at 620°C . Welds are usually naturally aged for a few weeks. Natural ageing regains up to 70% of the ultimate tensile strength of 7017 after 30 days. Multiple passes are avoided as they lead to a coarse precipitate and low mechanical strength.

Silver raises the GP zone solvus temperature and therefore the high strength due to zone formation can be obtained at a higher ageing temperature, which also improves SC resistance. However, silver also increases the quench sensitivity of the alloy and this effect on the precipitation processes requires a rapid quench rate and rapid heating to the higher ageing temperature to prevent a loss in strength due to coarse precipitation during heating and subsequent quenching. A heavy cost penalty is incurred in the use of silver although one German specification, designated 7009, contains 0.25 - 0.4% Ag, and a single ageing treatment at $160^\circ - 170^\circ\text{C}$ is employed.

2.2 STRESS CORROSION CRACKING

2.2.1 The corrosion of aluminium

Aluminium is a very reactive metal with a high affinity for oxygen. The metal is nevertheless highly resistant to most atmospheres and to a wide variety of chemical agents. This resistance is due to the inert and protective character of the aluminium oxide film which rapidly forms on the metal surface, and inhibits the bulk reaction predicted from thermodynamic data. In most environments therefore the rate of corrosion of aluminium decreases rapidly with time. In only a few cases e.g., in aqueous sodium hydroxide at high concentrations does the corrosion rate approximate to a linear relationship with time. A corrosion rate increasing with time is rarely encountered with aluminium, except in aqueous solutions at high temperatures (greater than 90 °C) and at high pressures.

If the surface film is prevented from forming the corrosion rate can be very high. For example, when a mercury amalgam is produced on the surface of aluminium in the presence of humid air, the corrosion rate is in the order of 1270 mm per year as compared with 0.005 mm per year for an Al 2.5% Mg plate in sea water.

The various equilibria of the Al-H₂O system have been collated by Pourbaix et. al. in a potential versus pH diagram which indicates the theoretical (thermodynamic) circumstances in which aluminium would show corrosion, forming Al³⁺ below about pH 4.5 and AlO₂⁻ above about pH 8.5. Passivity is due to hydrargillite.

(Al₂O₃ · 3H₂O) formed on the aluminium surface at near neutral pH's and immunity is shown at high negative potentials.

Aluminium is therefore soluble in strong acids or alkalis with the exception of concentrated nitric acid, glacial acetic acid and ammonium hydroxide. The oxide film formed on freshly exposed aluminium is very thin, 2.5 nm. and grows at a decreasing rate to a thickness of 20 - 30 nm. The oxide film formed in water, in air with a high relative humidity and in air at high temperature is much thicker, up to 1 μm. Even thicker films can be formed by conversion in hot acid or alkaline solutions or by barrier layer anodising where the film thickness can be grown up to 10 - 20 μm.

The oxide film formed on pure aluminium is Al₂O₃, which is an n-type semi-conductor and has a multiple protective effect in that it prevents the passage of metal ions and electrons to the oxide/atmosphere interface and is an effective barrier to embrittling hydrogen¹². The chemical and structural nature of this oxide film is modified by alloying additions. In AlZnMg alloys the oxide film is enriched in MgO. For example studies using a high purity Al 5.5%Zn 2.5%Mg alloy have shown that solution heat treatment at 475 °C for two hours produces an oxide film containing approximately 80% MgO at a distance of 1000 Å from the metal/oxide interface, decreasing to 30% at 3000 Å with the remainder being Al₂O₃ and very little ZnO¹³. The oxide film is also modified by the environment and temperature, forming bayerite (Al(OH)₃) and pseudoboehmite (AlO(OH)) in water and water vapour at 70 °C^{14,15}. The passivity of Al₂O₃ breaks down in the presence of

certain ions e.g., Cl⁻, Br⁻ and I⁻. Chloride ion concentrations as small as 10^{-4} molar are reported to disrupt the passivity of the oxide layer.

The electrode potential of pure oxide filmed aluminium versus a 0.1M calomel electrode in 1M NaCl is -0.85V, and aluminium alloys range from -0.69V to -0.99V, therefore aluminium is anodic to most metals and cathodic only to zinc (-1.10V) and magnesium (-1.73V). Sacrificial corrosion of aluminium will occur in galvanic couples with more cathodic metals, the magnitude depending upon the difference in electrode potential and the total polarisation of the galvanic circuit for a given solution composition and temperature.

Chromium and silicon in solid solution have little effect on corrosion resistance. Zinc causes a significant increase in electrode potential to -0.99V (in an Al - 1% Zn alloy), as does magnesium. An AlZnMg solid solution (with 4% MgZn) has an electrode potential of -1.07V. Copper has the greatest effect in reducing the corrosion resistance of aluminium and AlZnMg alloys, although a 0.05 - 0.2% Cu addition promotes a generalised corrosion attack and the extent of pitting is reduced, which can be beneficial. Pitting and intergranular attack occur in these alloys due to the presence of anodic and cathodic micro constituents and cause serious problems in the form of stress corrosion crack initiation and exfoliation corrosion. The latter

where;

v = crack velocity (m s^{-1})

i_a = anodic current density at the crack tip (A m^{-2})

M = atomic weight, (kg mole^{-1}) of metal of valency Z and density ρ (kg m^{-3}) undergoing dissolution

F = Faradays's constant (C mole^{-1})

The anodic current density at the crack tip, and hence v will depend upon the nature of the phase being dissolved and also upon the nature and location of any cathodic processes that occur elsewhere. It has been shown that the dissolution rate of iron in acid solutions undergoes a marked increase when straining passes from the elastic to the plastic regimes in dynamic straining experiments¹⁷. It has also been shown that this effect is due to the exposure of high index planes and edges of slip steps as well as increases in surface roughness as plastic deformation occurs. This is the mechanism by which stress (or strain) produces SOC by an increase in i_a .

For the crack to proceed along a narrow front and so maintain its geometry, most of the exposed area, including the crack sides, must remain inactive. This inactivity results from the formation of a passive layer (usually oxide). It is implied therefore that i_a represents the film free anodic current density. In this context the role of stress is to maintain the crack tip film free in film forming metal-environment combinations. This is the model of SOC originally proposed by Champion¹⁸ and Logan¹⁹.



Two crack propagation mechanisms are possible depending upon the presence or absence of segregate or precipitate structural features, usually at grain boundaries which cause a local galvanic cell to be set up. This is the pre-existing active path where the segregate or precipitate either acts as an anode or by acting as an efficient cathode may cause attack to be localised in the immediately adjacent matrix material. The function of stress is to prevent the dissolution reaction from becoming stifled by film formation.

Where pre-existing active paths are not present, or are inoperative because of environmental effects, the stress may act to disrupt a passive film thereby exposing bare metal and so maintaining the relatively localised anodic current density. The active path in this case is cyclically generated since the strain induced film disruption process allowing dissolution, and film growth processes compete with each other. Such strain generated active paths would be expected to result in transgranular SCC.

Three further mechanisms should be mentioned at this point, the tarnish (brittle film) rupture model, the stress sorption model and the tunnel model.

In the tarnish rupture model, propagation of cracks is by the repeated formation and rupture of a brittle film growing into the metal at the crack tip as proposed by Forty²⁰ and developed by McEvily²¹, to account for the SCC of copper-zinc alloys in aqueous ammonia. Here a brittle tarnish film grows into the grain

boundary and, in the absence of stress, attains a limiting depth. Under the influence of stress the film undergoes repeated rupture and a propagating crack develops. This model does not have the general acceptance given to the slip (film rupture) dissolution model. In particular the evidence for discontinuous crack propagation suggested by the model has not been shown. Moreover it has been demonstrated that the thick tarnish film does not extend to the crack tip, but is formed some distance behind the advancing crack front,²² and that penetration of the grain boundaries in unstressed specimens is due to their slower repassivation kinetics. This model has been extended to other systems where thick oxide films penetrate grain boundaries, in particular caustic embrittlement and nitrate cracking of low strength ferritic steels²³ and nitrate cracking of mild steels.

The stress sorption model postulates that specific species absorb and interact with strained bonds at the crack tip, reducing bond strength and giving rise to brittle fracture with a cleavage like appearance. This model has been applied to liquid metal embrittlement and to some forms of hydrogen embrittlement.⁴⁷

The tunnel model was first proposed by Swann²⁴ and suggests that cracking proceeds by arrays of fine corrosion tunnels which grow in length and diameter until the remaining metal ligaments fail by ductile rupture. This mode of crack propagation applies only to transgranular SCC. This mode of failure has been reported for

austenitic stainless steel in a sulphuric acid - sodium chloride
 25
 solution .

2.2.4 Hydrogen embrittlement mechanisms

The fracture stress, or theoretical stress, σ , to pull apart two planes of atoms in a metal lattice is given by;

$$\sigma = \left(\frac{E \gamma}{b} \right)^{1/2} \quad (2.2)$$

where;

- σ = theoretical fracture stress (N m⁻²)
- E = Youngs modulus of elasticity (N m⁻²)
- γ = surface energy of the lattice (N m⁻¹)
- b = interatomic spacing (m)

If the surface energy term is lowered so will the fracture stress of the solid.

The following equations due to Griffith⁵⁴ modify the equation to allow for a pre-existing crack;

$$\sigma = \left(\frac{2E \gamma}{\pi c} \right)^{1/2} \quad \text{for plane strain (2.3)}$$

$$\sigma = \left(\frac{2E\gamma}{\pi C (1 - \nu)^2} \right)^{1/2} \quad \text{for plane stress (2.4)}$$

where;

σ, E, γ are as defined previously (equation 2.2)

C = The crack half length (m)

ν = Poissons contraction

The same surface energy term appears and is modified by Irwin¹⁸⁸ to allow for real plastic materials;

$$\sigma = \left(\frac{EG}{\pi C} \right)^{1/2} \quad (2.5)$$

where;

σ, E, C are as defined previously (equation 2.4)

G = The strain energy release rate per crack tip (N m^{-1})

For a fully elastic material then;

$$G = 2\gamma \quad (2.6)$$

The strain energy release rate is a measure of toughness and the concept of a critical stress, σ_{crit} , or a critical strain energy release rate, G_{crit} , leads to fracture mechanics and a fracture mechanical approach to stress corrosion cracking.

The lowering of the surface energy term by an adsorbed species has been used by many researchers to explain some classes of SCC failures in metals or alloys.

The adsorbed species may act to embrittle the material in one of two ways:

- 1 Directly by adsorbing at the crack tip and lowering γ .
- 2 Indirectly by subsequent diffusion of the adsorbed species to some region in advance of the crack tip where the stress - strain conditions are favourable for the nucleation of cracks.

Diffusion is to the region of maximum triaxial (hydrostatic) stress at the elastic - plastic interface of the plastic zone formed at the crack tip.

In the case of the second mechanism, hydrogen is regarded as the only species that can diffuse sufficiently rapidly to explain observed crack propagation rates, but hydrogen embrittlement (HE) due to diffusion of hydrogen to the region of maximum triaxiality is still disputed.

The first proposed hydrogen embrittlement theory, due to Zapffe^{26, 27} and Sims, the so called "molecular pressure" theory, was developed to explain the decrease in steel plasticity at normal metallurgical hydrogen concentrations (0.001%). According to this model a small (5×10^{-8} weight percent) equilibrium solubility of

hydrogen in iron at room temperature results in excessive hydrogen precipitation at crystalline defects with subsequent formation of pores and fine cracks. The thermodynamic estimate of Zapffe and Sims showed that the equilibrium pressure of the gaseous hydrogen and methane formed from the hydrogen - carbon interaction in steel reaches 40,000 to 50,000 atm., which exceeds the ultimate strength of the steel in the absence of triaxiality which is of course present under plane strain conditions. The molecular pressure theory is unable to explain the kinetics of delayed failure by HE,²⁸ the reversibility of HE and its dependence on deformation rate²⁹

. The theory was proposed before delayed failure became an important problem, and was not intended to describe subcritical crack growth. The molecular pressure theory does explain irreversible structural variations in metals during hydrogen absorption resulting in plasticity reduction.

Troiano^{30, 31} obtained important results on the delayed failure of S.A.E.-A.I.S.I. 4340 high strength steel (0.4% C, Ni-Cr-Mo steel), and developed a theory covering both B.C.C. and F.C.C. alloys. The basis of the theory is that an increase in hydrogen concentration reduces the cohesive strength of the lattice. Dissolved hydrogen interacts with the stress field present and the hydrogen equilibrium concentration, C , increases to a level governed by the triaxial stress P , according to the relation;

$$C = C_0 \exp. \left(\frac{P\bar{V}}{RT} \right) \quad (2.7)$$

where;

R = Gas constant ($J K^{-1} \text{ mole}^{-1}$)

T = temperature (K)

C = equilibrium hydrogen concentration ($\text{cm}^3 \text{ mole}^{-1}$)

C_0 = initial hydrogen concentration ($\text{cm}^3 \text{ mole}^{-1}$)

P = triaxial stress (Nm^{-2})

\bar{V} = partial molar volume of hydrogen present (ppm H (wt))

Troiano developed the concept of a critical concentration of hydrogen to cause the loss of cohesive bond strength in the lattice. This critical concentration depends upon the level of stress. Delayed HE failure (inherent in the crack jump) would therefore require a critical combination of hydrogen concentration and stress. The critical hydrogen concentration at the triaxial stress maximum is produced by directed hydrogen diffusion. The time required to reach the critical combination corresponds to the period of growth (or jump) for the crack.

Current HE theories are based upon this concept of a critical hydrogen concentration but it is very difficult to determine this value quantitatively³².

An increase in the hydrostatic component of the stress field up to the value of the theoretical strength ($0.1 E$) according to equation (2.7) increases the hydrogen solubility in iron by about seven orders of magnitude. However, this estimate does not give

the critical hydrogen concentration as it does not allow for the real hydrostatic stress.

For delayed failure by HE, the restriction of plastic deformation is an important parameter. It is known that the critical stress intensity, and crack growth rate are higher under plane strain conditions, than under plane stress³³. Plane strain conditions are those which exhibit a hydrostatic stress, due to the development of a through thickness (σ_{33}) stress, this is shown schematically in Figure 4. This forms the basis of a quantitative kinetic theory of crack growth as a result of HE developed by Gerberich^{34, 35}. This theory is based upon the work of Troiano but proposes that when the critical stress intensity, K_{crit} , is reached, the equilibrium hydrogen concentration, C_{crit} , at the point of maximum triaxial stress is equal to C_{crit} , the critical hydrogen concentration. Gerberich gives the following K_{crit} dependence;

$$K_{crit} = \frac{\frac{RT}{\alpha \bar{V}} \ln \frac{C_{crit}}{C_0} - \sigma_y / 2\alpha \left[1 + \frac{0.28r}{B} \right]}{1 - \frac{2r}{B}} \quad (2.8)$$

where;

C_0, R, T, \bar{V} are as defined previously (equation 2.7)

r = plastic zone radius (m)

B = sample thickness (m)

σ_y = yield stress (Nm⁻²)

C_{crit} = critical hydrogen concentration (cm⁻³ mole⁻¹)

α = 0.4 mm^{-0.5}

K_{crit} = critical stress intensity (Nm^{-3/2})

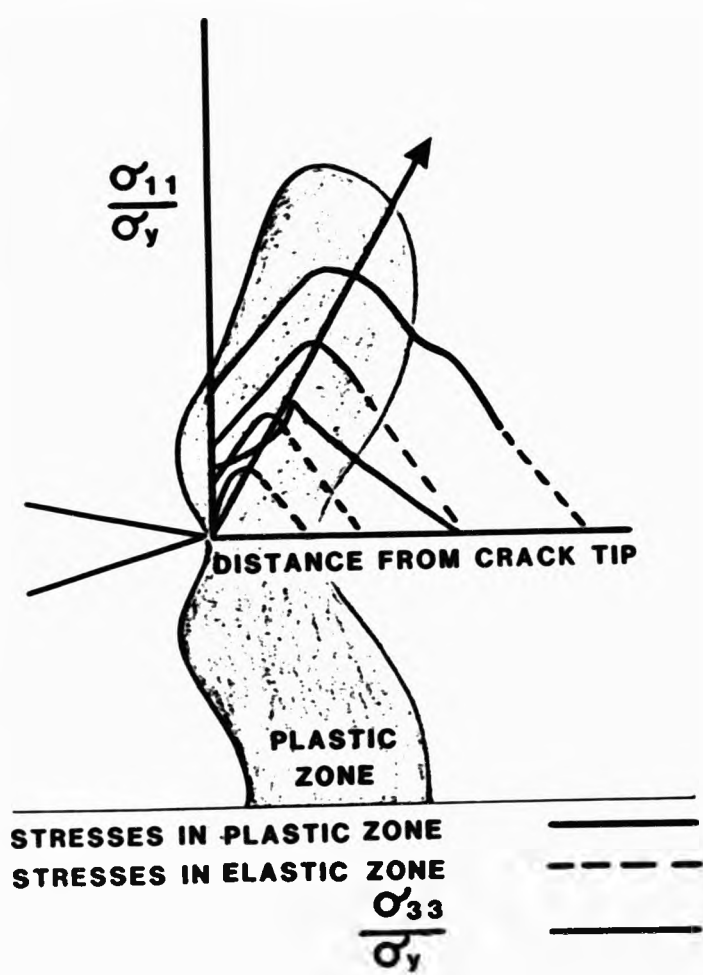


Fig 4. Schematic representation of the stress field ahead of a crack.

Equation (2.8) describes the plane strain condition when $2r/B \ll 1$, and shows a sharp increase in K_{1SCC} when the ratio $2r/B \rightarrow 1$, i.e., under plane stress. The equation contains the "indefinite" parameter: the critical hydrogen concentration.

In summary, Gerberich's theory employs the ideas of stepwise growth, the dependence of the hydrogen diffusion rate on the hydrostatic stress gradient, and the relation of the average jump distance to the steel microstructure and the stress intensity coefficient. From an analysis of data in the literature, Gerberich proposed that K_{crit} due to HE can be predicted a priori from the yield stress, the hydrogen content of the steel and the stress state. A good agreement between K_{crit} calculated from equation (2.8) and experimental results on martensitic high strength steels has been made.⁶⁴

^{36 - 38}
Oriani also postulated the reduction of the metal lattice cohesive strength with increasing hydrogen concentration, and the rupture of interatomic bonds when the critical hydrogen concentration is reached. The theory differs from that of Troiano in defining the zone in which the loss of cohesive strength occurs. According to Troiano the zone is located at some distance ahead of the crack tip (giving rise to a step wise crack growth by HE). Oriani proposes that the loss of cohesive strength occurs on the atomic level, from atom to atom, directly at the crack tip. Step wise crack growth in this theory is due to structural inhomogeneity of the material, and not directly connected with HE.

Oriani's approach is thermodynamic and gives a value for the critical hydrogen concentration, (1 atomic percent for steel)³⁹ which is inversely proportional to the stress intensity.

The two theories of Troiano and Oriani are mechanistically incompatible.

To return to equation (2.2), in cases where plastic deformation is involved, the equation must be modified to include a plastic work term γ_p .

$$\sigma = \left(\frac{E(\gamma_s + \gamma_p)}{b} \right)^{1/2} \quad (2.9)$$

where;

b, E, σ are as defined previously (equation 2.2)

$\gamma_s =$ specific surface energy (Jm^{-2})

$\gamma_p =$ work required for plastic deformation (Jm^{-2})

Generally γ_p is greater by several orders of magnitude than γ_s so that any reduction of γ_s by adsorption will have a negligible effect on the fracture stress. Further, plastic deformation associated with SOC is important since where it occurs it allows the crack tip to yaw, resulting in crack blunting. In these circumstances an adsorption model would not predict an increased crack growth rate. Specific adsorption then is only likely to be of significance in the cracking of less ductile materials where plastic deformation is negligible and γ_p is not very much greater than γ_s .

It is a commonly held view therefore that hydrogen embrittlement is the principal cause of stress corrosion cracking of high strength steels. With due regard to the proposed anodic dissolution mechanisms of SCC in AlZnMg alloys, it would not be unreasonable to propose a hydrogen embrittlement mechanism in these high strength and limited plasticity alloys, provided a diffusion mechanism for hydrogen can be shown in AlZnMg alloys that allows sufficient hydrogen to diffuse into and embrittle the alloy.

2.3 REVIEW OF THE STRESS CORROSION CRACKING OF HIGH STRENGTH ALUMINIUM ALLOYS, WITH PARTICULAR REFERENCE TO Al-Zn-Mg ALLOYS - ANODIC DISSOLUTION MECHANISMS

2.3.1 A summary of experimental observations of SCC in Al-Zn-Mg alloys

Stress corrosion cracking of the 7000 series aluminium based alloys has been a specific problem throughout the thirty year period of development of lightweight, high strength alloys for aerospace and military applications. Extensive study has been devoted to the mechanical aspects of crack growth, the effect of environment both gaseous, aqueous and organic based, the effect of pH, the effect of electrochemical polarisation and of metallurgical condition, especially heat treatment and alloy composition. These studies have been based both on flat specimens, using a total time to failure criteria to rank different effects, and, more recently, on pre-cracked specimens using crack growth rate and the threshold stress intensity below which crack propagation does not occur (K_{ISCC}). In the main these studies on pre-cracked specimens have concentrated on the results

obtained using double cantilever beam (DCB) specimens, where the stress intensity at the crack tip decreases as the crack grows.

These studies have been conducted with the underlying assumption that an anodic dissolution mechanism was responsible for crack growth. However, recently a whole series of additional experiments have been performed to look more closely at the mechanism operating during crack growth, and a hydrogen embrittlement mechanism has gained greater but not exclusive support.

The specific, well documented effects of environment, heat treatment etc, will not be dealt with at length except to summarise here the most important findings, and the reader is referred to two excellent review articles by Speidel^{10,63}. In later sections this literature review will concentrate on the disputed questions of crack growth mechanism.

2.3.1.1 Mechanical aspects

The dominant mechanical parameter controlling SCC growth is the crack tip stress intensity, and the stresses around the tip of the crack are fully characterised by the stress intensity factor, K , provided that plasticity around the crack tip is limited. Experiments relating crack growth rate to stress intensity (V-K) give characteristic curves (Fig 5), with a plateau region bounded by a stress intensity dependent region I, which terminates in a threshold stress intensity below which further crack growth does not occur (in practice this figure is probably arbitrary depending

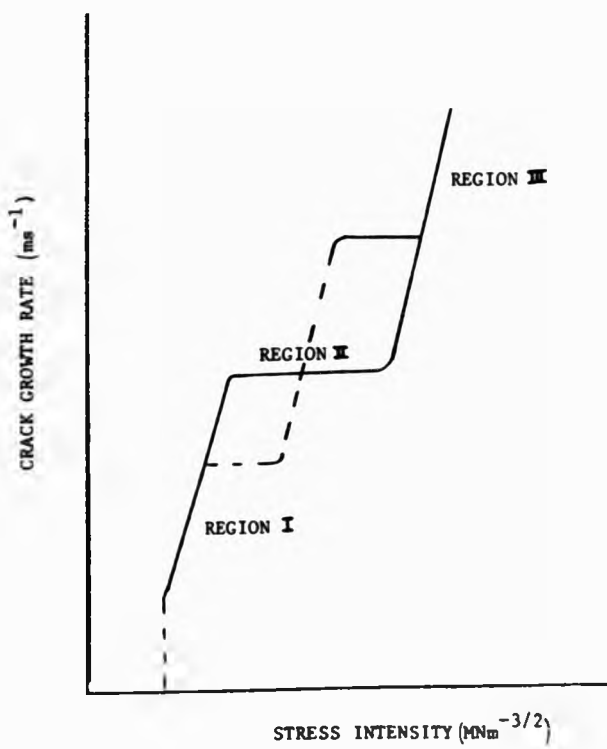


Fig 5 Schematic representation of the influence of stress intensity on stress corrosion crack velocity.

solely on the experimenter's patience). Region III is stress dependent and terminates at K_{1C} , the material fracture toughness. More complex curves show two distinct plateau regions with a number of stress intensity dependent regions of crack growth, possibly corresponding to different rate controlling processes.

Other mechanical parameters such as the state of stress and the loading rate are reported as being of minor importance (but see Section 2.4.5 on the effect of Mode III loading on hydrogen embrittlement). Of utmost importance is the orientation of non-recrystallised grains in relation to the applied stress direction. Cracks parallel to the preferred grain boundary orientation, with applied tensile stress perpendicular to it, grow up to 10 times faster than cracks oriented in other directions.

2.3.1.2 Environmental aspects

1) Gases

Crack growth is absent in all dry gases, including hydrogen, but crack growth is observed in gases containing water vapour (Fig 6) with the following results:

- a) Region II crack growth rate depends strongly on the water vapour partial pressure of the gas (Fig 7).
- b) Many different commercial high strength aluminium alloys, when exposed to gases with 100% relative humidity, exhibit region II crack growth velocities between 10^{-8} to 10^{-1} m s⁻¹

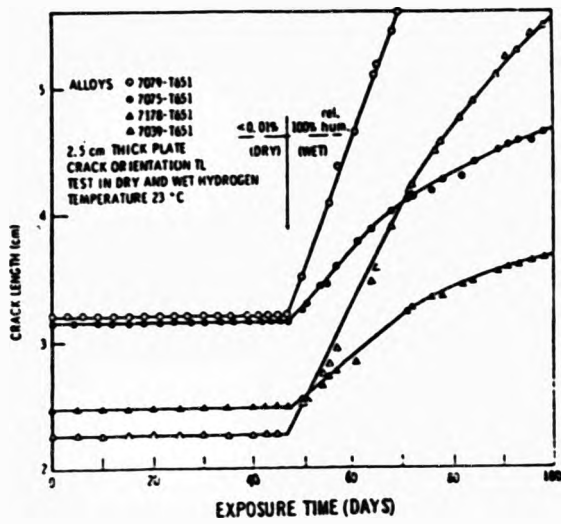


Fig 6 Effect of humidity on SCC growth of different aluminium alloys in hydrogen (after Speidel).

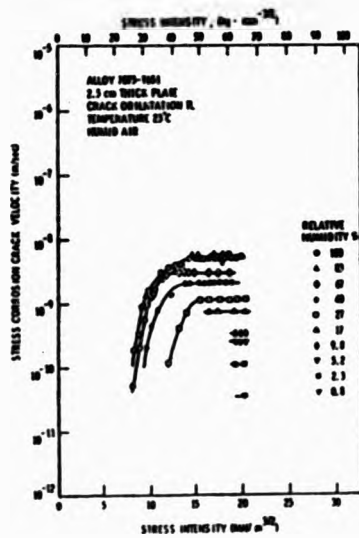


Fig 7 Effect of humidity and stress intensity on SCC velocity of a high strength aluminium alloy in air (after Speidel).

and 10^{-9} m s⁻¹, i.e. metallurgical parameters influence region II crack growth only mildly.

c) The stress dependent region I of the V-K curve for these alloys is strongly influenced by metallurgical parameters.

2) Organic Liquids

Crack growth rates in organic liquids are a function of the water content. Plateau velocities for crack growth in common solvents such as methanol, ethanol, acetone and benzene containing 0.05% water fall within the scatter band of crack velocities obtained in distilled water (Fig 8).

3) Aqueous Solutions

Most commercial aluminium alloys show little acceleration of SCC growth in region II of the V-K curve when the environment is changed from moist gas to distilled water.

In neutral solutions most cations tested (Li^+ , Na^+ , K^+ , Rb^+ , Cs^+ , Ca^{2+} , Al^{3+} and NH_4^+) do not appear to have any specific effect (Fig 9) except that they influence the solubility product and hence can govern the concentration of specific anions. Hg^{2+} and H^+ are the exceptions. H^+ is discussed under pH and Hg^{2+} can cause fast intergranular corrosion.

Of the anions tested, only Cl^- , Br^- and I^- (Fig 10) accelerate SCC in aqueous solution above the velocity measured in distilled

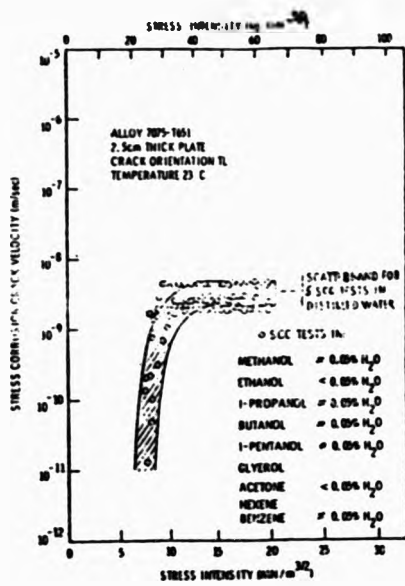


Fig 8 The effect of various organic liquids on subcritical crack growth in 7075 - T651 (after Speidel).

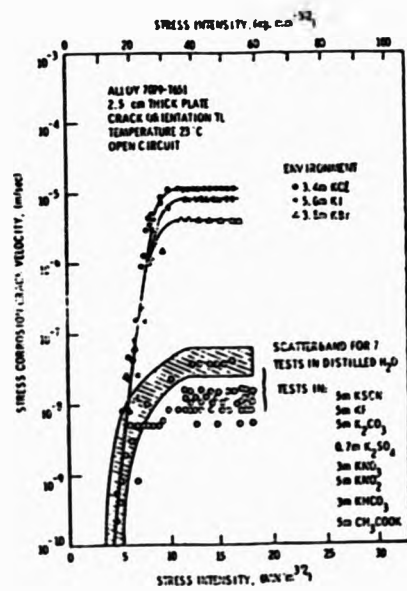


Fig 9 The influence of various anions on SCC velocity of 7079 - T651 in aqueous solution (after Speidel).

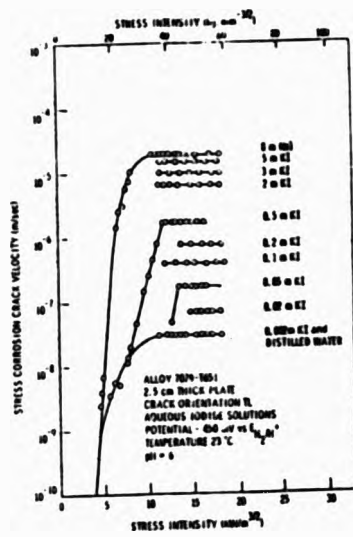


Fig 10 SCC velocity of 7075 - T651 immersed in aqueous solutions of various iodide concentrations (after Speidel).

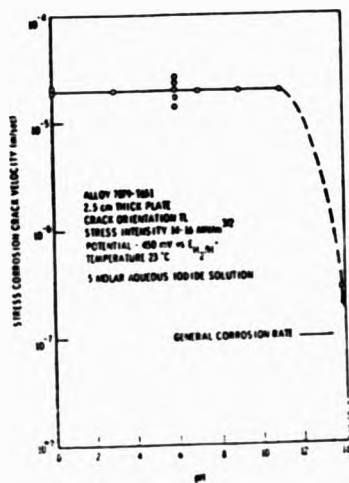


Fig 11 The effect of pH on stage II velocity of SCC in 7075 - T651 (after Speidel).

water. This result is obtained even under extreme conditions which include;

- a) the most susceptible alloys, eg 7079 - T651
- b) applied potentials from -1.55 to +14 volts (vs SHE)
- c) stress intensity levels near K_{IC} .

The halide ion F^- does not accelerate SCC growth. Cl^- , Br^- and I^- are the unique pitting agents for aluminium alloys and so they can influence both the rate of crack growth and the initiation of SCC by pitting reactions forming stress raisers. The acceleration of SCC by halides depends strongly on metallurgical factors, for example the maximum acceleration of SCC in 7075 - T651 in saturated sodium chloride is by a factor of four. The maximum acceleration of 7079 - T651 is by a factor of 10^3 (at 23 C).

The effect of increasing pH on plateau velocity is not apparent until around pH 11 when plateau velocity begins to fall (Fig 11). A decrease in pH from 11 to 0 causes a shift in Region I to markedly lower stress intensities (Fig 12). Part of the explanation of the effect of pH lies in the different chemistry found in the crack, as opposed to the bulk solution, where the $AlCl_3$ formed hydrolyses to acidify the solution forming a constant pH of 3.5. The pH within the SC crack has been measured and found to lie between pH 3.2 and 3.4.

The effect of temperature is to increase the plateau velocity of 7079 - T651 by an order of magnitude for a 100 C temperature

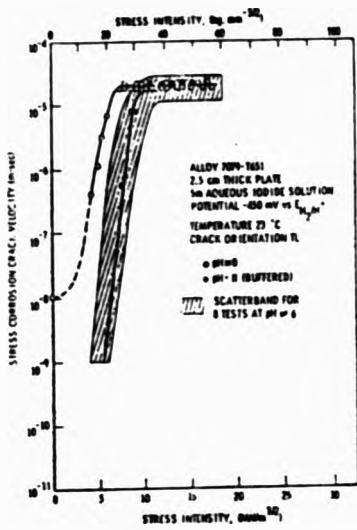


Fig 12 The effect of pH on stage I SCC velocity in 709 - T651 (after Speidel).

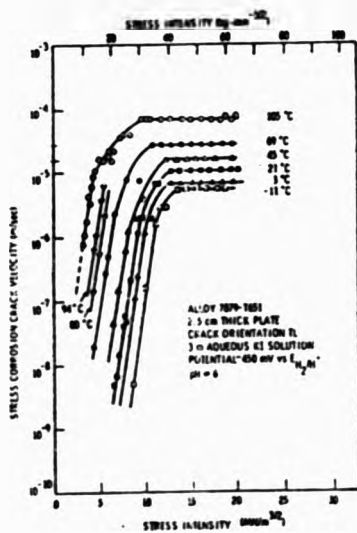


Fig 13 SCC velocity in 709 - T651 as a function of temperature (after Speidel).

increase from 0 to 100 °C. At higher temperatures, Stage I growth is shifted to lower stress intensities (Fig 13). The activation energy of Stage I and II crack growth has been measured and found to be 112.7 kJ/mole and 15.9 kJ/mole respectively which may indicate a change in the rate controlling processes. These values are similar to those found for titanium alloys.

The effect of applied potential from -250 mV anodic to -1000 mV cathodic, versus the Standard Hydrogen Electrode (SHE), is to reduce the plateau velocity from $1 \times 10^{-5} \text{ m s}^{-1}$ to $7 \times 10^{-9} \text{ m s}^{-1}$ in 7079 - T651 in 5 M KI at 23 °C, which is lower than that in distilled water ($6 \times 10^{-8} \text{ m s}^{-1}$). Stress intensities during stage I are similarly increased. These results indicate SCC is being suppressed by cathodic protection at these potentials (Fig 14).

Mechanical, chemical and metallurgical influences on SCC velocities are inter-related in a complex way. For example alloy 7079 - T651 at anodic potentials shows no effect of pH on stage II crack growth rates, but at cathodic potentials there is a marked effect: at -1.0 volt (vs SHE) and pH 6 the plateau velocity is 10^{-8} m s^{-1} , and at pH 0 the plateau velocity is $3 \times 10^{-5} \text{ m s}^{-1}$ (Fig 15).

The pH effect vanishes at the free corrosion potential. However, for alloy 7075 - T651 there is a marked pH effect on crack growth rate at the free corrosion potential, although at more anodic potentials the crack velocity becomes independent of pH (Fig 16).

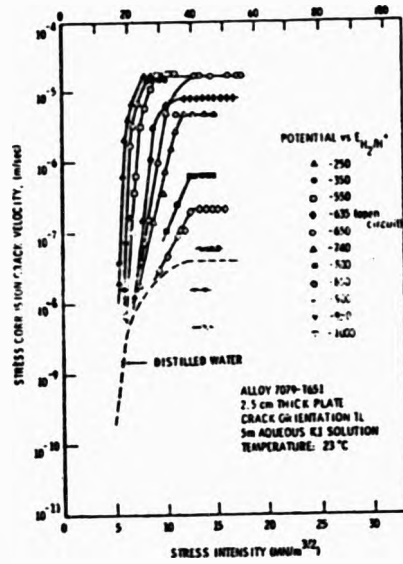


Fig 14 The effect of electrochemical potential on SCC in 7079 - T651 (after Speidel).

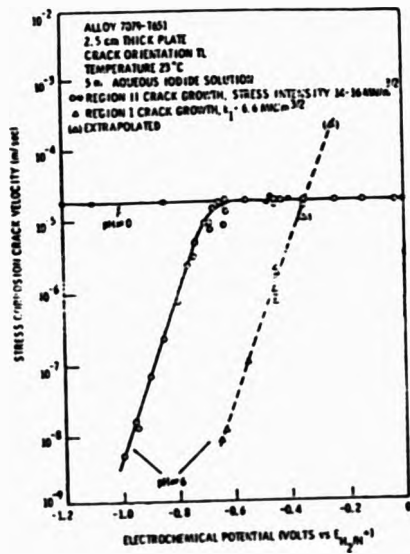


Fig 15 The influence of electrochemical potential and pH on SCC growth in 7079 - T651 (after Speidel).

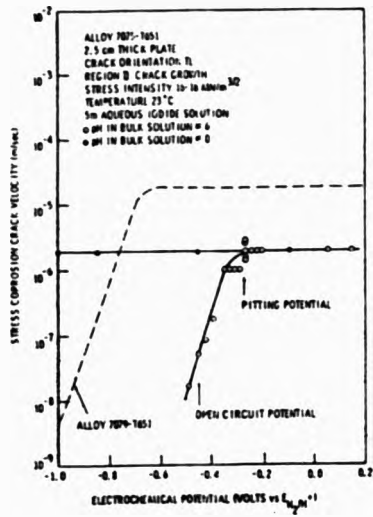


Fig 16 The influence of electrochemical potential and pH on SCC velocity in 7075 - T651 (after Speidel).

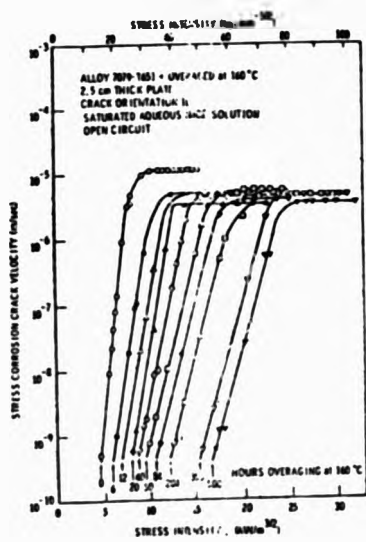


Fig 17 The effect of overaging on SCC velocity in 7079 alloy (after Speidel).

2.3.1.3 Metallurgical aspects

Alloy composition and heat treatment strongly affect SCC growth in 7000 series alloys. The subject is extremely complex since variations in alloy composition and heat treatment can affect not only mechanical variables such as the stress dependence of the crack velocity, but also environmental variables such as those previously discussed. So far no single metallurgical parameter has been identified which would control the susceptibility of the various AlZnMg alloys.

A number of trends are apparent, but there are numerous exceptions. The 7000 series alloys become more susceptible to SCC as the yield strength is increased and become more resistant to SCC as the alloy fracture toughness increases.

1) Alloy composition

This subject is dealt with to some extent in Section 2.1.5. The following general trends apply:

- a For any given alloy system, susceptibility to SCC increases with the amount of alloying additions that can be put into super-saturated solid solution.
- b SCC resistance of the ternary and quaternary alloy systems is influenced by the sum and ratios of alloying additions.
- c Small additions (0.1 to 0.5%) of Cr, Mn, Ag, Zr, Ti, V, Ni and Li to high purity ternary and quaternary alloys can reduce susceptibility to SCC.

2) Precipitation hardening

Precipitation hardening is of utmost importance to the strength of 7000 series alloys and has a strong effect on SCC.

Supersaturated solid solutions are quite resistant to SCC.

In the AlZnMg ternary alloys on overageing from the T651 condition there is initially a small decrease in plateau velocity (for 7079 at the free corrosion potential in saturated NaCl, from 1×10^{-5} to 7×10^{-6} m s⁻¹ as a result of overageing for 6 hours at 160 C) followed by no effect on plateau velocity for extensive periods of overageing (up to 500 hours at 160 C). The main effect of overageing is to increase K_{1SCC} from 4 MNm^{-3/2} in the T651 condition to 17 MNm^{-3/2} when overaged at 160 C for 500 hours (Fig 17). This increase in K_{1SCC} parallels the increase in K_{1C} and decrease in yield stress for the same thermal treatment (Fig 18).

The situation is different for AlZnMgCu type 7000 series alloys where overageing the 7178 alloy for 15 hours at 160 C causes a reduction in plateau velocity of just under three orders of magnitude from 10^{-8} m s⁻¹ to 3×10^{-11} m s⁻¹ (Fig 19). (Note the three orders of magnitude difference in plateau velocity for 7079 and 7178 alloys in the T651 condition). The full V-K curves have not been measured for the copper containing ternary alloys because of the very low crack velocities involved.

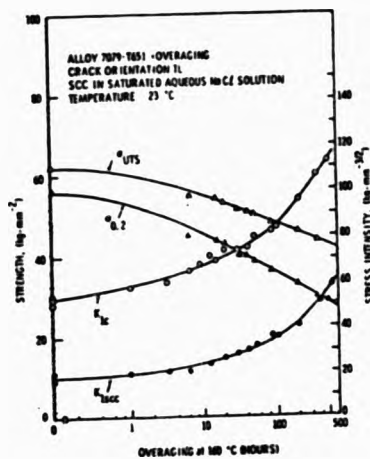


Fig 18 The influence of overaging on strength, toughness and SCC resistance of 7079 alloy (after Speidel).

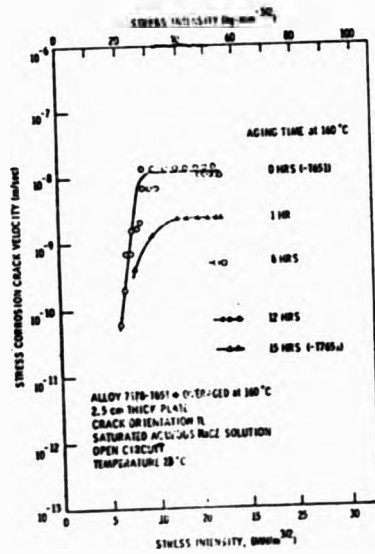


Fig 19 The effect of overaging on SCC velocity in the 7178 Cu containing alloy (after Speidel).

2.3.2 Electrochemical mechanisms

The first suggested mechanism of anodic dissolution in AlZnMg alloys was reported by Dix and co-workers⁴⁰⁻⁴² and is based upon the MgZn₂ grain boundary precipitate being anodic to the aluminium matrix. They concluded that MgZn₂ would dissolve preferentially leaving the grain boundary weakened and susceptible to tearing in the presence of stress.

A second early attempt to explain the influence of microstructure on the susceptibility to intergranular SCC concentrated on the mechanical properties of the precipitate free zones. It was proposed that preferential plastic flow would take place in the PFZ and preferential dissolution would occur along the regions where plastic flow had taken place^{11,55}. As a result of this theory attempts were made to control the susceptibility by controlling the width and strength of the supposedly weak PFZ⁵⁷.

To return to the model of SCC proposed by Dix. If the inter-particle spacings on the grain boundary are increased by employing a slower quench from the solution treatment temperature this results in a higher degree of stress-corrosion resistance^{43, 44}, and tends to confirm the model proposed by Dix. The effect of grain boundary precipitate distribution can also explain why concentrated alloys are more susceptible than dilute alloys.

The viewpoint that MgZn₂ grain boundary precipitates are detrimental to the SCC resistance of these alloys had led to the suggestion that eliminating or reducing the number of particles on

grain boundaries would be beneficial, and evidence to this effect^{40, 44, 45, 46} has been presented

However, it has been shown by McEvily et. al. that decreased susceptibility is correlated with an increase in grain boundary area fraction covered by precipitates (though the number may indeed be less), and this evidence⁴⁸ indicates that the precipitates have a beneficial role. They proposed, therefore, that MgZn₂ precipitates act as sacrificial anodes and retard cracking along the grain boundary. They argued that concentration polarisation limits the cathode current density (i_c) and therefore i_a depends upon the cathode to anode area ratio A_c/A_a according to equation 2.10

$$i_a = i_c \frac{A_c}{A_a} \quad (2.10)$$

The anode current density determines the rate at which precipitates dissolve and therefore the larger the anode area the slower the rate of dissolution. Overageing of the alloy (leading to fewer but larger grain boundary precipitates) is well known to improve SCC resistance. Peel⁴⁹ also favoured a sacrificial protection model and studied the effect of double ageing treatments and copper additions both of which improved SCC resistance, the former by increasing the line fraction of grain boundary precipitates. The effect of copper additions is less certain. Peel and Poole⁵⁰ show that grain boundary precipitates containing copper in the less susceptible quaternary alloy Al-5.6%

Zn -2.5%Mg -1.6%Cu have an electrode potential $\approx 75\text{mV}$ electropositive to MgZn_2 . In this condition they could still act as sacrificial anodes. Evidence from cathodic polarisation curves is at variance with an anodic protection or precipitate dissolution model of the beneficial aspects of copper additions, since increasing copper contents increase the rate of the cathodic reaction. Since the dissolution reaction is under cathodic control the rate of the anodic reaction should also be allowed to increase. However, Peel and Poole have shown evidence of sacrificial protection by a technique of anodic polarisation in aqueous sodium chloride followed by SEM investigation. They showed in the ternary AlZnMg alloy preferential grain boundary attack in the as-quenched condition due to high magnesium and zinc contents at the grain boundary and unattacked grain boundaries in the aged and overaged alloy (T6 and T73) due to solute depletion at the grain boundary. In the quaternary AlZnMgCu alloy they showed unattacked grain boundaries in the T6 condition with a superimposed central region of attack due to short-range copper depletion. In the T73 condition the quaternary alloy grain boundary was preferentially attacked. These results are shown schematically in Figure 20. These indicate that in the susceptible ternary alloy, dissolution occurs in the region adjacent to the solute depletion zone of the PFZ in peak aged and overaged tempers. In the less susceptible alloy dissolution again occurs in the region adjacent to the grain boundary solute depletion zone.

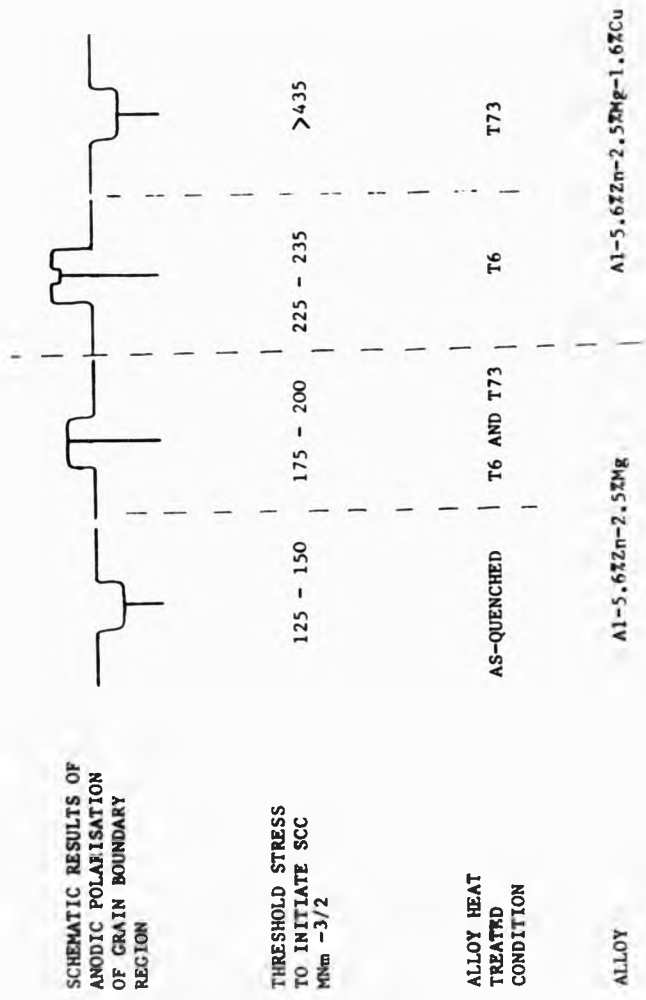
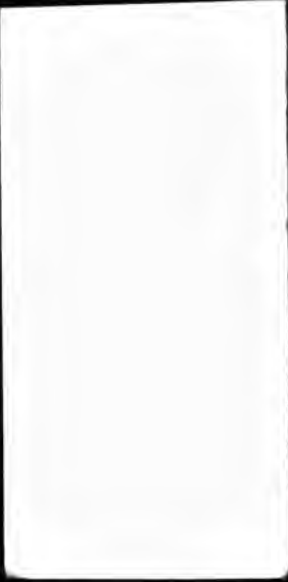


Fig 20 Schematic representation of SEM images obtained by anodic polarisation of AlZnMg and AlZnMgCu alloys in aqueous sodium chloride.



The development of an attacked grain boundary in the overaged quaternary alloy is taken as indicating cathodic protection (by preferential anodic dissolution of overaged grain boundary precipitates) in an alloy showing a much reduced susceptibility to SCC as evidenced by a higher threshold stress to initiate SCC ($>435 \text{ MNm}^{-2}$ compared with $125\text{-}150 \text{ MNm}^{-2}$ for the ternary alloy in the T6 temper). Peel and Poole concluded that any mechanism based upon the rapid dissolution of grain boundary precipitates as proposed by Dix had to be discounted in favour of a sacrificial anode theory, as being the only model which was able to explain the improvement in SCC resistance following overageing.

The development of a solute depletion zone and a precipitate free zone has also been investigated as being another microstructural feature with which SCC susceptibility can be correlated. Doig and Edington⁵¹ investigated a series of PFZs formed by vacancy and solute depletion zones in quench-interrupted Al-5.0% Zn-3.2% Mg alloys. They showed magnesium and zinc concentration profiles in the aged condition symmetrically depleted around the grain boundary (Fig 21).

The model of PFZ formation employed was dependent upon the immediate formation of a solute depletion and vacancy depletion zone during quenching. The solute depletion zone was produced by volume diffusion of solute to heterogeneously nucleated grain boundary precipitates on quenching to 330 C which is above the GP zone solvus. Further quenching to below the GP zone solvus results in re-solution of the smaller GP zones near the grain

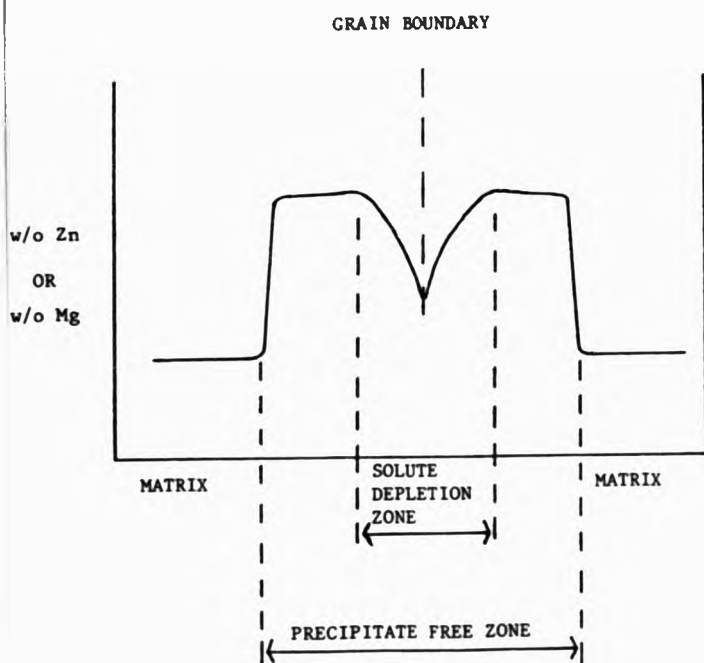


Fig 21 Solute profile of a quench-interrupted and aged Al-5.9% Zn-3.2% Mg alloy.

boundary giving rise to the final precipitate-free zone. This range of GP zone sizes results from their growth at a rate controlled by both the solute and vacancy profiles, which is shown schematically in Figure 22.

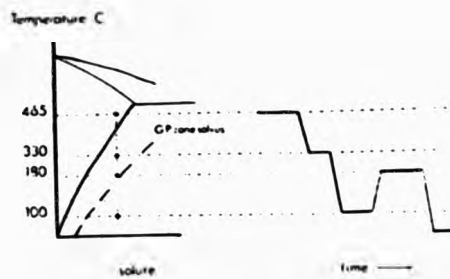
In their work Doig and Edington proposed on the basis of corrosion potential measurements that preferential grain boundary precipitate dissolution would occur ($E_{\text{corr}}^{\text{MgZn}} = -1300 \text{ mV}$ and $E_{\text{corr}}^{\text{matrix}} = -1050 \text{ mV}$, versus SCE), and that the dissolution reaction was under cathodic control, the local cathode being the region of solute depletion which increases on ageing to peak hardness, thus facilitating the anodic reaction.

There was a correlation evident between the extent of solute depletion and the SCC susceptibility, SCC susceptibility increasing with increasing solute depletion zone width. No correlation was found between these factors and the total PFZ zone width.

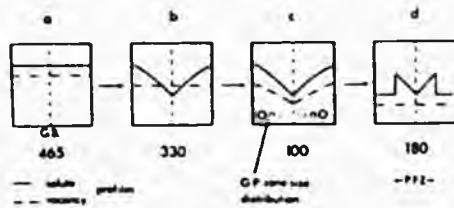
In the absence of direct observation it is possible that a similar result to that obtained by Peel and Poole pertained, with the zone sandwiched between the solute depletion zone and the matrix being the site of the anodic reaction.

Doig and Edington however concluded that;

- 1) The stress corrosion reaction was under cathodic control.
- 2) The solute depletion zone was the site of the cathodic



(a)



(b)

465°C — Solution treatment temperature
 330°C, 100°C — Quench interruption temperature
 180°C — Ageing temperature

Fig 22 (a) Schematic diagram of the heat treatment used to develop the PFZ in an Al-5.9 Zn-3.2 Mg alloy. The GP zone solvus temperature for this alloy is 170°C.
 (b) Schematic solute and vacancy profiles around the grain boundary aged as shown in (a) above.

reaction, which with increasing width produced by quench interruption for longer periods of time (10 minutes compared with 2 minutes), leads to greater grain boundary precipitate dissolution rates (Fig 23).

- 3) The kinetics of stress corrosion crack growth is explained in terms of a model which includes as a controlling factor the polarisation characteristics of the solute depleted region within the PFZ. For example, the improvement in stress corrosion susceptibility gained in overageing the 7075 alloy from the T6 to the T73 condition may be associated with the short range redistribution of copper within the PFZ.

⁵²
Raghavan has also studied PFZs in an Al-2.2 atomic percent Zn, 4.7 atomic percent Mg alloy formed by air cooling and ageing at 200 °C for times ranging between 0.1 and 75 hours; under these conditions the PFZ is formed by a different mechanism in that only a vacancy-depletion zone is assumed to form initially. GP-zones are not subsequently formed in regions of low vacancy concentration and on ageing no precipitates form due to the absence of GP-zones. No solute-depletion zone had formed prior to ageing as the quench from the solution temperature was uninterrupted. The solute-depletion formed on ageing develops very quickly (0.1 h) (see Fig 24) and in agreement with Doig and Edington's results the PFZ shows an increase in zinc and magnesium concentration between the matrix and the solute depletion zone.

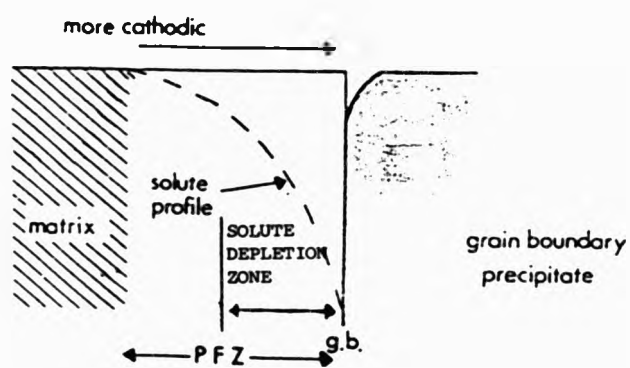
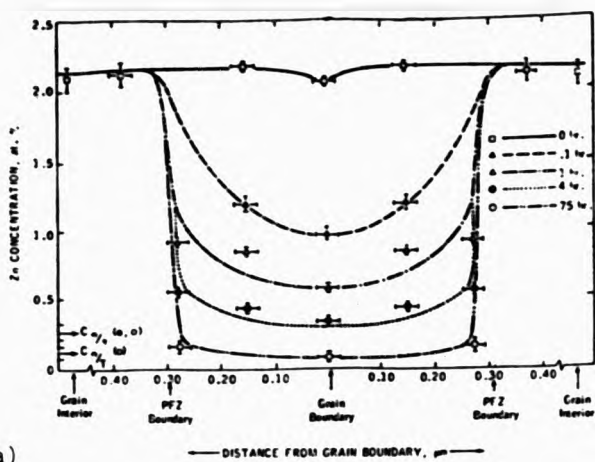
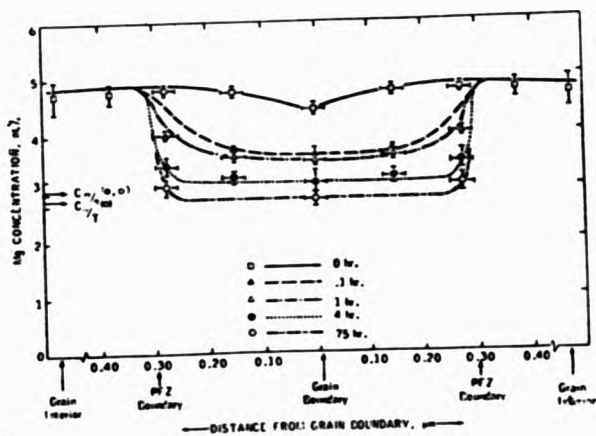


Fig 23 Schematic diagram showing the distribution of the corrosion reaction at the grain boundary in an aged Al-5.9% Zn-3.2% Mg alloy (after Doig and Edington).



(a)



(b)

Fig 24 (a) Zn concentration profiles across PFZ.

(b) Mg concentration profile.

Both for an Al-2.2% Zn-4.7% Mg alloy solution heat treated at 465°C, air cooled to room temperature and aged for the above times at 200°C. C^{η}/η and C^{τ}/τ are the ratios of the concentration of the η and τ phases respectively (after Raghavan).

Raghavan concluded that Doig and Edington's proposal to correlate SCC susceptibility with solute depletion zone width rather than PFZ width was more reasonable, in particular solute distribution within the zone of solute depletion.

Ward and Lorimer⁵³ have shown that in a copper containing 7075 alloy, no copper depletion occurred with a consequent improvement in SCC resistance. This result is however at variance with the result of Peel and Poole⁵⁰ that copper depletion causes a marked decrease in the rate of the cathodic and hence the anodic reaction.

2.3.3 Mechanical aspects of crack growth mechanisms

Recent work on the strength of the PFZ of AlZnMg and AlZnMgCu alloys which are most susceptible to SCC has shown that contrary to earlier views (Section 2.3.2), slip is not concentrated in the PFZ, but is concentrated in narrow bands across the whole grain.^{58,59}

The hypothesis of preferential flow has been used to explain the influence of the ageing process on the susceptibility to SCC of high strength aluminium alloys.¹¹ The following assumptions were made;

- 1) At maximum susceptibility slip occurs only, or at least preferentially in the PFZ.
- 2) At maximum susceptibility, grain boundary precipitates



formed a continuous film or interconnected rows, thus preventing slip across the grain boundary.

3) At maximum susceptibility, large areas near the grain boundary are free from precipitates.

4) Preferential corrosive attack occurs along the regions where preferential plastic flow has taken place.

In a series of experiments on Transmission Electron Microscope (TEM) specimens of AlZnMg and AlZnMgCu alloys at various stages of heat treatment, Speidel ⁶⁰ has shown that;

1) At maximum susceptibility slip occurs across the whole grain. No preferential slip near the grain boundary was observed.

2) No continuous or interconnected rows of grain boundary precipitates were observed, but slip transfer across the grain boundary was observed.

3) If preferential corrosive attack did occur along the regions where preferential plastic flow had taken place, one would expect transgranular SCC since slip is concentrated in narrow bands across the grain.

The dislocation patterns observed did however lead to two theories which relate to present research.

Stress concentration: Near the crack tip stress concentrations form due to dislocation pile-ups and limited plastic relaxation.



This was the dominant deformation substructure in susceptible alloys. The adsorption of the corrosive environment, or a constituent of it, would lower the strength of the strained atomic bonds at the crack tip (stress sorption cracking). Speidel also proposed that hydrogen may build up at grain boundaries under the influence of these highly localised stresses but assumed that these hydrogen rich areas would become anodic to the matrix and create a susceptible path for anodic dissolution.

The suggestion was also put forward that dislocation pile-ups at grain boundary precipitates may produce microcracks which would enhance crack growth. Crack propagation was assumed to be via a series of chemical and mechanical steps.

Slip Step height: Preferential attack occurs at the region of high local dislocation density i.e. the dislocation pile-ups observed at the grain boundary. Stress corrosion cracks would propagate by a series of rapid chemical attacks at dislocation sites and the linking of these sites to form a macrocrack.

A high slip step formed by dislocation pile-up (planar slip) would also facilitate oxide film rupture, under tensile stress, exposing new metal to an advancing crack front. This is of course a restatement of the slip-dissolution mechanism advanced by Scully^{61,62} and others to explain the mechanism of many alloy systems showing susceptibility to stress corrosion cracking.

2.4 REVIEW OF THE STRESS CORROSION CRACKING OF HIGH STRENGTH ALUMINIUM ALLOYS, WITH PARTICULAR REFERENCE TO Al-Zn-Mg ALLOYS - HYDROGEN EMBRITTLEMENT MECHANISMS

2.4.1 Environmental aspects

2.4.1.1 Crack growth in gaseous environments

It has already been reported (Section 2.3.1) that 7000 series alloys do not show crack growth in dry molecular hydrogen and that crack growth rates increase with increasing water vapour content. This is true even for a ambient hydrogen pressure of 70 MNm^{-2} and at stress intensities near to K_{1C} . Neither is increased fatigue crack growth detectable in hydrogen atmospheres in these alloys⁶⁶ where the constant exposure of fresh metal by fatigue, with no oxide to impede hydrogen entry, might be expected to enhance crack growth rates.

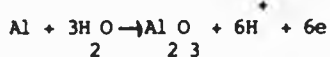
⁶⁷ Nelson dissociated molecular hydrogen on a tungsten filament heated to 2000 C and brought an atomic-molecular hydrogen gas mixture near to a pre-cracked specimen of 7075 alloy with no reduction in fracture toughness.

⁶⁸ More recently, Koch, has reported fracture of smooth tensile specimens of 7075-T6 held at 75% of their fracture load in ionised hydrogen at a pressure of $2 \times 10^3 \text{ Nm}^{-2}$. The cracks formed were predominantly brittle intergranular with areas of cleavage. A possible conclusion to be drawn is that only ionised gaseous hydrogen gives a large enough hydrogen fugacity to produce embrittlement in the gaseous state.

The crack growth rate of 7000 series alloys is strongly dependent upon the water vapour content of the environment (Section 2.3.1). The Kelvin equation predicts that no capillary condensation would occur in cracks at relative humidities below 30%⁶⁹. Therefore, at the lower humidities shown in Figure 7, the crack tip is probably not covered in liquid water and anodic dissolution therefore cannot take place, but significant crack growth does occur over a range of stress intensities.

A particular advantage of studying the stress corrosion cracking of these alloys in water vapour at low temperature is that corrosion of the crack sides is considerably reduced. This allows a detailed study of crack morphology, which is further discussed in Section 2.4.3.

At low relative humidities, where liquid water is not present at the crack tip, the observed subcritical crack growth must be due to a reaction of H₂O molecules with aluminium near the crack tip. Since water is known to react with aluminium according to the following summary reaction;



This leaves hydrogen embrittlement as the only convincing explanation. Subcritical crack growth in aqueous solutions at the free corrosion potential is attributable to the same mechanism. The reaction of water with aluminium is discussed in detail in Section 2.5.6.

The combined effect of Water Saturated Air Vapour (WSAV) and tensile stress at slow (10^{-3}) strain rates has also been studied⁷⁰. Specimens of an Al-6%Zn-3%Mg alloy were aged at temperatures between 20 and 200 C for 24 h. followed by exposure to WSAV at 70 C for 72 h. They were shown to exhibit a ductility trough in the temperature range 100-140 C. Dry control samples showed that this effect was partially due to age hardening; however, the extent of ductility loss was not as great (Fig. 25), the additional loss of ductility of the specimens exposed to WSAV being due to embrittlement.

The effect of isothermal exposure to WSAV at 120 C was also studied (Fig. 26). The samples were in the solution treated condition.

The curve shows four distinct regions: region 1 where ductility falls to 0.2-0.3% for samples exposed to WSAV, region 2 where there is a uniformly low ductility, region 3 where there is an abrupt recovery of ductility up to the value of dry specimens and region 4 where the specimens are again embrittled. During the ageing process precipitation in the grains and at the grain boundaries takes place and the precipitates grow continuously. During stage 1 and 2 no grain-boundary precipitates showed the presence of nucleated hydrogen bubbles. At the onset of stage 3 hydrogen bubbles were associated with grain-boundary precipitates while at the end of stage 3 and throughout stage 4 all grain-boundary precipitates nucleated hydrogen bubbles. At the

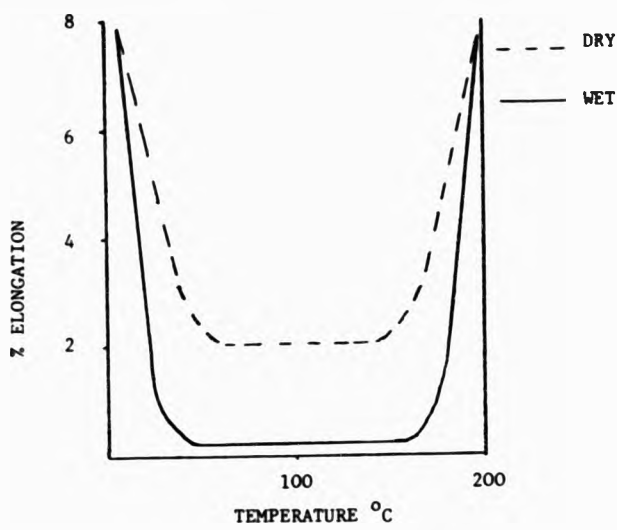


Fig. 25 The effect of ageing temperature on the embrittlement of Al-6% Zn-3% Mg exposed to WSAV at 70°C for 72 hours (after Christodoulou and Flower).

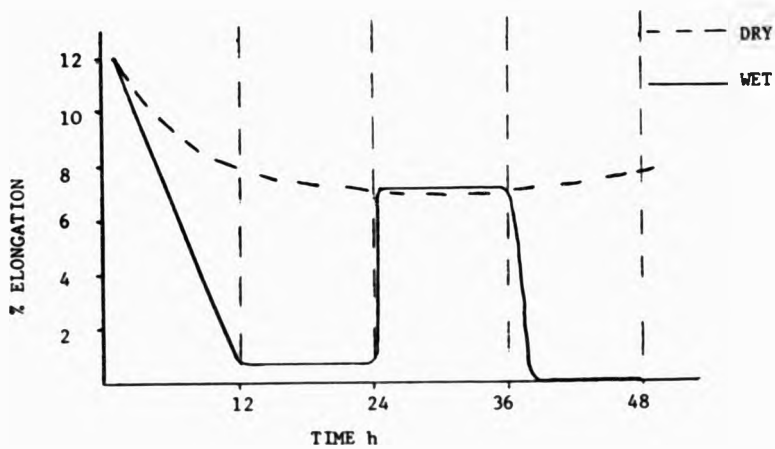


Fig. 26 Ductility of an Al-6% Zn-3% Mg alloy isothermally exposed to WSAV at 120°C and tested at various times (after Christodoulou and Flower).

beginning of stage 3 the grain boundary precipitates had grown to 200 Å.

The recovery of ductility in the isothermally-aged specimens precludes any possibility of an interpretation of mechanism in terms of anodic dissolution. Resistance to embrittlement, assuming a mechanism based on hydrogen as previously discussed, could be due to a variation in the rate of hydrogen entry, or to a difference in tolerance to the presence of hydrogen by different microstructures. An embrittlement mechanism based on the latter has been proposed on the basis of evidence from the isothermal tests. During stage 1, age-hardening and hydrogen accumulation both contribute to embrittlement, the age-hardening component being demonstrated by the dry specimens which reach a constant ductility of around 3%. Embrittlement in the WSAV samples reaches a critical level when the grain boundaries are fully embrittled, and stage 2 commences, with a ductility of 0.2-0.3%. Plastic deformation is still required to open up the fracture face as evidenced by a fully intergranular fracture with slip steps present.

The onset of stage 3 is associated with the heterogeneous nucleation of hydrogen bubbles on developing grain boundary precipitates. This event will reduce the grain boundary concentration of hydrogen and not immediately affect the matrix hydrogen concentration due to the lower hydrogen mobility in the matrix. This can be correlated with the fracture surface in stage 3 which shows evidence of intergranular followed by transgranular



fracture. Transgranular cracking occurs where the stress to propagate a crack in the grain is less than the stress required to propagate an intergranular crack due to the reduction in grain boundary hydrogen. Ductility is regained abruptly as a result of the overaged grain boundary precipitates acting as getters for grain boundary hydrogen.

As the level of hydrogen in the bubbles increases, the strain in the matrix also increases (giving rise to plastic deformation) as does the level of hydrogen in solution in the grain boundary in equilibrium with the growing bubble. Eventually the level of hydrogen in solution in the grain boundary reaches an embrittling level again - the getter effect of the grain boundary precipitates having been exhausted. This is the onset of stage 4 where fracture takes place below the macroscopic yield stress. The fracture is intergranular with no evidence of slip steps. This indicates that the fracture grows from pre-existing flaws which may be the hydrogen bubbles along the grain boundary.

Christodoulou and Flower also compared the effect of pre-exposure to WSAV at 120 C of solution treated and overaged specimens. The overaged specimens had been held at 150 C for 18 hours, creating an overaged grain boundary precipitate which is stable at the test temperature of 120 C.

In Figure 27 where the alloy has pre-existing grain boundary precipitates capable of nucleating bubbles, embrittlement does not commence until the samples have been pre-exposed for 36 hours.

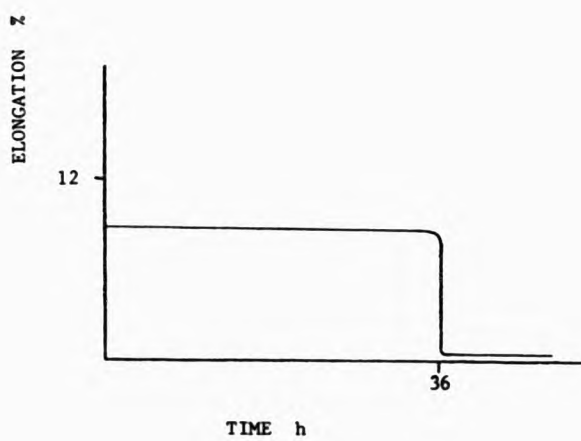


Fig. 27 Ductility of aged (18 hour, 150°C) material, slow strain rate tensile tested and pre-exposed to WSAV at 120°C.

This is due to the immediate ability of the grain boundary precipitate to getter hydrogen. The critical [H]_{grain boundary} is not reached until a 36-hour exposure has occurred, which corresponds to the second decrease in ductility in the pre-exposed solution treated material.

The results presented in Figure 26 can be described in terms of a critical hydrogen concentration to cause embrittlement. In Figure 26 embrittlement of the alloy as a result of hydrogen penetration of grain boundaries occurs immediately resulting, after 12 hours exposure, in a constant low ductility of less than 1%. After 24 hours, the development of a grain boundary precipitate allows hydrogen gettering and the decrease in the grain boundary hydrogen concentration results in an increase in ductility. After 36 hours pre-exposure the gettering effect of the grain boundary precipitates is effectively exhausted due to an equilibrium between [H]_{bubble} and [H]_{grain boundary}. The increased [H]_{bubble} results in an increasing partial pressure of hydrogen which, on reaching a critical value in relation to the constraint imposed by the metal lattice, causes the [H]_{grain boundary} to increase once again embrittling the alloy.

2.4.1.2 Crack growth in aqueous solutions

Whether or not stress corrosion cracking of AlZnMg alloys in aqueous solutions can be attributed to a mechanism involving hydrogen embrittlement is a major unsolved question. With a few exceptions (Ford⁷¹ and Peel and Poole⁵⁰), although later studies

by this group acknowledged the role of hydrogen in the SCC mechanism, e.g. Poole and Greenfield⁷³) most of the recent published literature attributes stress corrosion in these alloys to hydrogen embrittlement. The problem of course is that unlike steels and titanium alloys, conclusive demonstration of embrittlement in dry hydrogen has not been shown for an AlZnMg alloy⁷² . Secondly convincing electrochemical permeation experiments have not been documented in the literature.

Stress intensity (K) vs crack growth rate curves for AlZnMg alloys have been produced which exhibit the typical region I, II and III (Section 2.3.1) with region II being a K-independent plateau and region I being a K-dependent region showing a threshold stress for crack growth at low stress intensities. Region III which is also K-dependent is often missing as most reported tests are on DCB specimens in which the specimen is fatigue cracked and loaded below K_{IC} , and the specimen rapidly assumes a constant plateau velocity. CTS type specimens generally exhibit region III crack growth. The general shape of this curve is shown by many alloy/environment systems and a number of models of subcritical crack growth attempt to explain it, including those based primarily on anodic dissolution^{61, 74, 75, 76} and hydrogen embrittlement^{77, 78} . One proposed theoretical explanation of the shape of the stress intensity vs crack growth rate curve is due to Oriani (Section 2.2.4). The inference is that a threshold to HE crack growth should occur at a constant environing fugacity when K is slowly decreasing as in a DCB specimen. A K-independent plateau is also inferred, with the crack growth rate controlled by

processes at the input surface or in the environment and not by hydrogen diffusion in the metal. It has been suggested⁷² that, since the activation energy for subcritical crack growth is about the same for Ni, Fe and Al base alloys (40 KJmole⁻¹ in distilled water), a similar rate controlling step for H entry is involved in all the material/environment combinations.

2.4.1.3 Effect of pH

The effect of pH is shown in Section 2.3.1.2, Figures 11,12,15 and 16. At the open circuit potential there is no reduction in plateau velocity until pH 11 is reached (Fig. 11). There is a shift to lower stress intensities in region I when the pH is lowered from 11 to 0 (Fig. 12). At pH 0 there is no effect of potential (from -1.0 to 0 volts vs SHE) on the plateau velocity but at pH 6 the 7079 alloy shows a marked reduction in plateau velocity starting at -0.7 volts vs SHE (Fig. 15). For the 7075 alloy the reduction in plateau velocity at pH 6 starts at more anodic potentials (-0.3 volts vs SHE). The cathodic protection that occurs at potentials down to -1.0 volt in near neutral solutions, does not occur in acid solutions of pH 0, this behaviour is paralleled by titanium alloys in aqueous halide solutions; here too, cathodic protection against SCC growth is impossible at very low pH values.

The constant plateau velocities of AlZnMg alloys between pH 0 and 11 is due to the establishment of a constant pH within the crack which exhibits marked differences with the bulk solution

chemistry. Brown et al⁷⁹ first showed that a crack tip solution will attain a constant pH (pH 3.5) with the bulk solution pH in the range 1 to 6.2. The observation that the solution at a crack tip becomes acidic in a neutral bulk solution can be explained in terms of the hydrolysis of metal ions^{80, 81}. However, the formation of a crack tip solution of pH 3.5 from a bulk solution which is more acidic, requires reactions which will first consume hydrogen ions and then establish an equilibrium with regard to their consumption and generation.⁸² Sedricks, Green and Novak showed that in an isolated system, initially containing an acidified sodium chloride solution and a large volume fraction of aluminium (as is the case in a crack tip - the experiments were conducted on mixtures of fine 7075 alloy turnings with small liquid to solid ratios), dissolution of the aluminium alloy will cause an increase in pH which will then stabilise at a value determined by the solubility product for aluminium hydroxide.

It is clear therefore that whilst one would expect an SC crack mechanism involving hydrogen to exhibit a relationship of increasing crack velocity with increasing environing hydrogen fugacity, the insensitivity of crack growth rate to bulk pH is not inconsistent with a hydrogen embrittlement mechanism. Only when the pH is made extremely high (i.e. pH 14) will the crack growth rate be significantly reduced. Qualitatively, this would again be consistent with a hydrogen embrittlement mechanism.

2.4.1.4 Effect of electrochemical potential

The effect of potential is shown in Section 2.3.1.2, Figure 14, and as discussed, plateau crack growth velocities fall and region I stress intensities increase as the potential is made more cathodic. The results are presented for applied cathodic potentials down to -1.0 volt vs SHE. Other workers have investigated the effect of potential and have concluded that;

- a) cathodic protection of the specimen is occurring and
- b) that the mechanism of crack growth at anodic potentials is anodic dissolution, whilst the mechanism at cathodic potentials is disputed.

Nguyen, Brown and Foley⁸³ studied a 7075 type alloy at potentials down to -1.2 V vs SHE (Fig. 28) in sulphate, nitrate and chloride solutions. Hartman⁸⁴ studied the crack growth rate of a 7075 alloy down to -1.35 V vs SHE in a 3% sodium iodide solution and observed a slight increase in crack growth rate above -0.95V (Fig. 29), this study was conducted on CTS type specimens (showing the presence of region III crack growth). The beneficial effects of cathodic polarisation had been used as a strong argument against a hydrogen embrittlement mechanism. Recent work has shown this argument to be false. The critical observation is that there is a minimum in the crack growth rate at an intermediate potential, but that it increases again as the potential is made increasingly cathodic. This is illustrated in Figure 30. The minimum in both crack growth rate and permeability at intermediate potentials has also been observed in steels⁸⁵. It is thought that the minimum

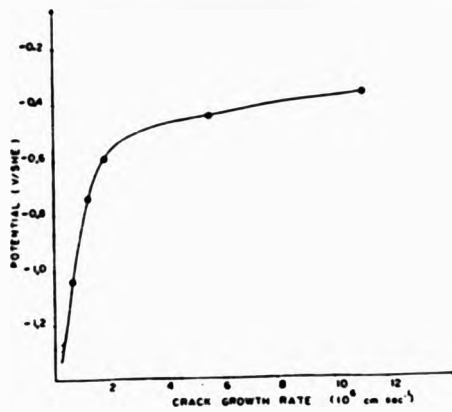


Fig. 28 The effect of potential on plateau growth rate of 7075-T651 alloy in 1M NaCl solution (after Nguyen, Brown and Foley).

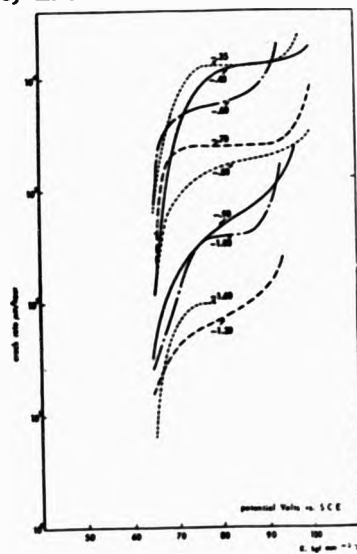


Fig.29 Crack growth rate vs stress intensity for 7075-T6 in 3% NaI solution at pH 7 showing the effect of applied potential (after Hartman).

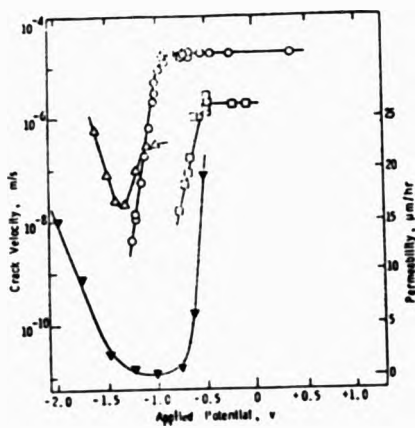
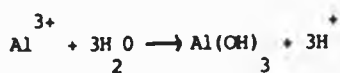


Fig.30 Dependence of crack velocity and permeability on applied potential (volts vs SCE) for several aluminum alloys, in the environments shown. Data on permeability for 7075-T651 (∇ , 3% NaCl solution) are those of Gest and Troiano⁸⁶; crack growth data for 7075-T651 (\square , 5M iodide solution) and 7079-T651 (\circ , 5M iodide solution) are from Speidel⁶³; those for 81Zn7Mg3 (Δ , 1M chloride solution) from Berggreen⁸⁷ (after Speidel⁷²).

corresponds to a minimum in the environmental fugacity of hydrogen, as shown by the permeability; increased permeation at high cathodic potentials is due to generalised hydrogen production at the specimen surface while increases with anodic polarisation are due to acid generated by hydrolysis in pits or cracks, leading to hydrogen generation locally even though the potential is more anodic than the free corrosion potential. The cathodic protection against SCC shown at intermediate potentials can be attributed to a reduced dissolution rate in the crack and a concomitant reduction in hydrogen evolution. Cathodic protection at intermediate potentials is thus no longer a counter argument against a HE mechanism, but is not proof of a HE mechanism.

The above rationalisation also provides an explanation of the specific role of Cl⁻, Br⁻ and I⁻ as SCC accelerators in AlZnMg alloys. These ions are known as specific pitting agents for aluminium alloys in aqueous solution and can prevent the high current densities at the crack tip from producing passivation, thus leading to the higher crack growth rates observed.

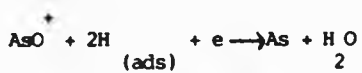
The hydrolysis reaction of the anodic product, Al³⁺ (aq) is given below.



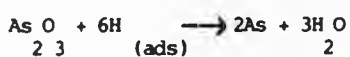
2.4.1.5 Effect of poisons and catalysts for the hydrogen recombination reaction

The hydrogen recombination poisons are group V metals or metalloids including P, As and Sb. They are well known to act as poisons of the hydrogen recombination reaction when added in compound form to corrosive environments. As such these additions have been employed to prevent corrosion in acidified corrosive environments where hydrogen reduction is the principle cathodic reaction taking place.

It is thought that while the proton reduction step $H^+ + e \rightarrow H_{ads}$ is allowed to go on unhindered, the subsequent combination of these adsorbed hydrogen atoms to form diatomic hydrogen molecules is largely prevented. The precise mechanism of the inhibition of recombination is uncertain but it has been suggested⁸⁸ that, for example, the arsenious ion AsO^+ is sufficiently surface active to adsorb at those sites at which hydrogen atoms may recombine (e.g. at growth edges). The arsenious ion may then be cathodically reduced by reactions such as;



or



The introduction of arsenical compounds into mildly acidic environments can result in a high population of uncombined hydrogen atoms on the metal surface, thereby facilitating the

absorption of hydrogen into the metal lattice, resulting, if the metal is susceptible, in enhanced hydrogen embrittlement cracking.

Additions of platinum in the form of chloroplatinic acid cause cathodically polarised sites to be decorated with platinum black. The latter exhibits a high exchange current density and low overpotential for the hydrogen evolution reaction and consequently any hydrogen ions reduced at these sites will be more readily evolved as molecular hydrogen, than be absorbed into the metal lattice to produce hydrogen embrittlement. Consequently, if cracking is a result of hydrogen embrittlement, the susceptibility towards cracking should be decreased by chloroplatinic acid additions to the test solution.

⁸⁹
Green et.al. showed that additions of sodium arsenite enhanced the crack growth rate of 7075-T6 alloys in an aqueous chloride - chromate environment. However when pre-cracked specimens were loaded in torsion i.e. in mode III, the susceptibility to SCC was considerably reduced and arsenic additions inhibited cracking. Green et. al. interpreted these results to mean that mode III failures occurred by anodic dissolution, while the additional susceptibility in mode I was attributed to hydrogen. Thus the reduced, but not zero, susceptibility to SCC in mode III suggests that both hydrogen embrittlement and electrochemical dissolution processes are occurring together and co-operatively. Green et. al. rationalised the behaviour of arsenic in the same way as for ⁹⁰stainless steels (by Kim and Wilde). Under tensile loading the

addition of arsenic retards the kinetics of hydrogen evolution, increases the hydrogen concentration within the metal and enhances hydrogen embrittlement. However, since arsenic retards the cathode kinetics of the dissolution reaction (again the recombination of hydrogen ions), crack propagation by anodic dissolution is retarded under torsional loading.

91
Hardie and Holroyd⁹¹ in a series of slow strain rate experiments on tensile specimens of 7179-T651 alloy noted a reduction in the 0.2% proof stress as a result of 25 ppm arsenic additions to a tap water environment at 70 C. The proof stress dropped from 497 to 466 MNm⁻² after 3 days pre exposure in tap water and to 454 MNm⁻² after 3 days pre-exposure in the same environment containing 25 ppm arsenic.

92
Green and Montague⁹² in an earlier piece of work studied the effect of cadmium and arsenic alloying additions to an Al-5.5% Zn-2.5% Mg alloy. Their starting point was to assume an anodic dissolution mechanism and to see if cadmium or arsenic additions would poison the rate controlling cathodic reaction in acid solutions which is predominantly the recombination of hydrogen ions. They assumed that cadmium and arsenic would segregate to the grain boundary region where the additions would retard the cathodic reaction and control the rate of dissolution of solid solution at the grain boundary and hence the overall rate of crack propagation.



The stress corrosion results of constant load flat specimens showed that the ternary alloy and the quaternary cadmium containing alloy did not fail in 300 hours when loaded up to the yield stress - however the arsenic containing quaternary alloy failed in 1/2 h. Green and Montague concluded that another effect of the arsenic addition was more important. The arsenic containing alloys showed a decreased grain boundary precipitate size together with decreased inter-particle spacing and significantly higher concentrations of magnesium and, to a lesser extent zinc, on the intergranular fracture surfaces for a depth of 250A. Cadmium additions resulted in similar magnesium concentrations actually on the fracture surfaces, but these showed a sharp reduction with depth, decreasing to the bulk matrix concentration within 100A.

From the viewpoint of an anodic dissolution mechanism where the effect of an arsenic addition may be expected to decrease susceptibility to SCC, clearly the experimental evidence points to the other effects of arsenic, in increasing segregation of alloying elements to the grain boundary and decreasing grain boundary precipitate size and spacing, as being most important. However from the viewpoint of a hydrogen embrittlement mechanism, which the authors did not consider, the results are clearly consistent with, but not proof of, the arsenic addition acting to poison the hydrogen recombination reaction thereby allowing more hydrogen to enter the alloy and embrittle it. The effects of arsenic on the other grain boundary microstructural features are



also consistent with a HE mechanism. It is proposed (Section 2.5.4.2) that overaged grain boundary precipitates are effective in trapping hydrogen and rendering it innocuous. In order to obtain comparable mechanical properties, the different alloys used were subjected to differing solution treatment times but to identical ageing treatments (5 hours at 130 C). There is clearly a complex relationship between composition and heat treatment, but the arsenic addition has resulted in a small, finely spaced grain boundary precipitate, less effective in trapping hydrogen. In fact quaternary alloys containing zirconium with a similar small grain boundary precipitate and interparticle spacing were also tested and failed in 85 hours, indicating that the effect of arsenic (failure in 1/2 hour at the same load) is not solely due to the effect of arsenic on the microstructure. Similarly, the effect of segregation of magnesium to the grain boundary on failure time is also consistent with a HE mechanism. It is proposed (Sections 2.5.4.2 and 2.4.3) that segregation of magnesium to the grain boundary results in magnesium hydride formation, and it is magnesium hydride formation that embrittles the alloy along the grain boundary plane. The greater the amount of magnesium, the greater the embrittling effect of hydrogen resulting from similar environmental fugacities. Again the increase in magnesium content in the region adjacent to the grain boundary was also shown by the quaternary zirconium containing alloy and so the effect of arsenic is not solely due to its effect on microstructure, but may be principally due to its effect as a poison, if hydrogen embrittlement is the main cause of susceptibility.

2.4.2 The role of heat treatment and its effect on grain boundary segregation in the hydrogen embrittlement of Al-Zn-Mg alloys.

A number of papers in the literature have pointed to a marked segregation of magnesium and zinc to the grain boundary in AlZnMg ternary alloys^{92,93}.

Chen et. al.⁹³ studied a high purity ternary alloy containing 5.49% Zn and 2.47% Mg. Fracture surfaces of this alloy were studied by Auger depth profiling, and it was noted that;

a) The grain boundary magnesium and zinc concentrations were 5.4 atomic pct and 4.5 atomic pct respectively. If all the magnesium and zinc segregation were due to MgZn precipitates, the Mg:Zn ratio should be 1:2. The grain boundary therefore contains excess magnesium. About 40% of the total magnesium is in the precipitates and 60% is localised within a few atomic layers of the grain boundary.

b) Under both solution heat treated, peak aged and overaged conditions there is a marked segregation of magnesium to the grain boundary. The grain boundary concentrations are 3 to 5 times the bulk concentration. This is in sharp contrast to the results of Doig and Edington⁵¹ reported in Section 2.3.2. They obtained a much less dramatic accumulation of magnesium at the grain boundary for as-quenched samples and a depletion of magnesium in over-aged samples.

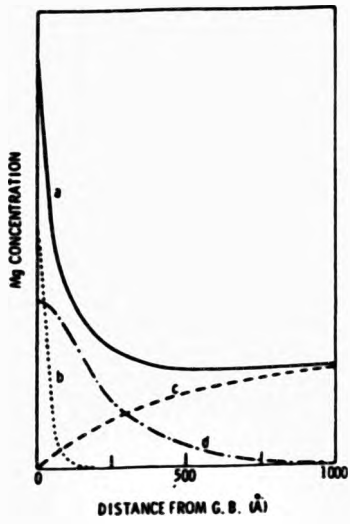
c) The width of the segregated zone is of the order of 10\AA for as-quenched samples and 100\AA for overaged samples.

The different results obtained by Doig and Edington were put down to differences in the information obtained from the Transmission Electron Microscope (TEM)-plasmon loss technique they employed. The TEM-plasmon loss technique used by Doig and Edington employed a 100\AA electron beam which traversed the grain boundary which was perpendicular to the specimen surface, the TEM technique was therefore incapable of measuring the magnesium content to within 50\AA of the grain boundary. The AES technique on the other hand, being a surface technique employed on specimens with intergranular fractures, was ideally suited to detect these accumulations.

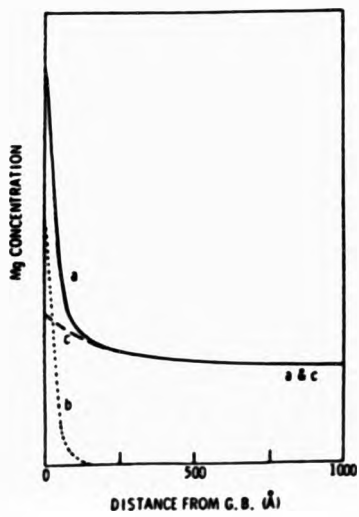
The plasmon loss of Auger electrons was used to determine the chemical environment of the magnesium and zinc solutes. Whilst 60% of the magnesium is not associated with MgZn_2 precipitates at the grain boundary, all the zinc is in the MgZn_2 precipitates.

A schematic illustration of the various contributions to the magnesium depth profile of the overaged sample is shown in Figure 31a. The total magnesium profile (curve a) is the sum of the profile at the grain boundary (curve b), the profile within the PFZ (curve c) and the profile of the precipitate (curve d).

Similarly a magnesium depth profile can be constructed for the as-quenched samples. Because of the absence of grain boundary



a) Schematic diagram of the various contributions to the Mg depth profile for overaged samples (a, resultant profile; b, profile at g.b; c, profile in PFZ; d, profile of precipitates).



b) Schematic diagram of the various contributions to the Mg depth profile for as-quenched samples (a, resultant profile; b, profile in the grain boundary; c, profile in the precipitate free zone).

Fig. 31 (After Chan et al ⁹³).



precipitates in this case, the profile (Fig. 31b) is simply obtained by adding the profile within the grain (curve c) to the narrow profile representing the grain boundary concentration of magnesium (curve b). It is proposed⁹⁴ that the solute segregation is produced during the quench by a process of vacancy drag. In this process the binding energy of the solute to the vacancy is the most important factor. For magnesium the binding energy is approximately 0.3 eV and for zinc it is 0.1 eV. Solute atoms are dragged to the grain boundary by vacancies during the quench. Viswanadham et. al.⁹⁵ point out that if the solute segregation produced during the quench is indeed by vacancy drag, then one would expect alloying additions such as copper, which have a very low (≈ 0) binding energy to vacancies, would exert a significant influence on the level of segregation. For example, the stress corrosion cracking resistance of weldable AlZnMg alloys without copper is highest when slow cooled, while for alloys with substantial additions of copper, the SCC resistance is highest when rapidly cooled.

The presence of free magnesium on the grain boundary has important implications for the mechanism of hydrogen embrittlement in AlZnMg alloys. In Section 2.2.1 it was noted that the solution heat treated oxide films are composed primarily of MgO, nucleated at the grain boundaries from magnesium segregated to the grain boundary¹³. Growth of these MgO nuclei results in boundaries in the MgO oxide film that are unrelated to the grain boundaries of

the metal substrate. During subsequent exposure to 100% relative humidity at 50 C further growth of a hydrated aluminium rich oxide by outward diffusion of aluminium occurs at the boundaries of the MgO film. It was proposed by Viswandham et. al.¹³ that the reaction between the outward diffusing Al³⁺ and H₂O² resulted in the formation of hydrogen (see Section 2.5.6). In the absence of a MgO oxide film, an aluminium oxide film would allow the recombination of atomic hydrogen to molecular hydrogen. The role of the magnesium being to combine with the hydrogen, minimising recombination, and allowing more time for hydrogen diffusion to the grain boundaries.

It was noted that the magnesium content of the solution heat treated oxide film is a maximum at 475 C and decreases at higher and lower temperatures. This maximum corresponds to a minimum in the ductility of pre-exposure embrittlement tests of a range of tensile samples solution heat treated between 440 and 500 C⁹⁶.

In considering a hydrogen embrittlement mechanism, it is essential to consider the following factors;

- i) The generation of hydrogen
- ii) Entry of hydrogen through the protective surface film and
- iii) Concentration of hydrogen in a localised region to cause embrittlement.

The first two steps have been dealt with in the preceding Sections. The local concentration of hydrogen at the grain

boundary is also an effect of the segregation of free magnesium to the grain boundary in AlZnMg alloys. There is a large body of circumstantial evidence in the literature on possible Mg-H interactions. These are dealt with by Viswanadham et. al.⁹⁴ It is well known in vacuum technology that magnesium acts as an effective getter of hydrogen. Alani and Swann⁹⁷ noted that hydrogen bubbles nucleated more readily from MgZn precipitates in higher magnesium content alloys pre-exposed to water vapour in a TEM, under the action of the electron beam. More recently Tuck⁹⁸ has produced more direct evidence for Mg-H formation in AlZnMg alloys by pre-exposing AlMg and AlZnMg alloy samples to water saturated air vapour for 50 days and comparing these differential scanning calorimetry traces with those obtained from a sample of magnesium hydride powder contained in an aluminium phial. All samples were heated at a rate of 50 C per minute. Tuck concluded that Mg-H was formed in the AlZnMg and AlMg alloys during pre-exposure, and that when a tensile stress is applied to grain boundaries containing magnesium hydride (formed at the grain boundary as a result of magnesium segregation), if enough hydride is present, the grain boundary will separate in a brittle manner. This process would occur at the surfaces of slow strain rate and pre-exposed tensile samples and continuously in the region behind the crack tip in pre-cracked CT or DCB specimens.

Controlling the grain boundary structure may provide a means of controlling SCC susceptibility. Chaturvedi and Malis⁹⁹ showed that low angle grain boundaries in an Al-8Mg alloy had very few

grain boundary precipitates, did not show magnesium enrichment and, in specimens pre-exposed to water saturated air vapour, were not subject to hydrogen bubble formation under excitation by the electron beam in a TEM, unlike high angle boundaries in the same specimen. Vacancy and solute movement to low angle grain boundaries would be limited. They suggested that the solution treatment temperature will not only influence the concentration of quenched-in vacancies, which can influence the migration of solute atoms to the grain boundaries, but will also affect the structure of the grain boundaries, which also influences the segregation and distribution of magnesium atoms on them, i.e. a high solution treatment temperature or slow quenching rate reduces the level of grain boundary magnesium segregation.

2.4.3. Microstructural aspects of hydrogen embrittlement in Al-Zn-Mg alloys - the crack path

100
Montgrain and Swann produced the first microstructural evidence against an anodic dissolution mechanism. In stress corrosion tests on an Al-7%Zn-3% Mg U bend specimen exposed to laboratory air and viewed in a million volt electron microscope they noted that;

- 1) Stress corrosion cracks propagate along the grain boundary and not in the precipitate free zone.
- 2) The grain boundary precipitates are not dissolved during crack propagation.

3) The cracks propagate without evidence of plastic deformation in the vicinity of the crack faces. The separation of adjacent grains is totally brittle.

4) Cracking will occur immediately on application of the applied stress in dry air, if the specimens have been pre-exposed to water vapour before stressing. The length of the instantaneous crack is related to the time of pre-exposure.

In a separate experiment involving fracturing a pre-exposed specimen in a vacuum chamber, and analysing any liberated gas in a mass spectrometer, it was noted that hydrogen was given off during fracture. Control specimens were used to eliminate hydrogen given off by the hydrated oxide film during deformation.

More recently Scamans^{101, 102, 103} has presented two pieces of evidence for a hydrogen embrittlement mechanism in AlZnMg alloys. Firstly, the presence of long continuous parallel striations on the intergranular fracture surface, not previously observed in stress corrosion failure of these alloys. The crack surfaces are striated by arrest markings which match precisely on both fracture faces, each striation is formed by the corrosion product of the hydrogen generation reaction required to induce the next burst of brittle grain boundary fracture. These matched arrest markings have been observed on both failures produced in water vapour at 40 C and chromate inhibited 2% NaCl solutions at 22 C. Non-inhibited environments or higher temperatures produce corrosion

products which mask the very fine detail of the striations. One set of results on DCB specimens of 7017 and 7079 alloys (7017 is a medium strength weldable alloy, 7079 is a high SCC susceptibility early aircraft alloy now used for less critical applications) at 40 °C and 95% relative humidity showed that the average striation spacing was not a strong function of the applied stress intensity. The results can be interpreted in terms of crack jump rate vs stress intensity.

The crack jump rate is 500 h^{-1} in region II for the 7079 alloy and 50 h^{-1} in region I i.e. the average arrest time was 7.2 seconds during region II growth and 72 seconds during region I growth. The approximately constant striation spacing was 1350 \AA for this alloy and 3700 \AA for the 7017 alloy. The effect of overageing halved the crack jump frequency but left the striation spacing unaffected. Decreasing the quench rate after solution treatment by hot water quenching or controlled cooling of $8 \text{ }^\circ\text{C}$ per sec from $400 \text{ }^\circ\text{C}$ to $200 \text{ }^\circ\text{C}$ also left the striation spacing within the scatterband of the cold water quench striation spacing.

This discontinuous stress corrosion cracking was interpreted as repeated sequences of pre-exposure embrittlement and rapid brittle fracture. If it is assumed that the number of available trap sites or local getters for the diffusing embrittling species ahead of the crack tip is fixed by the alloy composition and thermal treatment, then the applied stress across the grain boundary must exert its influence through its effect on the grain boundary

hydrogen diffusion rate, such that the trap sites are saturated more rapidly and brittle fracture can then be induced by the accumulation of atomic hydrogen.

The lower crack jump distances in the 7079 alloy were attributed to its higher magnesium and copper contents. The net effect on the v-K curve was not very significant as the 7079 cracking frequency was increased to give an equivalent propagation rate. Scamans attributed the observed grain boundary decohesion to an interaction of the segregated magnesium atoms and atomic hydrogen. Whether at the point of failure this can be described as a chemisorbed monolayer of hydrogen on magnesium or a planar sheet of magnesium hydride would need further experimentation to establish. The area of crack advance represents the area of grain boundary where this detrimental atomic hydrogen concentration has been achieved.

To achieve a macroscopic growth rate of $1 \times 10^{-1} \text{ mm h}^{-1}$ with crack jumps of 1350 \AA would require a grain boundary hydrogen diffusivity in the order of $3 \times 10^{-9} \text{ cm}^2 \text{ s}^{-1}$. Measured diffusion rates of hydrogen in AlZnMg are between 2×10^{-9} and $10^{-10} \text{ cm}^2 \text{ s}^{-1}$ (Section 2.5.7.3). However, since in the 7079 alloy SCC is a factor of 10^3 faster in aqueous chloride solutions, hydrogen diffusivities would need to be in the order of $3 \times 10^{-6} \text{ cm}^2 \text{ s}^{-1}$. Measured diffusivities have been on unstressed samples. Scamans¹⁰⁴ has suggested that stress assisted diffusion may make hydrogen diffusivities as high as $10^{-6} \text{ cm}^2 \text{ s}^{-1}$ not unreasonable.



The second observation was stereo pair micrographs of total immersion C-ring specimens of 7018 alloy in an acidified chloride environment¹⁰¹. The micrographs show no evidence of dissolution, with both the grain boundary precipitates and dispersed particles remaining on the fracture surfaces.

The observations of a striated fracture surface with crack arrest markings and no evidence of dissolution, in both conditions of total immersion and in water vapour, lead to the conclusion that essentially the same failure mechanism operates in both environments.

2.4.4 Slow strain rate testing of Al-Zn-Mg alloys

Holroyd and Hardie in a series of experiments on slow strain rate testing of 7000 series alloys have demonstrated that pre-exposure embrittlement and recovery occurs in these alloys^{91,105,106,107}.

The specimens used were modified Hounsfield tensile specimens machined with their principal axis parallel to the short transverse direction of the plate material. The plastic reduction in area at fracture proved to be the most consistent and meaningful parameter in assessing the degree of embrittlement. The alternative parameters of plastic elongation and fracture energy suffer from the effects of secondary cracking which introduces a spurious contribution to the measured elongation. The importance of the strain rate used in conducting these tests⁹⁶ had not previously been appreciated. Scamans et. al.

found no difference in the strain rate sensitivity of AlZnMg specimens stressed in vacuum and air after 3 days pre-exposure to water saturated air vapour at 90 C at strain rates from 4.2×10^{-4} to 4.2×10^{-2} s⁻¹. In fact strain rates below 10^{-4} and between 10^{-4} and 10^{-7} s⁻¹ are required to show the embrittlement effects.

Commercial alloys are less susceptible to embrittlement effects than their high purity analogues and the most resistant alloys need to be tested at particularly slow strain rates. Comparisons of the degree of embrittlement between alloys makes no assumptions about the source of embrittlement in stress corrosion tests, although pre-exposure effects and recovery effects are attributed to hydrogen diffused into the alloy as a result of interaction with the environment. If hydrogen is involved, the effect of strain rate may readily be interpreted in terms of the time required for hydrogen to diffuse to those sites where its concentration becomes sufficient to induce brittle decohesion of the material.

When using a ductility ratio to express the degree of embrittlement, care must be taken in choosing the reference environment which should be vacuum or air dried with, for example, anhydrous magnesium perchlorate. Laboratory air with a typical relative humidity of 60% is an aggressive environment and its use by some investigators leads to misleading results.

The effect of time of immersion during the test and of pre-¹⁰⁵exposure in an aggressive environment are additive (Fig. 32). The period of immersion in an aggressive environment during testing can itself make a significant contribution to the embrittlement.

Testing of specimens of 7049-T651 after prior immersion in sea⁻⁵ water gives the same ductility at strain rates faster than 5×10^{-1} s⁻¹ whether the test environment is laboratory air or sea water.

The reduction in area ratios diverge at slower strain rates because of the more aggressive nature of sea water. The embrittlement of the pre-exposed specimen in laboratory air changes very little between 5×10^{-5} s⁻¹ and 2.5×10^{-6} s⁻¹ because the test environment makes little additional contribution, whereas testing in sea water causes increasing embrittlement. Below 2.5×10^{-6} s⁻¹ the contribution caused by laboratory air to the embrittlement becomes significant and the results of the pre-exposed specimens tested in both environments converge.

The effect of pre-exposure time and recovery is shown in Figure¹⁰⁷ 33. The effect of pre-exposure reaches a maximum in 30 days. The recovery from 30 days pre-exposure to sea water is also shown. Recovery of ductility occurs in dry air and vacuum at strain rates below 5×10^{-5} s⁻¹. Recovery from the embrittlement produced by pre-soaking is only produced by subsequent straining and not simply by storage of the specimen in the less embrittling environment (dry air or vacuum). It is interesting to note that

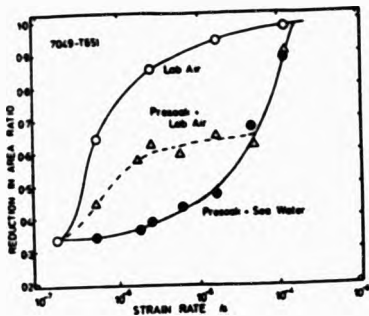


Fig. 32 The effect of strain rate on the reduction in area in laboratory air and sea water compared with that in vacuum for specimens of 7049-T651 with and without prior immersion in sea water for 72 hr. (after Bolroyd and Hardie 105).

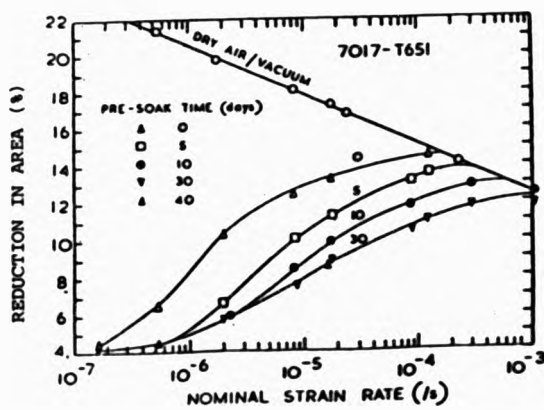


Fig. 33 The effect of strain rate upon reduction in area at fracture for 7017-T651 tested in dry air or vacuum and sea water after prior exposure to sea water at ambient temperature. (after Bolroyd and Hardie 107).

at high hydrogen levels, i.e. slow strain rates in aggressive environments such as sea water, Holroyd noted a transition from the normal transgranular brittle fracture to intergranular brittle fracture. Since recovery after exposure is dependent upon straining, dislocation transport of hydrogen is implied. However the rate of plastic deformation in the embrittlement process itself is far from clear. That there is a role played by plastic deformation in embrittlement is suggested by the observation that no embrittlement is detected even when sufficient hydrogen is present, if the strain rate is too high. It also seems likely that transport of hydrogen to the embrittling site during straining is a pre-requisite for embrittlement. Transgranular cracking of slow strain rate specimens was attributed by Holroyd and Hardie to transport of hydrogen from the grain boundary regions by dislocations. When an adequate supply of hydrogen is available to replenish the grain boundary hydrogen and sufficient time is allowed for this to occur (i.e. at slow strain rates) intergranular failure may still take place. Such a model assumes that a higher local concentration of hydrogen is necessary for intergranular than for transgranular cracking, but that transgranular cracking occurs if sufficiently high stresses are attained.

2.4.5 Mode III (torsional) and mode I (tensile) testing of pre-cracked specimens

In mode III loading there is no hydrostatic stress component due to the absence of any through thickness σ_{33} stress. It is the hydrostatic stress component which could cause hydrogen

accumulation behind the crack tip as hydrogen diffuses to the
108,109 region of maximum hydrostatic stress . A comparison of SCC
susceptibility between specimens loaded in torsion (where hydrogen
would not play a role) and tension (where hydrogen may play a
role) could distinguish between the anodic dissolution and
hydrogen embrittlement mechanisms. If crack growth in torsion was
similar to that observed in tension, then anodic dissolution is
likely to be the dominant mechanism. Green et. al.⁸⁹ tested
pre-cracked specimens of 7075-T6 alloy in torsion and tensile
loading over a range of stress intensities and measured the time
to failure in an inhibited chloride environment. The results are
shown in Figure 34. It is evident that SCC susceptibility is
greatly reduced in torsion, but is not eliminated. Green et. al.
suggest that hydrogen embrittlement and anodic dissolution are
acting in a co-operative manner.

In a separate set of experiments on a 7091 alloy produced by a
powder metallurgy route Pickens et. al.¹¹⁰ showed similar
behaviour under torsional loading (Fig. 35). Similar conclusions
were drawn in that as the increase in time to failure at a given
stress level is approximately one order of magnitude, some
complementary anodic dissolution takes place allowing crack growth
in mode III loading, but the majority of the crack advance in mode
I is by hydrogen embrittlement.

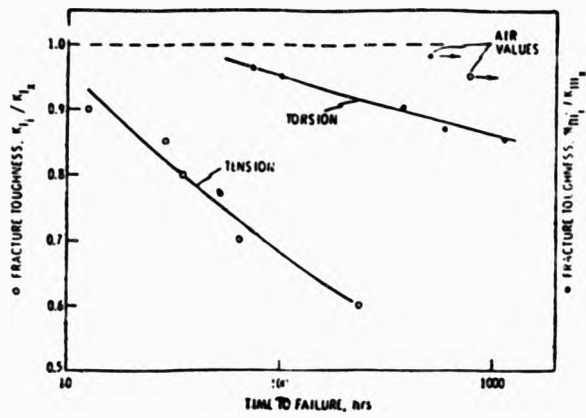


Fig. 34 Resistance to SCC of 7075-T6 as a function of loading mode, in an environment of 3.5% NaCl + 3.0% $K_2Cr_2O_7$ in water, at pH 3.2. (after Green et al 89).

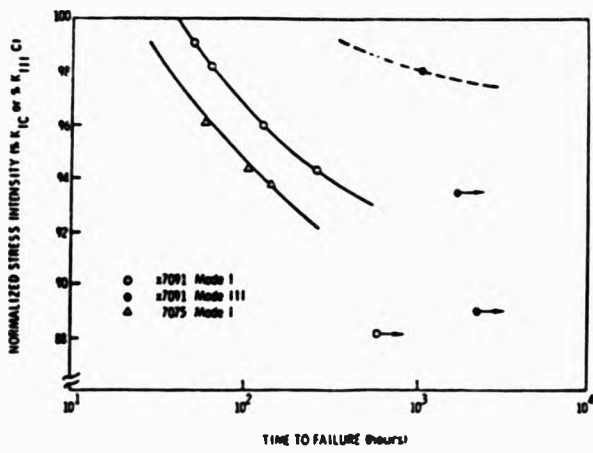


Fig. 35 The effect of loading mode on the SCC of X7091 (from a powder metallurgy route) and 7075 (from an ingot metallurgy route). (after Pickens et al 110).

2.5 HYDROGEN DIFFUSION

2.5.1 Introduction

This is an abridged review of hydrogen diffusion theory, in which particular attention has been paid to the relatively small amount of work that has been undertaken on hydrogen diffusion in aluminium and aluminium alloys, in particular the AlZnMg group of high strength alloys.

The earliest observations on the dissolution of hydrogen in metals date back to the experiments of Cailletet in 1864¹¹¹. Thomas Graham published the results of his classic study of the Pd-H system in 1866¹¹². However, the systematic study of hydrogen in metals only began with Sieverts around 1900^{113,114,115}. The phenomenon of hydrogen embrittlement was also discovered around this time^{26,27}.

2.5.2 Sources of hydrogen

Hydrogen can enter metals from a variety of sources. These include;

- 1) Dissolution in molten metal from a hydrogen containing atmosphere, some of the hydrogen being retained during solidification. This occurs during casting and welding where water vapour generated from the moisture present in refractory brick, metal charge, or welding electrode flux, breaks down to form hydrogen.

2) Absorption of hydrogen when the metal is exposed to a hydrogen containing atmosphere, particularly at high temperatures e.g. during annealing.

3) Cathodic hydrogen absorbed by the metal during acid pickling, electroplating, phosphating and cathodic protection.

4) Corrosion processes encountered in service where hydrogen is evolved as the cathodic reactant.

In the present context, which is primarily concerned with hydrogen entry from aqueous solutions and water vapour at ambient temperatures, emphasis will be placed on the entry of cathodic hydrogen (i.e. 4 above).

2.5.3 Metals and hydrogen

Metals are divided into three main classes according to their behaviour towards hydrogen^{116,117} ;

- 1) Metals which form ionic hydrides i.e. Na, K, Ca, and Li.
- 2) Metals and metalloids which form intermediate and covalent gaseous hydrides i.e. Mg, Al, Si, As, Zn, Cd, etc.
- 3) Metals which are either inert (W, Au) or absorb hydrogen, but without any chemical reaction (diffusive occluders). This group of metals is further subdivided into two classes:

a) The endothermic occluders i.e. Fe, Ni, Co, Mo, Pt, Cr, Mn, Cu, Ag, Al, Mg.

b) The exothermic occluders i.e. Nb, Ta, Ti, V, Pd, Zr.

In relation to hydrogen embrittlement, class 3 metals are the most important. Aluminium, along with other elements, whilst it is in class 2, forming a gaseous hydride, is also an endothermic occluder in its behaviour to hydrogen ¹¹⁸.

Hydrogen has no appreciable solubility in zinc or other metals in the same periodic group, e.g. cadmium and mercury (group IIB), or in metals and metalloids in the adjacent group, e.g. gallium, indium and thallium.

Magnesium, which only forms a metastable ionic hydride, is an endothermic occluder. The transition metal hydrides are generally classified as either endothermic or exothermic occluders.

In the case of exothermic occluders the behaviour is complicated by the formation of pseudo-metallic hydrides. Exothermic occluders absorb a total quantity of hydrogen that decreases as the temperature increases, and which varies as the square root of the pressure only over certain pressure ranges. Simple solution, where hydrogen enters into solid solution in the atomic form, is endothermic and the solubility of hydrogen increases with increasing temperature.

In simple solution hydrogen solubility increases with the square root of the hydrogen pressure at constant temperature according to Sieverts law (Section 2.5.7.1). The solubility of hydrogen in aluminium is however very low at room temperature, rising to a bulk solubility of 4.5×10^{-7} moles of hydrogen per mole of aluminium at 600 C.

2.5.4 Mode of distribution and form of hydrogen in aluminium

2.5.4.1 Lattice hydrogen

Diffusion of hydrogen has been investigated mainly in BCC metals, and relatively little has been published on FCC metals such as aluminium and its alloys.

The state of hydrogen in interstitial solution in metals has been considered by many workers who have suggested that hydrogen exists as atoms¹²⁰⁻¹²², protons, screened protons and positive ions¹²³⁻¹²⁵. Oriani¹²⁶ favours the screened proton form, but states that the type of interstitial site is still uncertain.

Consideration of the hydrogen atomic size factor (diameter of atomic hydrogen = 0.106 nm) and the fact that the concentration of hydrogen in solid solution in aluminium obeys Sieverts law, indicates that hydrogen forms an interstitial solid solution. It will be assumed for the present purpose that interstitial hydrogen is present in the monatomic form, although the exact nature of occluded hydrogen is still a subject of controversy.

2.5.4.2 Hydrogen in traps

Internal friction studies¹²⁷ support the view that cathodic hydrogen in true interstitial solution at ambient temperatures constitutes only a fraction of the total hydrogen occluded by aluminium. Generally for metal-hydrogen systems at temperatures above 200 °C, solubility, permeation and diffusion data can be readily explained solely in terms of interstitial solution, but below 200 °C and particularly at ambient temperatures, hydrogen contents are greater and diffusion coefficients are lower than predicted from higher temperature data using the interstitial solution model^{128,129}.

Darken and Smith¹³⁰ postulated that at ambient temperatures trapping of hydrogen occurs at imperfections in the lattice thus accounting for the anomalously high hydrogen contents and low diffusion rates for steels. This concept of trapping has been confirmed by several workers and many types of traps have been suggested including vacancies, dislocations¹³¹, stacking faults, microcracks¹³², grain boundaries, non-metallic inclusions¹³³, phase boundaries¹³⁴, and micropores¹³⁵.

In aluminium trapping has been shown to occur at grain boundaries^{94,98,136}, dislocations¹²⁷, and grain boundary precipitates^{70,137}. Tuck⁹⁸ used differential scanning calorimetry to estimate the grain boundary hydrogen coverage of an Al-5%Mg alloy pre-exposed at 70 °C to water saturated air vapour (WSAV) for 50 days. He proposed that preferential enrichment of magnesium on the grain boundary plane leads to the formation of

magnesium hydride (MgH_2) and estimated a grain boundary hydrogen coverage in $50 \mu m$ grain size material of 8×10^{16} atoms of hydrogen cm^{-2} . This corresponds to an average depth of 25 \AA which is about 10 monolayers of MgH_2 .

Edwards¹³⁶, using a different technique of pre-charging tensile specimens of a high purity Al-6.1%Zn-2.9% Mg alloy with tritiated water, measured the tritium given off during fracture and gave similar estimates of grain boundary hydrogen coverage. For $300 \mu m$ grain size material he estimated the grain boundary hydrogen coverage to be 2.5×10^{16} atoms cm^{-2} for underaged material and 5×10^{16} atoms cm^{-2} for peak aged material, corresponding to approximately 3 and 7 monolayers of magnesium hydride respectively. Fracture of the specimens was brittle intergranular. The studies on the Al-5% Mg alloy showed higher grain boundary hydrogen coverage but the alloys had a higher magnesium content than the Al-6.1%Zn-2.9%Mg alloy used by Edwards and were pre-exposed for a longer time.

The peak aged alloy absorbs more hydrogen in a given exposure time than the underaged alloy. However, the underaged alloy is embrittled faster. This is evidence in favour of the theory that grain boundary precipitates, which grow during ageing, act as traps for hydrogen⁷⁰. Trapping would be expected to reduce the hydrogen coverage on the intervening grain boundary while at the same time lowering the effective diffusion coefficient.

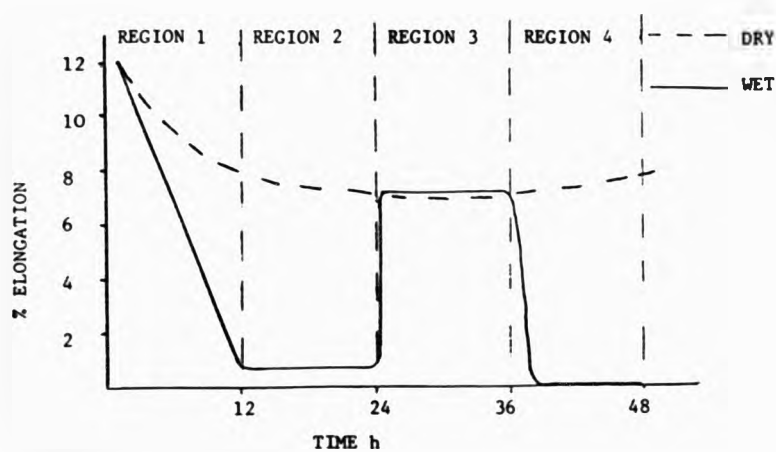
137

Scamans⁷⁰ has shown that under the influence of the transmission electron microscope electron beam, AlZnMg alloys pre-exposed to WSAV, nucleate hydrogen bubbles preferentially on grain boundary precipitates and, to a lesser extent, on intermetallic compounds. Nucleation of a hydrogen bubble from hydrogen chemically combined or chemisorbed on the grain boundary is possible due to the elastic stress constraint relaxation in the thin foil used in the study. However, Scamans and Christodoulou have proposed that the grain boundary precipitates act as hydrogen traps. Christodoulou⁷⁰ in a series of experiments involving the slow strain rate testing of AlZnMg alloys in the solution treated condition, isothermally exposed to WSAV at 120 °C and exposed for different times, showed four regions of ductility. As ageing of the alloy was proceeding during the time of the experiment, regions 1,2,3 and 4 were identified as shown in Figure 36. (see Section 2.4.1.1.)

The detailed mechanisms of hydrogen embrittlement in these alloys have been discussed in the preceding Section (2.4).

127

Gest and Troiano¹³⁸ have measured the internal friction of an AlZnMg (7075 type) alloy in the T6 condition and compared the results with studies on an FCC stable austenitic stainless steel. One important feature of hydrogen embrittlement is the interaction of hydrogen with lattice defects and especially dislocations. In the previous study on stainless steel, Troiano¹³⁸ demonstrated well defined hydrogen - dislocation relaxation peaks in austenitic stainless steel. Specifically a very strong peak identified as



Region 1 - Decreasing ductility due to ageing and hydrogen embrittlement.

Region 2 - Uniform low ductility due to aged microstructure and embrittlement by hydrogen.

Region 3 - Gettering of hydrogen by developing grain boundary precipitates and an increase in ductility.

Region 4 - Gettering effect of grain boundary precipitates exhausted and a reversion to zero ductility.

Fig. 36 Ductility of an Al-6Zn-3Mg alloy, isothermally exposed to WSAV at 120°C and tested at various times.

the result of a hydrogen - substitutional atom pairing, and a second, broader, less pronounced peak, resulting from a hydrogen-dislocation interaction. Hydrogen is also known to lower the stacking fault energy of austenitic stainless steels¹³⁹. This can be expected to reduce ductility by making cross slip more difficult. Corresponding peaks to those exhibited by austenitic stainless steel are shown in Figure 37 for the AlZnMg alloy. A high intensity peak at 130° K is attributed to hydrogen - substitutional pairing and a weak peak at 170° K is attributed to hydrogen-dislocation interaction.

As in the stainless steel study¹³⁸, cold work (approximately 15% reduction) of the AlZnMg alloy greatly reduced the intensity of the interstitial hydrogen peak at 130° K and increased the intensity of the hydrogen-dislocation peak at 170° K (Fig. 38). This change of peak intensities with cold work represents a redistribution of hydrogen from interstitial solution to traps, the most probable trap being dislocations arising from the deformation.

In the same study the influence of cathodic polarisation in HCl and also NaCl at -1700 mV (vs SHE) on the lattice parameter confirms the permeation and internal friction data in terms of the presence of interstitial solid solution hydrogen (Fig. 39). Outgassing reduced the lattice parameter essentially back to the original uncharged value confirming the reversibility of hydrogen induced damage.

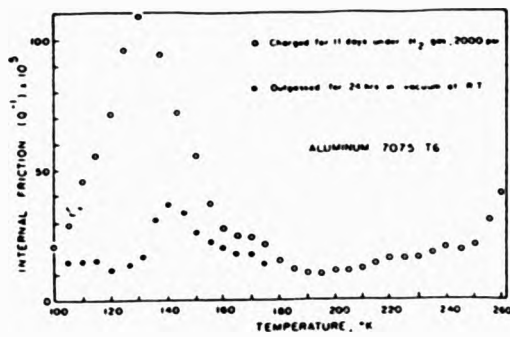


Fig 37 Internal friction versus temperature for hydrogen gas charged 7075-T6 aluminium alloy.

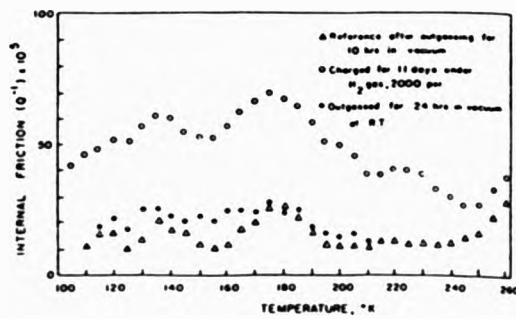


Fig 38 Internal friction versus temperature for hydrogen gas charged 7075-T6, 15% cold worked, aluminium alloy.

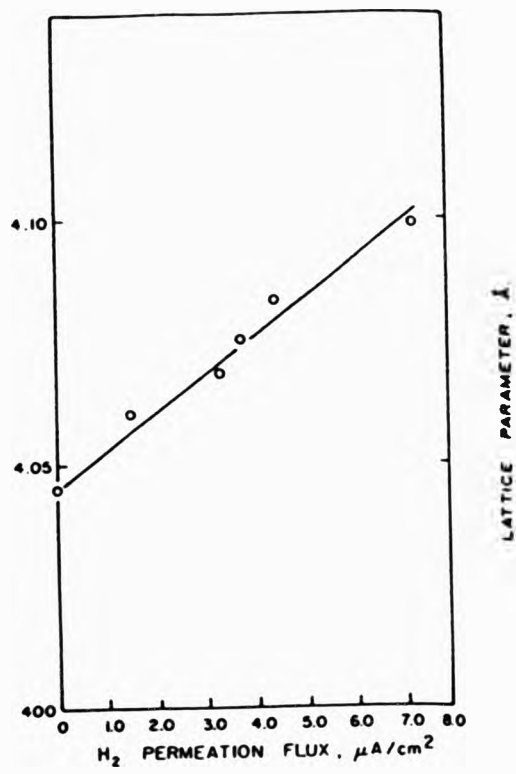


Fig. 39 The effect of permeation on the lattice parameter for a 7075-T6 alloy charged in HCl (pH 1) at -1700 mV (vs SHE).

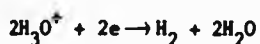
2.5.5 Hydrogen evolution reaction on aluminium and on aluminium alloys

The hydrogen evolution reaction on aluminium and the reaction of aluminium with water saturated air vapour are of particular importance in the study of hydrogen entry into aluminium alloys and in particular magnesium containing alloys like the 7000 series. The WSAV reaction is discussed in the next Section. The hydrogen evolution reaction is complex and involves several steps.

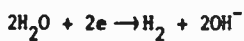
The most important cathodic reactions in aqueous solutions (in the absence of reducing agents) are the reduction of dissolved oxygen to hydroxyl ions by the following equation;



and the reduction of hydrogen ions (hydrogen evolution) by the overall equations;



for acid solutions, and

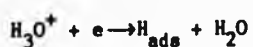


for neutral or alkaline solutions. Oxygen reduction can be excluded by purging the electrolyte with nitrogen gas.

Considering the main cathodic reaction for acid solutions, this

reaction consists of a number of steps.

The discharge step;



followed by either a chemical desorption step (also referred to as "combination", "recombination" or "Tafel recombination");



or an electrochemical desorption step (ion atom desorption);

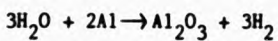


On aluminium surfaces the second step is slower and determines the overall rate of hydrogen gas generation ¹⁴⁰.

The extent to which hydrogen absorption occurs depends on the nature of the metal and the degree of surface coverage with adsorbed hydrogen; coverage will vary with the mechanism of the hydrogen evolution reaction, the overpotential, the nature of the metal and the nature of the solution. Whilst these mechanisms have been studied in some detail for iron alloys, nickel, titanium and some refractory metals there is very little data available for aluminium alloys.

2.5.6 Water saturated air vapour reaction on aluminium and aluminium alloys

It is well known that aluminium reacts with water or water vapour to produce hydrogen⁶ by the following reaction;



The reaction of aluminium with water in the liquid phase has received significant attention for over fifty years and the results of this work have recently been comprehensively reviewed.¹⁴

Basically the reaction of aluminium with water at 70°C produces a duplex film consisting of a layer of pseudoboehmite next to the metal and a layer of bayerite crystals in contact with the solution. Pseudoboehmite is an aluminium oxyhydroxide similar to boehmite (AlO.OH) but containing more water, whereas bayerite is a form of aluminium hydroxide (Al(OH)₃). Pseudoboehmite and bayerite are thermodynamically metastable phases at 70°C and 1 atm. pressure, the equilibrium phase being gibbsite. The formation of either 1 mole of pseudoboehmite or bayerite involves the production of 1.5 moles of hydrogen.

The reaction on oxide filmed aluminium involves an induction period at 70°C of the order of one minute; this is followed by a period of rapid growth, which then slows down after ten minutes. During the induction period the amorphous oxide film thickens to about 100 Å and is penetrated either by hydroxyl ions or water

until conditions for hydrolysis are established and a soluble aluminium species is produced. Dissolution is then accompanied by the simultaneous precipitation of hydrous oxide which subsequently transforms to pseudoboehmite. When a layer of pseudoboehmite has formed the rapid growth rate period ends and further growth must occur by diffusion through this layer, the need for dissolution to occur as a stage in the reaction being inferred from studies involving the ageing of hydroxide gels which similarly produce pseudoboehmite¹⁴¹. The rate determining step during the slow growth stage is the inward diffusion of water rather than the outward migration of Al^{3+} ions which suggests that new hydrous oxide develops under the existing film¹⁴². The mode of bayerite formation is not clear but this is also considered to involve a dissolution and precipitation process, presumably of the pseudoboehmite surface in contact with the solution. Measured film thicknesses are of the order of 2 to 3 μm and growth ceases where the surface is covered in bayerite¹⁴³.

The bayerite crystals are not embedded in the surface nor joined to the pseudoboehmite and may be removed by mechanical means. They appear as cones, wedges and rods and have been given the general classification of somatoids¹⁴. Pseudoboehmite takes the form of platelets which appear as fibrils or needles. Bayerite and pseudoboehmite are therefore readily identifiable by their characteristic morphologies.

The reaction of aluminium with water vapour as opposed to water at 70°C has received little attention. Vedder and Vermilyea¹⁴⁴



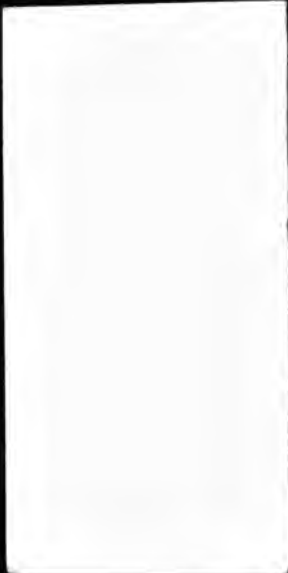
concluded from vapour phase studies at 90 and 100°C that condensation was essential for hydroxide growth to occur, that the induction period was greatly extended and that the growth rate was much reduced; for example the induction period increased to 27 hours and, after 70 hours reaction, the weight gain was only equivalent to that achieved within 25 minutes in liquid water. No morphological information was reported in this work although it was suggested that the same dissolution/precipitation reaction processes that form pseudoboehmite and bayerite were in operation.

Scamans and Rehal¹⁴⁵ have examined the water vapour reaction of pure aluminium, AlMg and AlZnMg alloys made from "virgin" alloying material. Examination was by SEM and Scanning Transmission Electron Microscopy (STEM) techniques after pre-exposure of prepared thin foils to water vapour at 100% relative humidity at 70°C. It was noted that the reaction proceeds by random nucleation of circular "islands" of hydroxide within the first few minutes of reaction. This reaction proceeds until the specimen area is covered in a hydroxide layer, which at high magnification was shown to consist of many small blisters. These had decohered and fractured as a result of hydrogen generated at the amorphous oxide-metal interface, and had defilmed the immediate area of the blister. The debris from the blister wall continues to grow to form bayerite somatoids, in a matrix of pseudoboehmite. The blisters were made more visible by thickening the amorphous surface film by storage in dry air after electropolishing. These reaction sites were shown to be regions where droplet formation had not occurred. Regions where droplet formation did occur

rapidly produced a much thicker hydroxide layer which extended over the area of droplet surface coverage. Conditions here were more typical of total immersion in water.

Reaction of alloy specimens (AlMg and AlZnMg) in WSAV at 70°C also results in surface film blistering and defilming followed by growth of a duplex hydroxide film. Whilst examination, in the Scanning Transmission Electron (STE) mode, of reaction sites on pure aluminium revealed no metallurgical features that would have enhanced the reaction, examination of reaction sites on alloy specimens revealed underlying grain boundaries. Preferential reaction at grain boundary - metal surface intersections is a characteristic of the reaction on magnesium containing alloy specimens. This reaction selectivity was found to be a strong function of solution heat treatment temperature, where at solution temperatures of 550°C and 450°C preferential grain boundary attack, with numerous reaction sites lining up along the grain boundary occurred, whilst at 350°C no such preferential reaction siting was observed. Where preferential grain boundary reaction does occur, general attack continues in the grain interiors. Not all the grain boundaries are attacked but the factors which produce the grain boundary immunity are not fully understood.

After extended reaction times (24 h) the duplex hydroxide layer continues to grow and the pseudoboehmite exhibits its characteristic morphology appearing as fibrils or needles. The fully developed bayerite crystals grow from the metal surface, as distinct from the mode of growth under conditions of total



immersion. The development of the WSAV - aluminium reaction is shown schematically in Figure 40.

Using conventional Transmission Electron (TE) imaging the reaction sites cannot be readily observed except where revealed by the penetration of hydroxide into the metal surface after very long (24 h) exposures. However, evidence of hydrogen penetration of grain boundaries is readily apparent where for AlMg and AlZnMg alloy specimens reacted for 10 minutes at 70°C the grain boundary shows hydrogen bubbles, imaged by strain field contrast, and fully contained within the thin foil. Hydrogen bubbles have been observed¹³⁷ to nucleate on dislocations, grain boundary precipitates and manganese and chromium rich intermetallic phases.

It was proposed that hydrogen bubble formation takes place due to the heating affect of the electron beam and the relaxation of the elastic stress constraint in the thin foil, and that bubble formation would not therefore take place in bulk specimens. It was also proposed that the grain boundary precipitates, in particular overaged precipitates and primary manganese and chromium containing intermetallics act as hydrogen traps, locally "gettering" hydrogen, and rendering it innocuous during the hydrogen embrittlement stress corrosion cracking of these alloys.

The activation energy for bubble formation must be small as indicated by the ease of hydrogen bubble formation under the stimulation of the 120 kV electron beam.

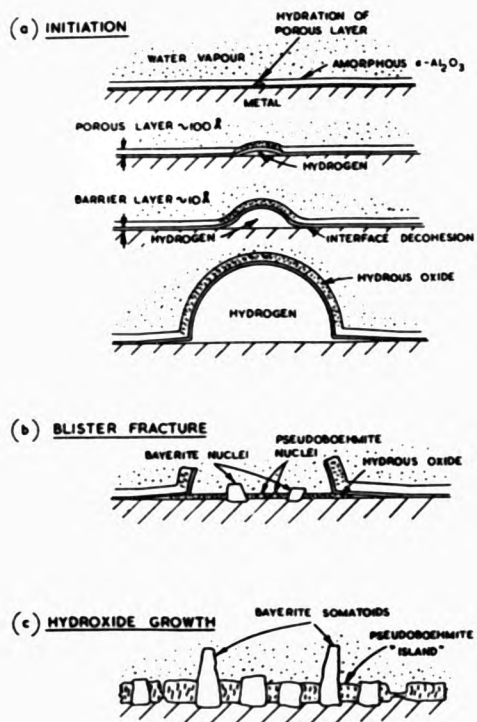


Fig. 40 Schematic illustration of the Water Saturated Air Vapour (WSAV) - Aluminium reaction at the metal-oxide interface.



The specificity of the WSAV reaction at the grain boundary in AlMg and AlZnMg alloys produces hydrogen at a convenient site for entry into the underlying grain boundary; stress corrosion in these alloys being a predominantly intergranular phenomenon.

The observation that some grain boundaries are immune to WSAV attack is clearly important in the development of a stress corrosion resistant alloy. It is thought that magnesium segregation onto the grain boundary plane is an important factor, and whilst this has not been confirmed in the study,¹⁴⁵ much research effort continues in this field. (See Section 2.4.2).

2.5.7 Diffusion and permeation of hydrogen

The entry of hydrogen into metals involves three essential stages.

- a) Adsorption of hydrogen on the metal surface.
- b) Solution of hydrogen in the metal.
- c) Diffusion of hydrogen into the metal.

These three stages give rise to the phenomenon of permeation of hydrogen through a metal foil in which hydrogen enters on one side and leaves on the other. Diffusion and permeation rates of hydrogen in metals govern, in part, their susceptibility to hydrogen embrittlement.

2.5.7.1 Adsorption of hydrogen

Gases may be adsorbed on solid surfaces in various ways, and when the adsorbed species is held by the residual unsaturated field of

forces of the surface atoms around the gas molecules, the process is referred to as physical or Van der Waals adsorption. Physical adsorption is reversible and the adsorbed gas can be removed by vacuum treatment or by heating to moderate temperatures, since the enthalpy of physical adsorption is small (<1kJ/mol). Langmuir¹⁴⁶ suggests that adsorbed layers are not more than one molecule thick. At moderate pressures the quantity of gas adsorbed onto a unit area of a surface is a hyperbolic function of gas pressure. At low pressures when the adsorbed layer is incomplete the total amount of gas adsorbed is proportional to the square root of the pressure, thus the dissociation of H₂ molecules into two hydrogen atoms will give the following relationship at constant temperature;

$$S = KP^{\frac{1}{2}} \quad (2.11)$$

where;

S = solubility (volume H₂ in cm³ per 100 gm of metal)

P = pressure (Atm)

K = constant

This is referred to as Sieverts law. In endothermic occluders the solubility of hydrogen can be expressed as a function of temperature and pressure by an equation of the form;

$$S = S_0 \sqrt{P} e^{-(Q/2RT)} \quad (2.12)$$

where;

S = solubility (volume H_2 in cm^3 per 100 gm of metal)

S_0 = constant (volume of H_2 in cm^3 at $0^\circ C$ and one atm)

P = pressure (atm)

Q = heat of solution ($J\ mol^{-1}$)

R = gas constant ($JK^{-1}\ mol^{-1}$)

T = temperature ($^\circ K$)

Whilst hydrogen in the gaseous state may adsorb onto aluminium, and small quantities may enter into solution and diffuse into the bulk, there is no evidence that gaseous hydrogen causes embrittlement of aluminium alloys, whereas the embrittlement of iron alloys and steels by gaseous hydrogen is readily demonstrated.

In chemisorption or activation adsorption¹⁴⁷, the adsorbed layer is chemically combined by covalent or ionic forces to the metal and removal of these layers involves vacuum treatment at high temperatures; the enthalpy of chemisorption is at least $2\ kJ\ mole^{-1}$ and the bond between the metal and the surface is almost as strong as in stoichiometric compounds. Hydrogen is chemisorbed due to the pronounced activity of the atomic hydrogen produced during thermal dissociation or during the cathodic hydrogen evolution reaction.

2.5.7.2 Solution of hydrogen

Diffusion and permeation of hydrogen in metals will proceed following the endothermic solution process. In the case of those

metals in which interstitial solubility of hydrogen occurs without compound formation (Fe, Ni, Pt and Al etc.), the solubility increases as temperature increases and thus the solubility of hydrogen in endothermic occluders can be expressed in terms of temperature and pressure (2.12).

The relationship between the saturated hydrogen content and the cathodic current density can be used to infer the mechanism of absorption and solution of hydrogen.

Scheutz and Robertson¹⁴⁸ found the following relationship for martensitic steel polarised in H_2SO_4 .

$$C_s = a + b \log i \quad (2.13)$$

where;

C_s = the saturated hydrogen content (volume H_2 in cm^3 per 100 gm of metal)

i = the cathodic current density ($mA\ cm^{-2}$)

a, b = constants.

Exothermic occluders which form hydrides (Ti, V, Nb and Zr etc.) show an inverse relationship between solubility and temperature. Care must be taken to distinguish between hydrogen in solid solution (similar to the situation in endothermic occluders) and hydrogen in solid solution which has gone to form a metal hydride. Thus the absorbed hydrogen may exceed the solubility limit, and depend upon the kinetics (and extent) of hydride formation.

2.5.7.3 Diffusion of hydrogen

Diffusion is concerned with the transport of matter through media resulting from concentration gradients or differences of chemical potential. Fick's first law relates the rate of flow of the diffusing substance with the concentration gradient.

$$J = D \frac{\delta c}{\delta x} \quad (2.14)$$

where;

J = the amount of substance passing perpendicularly through a unit area in a unit time ($\text{mole cm}^{-2} \text{s}^{-1}$)

$\frac{\delta c}{\delta x}$ = the concentration gradient (mole cm^{-1})

D = the diffusion coefficient ($\text{cm}^2 \text{s}^{-1}$)

Fick's second law gives the rate of change of concentration at any point.

$$\frac{\delta c}{\delta x} = D \frac{\delta^2 c}{\delta x^2} \quad (2.15)$$

The diffusion coefficient conforms to an Arrhenius type of equation.

$$D = D_0 e^{(-Q/RT)} \quad (2.16)$$

Where;

D_0 = pre-exponential factor (constant frequency factor) (cm^2s^{-1})

D = diffusion coefficient (cm^2s^{-1})

Q = activation energy for diffusion (Jmol^{-1})

R = gas constant ($\text{JK}^{-1}\text{mol}^{-1}$)

T = temperature ($^{\circ}\text{K}$)

The constant D_0 has been evaluated theoretically by West and Zener¹⁴⁹ to be:

$$D_0 = 1/6 \gamma a^2 \exp\left(\frac{\Delta S}{R}\right) \quad (2.17)$$

Where;

a = the lattice spacing (cm)

γ = the frequency of vibration at equilibrium (s^{-1})

ΔS = the entropy of activation ($\text{JK}^{-1}\text{mol}^{-1}$)

R = the gas constant ($\text{JK}^{-1}\text{mol}^{-1}$)

D_0 = pre-exponential factor (constant frequency factor) (cm^2s^{-1})

For metals such as iron in which hydrogen diffusion behaviour has been extensively researched, there is reasonable agreement between the values of diffusivity obtained by different workers above 400°C . Diffusion behaviour below approximately 400°C is inconsistent with high temperature observations, and there is poor agreement between different workers, particularly at ambient temperatures where values of the apparent diffusion coefficient ranging from 10^{-6} to $10^{-9} \text{cm}^2\text{s}^{-1}$ have been reported. There is a break in the Arrhenius plot for iron at about 400°C (Fig. 41). This anomalous type of diffusion behaviour has been observed by

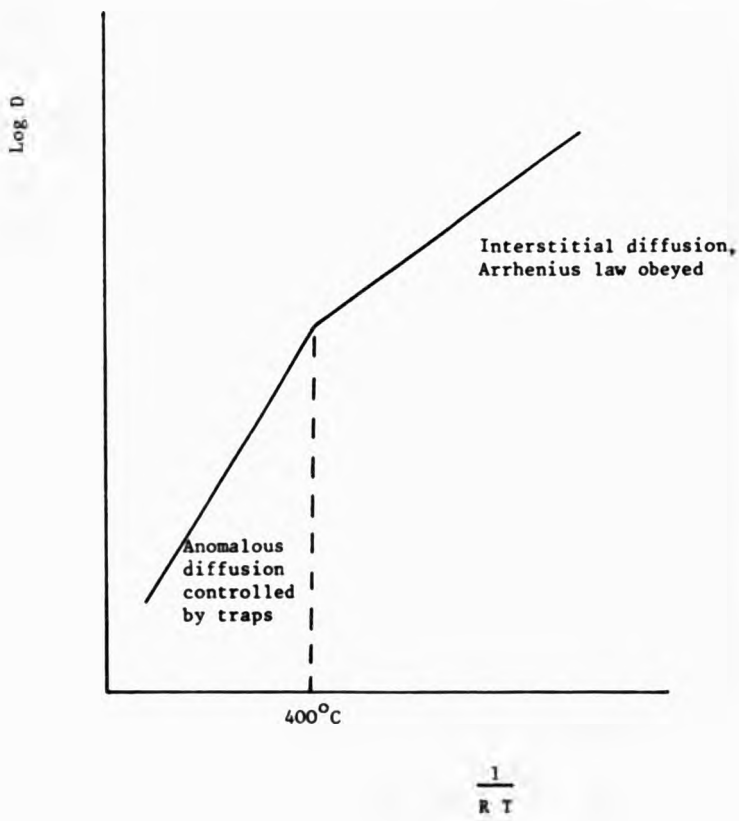


Fig. 41 Illustration of the diffusion behaviour of iron alloys as a function of temperature.

several workers¹⁵⁰⁻¹⁵². Diffusion at lower temperatures is controlled by the rate of escape of hydrogen from traps, which requires high activation energy and results in a large decrease in diffusivity. It follows that the nature and density of traps will control the apparent diffusion coefficient. Traps are metallurgical features such as second phase particles, point defects, intermetallic compounds, and dislocations whose distribution is a function of the amount of cold work. Hydrogen diffusion coefficients are also a function of grain size, applied stress level and grain boundary and sub-grain grain boundary structure. Hydrogen diffusion at temperatures below 400°C in iron is very dependent upon metallurgical structure. The binding energy between hydrogen and different traps, and hence the significance of different types of traps, remains controversial and is the subject of continuing study.

Oriani^{126, 153} has reviewed the trapping theories which have been postulated to account for the anomalous diffusion and permeation data. McNabb and Foster's theory^{154,155} postulates that trapped hydrogen is in local equilibrium with lattice hydrogen and that the apparent activation energy, E_{app} for the release of trapped hydrogen is given by:

$$E_{app} = E_q + E_t \quad (2.18)$$

Where:

E_q = the activation energy for the diffusion

E_t = the trap depth.

Caskey and Pillinger¹⁵⁶ have examined McNabb and Foster's mathematical analysis of diffusion plus trapping. Diffusivities are commonly calculated from results of a permeation experiment by the time-lag method or at the inflection point of the permeation versus time curve using expressions derived from simple diffusion theory (see Section 3.3.5.5). Caskey and Pillinger show that trapping will modify the course of the experiments however, and render such calculations invalid. A time-lag expression derived by McNabb and Foster relates the intercept of the integrated flux on the time axis to the parameters that describe reversible trapping. This intercept is at a longer time than for simple diffusion and depends on the trap density and the ratio of the trap to release rates. Unless the lattice diffusivity is known accurately from another independent experiment, a single time-lag experiment will not itself detect the presence of trapping. Time-lag experiments on specimens with varying trap densities, such as specimens with successively greater cold-work, would detect trapping.

Aluminium and aluminium alloys have received very little attention in their hydrogen diffusion behaviour. This situation has changed recently due to the increased interest in the hydrogen embrittlement mechanism for stress corrosion cracking of AlZnMg and AlMg alloys. For hydrogen embrittlement of these alloys to occur, hydrogen diffusion must also take place although the ability of hydrogen to diffuse into these alloys to the extent necessary to cause embrittlement is still a matter of debate.

A certain limited amount of data is available for hydrogen diffusion in aluminium alloys which has been obtained by a number of different techniques.

Papp and Kovács-Csetényi¹⁵⁷ obtained values for the hydrogen diffusion coefficient in pure (99.8%) aluminium over a range of temperatures by desorption and analysis in a mass spectrometer. They showed that over the temperature range studied (440-560°C) there is a straight line relationship between $\log D$ and $1/T$, and the Arrhenius law is valid for hydrogen diffusion in pure aluminium over this temperature range. They obtained values for D_0 of $2.5 \times 10^{-6} \text{ m}^2 \text{ sec}^{-1}$ and for the activation energy of 90 kJ mol^{-1} . These values differed from those obtained by other workers and this was attributed to the purity of the aluminium and the nature of the oxide film. Increasing purity to 99.99% and 99.999% Al causes an increase in activation energy and a decrease in the diffusion constant (D_0). In high purity aluminium diffusion of hydrogen through the oxide film is rate determining and an Arrhenius type temperature dependence of the diffusion coefficient is not obtained. As the purity of the aluminium decreases, hydrogen desorption is controlled by its bulk diffusion and not its diffusion through the oxide film. Actual diffusion coefficients obtained in this study were $7 \times 10^{-4} \text{ cm}^2 \text{ sec}^{-1}$ at 560°C and $8 \times 10^{-5} \text{ cm}^2 \text{ sec}^{-1}$ at 441°C. Assuming that anomalous diffusion does not take place this gives a value for D of $8 \times 10^{-12} \text{ cm}^2 \text{ sec}^{-1}$ at 70°C, ($5 \times 10^{-14} \text{ cm}^2 \text{ sec}^{-1}$ at 20°C).

Extrapolated high temperature data for pure aluminium at 70°C from the results of Eichenauer and Pebler¹⁵⁸ gives a value of $1 \times 10^{-9} \text{ cm}^2 \text{ sec}^{-1}$.

Ransley and Talbot¹⁵⁹ give a diffusivity of $1.2 \times 10^{-10} \text{ cm}^2 \text{ sec}^{-1}$ for hydrogen diffusion in aluminium at 20°C.

Gest and Troiano⁸⁶ in a study on the 7075 type AlZnMg alloy in the T6 condition obtained a value of D of $2 \times 10^{-9} \text{ cm}^2 \text{ s}^{-1}$ at room temperature by the electrochemical permeation technique. The experiments were carried out under potential and current control with a HCl charging solution (pH 1). Although the permeation transients obtained have not been published, they noted that hydrogen permeation occurred at cathodic potentials due to hydrogen evolution and also at anodic potentials due to pitting reactions. Gest and Troiano also noted that the diffusion coefficient was comparable to that of austenitic stainless steels (also with an f.c.c. lattice structure).

Scamans and Tuck¹⁶⁰ obtained a diffusion coefficient of $1 \times 10^{-10} \text{ cm}^2 \text{ sec}^{-1}$ for a super-pure Al-4.3%Zn-2.5% Mg alloy at 70°C by a technique involving exposing a 0.5 mm sheet of the alloy to WSAV and measuring the permeated hydrogen on the other side of the membrane by gas chromatography. They attributed the diffusion to hydrogen transport along the grain boundary plane.

Holroyd and Hardie¹⁶¹ in a study of the dependence of mode of

fracture (from brittle intergranular to brittle transgranular) in the corrosion fatigue of the 7017 type AlZnMg alloy in the T651 temper, upon frequency and stress intensity range, and assuming hydrogen diffusion to be the rate determining step, derived a diffusion coefficient of $3.2 \times 10^{-9} \text{ cm}^2 \text{ sec}^{-1}$, which compares favourably with other published data.

Edwards¹³⁶ performed slow strain rate tests on gold coated tensile specimens, cathodically charged at constant potentials for periods of time up to 240 h. Diffusion coefficients were calculated based upon the time required to give a constant reduction in ductility. For a naturally aged and overaged high purity Al-6.1% Zn-2.9% Mg alloy the values reported were $5 \times 10^{-10} \text{ cm}^2 \text{ sec}^{-1}$ and $5 \times 10^{-11} \text{ cm}^2 \text{ sec}^{-1}$ respectively.

2.5.7.4 Permeation of hydrogen

The term permeation is used to denote the combined effect of three processes - entry, passage within and exit of a gas through a material. In the case of a trap free metal the rate of flow of the gas is controlled by the laws of diffusion, and it has been established that diffusion is rate controlling. During permeation the quantity of gas, J, passing through a membrane of thickness, L, and area, A, in time, t, under equilibrium conditions is given by:

$$J = \frac{DA (C_2 - C_1) t}{L} \quad (2.19)$$

where;

C_2 = the concentration of the gas in the metal at the entry point (mole cm^{-3})

C_1 = the concentration of the gas in the metal at the exit point (mole cm^{-3})

D = the diffusion coefficient ($\text{cm}^2 \text{sec}^{-1}$).

J = for an electrochemical permeation experiment, the steady state current of permeating hydrogen (A cm^{-2}).

If $A = 1 \text{ cm}^2$, $L = 1 \text{ cm}$ and $t = 1$ second, then the volume of gas passing through the membrane is known as the permeability of the metal or the permeation rate.

$$P = D (C_2 - C_1) \quad (2.20)$$

where;

P = permeability (moles $\text{cm}^{-1} \text{sec}^{-1}$)

The permeability, P , is related to the solubility, S , and the diffusion coefficient, D , by the following relation;

$$P = \frac{SD}{L} \quad (2.21)$$

where;

S = solubility or average concentration, \bar{C} (mole cm^{-3})
 P, D, L are as previously defined (equation 2.19 and 2.20)

The permeability, solubility and diffusivity are consistent with

each other and represent an intrinsic property of the system. This relationship does not apply if traps are present.

Note that from equation 2.21, permeability is inversely proportional to the thickness of the membrane.

The effect of temperature on the permeability of gases through metals is given by:

$$P = P_0 e^{-(E_p/RT)} \quad (2.22)$$

where;

E_p = the activation energy for permeation (Jmol^{-1})

P_0 = constant ($\text{moles cm}^{-1} \text{sec}^{-1}$)

P, R, T are as previously defined (equation 2.16 and 2.20)

The activation energy, obtained from the slope of the $\log P$ versus $1/T$ curve is considered to be the sum of the activation energy of diffusion, E_a and the heat of solution, H ;

$$E_p = E_a + H \quad (2.23)$$

West and Zener¹⁴⁹ considered E_a to be a strain energy term for the lattice undergoing diffusion by some species.

2.5.8 Promoters and inhibitors

It is well known that certain elements, particularly those of groups V and VI in the periodic table, can markedly increase the entry of hydrogen into steel during cathodic polarisation;

substances that produce this effect are termed "promoters" or "poisons" as their action is to poison the hydrogen recombination reaction and therefore to increase the fugacity of hydrogen atoms and thereby increase the permeation rate.

Inhibitors, by their action in catalysing the hydrogen recombination reaction, markedly decrease the entry of hydrogen into steel. These substances are found particularly in group VIII of the periodic table and platinum is a commonly used inhibitor. The high exchange current density of platinum for hydrogen evolution means that platinum acts as the cathodic surface on which hydrogen is evolved, and reduces the quantity of hydrogen available for diffusion into the substrate.

The effects of poisons have been studied to a greater extent than catalysts and Radhakrishnan and Shreir¹⁶² have ordered the effectiveness of various elements in increasing permeation of steel cathodically charged in H_2SO_4 as follows:

As > Se > Te > S

The mechanism of the poisoning action is controversial and has only been studied in detail for steels and will therefore not be dealt with in detail here.

The effect of arsenic on permeation and hydrogen embrittlement of susceptible aluminium alloys has been studied, and is reported in Section 2.4.1.5.

2.5.9 The determination of hydrogen diffusion coefficients

A number of methods for determination of hydrogen content and diffusion coefficients in metals have been mentioned in Section 2.5.7.3. These include direct methods such as vacuum extraction and analysis in a mass spectrometer¹⁵⁷, electrochemical permeation⁸⁶, permeation of hydrogen by charging in WSAV and analysis by gas chromatography¹⁶⁰ and indirect methods such as measurement of the time to a constant loss in ductility of slow strain rate tested tensile specimens, where the loss in ductility is due to hydrogen embrittlement¹³⁶. Other methods include thermal conductivity, where the hydrogen content of a gas surrounding a heated platinum wire can be measured by calibrating the hydrogen content against the electric current required to maintain the wire at a specified temperature.

Hydrogen can be determined by titration. In this technique, hydrogen is carried by argon gas to hot copper oxide where it is oxidised to water. The water is passed over carbon to form carbon monoxide. Carbon monoxide is then further oxidised to carbon dioxide and absorbed in an alkaline solution. The hydroxide necessary to restore the original pH is determined by titration and the quantity of hydrogen can be calculated.

Electrochemical hydrogen permeation techniques have been used extensively in the study of hydrogen diffusion. The hydrogen produced on one side of a membrane by cathodic charging, or any

other method of generating hydrogen, is measured on the exit side by one of the following methods.

1) The volume of diffusing gas is measured directly using a burette or a capillary tube.

2) The diffusing side is kept under a constant vacuum and the rise in pressure due to the hydrogen is a direct measure of the permeating hydrogen.

3) Permeating hydrogen can be reduced by chemical reaction with methylene blue or ceric sulphate.

4) The electrochemical hydrogen permeation method developed by Devanathan and Stachurski¹⁶³ offers a powerful tool for the exploration of the problem of correlating hydrogen absorption with hydrogen embrittlement. The hydrogen atoms arriving at the exit side are oxidised at a constant anodic potential by potentiostatic control. The anodic current is a direct measure of the permeating hydrogen and a plot of the current as a function of time is the permeation transient, which can be used to calculate apparent diffusion coefficients and solubility.

A pre-requisite for reliable calculation of the maximum hydrogen concentration is the determination of the hydrogen diffusion coefficient, which must therefore be determined with the highest precision. The electrochemical permeation method satisfies this requirement. McBreen, Manis and Beck¹⁶⁴ have compared this method

with the conventional manometric time-lag method. They have emphasised that the superiority of the electrochemical method lies in the fact that, in addition to much higher sensitivity, the boundary conditions are sharply defined. This is in contrast to the manometric method, where the pressure builds up at the exit side of the membrane during the permeation process. Consequently the equilibrium of hydrogen does not remain constant. This gives rise to a situation of shifting boundary conditions and may lead to erroneous values for permeation rates and diffusion coefficients which is corrected in the electrochemical technique.

3.0 EXPERIMENTAL PROCEDURE

3.1 MATERIALS

The material used in these investigations was nominally a commercial 7017 grade medium strength, weldable AlZnMg alloy supplied by the Banbury Laboratory of Alcan International Ltd. The material was received in the form of rolled plate of two thicknesses from which the following specimens were machined.

38mm plate - Short transverse CT specimens and electrochemical hydrogen permeation coupons.

70mm plate - Short transverse DCB specimens and cylindrical hydrogen diffusion experiment specimens.

The composition limits of 7017 are given in Table 3. The material was supplied in the T651 condition.

Surface reaction studies were also carried out on a high purity version of 7017 with the composition given in Table 4 .

This material was in the form of 3mm sheet and was hot and cold rolled from a scalped and homogenised direct chill cast ingot (ingot cross section 200mm x 65mm). Solution heat treatment was carried out in a laboratory muffle furnace for 30 min at 465°C followed by cold water quenching. The specimens were then left at room temperature for 48h followed by ageing at 120°C for 100h to the T6 condition.

Element	Composition (weight percent)
Silicon	0.35 max
Iron	0.45 max
Copper	0.20 max
Manganese	0.05 - 0.50
Chromium	0.35 max
Zinc	4.0 - 5.2
Magnesium	2.0 - 3.0
Nickel	0.10 max
Zirconium	0.10 - 0.25
Titanium	0.15 max
Others each	0.05 max
Others total	0.15 max
Aluminium	remainder

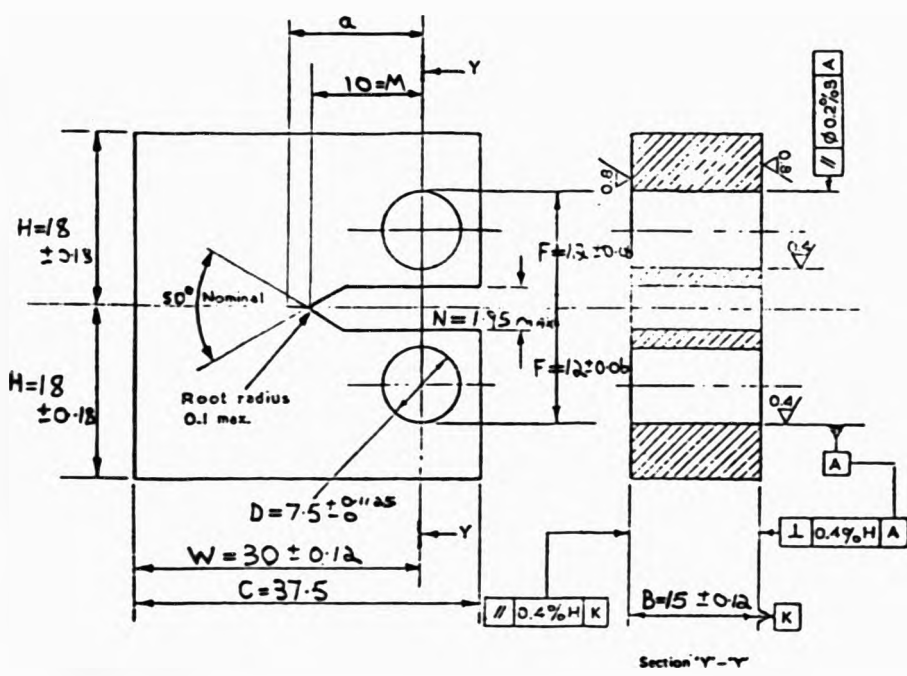
Table 3 Composition limits of commercial 7017 alloy.

3.2 SPECIMEN PREPARATION

3.2.1 Compact tension specimens

Compact tension specimens were fabricated generally in accordance with BS 5447¹⁶⁵.

Blanks were prepared from the as-received plate and machined to a thickness of 15 ± 0.12 mm. From the blanks the specimens were machined to the final dimensions shown in Figure 42.



- W = Net width 30mm
- C = Total width 37.5mm (1.25W)
- B = Total thickness 15mm (0.5W)
- H = Half height 18mm (0.6W)
- D = Hole diameter 7.5mm (0.25W)
- F = Half distance between outerhole edges 12mm (1.6D)
- N = Notch width 1.95mm (0.065W)
- M = Effective notch length 10mm (0.25 to 0.40W)
- a = Effective fatigue pre-crack

Fig. 42 Compact tension specimen dimensions.

Element	Composition (weight percent)
Aluminium	remainder
Silicon	0.05
Iron	0.11
Copper	-
Zinc	4.9
Magnesium	1.84
Titanium	0.01
Boron (ppm)	13

Table 4 Composition of high purity alloy version of 7017.

The blanks were cut such that the fatigue pre-crack plane was oriented to be coincident with the principal working force of the rolled plate and such that crack growth would be in the longitudinal direction. Specimens were therefore cut short transverse - longitudinal (Z-I) in the fracture plane reference system of BS 5447¹⁶⁵.

To ensure that plane strain conditions prevailed throughout the test the specimen thickness was chosen such that¹⁶⁶;

$$B > 2.5 \left(\frac{K_{IC}}{\sigma_y} \right)^2 \quad (3.1)$$

where;

B = specimen thickness (m)

K = fracture toughness of the material $\text{MNm}^{-3/2}$

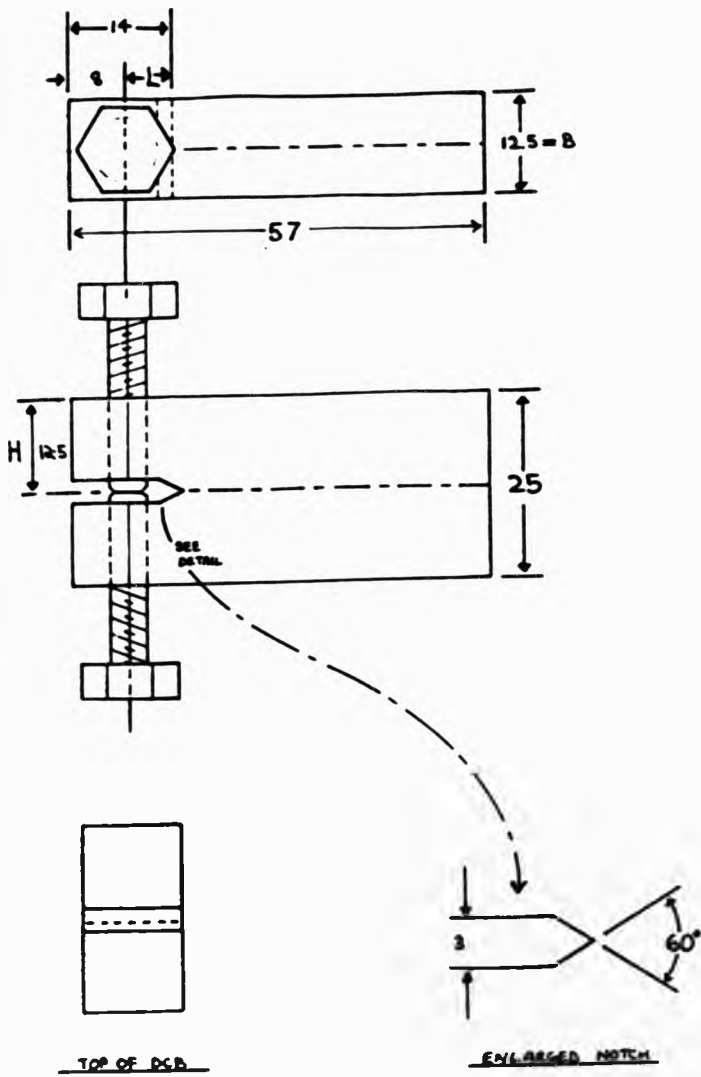
σ_y = yield stress MNm^{-2}

For 7017 material, with a short transverse fracture toughness of $25 \text{ MNm}^{-3/2}$ and a 0.2% proof stress of 435 MNm^{-2} , the specimen thickness should be greater than 8.26mm. A specimen thickness of 15mm was chosen. During the stress corrosion test, the absence of shear lips on the stress corrosion cracked section or the mechanical overload section of the specimen would confirm the predominance of plane strain conditions and the development of a through thickness (σ_{33}) stress during the test. These conditions having been met, valid crack tip stress intensity values can be calculated.

3.2.2 Double cantilever beam specimens

The DCB specimen was essentially the same as that used by Smith and Piper¹⁶⁷ (Fig. 43).

As with the CT specimen, blanks were prepared from the as-received plate but machined to a thickness of 12.5mm. The DCB specimen crack plane orientation was short transverse - longitudinal. A specimen thickness of 12.5mm would satisfy the plane strain criteria. As the blanks were cut from 70mm thick plate, the plate was cut in half, perpendicular to the short transverse direction and DCB specimen blanks machined from both halves of the plate.



B = Total thickness = 12.5mm
 H = Half height = 12.5mm
 L = Notch depth from the loading line = 6mm
 V = Crack opening displacement at the loading line

Fig. 43 Double cantilever beam specimen dimensions.

3.2.3 Hydrogen diffusion experiment specimens

a) Steel specimens to validate the experimental technique

Cold rolled sheet specimens of EN8 mild steel, 0.13mm thick, were used to determine the hydrogen diffusion coefficient of mild steel and thereby prove the electrochemical hydrogen permeation equipment developed for hydrogen diffusion experiments on the 7017 alloy samples. This was thought to be necessary in order to assist in familiarisation of the apparatus and to confirm it's correct functioning. Data for steels for comparison with the experimental results obtained is readily available.

b) 7017 electrochemical hydrogen diffusion experiment coupons

Coupons for the electrochemical hydrogen permeation experiments on 7017 alloy plate were made by cutting a 1.5mm section from the plate such that the short transverse face is exposed to the solutions in the charging and analysing cells. (Fig. 44 i). The 1.5mm thick section was then mounted on a Perspex block with double sided tape and ground on 150, 300, 500 and 600 grade silicon carbide papers followed by 5 and 1 micron diamond paste to give a final thickness of between 0.10 and 0.25mm.

c) 7017 cylindrical specimens for hydrogen diffusion experiments with environmental charging and gas chromatography analysis

Cylindrical flat bottomed specimens 60mm long, 6mm diameter, 1mm wall thickness and with a 1mm thick flat bottom were machined from

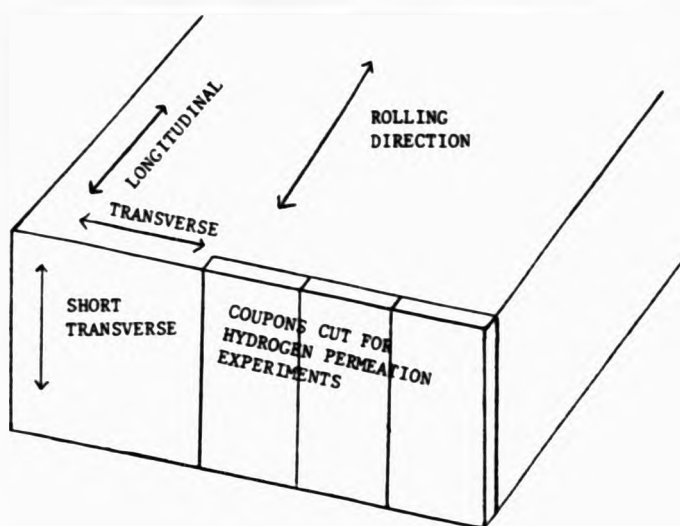


Fig. 44 (i) Orientation of coupons cut from the as-received plate for electrochemical hydrogen diffusion experiments.

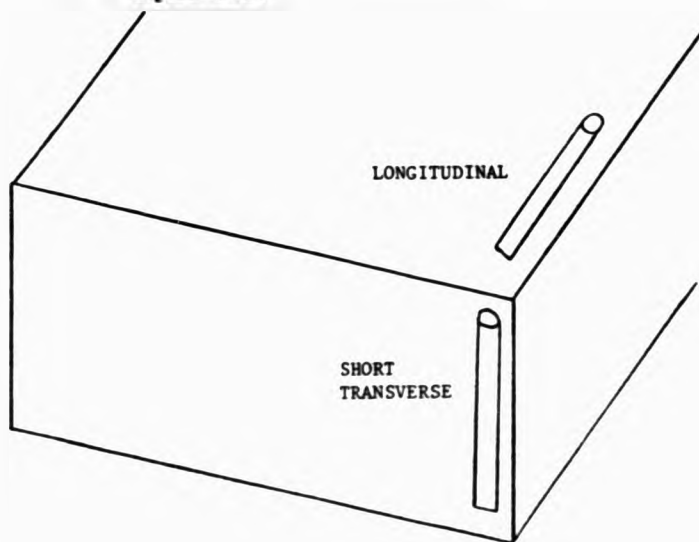


Fig. 44 (ii) Orientation of cylindrical tubular specimens machined from the as-received plate for hydrogen diffusion experiments by gas chromatography.

the as-received plate. Two types of specimen were made with the long axis of the cylinder in the short transverse and longitudinal directions (Fig. 44 11).

3.3 EQUIPMENT AND PROCEDURE

3.3.1 Fatigue pre-cracking

A Dartec M1000 machine was used to introduce pre-cracks into the CT and DCB specimens. Special grips were fabricated to hold the specimens between the servo-hydraulic jack jaw and the jaw fixed on the frame of the machine. Pre-cracking was carried out at 50 Hz under sine wave loading, and the following approximate loading conditions were employed. The actual fatigue loads for each test are given in Table 5 (Section 4.1.1).

Fatigue mode	-	load control
P_{max} - maximum load	-	2.9 kN
P_{mean} - mean load	-	1.5 kN
P_{min} - minimum load	-	0.1 kN
P - load range	-	2.8 kN

The fatigue pre-crack was grown 3.5mm such that the effective pre-crack length, a , was 13.5mm ($a/w = 0.45$) and the stress intensity at the crack tip at the end of the fatigue crack growth, K_f was less than $0.7 K_{IC}$. During fatigue crack growth the ratio of minimum to maximum load, R , was less than 0.1. These criteria are all as recommended in BS 5447¹⁶⁵.

The length of the fatigue pre-crack was measured on each side of the specimen using a travelling microscope.

All fatigue pre-cracking was conducted in air at ambient temperature and at the prevailing relative humidity.

3.3.2 Constant load compact tension specimen machine

A commercial Distington machine was used for the constant load tests. The load was applied to the specimen via a single 30:1 ratio arm. The machine was equipped with an electrical resistance heating jacket. The CT specimen assembly was held in a glass container sealed onto the lower tension rod with rubber gaskets. The specimen grips were made from low alloy steel and fully plastic coated. The CT specimen was mounted in the grips with Tufnol sleeves separating the stainless steel loading pins from the specimen and electrically isolating the specimen. The experimental assembly is shown in Figure 45.

3.3.3 Compact tension specimen crack growth monitoring

A crack opening displacement (COD) compliance technique was developed to monitor the crack growth in CT specimens. This system was similar to that used by Hartman⁸⁴.

The opening displacement of the crack was transferred mechanically by two arms to a position where the clip gauge would be free of any liquid environment surrounding the CT specimen (Fig. 46 i). Knife edges were machined on the extension arms to accept the knife edges on the titanium arms of the clip gauge. The extension

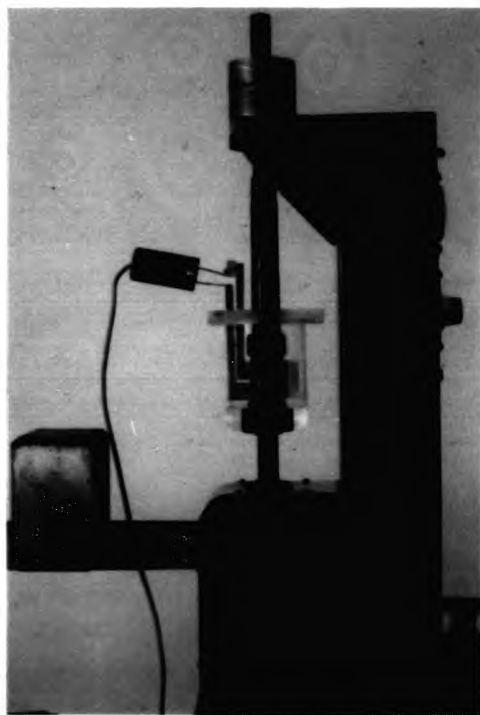


Fig. 45 Compact tension specimen stress corrosion test assembly.

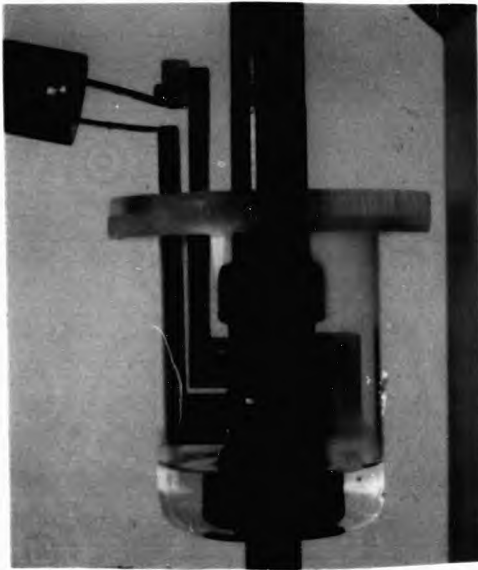


Fig. 46 (i) Compact tension specimen showing the extension arms and clip gauge assembled in the stress corrosion cell.

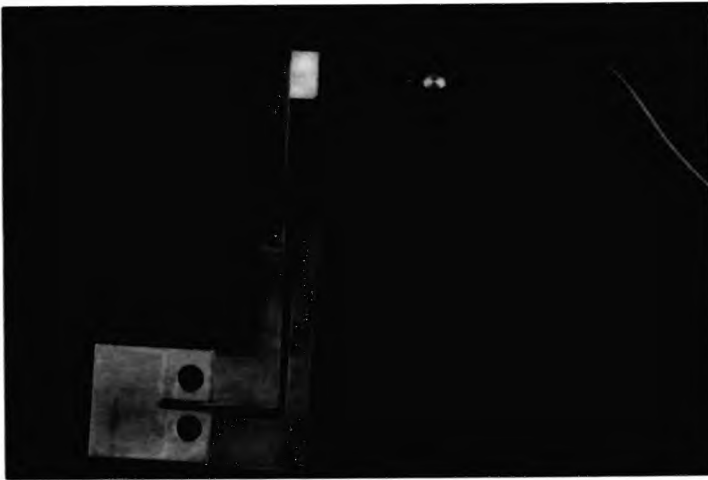


Fig. 46 (ii) Compact tension specimen showing in detail the extension arms used to transfer the crack opening displacement to the clip gauge.

arms were positively located on the CT specimen by lips machined into the arms (Fig. 46 11) and were attached to the CT specimen by bolts. The extension arms were machined from 7017 alloy plate to prevent any galvanic effects from dissimilar metals in contact in the test environment.

The clip gauge was a Welwyn Strain Measurement model 101 and had the following specification.

Temperature range	-	-40 to +80°C
Bridge resistance	-	1000 ohm
Supply voltage (max)	-	15 volts
Deflection range	-	4 to 12.5mm
Nominal sensitivity	-	15mV/volt/cm

The clip gauge supply voltage was 15 volts, obtained from a Farnell Instruments stabilised power supply model LT30-1. The potential output from the clip gauge was backed-off by a constant potential source to give maximum sensitivity and monitored on a Bryans 28000 chart recorder.

Crack length calibration was accomplished by producing a number of CT specimens with a range of fatigue crack lengths.

Each specimen was loaded in tension on the Distington machine with a range of dead loads from 1 to 10 kg. This produced a family of straight line curves of load vs clip gauge output for a range of



crack lengths (Fig. 47). From these curves a second family of crack length calibration curves was constructed of COD clip gauge output vs crack length for a range of dead loads applied to the CT specimen (Fig. 48).

The calibration curves were produced for each of the three clip gauges used in the experimental work and were checked for repeatability after every five stress corrosion experiments.

The extension arm arrangement was an improvement over the direct attachment of the clip gauge to the specimen used by Hartman⁸⁴ as pitting corrosion at the attachment point led to apparent changes in COD not due to crack extension. The method adopted is also an improvement on measuring displacement at the loading lever since it rules out any effect of creep in the loading machine, but not deformation produced as a result of specimen creep.

The calibration cracks were produced by fatigue and any differences between these and stress corrosion cracks are not accounted for. It is clear from Figure 48 that the calibration is more sensitive at longer crack lengths, however it is felt that at these higher crack opening displacements the crack length calibration is less accurate.

Stress intensity calibration for CT specimens is usually based upon the following equation from BS 5447¹⁶⁵.

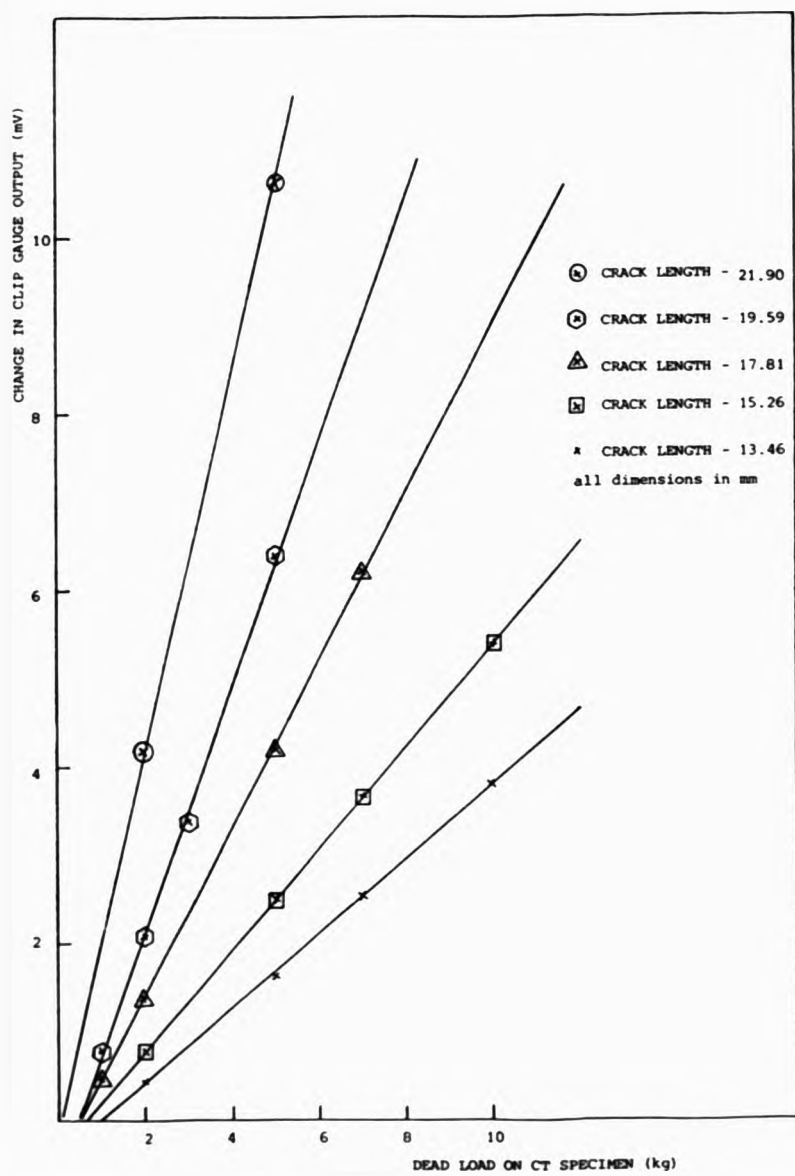


Fig. 47 Family of curves of clip gauge output vs dead load applied to the CT specimen for a range of crack lengths produced by fatigue.

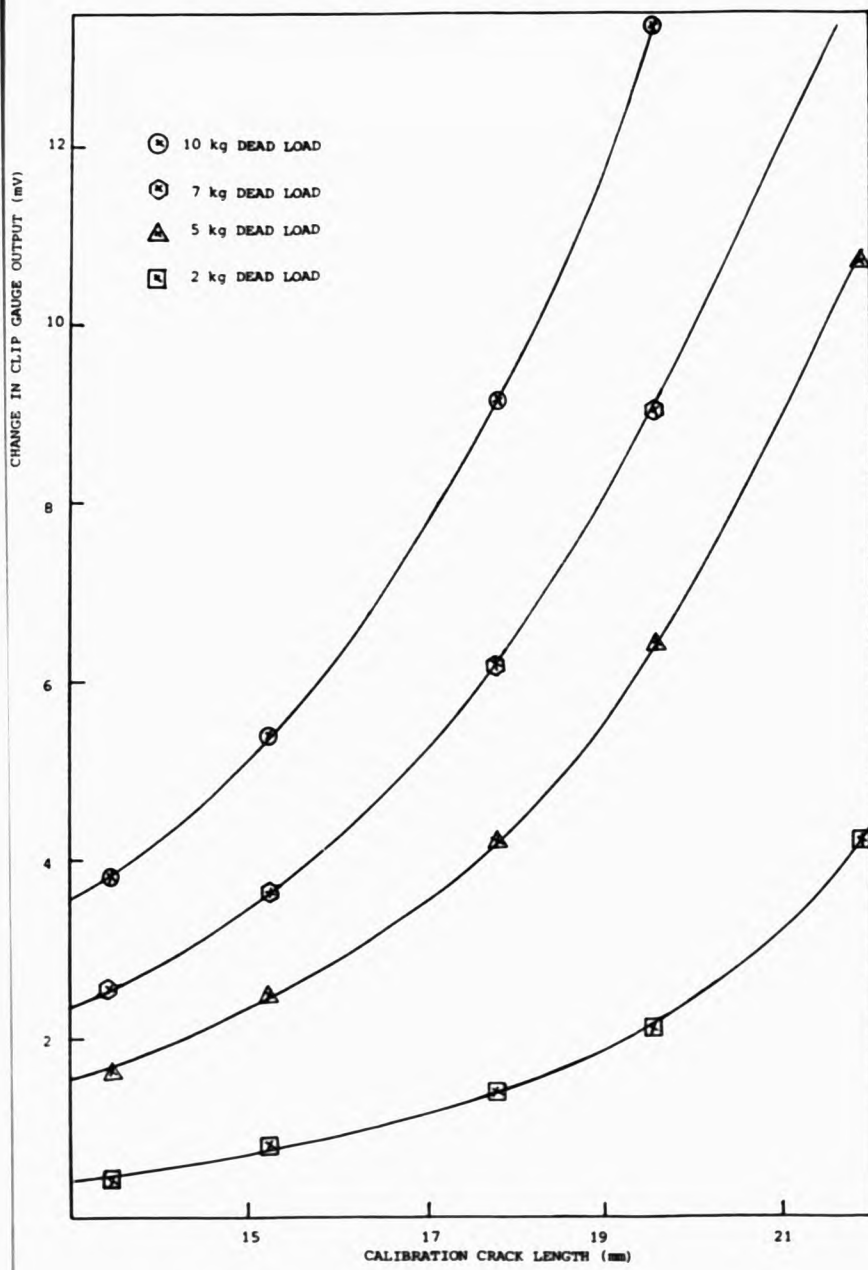


Fig. 48 Family of crack length calibration curves for a range of dead loads applied in tension to the CT specimen.

$$K = \frac{P}{B \cdot W^{\frac{3}{2}}} \left[29.6 \left(\frac{a}{W}\right)^{\frac{1}{2}} - 185.5 \left(\frac{a}{W}\right)^{\frac{3}{2}} + 655.7 \left(\frac{a}{W}\right)^{\frac{5}{2}} - 1017 \left(\frac{a}{W}\right)^{\frac{7}{2}} + 638.9 \left(\frac{a}{W}\right)^{\frac{9}{2}} \right] \quad (3.2)$$

where;

K = Stress intensity in Mode I ($\text{MNm}^{-3/2}$)

P = Load (MN)

B = Specimen thickness (m)

W = Specimen net width (m)

a = Crack length (m)

The polynomial expression in brackets is a compliance function for the particular specimen geometry.

Equation 3.2 should not be used outside the range of a/w from 0.45 to 0.55. In the present study stress corrosion cracks outside this range are encountered and an expression due to Scrawley¹⁷² for the compliance function is used.

$$K = \frac{P}{B \cdot W^{\frac{3}{2}}} \cdot \frac{2 + (a/W)}{(1 - (a/W))^{\frac{3}{2}}} \left[0.866 + 4.64 \left(\frac{a}{W}\right) - 13.32 \left(\frac{a}{W}\right)^2 + 14.72 \left(\frac{a}{W}\right)^3 - 5.6 \left(\frac{a}{W}\right)^4 \right] \quad (3.3)$$

K, P, B, W, a are as defined previously (equation 3.2).

This expression is valid for the CT specimen over a range of a/w from 0.2 to 1, and is at least as accurate as the equation in BS 5447.

3.3.4 Double cantilever beam specimens, constant displacement loading

Tests on DCB specimens, which were bolt loaded to a constant initial deflection of the loading arm, were conducted in glass beakers containing the stress corrosion environment. Tests at elevated temperatures, up to 90°C, were performed in electric ovens with the specimens placed close to the thermometer indicating oven temperature. The level of the environment was kept below the level of the black steel bolt and above the machined notch on the specimen in order to avoid galvanic effects. Any solution losses by evaporation were made up by adding distilled water to the correct level in the beaker. The bolts were covered in a water resistant silicon grease (Fig. 49). Stress corrosion crack length and the loading arm deflection were both measured by a travelling microscope to 0.01mm.

Two sets of tests were conducted on DCB specimens. One set where the stress corrosion crack grew from a "pop-in" failure brought about by bolt loading the specimen to K_{IC} . The resulting ductile fracture grew for a few millimeters and stopped when the crack tip stress intensity was approximately equal to K_{IC} . The other set of tests were performed on DCB specimens in which a fatigue pre-crack had been grown in a manner similar to the CT specimens. Bolt loading of these specimens was carefully conducted to raise the crack tip stress intensity to a value below the material fracture toughness, avoiding any ductile overload failure.

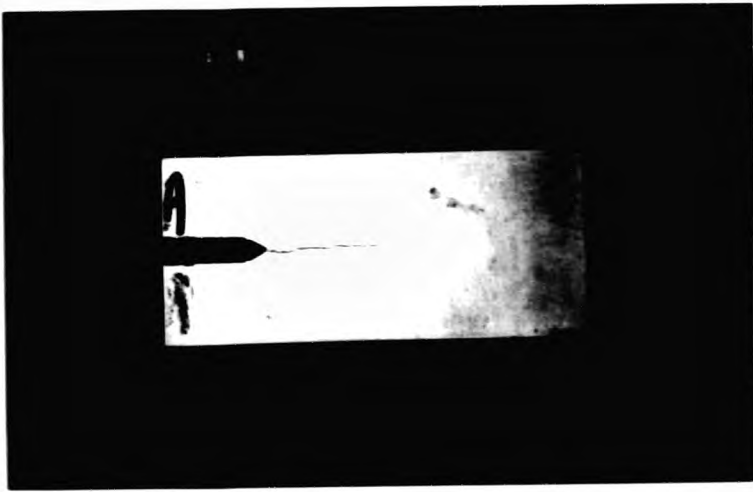


Fig. 49 Bolt loaded DCB specimen.

Stress intensity calibration for DCB specimens is usually based upon the work of Mostovoy et. al.¹⁶⁸, who derived the following expression for compliance for a uniform DCB test piece.

$$C = \frac{2}{3EI} [(a + a_0)^3 + h^2 a] \quad (3.4)$$

where;

C = Compliance

I = The moment of inertia of one of the test piece arms,

$$I = \frac{bh^3}{12}$$

h = specimen half height (m)

E = modulus of elasticity (MNm⁻²)

a = crack length measured from the load line (m)

a₀ = an empirical rotation factor equal to 0.6h

b = specimen thickness (m).

The following expression for stress intensity factor, K_I, at the crack tip of a loaded DCB test piece may be derived from 3.4.

$$K_I = \sqrt{vEh} \frac{[3h(a + 0.6h)^2 + h^3]^{1/2}}{4[(a + 0.6h)^3 + h^2 a]} \quad (3.5)$$

where;

v = the total displacement of the two arms of the DCB test piece at the load line (m).

a, E, h are as defined previously (equation 3.4).

The term $0.6h$ in equation 3.5 is an empirical correction which has been shown to apply to test pieces where h is in the range 6.5 to 50mm and where the crack length, a , does not exceed 250mm¹⁶⁹.

The derivation of equation 3.5 assumes that the cracked test piece acts as two cantilever beams of half the thickness of the test piece, but it can be seen from Figure 43 that this is not the case for test pieces used in the present work, owing to the relatively wide (3.0mm) machined notch. It follows that when these test pieces are loaded the deflections will be larger than those resulting from identically loaded test pieces containing very narrow slits, and thus the values of K_I calculated from equation 3.5 will be erroneously high. Peel and Poole¹⁶⁹ have modified the equation due to Mostovoy to take into account the length (l) measured from the load line, and the width (d) of the slit (see Fig. 43), and the following expression for K_I was derived for a DCB test piece.

$$K_I = \frac{veh^{3/2} \left[6a^2 + (2l + 7.2h)a + 1.8hl + 4.16h^2 - 0.216h^3 \left(\frac{l}{a^2} \right) \right]^{1/2}}{2.83 \left[2a^3 + (1 + 3.6h)a^2 + (1.8hl + 4.16h^2)a + 0.216h^3 \left(\frac{l}{a} \right) + 2.08h^2l + 0.432h^3 \right]}$$

(3.6)

where;

v = the total displacement of the two arms of the DCB test piece
at the load line (m)

L = the notch depth from the load line (m)

E = Youngs Modulus (MNm^{-2})

a , B and H are as defined previously (equation 3.4).

In constant displacement specimens such as the DCB test piece, the stress corrosion test runs from high values of K to low values of K .

At low K values the crack growth rate is low and falls in region 1 of the crack growth rate vs stress intensity curve. For these DCB test pieces the following relationships also apply -

$-K_I$ decreases less rapidly as crack extension increases.

$-K_I$ decreases more rapidly for short cracks and small deflections than for long cracks and large deflections.

Thus, stress corrosion cracks growing in DCB test pieces from short initial cracks may be expected to decelerate more rapidly than those growing from long initial cracks loaded to the same K_I .

Equation 3.6 was used to calculate the crack tip stress intensity in the results reported in Section 4.

The "pop-in" failure of DCB specimens results in a curved ductile fracture crack arrest front from which the stress corrosion crack starts. The final SC crack has a straight crack front and so the bow gradually disappears during SC crack growth and the apparent average SC crack length at the specimen sides is initially shorter than the actual average SC crack length. This is accounted for by assuming that the bow disappears linearly during the growth of the SC crack. The crack length upon which SC crack velocities are based is given by the following equation:

$$a_{\text{actual}} = a_{\text{measured}} + \left[b - \left(\frac{a_{\text{measured}} - a_{\text{initial}}}{a_{\text{total}}} \right) \times b \right] \quad (3.7)$$

where;

- a_{actual} = actual SC crack length (mm)
- a_{measured} = SC crack length as measured on specimen sides during test (mm)
- a_{initial} = initial length of "pop-in" failure as measured on specimen sides (mm)
- a_{total} = total length of SC crack (mm)
- b = length of bow (mm)

The bow length is measured at 0.25, 0.50 and 0.75 of the specimen width after the specimen has been broken open, and the average value calculated.

The crack front that forms the bow is quite steep and an example can be seen in Figures 112 and 113. Where corrosion of the specimen surface prevents the bow from being measured, an average value (4.91mm) has been taken. This is reasonable as the conditions under which the "pop-in" failure occurs result in a narrow range of bow lengths varying from 4.15 to 5.74mm as shown in Table 13.

Valid K values are given when the following conditions are met;¹⁶⁷

$$a, B, \text{ and } (w-a) > 2.5 \left(\frac{K}{\sigma_y} \right)^2 \quad (3.8)$$

where;

- a = effective crack length from the load line (m)
- w = specimen length from the load line (m)
- B = specimen thickness (m)
- K = Fracture toughness of 7017-T651 (25 MNm^{-3/2})
- σ_y = Yield stress of 7017-T651 (435 MNm⁻²)

Since $2.5 \left(\frac{K}{\sigma_y} \right)^2 = 8.3\text{mm}$, the specimen thickness and initial

crack length both meet this criteria. For the "pop-in" specimens the minimum a value is 7.05 mm, and, for the fatigue pre-cracked specimens the minimum a value is 13.17mm.

The DCB specimen is (w-a) indifferent up to a total SC crack

length of 40.7mm, which is the maximum crack length to give a valid stress intensity calculation. With the exception of SC crack growth at 90°C, no crack growth beyond 40.7mm was recorded. At 90°C the crack growth beyond 40.7mm is in the low crack growth rate region of stage I and it is felt that the results are not substantially affected.

3.3.5 Electrochemical hydrogen permeation experimental procedure

3.3.5.1 Introduction

The electrochemical hydrogen permeation technique is a method in which hydrogen diffusing through a metal membrane is detected by means of a permeation current. Since permeation currents of less than $1.0 \mu\text{A cm}^{-2}$ ($= 10^{-11}$ moles $\text{cm}^{-2} \text{s}^{-1}$ hydrogen) can be detected, its sensitivity is comparable to that of the mass spectrograph.

The material of which the hydrogen permeability is to be investigated is made to function as a bipolar electrode in the permeation cell, and hydrogen is produced by cathodic polarisation at a constant current density on one side of the membrane. The potential of the cathodic side of the membrane is measured by a reference electrode. Most of the hydrogen produced forms gaseous bubbles, but a proportion of the hydrogen is absorbed by the membrane and diffuses to the opposite side, where it is instantaneously oxidised and turned into an equivalent current.





This hydrogen oxidation current in the anodic (analysis) side of the permeation cell can be amplified and recorded as a "permeation transient". The instantaneous oxidation of hydrogen is achieved by maintaining the potential on the anodic side at a sufficiently high positive value with respect to the reversible hydrogen potential by means of a potentiostatic circuit.

3.3.5.2 Solutions

Permeation of cathodic hydrogen is very sensitive to the presence of trace impurities in the electrolyte solution, and for this reason the purity of all the charging solutions must be carefully controlled. All solutions of sodium hydroxide, sulphuric acid and boric acid were prepared from Analar grade chemicals and freshly made double distilled water. The containers were kept tightly stoppered to prevent ingress of atmospheric CO₂.

Dissolved oxygen in the solutions undergoes reduction at the cathode at low overpotentials, and this will reduce the rate of hydrogen entry into the metal. Oxygen free nitrogen was therefore bubbled through the solutions for 24 h before the solutions were used. All solutions were pre-electrolysed for a period of 12 h at a current of 25 mA in order to further reduce their impurity content.

3.3.5.3 The permeation cell

The permeation cell used for these studies is shown schematically in Figure 50 and is similar in design to that used by Devanathan and Stachurski¹⁷⁰.

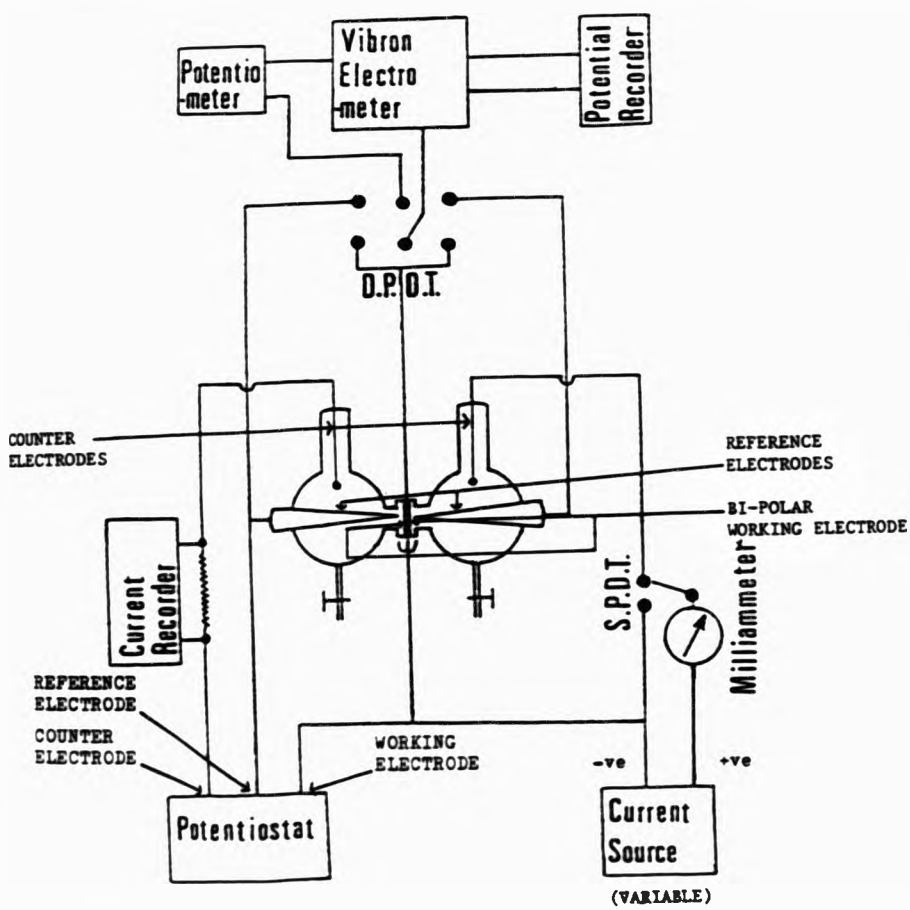
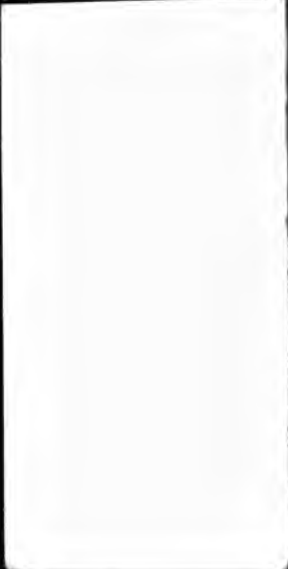


Fig. 50 Hydrogen permeation cell and schematic circuit diagram.



The cell itself consists of two identical half cells, each of which is constructed from 150 ml round bottomed flasks. Two standard quick-fit Pyrex flanges are incorporated on one side of each flask to accept the specimen holder. Each flange has a diameter of 1.5 cm. The counter electrodes in each cell are of expanded platinum mesh strips, spot-welded to platinum wires. In order to minimise any effect of oxygen on the cathode reactions, the counter electrodes are isolated from the main compartments of the half cells by float and sintered disk combinations around the counter electrode units. Oxygen free nitrogen is bubbled into the electrolyte through bubbling tubes which terminate close to the specimen under test in each cell. The gas after passing through the cell compartments escapes through bubblers on each cell. The reference electrodes fitted to each cell are placed in quickfit sockets coupled to Luggin capillaries which terminate at each side of the specimen. In order to minimise contamination of electrolytes due to diffusion, the electrodes are isolated from the cell by housing sintered glass disks in the Luggin capillaries. In order to facilitate easy removal of the electrolytes, taps are located at the bottom of each half cell. The specimen is mounted between the cell flanges by a plastic holder and O-rings, ensuring that a specimen area of 1.767 cm^2 is exposed to the electrolytes in each compartment. A "G" clamp over the flanges and the O-rings ensure that no leakage of solution occurs at the flanges.

A $\text{Hg} \backslash \text{Hg}_2\text{SO}_4, \text{K}_2\text{SO}_4$ (satd.) half cell ($E_0 = + 0.642\text{V}$ vs SHE at 22°C) was used as a reference electrode and was prepared according to Ives and Janz¹⁷¹. The reference electrodes were regularly checked against a saturated calomel electrode ($E_0 = + 0.242\text{V}$ vs SHE at 22°C) supplied by Beckman Instruments.

The electrical circuitry basically comprised two parts; a galvanostatic circuit and a potentiostatic circuit (Fig. 50). The two circuits were electrically isolated from each other. Cathodic charging of the cathodic side of the membrane was effected using a constant current source (Vokam Shandon Southern SAE 2761), and the current was measured by a Sangamo Weston DC milliammeter (model S.82). A set of variable resistances in series facilitated accurate control of the charging current. The current density was calculated from the specimen area exposed to the solution.

A Wenking 70TS1 potentiostat was used to maintain the anodic side of the specimen at a pre-determined constant potential. The hydrogen ionisation current was measured by the potential drop across a suitably sized precision resistor (Cropico Instruments Ltd) in series with the cathode. This e.m.f. was fed directly into a Bryans chart recorder thus giving a continuous measure of permeation current. Potential measurements were made on a high input impedance ($10^{13}\Omega$) valve voltmeter (Vibron Electrometer model 33B-2) backed off by a potentiometer (Pye 7569D) capable of supplying 1.7 volts. For instantaneous monitoring of anodic and

cathodic potentials a double pole, double throw (D.P.D.T.) switch was placed in the potential measuring circuit. Potential - time traces were also recorded on a Bryan recorder.

3.3.5.4 Specimen preparation

A very thin layer of palladium was electrodeposited on the side of the specimen that would be in the anodic compartment of the permeation cell. This was known to prevent anodic dissolution or passivation of the steel specimens without materially decreasing the permeation rate of hydrogen.

For steel specimens 2ml of palladium chloride (200 mg/l) was added to the 100 ml of 0.1 M NaOH in the anode compartment and the polarity of the electrodes reversed in order to plate the palladium. Plating conditions were 30 mA cm^{-2} for 1 minute followed by 3 mA cm^{-2} for 4 minutes. The effect on the permeation of hydrogen in steel was studied by increasing the palladium coating thickness by a factor of five. This increased amount of palladium was electrodeposited onto the AlZnMg specimens in an attempt to prevent its anodic dissolution, i.e. by reducing the levels of porosity in the palladium coating. Plating conditions for the AlZnMg specimens were similar except that plating was performed outside the permeation cell and the specimen was pre-treated in a bath containing a 2:1 ratio of 50% H_2SO_4 and 40% HF in order to dissolve the oxide film. The specimen was transferred wet to the plating bath with a voltage already applied to the specimen to prevent the formation of an immersion deposit.

After electroplating the specimens were washed in distilled water and acetone before assembling into the permeation cell.

3.3.5.5 Analysis of the permeation transient

Consider a metal membrane of thickness L having a diffusion coefficient for hydrogen, D , where diffusion is in the direction of decreasing concentration. Let the concentration at $X = 0$ be maintained at C_2 while at $x = L$ it is kept at C_1 . The initial uniform concentration of the membrane is C_0 . A finite time, t , is required before a steady state concentration gradient is set up. During this time the concentration of the hydrogen in the membrane at a distance X , $C_{x,t}$ is given by ¹⁷³ ;

$$C_{x,t} = C_2 + (C_2 - C_1) \frac{x}{L} + \frac{2}{\pi} \sum_{n=1}^{\infty} \frac{C_2 \cos n\pi C_1}{n} + \frac{\sin n\pi x}{L} e^{-\frac{Dn^2\pi^2 t}{L^2}} + \frac{4C_0}{\pi} \sum_{m=1}^{\infty} \frac{1}{(2m+1)} \frac{\sin (2m+1)\pi x}{L} e^{-\frac{D(2m+1)^2\pi^2 t}{L^2}} \quad (3.9)$$

For a membrane initially at zero concentration, the permeation rate from the side $X = 0$, at time t is given by:

$$P = D \left(\frac{\delta c}{\delta x} \right)_{x=0} \quad (3.10)$$

Differentiating equation 3.9 with respect to x , multiplying by the diffusion coefficient D and putting $x, c_0 = 0$;

$$P = \frac{D(c_2 - c_1)}{L} + \frac{2D}{L} \sum_{n=1}^{\infty} (c_2 \cos n\pi - c_1) e^{-\frac{Dn^2\pi^2 t}{L^2}} \quad (3.11)$$

When the steady state is obtained, t approaches infinity, and the permeation P is given by;

$$P = \frac{D(C_2 - C_1)}{L} \quad (3.12)$$

The diffusion coefficient of hydrogen in a membrane can be evaluated from a typical permeation transient represented by Figure 51. The time lag T_L is the time at which the quantity of hydrogen diffusing through the membrane is considered to be the same as at the steady state condition. Thus the shaded areas of the permeation transient become equal to each other at time T_L . This time interval corresponds to a permeation rate of 0.6299 times that of the steady state permeation.

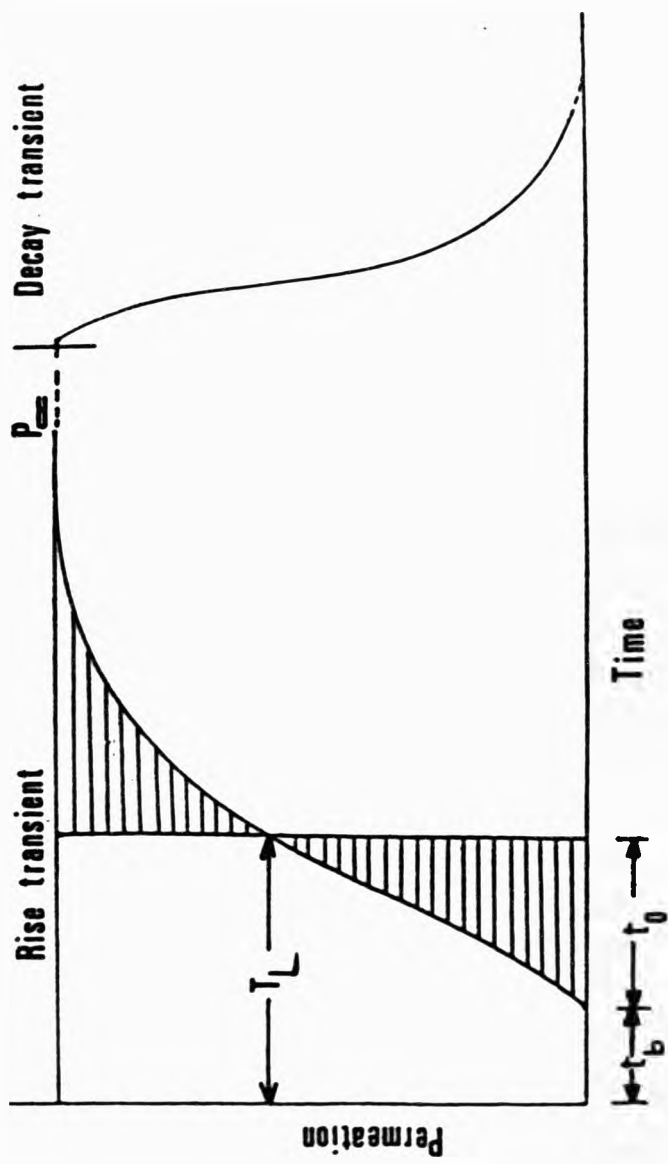


Fig. 51 Schematic rise and decay transients for hydrogen permeation.

By integrating equation 3.11 with respect to t as $t \rightarrow \infty$, P is given by;

$$P = \frac{D}{L} (C_2 - C_1) t \left[1 - \frac{L^2 (C_2 + 2C_1)}{6Dt(C_2 - C_1)} \right] \quad (3.13)$$

If P is extrapolated to zero it will cut the time axis at say T_L which will then be given by;

$$T_L = \frac{L^2 (C_2 + 2C_1)}{6D(C_2 - C_1)} \quad (3.14)$$

if $C_2 \gg C_1$ then;

$$T_L = \frac{L^2}{6D} \quad (3.15)$$

The time lag, T_L is the sum of the breakthrough time t_b and the rise time constant t_0 i.e.

$$T_L = t_b + t_0 \quad (3.16)$$

The diffusion coefficient is related to the breakthrough time and rise time constant as follows;

$$t_b = \frac{L^2}{D} \left(\frac{1}{6} - \frac{1}{11.2} \right) = \frac{L^2}{15.3D} \quad (3.17)$$

$$\text{and } t_0 = \frac{L^2}{\pi^2 D} \quad (3.18)$$

When the supply of hydrogen is completely stopped after steady state is obtained, it can be shown that the equation for the decay transient is given by ¹⁷³;

$$P_{(x=0)t} = P_{(x=0),t=0} e^{-t/t_0} \quad (3.19)$$

$$\text{or } P_t = P_0 \cdot e^{-t/t_0} \quad (3.20)$$

For the decay transient at $t = 0$, $P_0 = P_\infty$

$$\frac{\log P_t}{P_\infty} = \frac{-t}{2.3t_0} \quad (3.21)$$

$$\text{or } -\log (P_t/P_\infty) = \frac{t}{2.3t_0} \quad (3.22)$$

The plot of $-\log \frac{P_t}{P_\infty}$ versus t gives a slope of $\frac{1}{2.3t_0}$, D is

calculated by using a similar relationship between t_0 and D as in equation 3.18.

3.3.6 Hydrogen diffusion experiments with environmental charging and gas chromatography analysis

The reaction between an AlZnMg alloy and a water vapour or an aqueous environment has been discussed (Section 2.4.1 and 2.5.6). This technique for determining hydrogen diffusion rates involves diffusion of hydrogen through a cylinder machined from an AlZnMg rolled plate (Section 3.2.3). The cylinder is mounted in a glass container filled with the environment (Fig. 52). Generation of hydrogen is on the outside surface of the cylinder. Fitted to the open top of the cylinder is a Crawford gas fitting containing a septum (Fig. 53). The volume inside the cylinder can be sampled with a 1.0 ml volume syringe (Hamilton Gas Company Gastight No 1001). The sample of gas from the diffusion experiment cylinder is analysed in a Pye Unicam Chromatograph (Model LC2). The chromatograph is fitted with a Katharometer power supply, a Tekman chart recorder, and an output attenuator. The chromatograph operating conditions are:

Coil temperature - 150°C
Argon gas pressure - 30 psi
Argon gas flow rate - 20-80 cc/min
Filament bridge current - 80 mA

The analysis of diffusion through cylindrical specimens is discussed in the results, Section 4.4.3.



Fig. 52 Arrangement for measuring hydrogen diffusion by environmental charging and gas chromatography analysis.

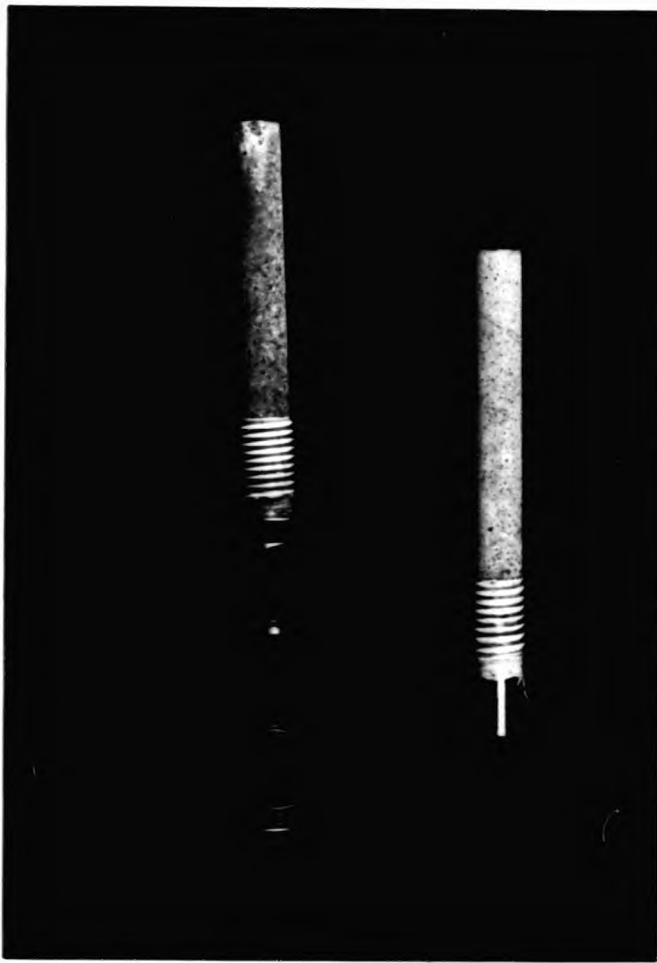


Fig. 53 Arrangement for sampling gas from the cylindrical hydrogen diffusion specimen.

3.3.7 Hydrogen evolution rate experimental procedure

In order to study the rate at which hydrogen is generated from the surface of an AlZnMg alloy in different environments, a simple experiment was devised in which a known surface area of the alloy was exposed to the environment in an enclosed container fitted with a septum to allow sampling of the free space above the sample (Fig. 54). The free space was sampled at various times and the gas analysed by gas chromatography in a similar manner to that described for the hydrogen diffusion experiments (Section 3.3.6).

3.4 ENVIRONMENTS

The following environments were used in the present work.

- 1) Water Saturated Air Vapour (WSAV) at various temperatures between 25°C and 90°C.
- 2) Double distilled water at various temperatures between 25°C and 90°C.
- 3) 3.0 Wt% NaCl (0.5 molar NaCl) at various temperatures between 25°C and 90°C.

In addition, some tests were performed in which the following additions or modifications were made to the basic 3.0 Wt % NaCl solution.

- 4) Pre-exposure to WSAV.
- 5) Pre-charging at -1750 mV vs SHE (60 mA cm^{-2}).

All chemicals were AnalaR grade and made up with double distilled

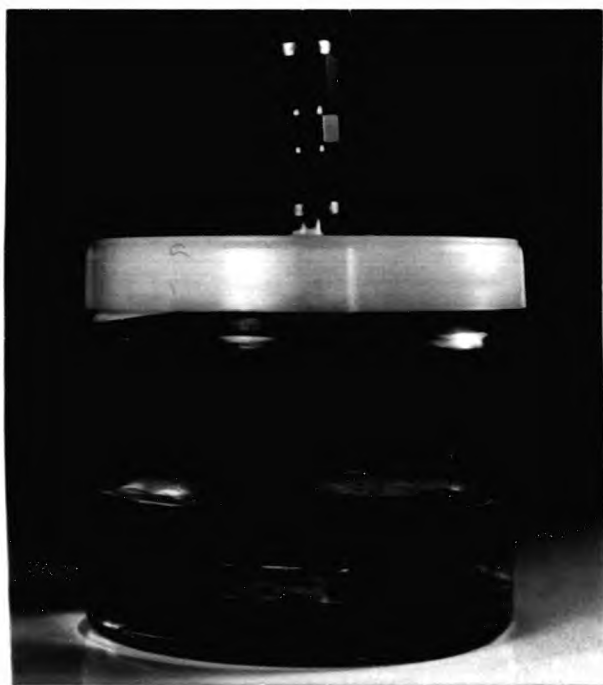


Fig. 54 Experimental arrangement for measuring the hydrogen evolution rate on AlZnMg alloy surface.



water. The environments used in the permeation experiments are discussed in the results, Section 4.4.

3.5 MICROSCOPY

3.5.1 Optical microscopy

Specimens for examination under the optical microscope were prepared by mounting in Bakelite, if necessary, polishing on silicon carbide paper to 800 grit and finally on diamond impregnated Selvyt to $1/4 \mu$ diamond.

Two etchants were used;

- i) Wasserman's etch for general metallography
(0.5ml HF, 100ml H₂O, 1ml HCl, 10ml HNO₃ and 50ml K₂Cr₂O₇)
- ii) A macro etch (15ml HF, 45ml HCl, 15ml HNO₃ and 25ml H₂O)

An exposure time of 30 seconds was found to be adequate for both etchants.

3.5.2 Scanning electron microscopy (SEM)

The scanning electron microscope was used in these investigations principally for examination of fracture surfaces and surface reaction products.

The specimens were mounted on 0.5 inch diameter aluminium stubs with silver paint providing the adhesive and electrical contact.

To overcome problems of the specimen charging up under the electron beam and reducing resolution, due to the oxide film, some specimens were given a fine gold coating deposited in a Nanotech spluttering machine.

3.5.3 Transmission electron microscopy (TEM) and scanning transmission electron microscopy (STEM)

The transmission electron microscope was used to characterise the fine structure of the alloy. Thin foils made for TEM work were also used in the JEOL 100C Teascan electron microscope stage with the microscope in the secondary electron imaging (SEI) mode to study pre-exposure surface reactions with high quality scanning electron micrographs.

The thin foils were produced by electrochemical thinning after mechanical thinning to 0.2mm thickness. The electrochemical thinning was in a Struers jet impingement machine using 70% Ethanol, 20% Glycerol and 10% Perchloric acid at 30 volts and 10°C.

Fresh polishing solution was made up from AnalaR reagents and prepared samples were rinsed in successive baths of methanol. The prepared specimens were monitored by light microscopy to ensure that no surface artifacts i.e. dust particles or polishing solution residue were present after the rinsing treatment. After preparation, specimens were stored in a dessicator at room temperature for a minimum period of 24 h in order to develop the normal amorphous γ -Al₂O₃ air formed film.

4.0 RESULTS

4.1 THE INFLUENCE OF ENVIRONMENT ON STRESS CORROSION CRACK GROWTH IN COMPACT TENSION SPECIMENS

It has been noted in the literature review that studies of stress corrosion cracking in AlZnMg alloys using pre-cracked specimens have concentrated on the DCB specimen geometry where the crack tip stress intensity decreases as the crack grows. It was thought that further insight into the mechanism of stress corrosion cracking might be obtained by conducting a series of experiments in different chemical environments using CT specimens, where the crack tip stress intensity increases as the crack grows. These experiments were conducted in environments which duplicated environments commonly used during DCB stress corrosion testing, and were performed over a range of temperatures from 20 to 90 C. All the CT specimens were fatigue pre-cracked on a Dartec M1000 machine as described in Section 3.3.1. The results of the pre-cracking for all CT specimens are tabulated below (Table 5).

4.1.1 The influence of temperature

The influence of temperature was studied for both double distilled water and 3% (0.5M) sodium chloride environments. The data obtained for double distilled water environments is shown in Figure 55 and the data obtained from 3% sodium chloride environments is shown in Figure 56. Also included in the water environment results is the crack growth rate versus stress intensity for a CT specimen exposed to Water Saturated Air Vapour (WSAV) at 70 C.

Specimen No.	FATIGUE PRE-CRACK GROWTH (mm)		DISPLACEMENTS		LOADS (kN)		Fatigue Ratio R	Mo of cycles					
	Side A		Effective Fatigue Pre-crack Length-a	Max Dis- placement (mm)	Min Dis- placement (mm)	Max Load			Ave Load				
	From to length	From to length								(mm)	(mm)	(kN)	(kN)
8	10.0	13.91	3.91	10.0	5.50	5.50	1.562	0.134	5.3	10.12	0.048	44060	
9	10.0	12.48	2.48	10.0	15.36	5.36	2.855	1.544	0.141	9.6	9.52	0.049	43790
11	10.0	12.88	2.88	10.0	13.26	3.36	2.865	1.542	0.160	1.6	8.87	0.056	50530
19	10.0	13.01	3.01	10.0	12.99	3.00	2.960	1.572	0.075	0.07	9.06	0.035	48670
20	10.0	13.10	3.10	10.0	13.46	3.46	2.863	1.534	0.147	1.2	9.01	0.051	39400
21	10.0	11.21	1.21	10.0	14.26	4.26	2.880	1.542	0.185	10.2	8.62	0.064	61010
23	10.0	12.44	2.44	10.0	15.26	5.26	2.860	1.541	0.179	9.4	9.50	0.063	50030
24	10.0	13.13	3.13	10.0	12.35	2.35	2.827	1.569	0.207	2.6	8.47	0.073	34310
26	10.0	12.85	2.85	10.0	14.11	4.11	2.835	1.554	0.202	4.2	9.07	0.071	37270
28	10.0	12.13	2.13	10.0	15.13	5.13	2.851	1.551	0.137	10.0	9.26	0.048	41010
29	10.0	13.63	3.63	10.0	13.34	3.34	2.922	1.558	0.122	0.97	9.38	0.042	47000
31	10.0	13.32	3.32	10.0	12.74	2.74	2.837	1.535	0.501	1.9	8.71	0.177	100880
32	10.0	13.70	3.70	10.0	12.91	2.91	2.807	1.519	0.532	2.6	8.84	0.190	78600
49	10.0	13.77	3.77	10.0	12.35	2.35	2.863	1.559	0.360	4.7	8.81	0.126	75480
39	10.0	12.65	2.65	10.0	12.45	2.45	2.843	1.604	0.489	0.7	8.26	0.172	68400
34	10.0	11.68	1.68	10.0	13.31	3.31	2.771	1.445	0.255	5.5	8.12	0.092	67710
37	10.0	13.06	3.06	10.0	11.58	1.58	2.809	1.566	0.432	5.0	8.10	0.153	75630

Table 5 Summary of the results of fatigue pre-cracking for Compact Tension stress corrosion specimens.

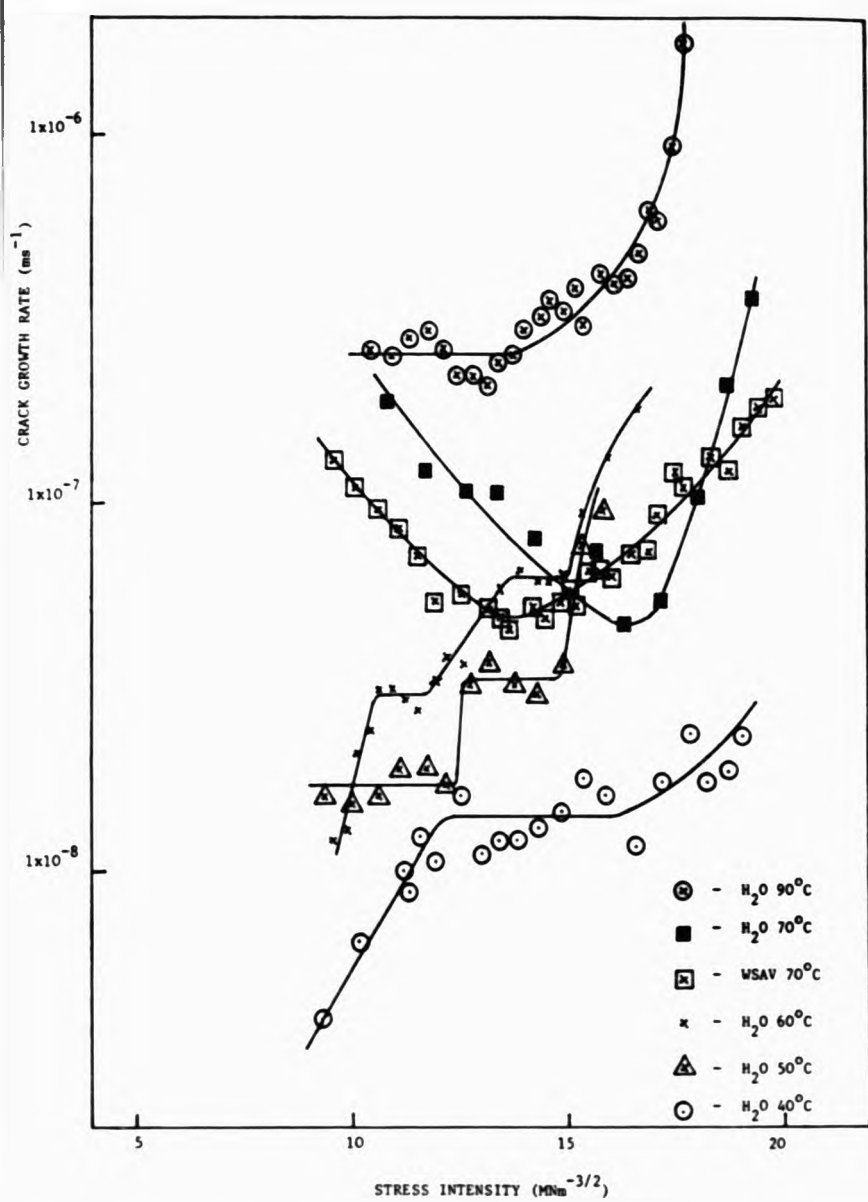


Fig.55 Crack growth rate versus stress intensity of 7017 type AlZnMg alloys, T651 condition at different temperatures in double distilled water and water saturated air vapour.

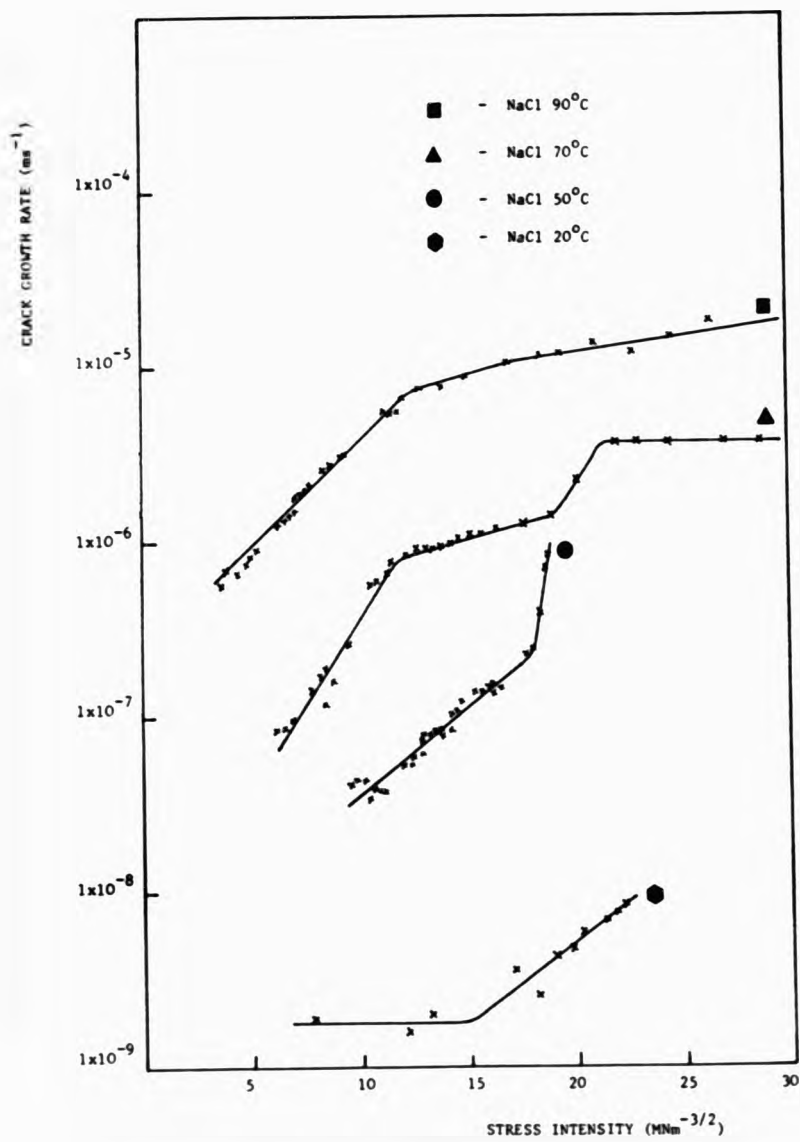


Fig.56 Crack growth rate versus stress intensity of 7017 type AlZnMg alloys, T651 condition at different temperatures in 3%NaCl solution.



The data obtained from all CT specimen SCC tests and from the fracture surfaces is summarised in Table 6.

A number of crack growth rate versus stress intensity determinations were repeated in order to demonstrate the reproducibility of the technique. The experiments for stress corrosion crack growth in double distilled water at 70 °C and 3% NaCl at 20 °C are shown in Figure 57 and Figure 58 respectively. Due to the time taken for individual crack growth rate versus stress intensity determinations to be made, it was not possible to repeat all CT specimen crack growth results. The crack growth rate determinations are repeatable although initial and final stress intensities cover a range of up to 5 MNm^{-3/2}. In all experiments the bulk pH of the solution remained in the range pH 5.5 - pH 7.

Crack growth in all the specimens was intergranular and both the macro surfaces of the fractured specimens and the etched photomicrographs of the alloy illustrate this (Figs 59 to 61). The grain structure of the alloy can be seen in the macro structure of the CT specimen after breaking open. Where crack branching on a very small scale has taken place, the "lifted" grains can be seen on the fracture surface. The fracture surfaces of the CT specimens exposed to a double distilled water environment are shown in Figure 61. The fracture surfaces are flat, with no indications of shear lips at the specimen edges. Plane strain conditions were therefore maintained throughout the tests.

TABLE 6 SUMMARY OF STRESS CORROSION CRACK GROWTH EXPERIMENTS ON CT SPECIMENS

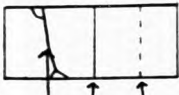
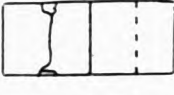
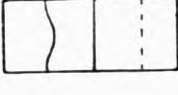
SPECIMEN No.	ENVIRONMENT	K _{initial} MNm ^{-3/2}	K _{final} MNm ^{-3/2}	TIME TO FRACTURE HOURS	SC CRACK SCHEMATIC Scale 1:1	REMARKS
9	Double distilled water - 70°C	10.8	19.4	14.73 end of SC crack machined notch load line		U shaped crack growth rate versus stress intensity curve Bright facets on fracture surface on specimen edge at end of SC crack Load 2.942 kN
19	Double distilled water - 50°C	9.4	15.9	77.07		Bright facets on fracture surface on specimen edge at end of SC crack Load 2.942 kN
20	Double distilled water - 40°C	9.4	19.2	146.50		 Load 2.942 kN

TABLE 6 SUMMARY OF STRESS CORROSION CRACK GROWTH EXPERIMENTS ON CT SPECIMENS (CONTINUED)

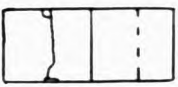
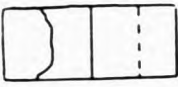
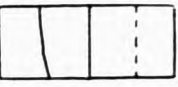
SPECIMEN NO.	ENVIRONMENT	$K_{initial}$ -3/2 MN/m	K_{final} -3/2 MN/m	TIME TO FRACTURE HOURS	SC CRACK SCHEMATIC Scale 1:1	REMARKS
21	Double distilled water - 60°C	9.6	16.6	45.80		Bright facets on fracture surface on specimen edge at end of SC crack Load 2.942 kN
23	Double distilled water - 90°C	10.3	17.8	4.4R		 Load 2.942 kN
26	Water saturated air vapour - 70°C	9.65	19.55	23.13		U shaped crack growth rate versus stress intensity curve Load 2.942 kN

TABLE 6 SUMMARY OF STRESS CORROSION CRACK GROWTH EXPERIMENTS (CONTINUED)

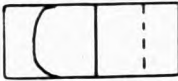
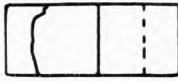
SPECIMEN	ENVIRONMENT	$K_{initial}$ -3/2 MNm	K_{final} -3/2 MNm	TIME TO FRACTURE HOURS	SC CRACK SCHEMATIC Scale 1:1	REMARKS
8	3% NaCl - 20°C	7.8	22.4	402.9		Load 3.530 kN
32	3% NaCl - 50°C	9.5	18.7	27.1		Load 2.942 kN
28	3% NaCl - 70°C	6.3	24.80 *	7.02		Crack length calibration inaccurate after crack growth to 25mm from machined notch. * calculated from actual crack length Load 1.764 kN

TABLE 6 SUMMARY OF STRESS CORROSION CRACK GROWTH EXPERIMENTS (CONTINUED)

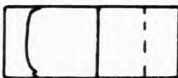
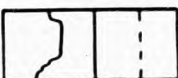
SPECIMEN	ENVIRONMENT	$K_{initial}$ -3/2 MN/m	K_{final} -3/2 MN/m	TIME TO FRACTURE HOURS	SC CRACK SCHEMATIC Scale 1:1	REMARKS
31	NaCl - 90°C	4.0	27.84 *	2.49		Crack length calibration inaccurate after crack growth to 25mm from machined notch * calculated from actual crack length Load 1.177 kN
11	Double distilled water - 70°C	9.7	16.5	19.0		U shaped crack growth rate versus stress intensity curve Pronounced crack growth at specimen sides. Load 2.942 kN
24	Double distilled water - 70°C	8.8	14.2	16.2		U shaped crack growth rate versus stress intensity curve Pronounced crack growth at specimen sides. Load 2.942 kN

TABLE 6 SUMMARY OF STRESS CORROSION CRACK GROWTH EXPERIMENTS (CONTINUED)

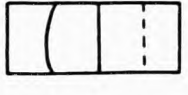
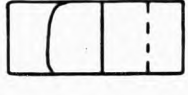
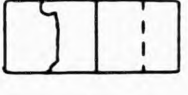
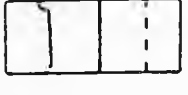
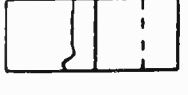
SPECIMEN	ENVIRONMENT	$K_{initial}$ -3/2 MPa	K_{final} -3/2 MPa	TIME TO FRACTURE HOURS	SC CRACK SCHEMATIC Scale 1:1	REMARKS
49	3% Sodium Chloride 20°C	8.7	19.0	504.2		Load 2.942 kN
39	WSAV 70°C	9.0	18.0	24.5		Specimen sides blanked off.
34	WSAV 70°C	4.4	13.7	- *		Load 2.942 kN Pre-exposed to WSAV for 50 hours * Experiment interrupted, see Section 4.2.2. Load 1.471 kN

TABLE 6 SUMMARY OF STRESS CORROSION CRACK GROWTH EXPERIMENTS (CONTINUED)

SPECIMEN	ENVIRONMENT	$K_{initial}$ -3/2 MPa	K_{final} -3/2 MPa	TIME TO FRACTURE HOURS	SC CRACK SCHEMATIC Scale 1:1	REMARKS
37	MSAV 70°C	4.4	15.4	- *		Pre-charged at -1.75 volts versus SHE for 50 hours. * experiment interrupted, see Section 4.2.2.
29	MSAV 70°C	6.7	-	- *		Load 1.471 kN * SC crack stopped at intermediate stress intensity.
						Load 2.059 kN

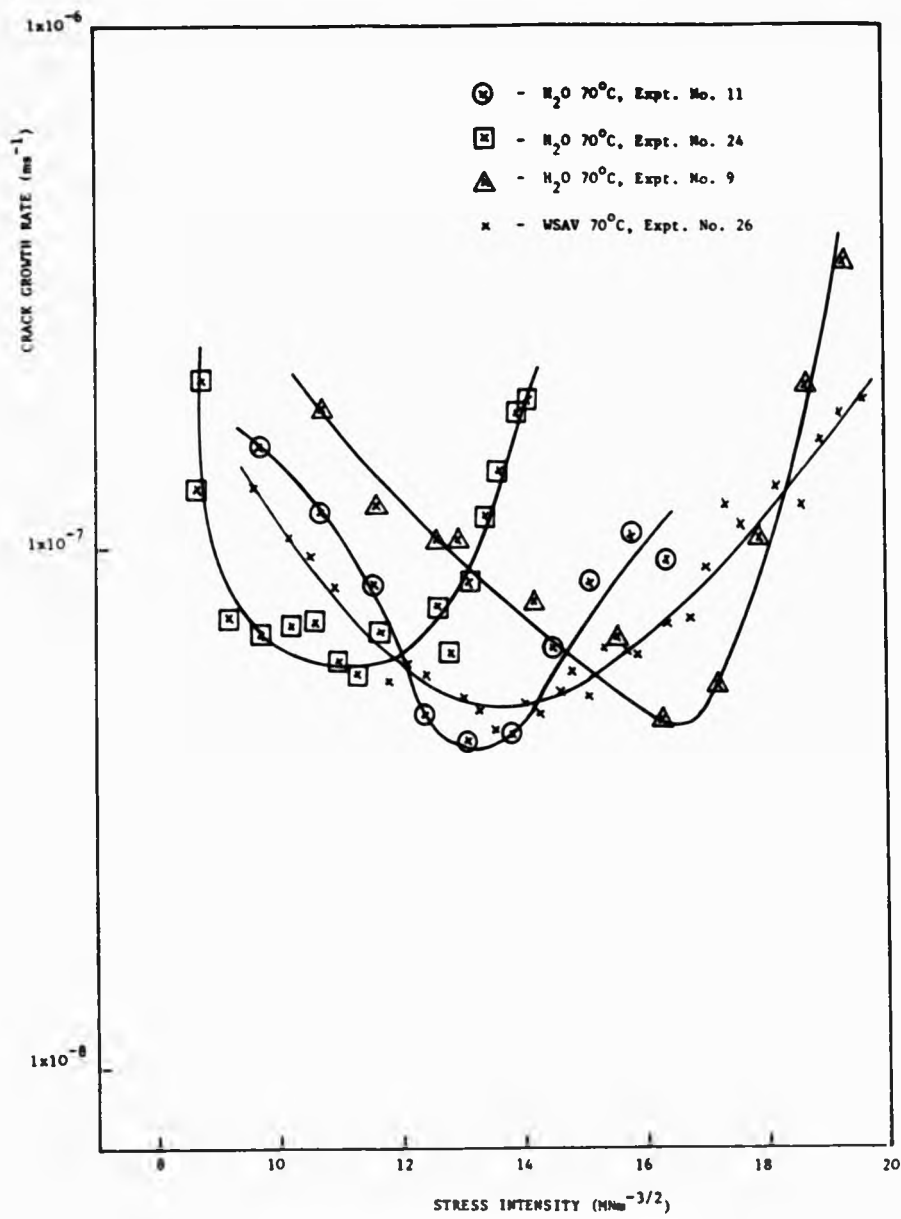


Fig.57 Crack growth rate versus stress intensity of 7017 type AlZnMg alloys, T651 condition at 70°C in double distilled water and WSAV, reproducibility experiments.

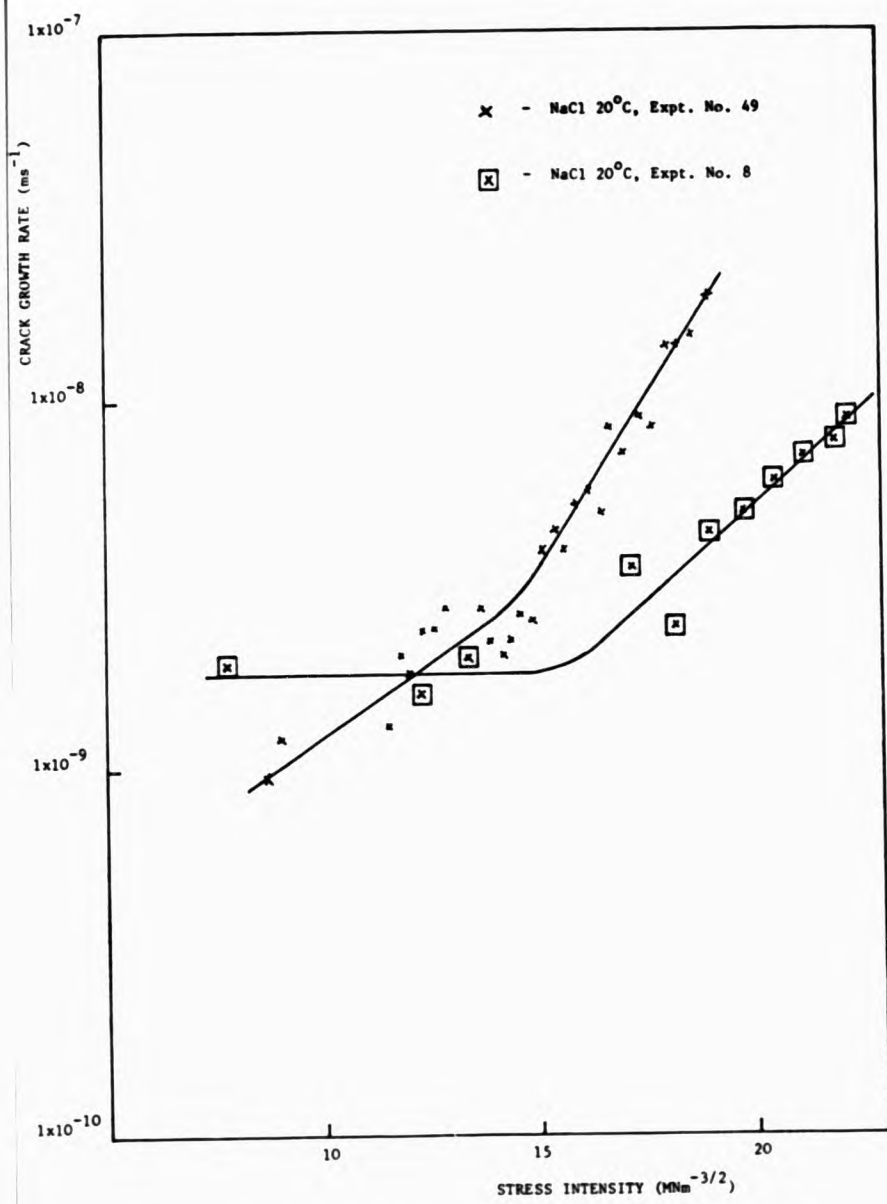


Fig.58 Crack growth rate versus stress intensity of 7017 type AlZnMg alloys, T651 condition at 20°C in 3%NaCl solution, reproducibility experiments.



Fig 59 7017 type AlZnMg alloy shown looking in the longitudinal direction and showing elongated pancake-like grains.
Magnification x100



Fig 60 7017 type AlZnMg alloy showing the intergranular stress corrosion crack.
Magnification x600

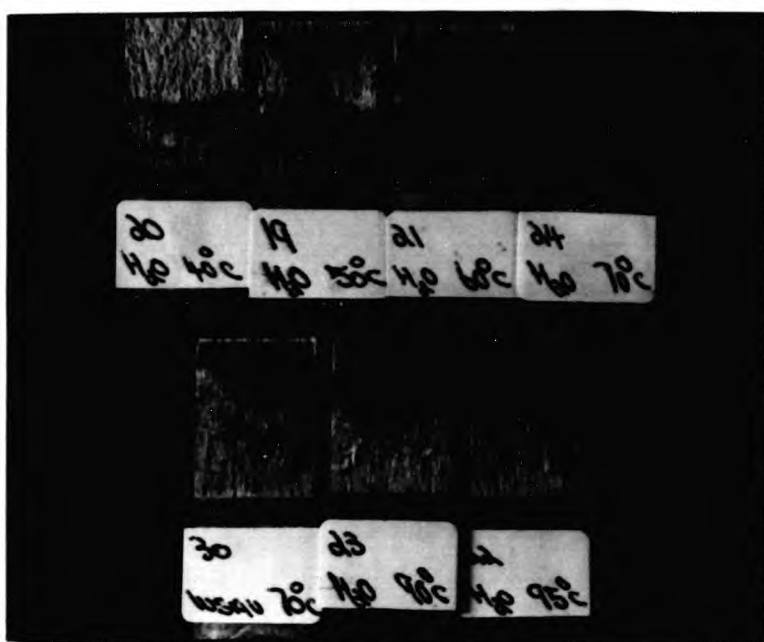


Fig 61 General appearance of fracture surface of stress corrosion cracks grown in double distilled water over a range of temperatures.

Magnification x1.5

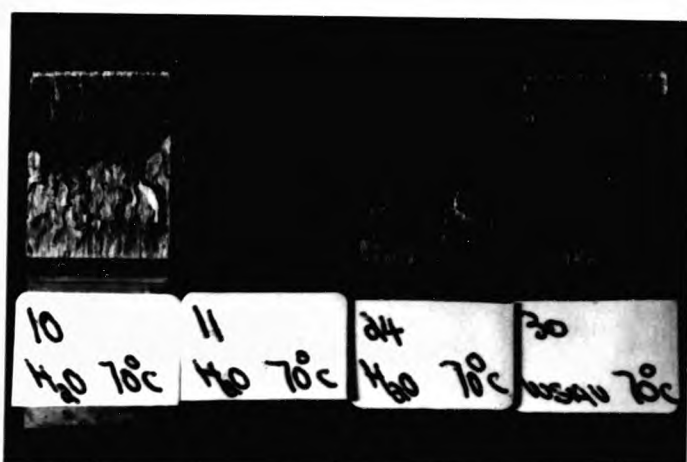


Fig 62 Fracture surfaces in double distilled water and WSAV at 70°C showing greater crack growth at the specimen edges than at the centre.

Magnification x1.8

Stress corrosion crack growth tests in double distilled water show a number of features;

- 1) Whilst in a number of tests at 90, 60, 50 and 40 °C the Stage III crack growth is apparent, the Stage I crack growth was not observed at 90, 70, and 50 °C. Stage I crack growth was only observed at 60 and 40 °C. This is in contrast to DCB tests where the specimen tends to miss out Stage III crack growth and drop immediately into Stage II growth, followed by Stage I growth.

The absence of Stage I growth in most specimens is probably due to the nature of the experiment, where specimen load is increased if no growth is observed at a given load after 1 hour.

- 2) Crack growth both in double distilled water and water saturated air vapour at 70 °C exhibits an initial reduction in crack growth rate, followed by an increase in crack growth rate up to a value slightly greater than the original. This aspect was consistently observed at 70 °C and is discussed later (Section 4.2.3).
- 3) The following comparisons have been made with published data (Table 7).

Alloy	Experimental conditions for published results	Specimen type	Stage II crack growth rate (μs^{-1})	Reference	Stage II crack growth rate Present work (μs^{-1})	Specimen No.
7039-T61	Distilled water, open circuit 59°C	DCB	6×10^{-8}	Speidel 72	Double plateau 3×10^{-8} and 6.3×10^{-8}	21
7039-T61	Distilled water, open circuit 43°C	DCB	4×10^{-8}	Speidel 72	1.3×10^{-8}	20
7017-T61	95% relative humidity 40°C	DCB	5×10^{-9}	Scanans 101	1.3×10^{-8}	20

Table 7 Comparison of some published Stage II crack growth data in water and VSAV environments with results obtained from the present studies.

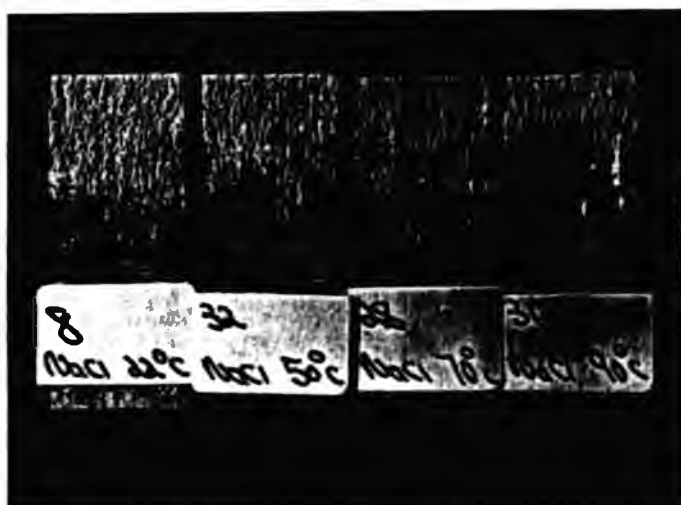


Fig. 6) General appearance of fracture surface of stress corrosion cracks in 3% NaCl over a range of temperatures.

Magnification x 1.8

The 7039 alloy has a nominal composition of Zn-4.0%, Mg-2.8% and a Zn:Mg ratio of 1.4, it generally exhibits a SC crack growth plateau velocity higher than the 7017 range of alloys in comparative tests (¹⁷⁴ from low frequency corrosion fatigue data.) However, the results reported here, for CT specimens, compare with the results obtained by Speidel ⁷² for 7039 alloys using DCB ¹⁰¹ specimens. The plateau velocity reported by Scamans for a 7017 alloy, again using a DCB specimen, is just over half an order of magnitude slower than that found in the present studies. The result reported by Scamans was for SC crack growth in a 95% relative humidity atmosphere and it may therefore be argued that the increase in crack growth rate observed in the current work is due to either the effect of specimen geometry or the effect of complete water coverage on the crack growth rate. The results presented in Section 4.5.1 indicate that similar quantities of hydrogen are generated on flat 7017 alloy surfaces in double distilled water and WSAV environments. Therefore, if hydrogen plays a part in the stress corrosion of these alloys, the difference between water and WSAV environments is not significant. In both cases any apparent effect of specimen geometry is for the CT specimen geometry to increase the SC crack plateau velocity in water and WSAV environments. For all comparisons, the crack growth was in the L (longitudinal) direction with the applied stress normal to this and in the ST (short transverse) direction.

4) The fracture surfaces show a number of features on a macro scale. The stress corrosion cracks grown at 50, 60 and 70 °C show distinctive bright facets at the end of the SC crack on the specimen edges. It is thought from SEM examination that these are areas of rapid crack growth prior to fracture of the specimen, where little corrosion of the fracture surface has been able to take place due to the short exposure time to the environment. A second feature of these tests is the presence, in most specimens, at 70 °C, of greater crack growth at the specimen edge than at the specimen centre. This is illustrated in Figure 62.

The general appearance of the fracture surfaces of specimens exposed to 3% NaCl over a range of temperatures is shown in Figure 63. Stage III crack growth was observed in tests at 20, 50, 70 and 90 °C, although the Stage III crack growth at 70 °C and 90 °C is not reported due to inaccuracies in the clip gauge output at long crack lengths (>25 mm). Stage I crack growth was observed at 50, 70 and 90 °C.

The following comparisons have been made with published data (Table 8).

The 7079 alloy has a nominal composition Zn-4.3%, Mg-3.3% and a Zn:Mg ratio of 1.3. In the series of experiments reported by Speidel⁶³, the conditions of the current work are not entirely duplicated. Crack growth rates reported by Speidel are higher due to either anodic polarisation of the DCB specimen, increased

Alloy	Experimental conditions for published results	Specimen type	Stage II crack growth rate (ms^{-1})	Reference	Stage II crack growth rate Present work (ms^{-1})	Specimen No.
7079-T651	0.5M KI, -450mV vs SHE 23°C pH6	DCB	2×10^{-6}	Speidel 63	1.4×10^{-9}	8
7079-T651	3.0M KI, -450mV vs SHE 69°C pH6	DCB	4×10^{-5}	Speidel 63	3.7×10^{-6}	28
7079-T651	5.0M KI, open circuit 23°C	DCB	9×10^{-6}	Speidel 63	1.4×10^{-9}	8
7075-T651	3.5% NaCl, 23°C	DCB	2×10^{-8}	Speidel 10	1.4×10^{-9}	8
7075-T651	3%NaCl, open circuit 21°C pH7	CTS	8.3×10^{-7}	Hartman 84	1.4×10^{-9}	8

Table 8 Comparison of some published Stage II crack growth rate data in aqueous halide environments with results obtained from the present studies

halide ion concentration, or the use of 7079 alloy which generally exhibits a SC crack growth plateau velocity of the same order of magnitude as the 7039 alloy¹⁷⁴. It is clear that from the data presented by Hartman⁸⁴ for the 7075 alloy, with a nominal composition Zn-5.6%, Mg-2.5% and a Zn:Mg ratio of 2.2, and under very similar test conditions including the use of CT specimens, that there is a considerable difference in the SC crack growth plateau velocity. The result presented by Speidel for a 7075 alloy in 3.5% sodium chloride using a DCB specimen is just over an order of magnitude faster than that in the present work for a 7017 alloy under similar conditions using a CT specimen.

The results of the SEM investigations of fracture surfaces of the stress corrosion tests in double distilled water and 3% NaCl are presented here together with the observations of the fatigue and overload fractures to complete the fractography of the alloy.

Figures 64 - 67 show the fatigue fracture for specimen 23. Fatigue is intergranular at low stress intensities with the grain structure of the alloy and fatigue striations apparent (Figs. 64, 65 and 66). At higher stress intensities, near the interface with the stress corrosion crack, the fatigue becomes transgranular with cleavage facets visible on the fracture surface (Fig. 67).

Crack growth direction

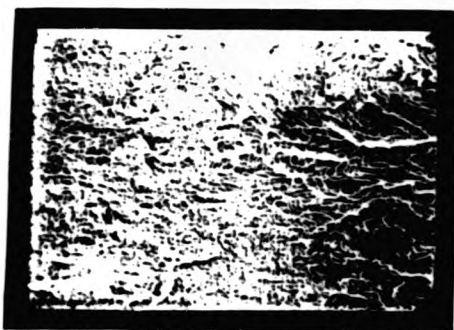
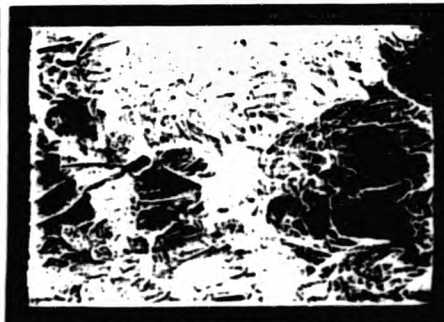


Fig 64 Specimen 23, intergranular fatigue.

100u
Fig 65 Specimen 23 intergranular fatigue.
(x200)



20u
Fig 66 Specimen 23, intergranular fatigue.
(x1000)

50u
Fig 67 Specimen 23, transgranular fatigue showing evidence of cleavage.
(x400)



Figures 68 - 70 show the interface between the transgranular fatigue pre-crack and the SC crack in specimen 23 (double distilled water, 90 C). The high magnification view in Figure 70 (x 5000) clearly shows the transition between the fatigue crack and the stress corrosion crack, with the SC crack partially penetrating the underside of the grain which subsequently became the grain boundary where the dominant SC crack growth took place. At this magnification the SC crack surface is essentially featureless showing only some evidence of second phase particles embedded in it.

Figure 71 is a general view of a typical section of a SC crack (for specimen 9, H₂O 70 C) showing the intergranular crack growth evidenced by the clearly visible elongated, flat pancake grain structure. A number of grains have "lifted" indicating that crack branching has taken place, however the extent of branching is much less than that found in DCB tests. The SC crack/overload fracture interface is seen on the extreme right of the specimen.

At high stress intensities in CT specimens there is some evidence of a ductile crack extension mechanism occurring in conjunction with the SC crack growth. Figures 72 and 73 show evidence of microvoid coalescence, in this case 1.23 mm back from the SC crack/overload fracture interface. This ductility was noted in specimen 28 (3% NaCl, 70 C) but has been seen in most specimens (Figs. 93 and 94). Figures 74 and 75 show a high magnification view of the SC crack surface which, apart from evidence of secondary cracking, shows only a fine film of corrosion product

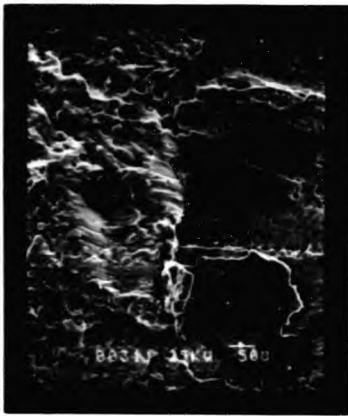


Fig 68 Specimen 23, fatigue pre-crack/SC crack interface, (H_2O 90°C).

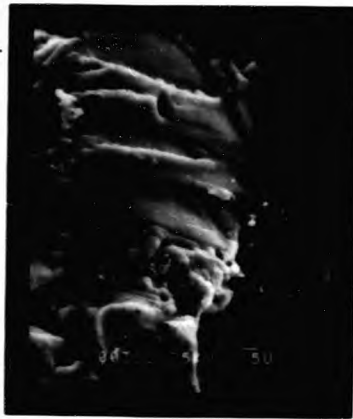


Fig 69 Specimen 23, fatigue pre-crack/SC crack interface, (H_2O 90°C).

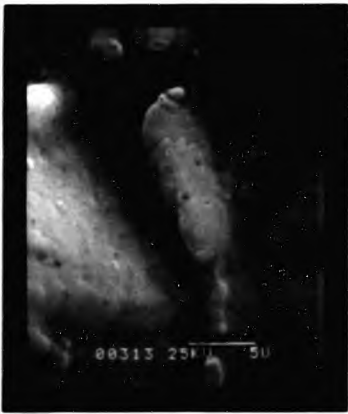


Fig 70 Specimen 23, fatigue pre-crack/SC crack interface, (H_2O 90°C).



Fig 71 Specimen 9, stress corrosion crack, (H_2O 70°C).

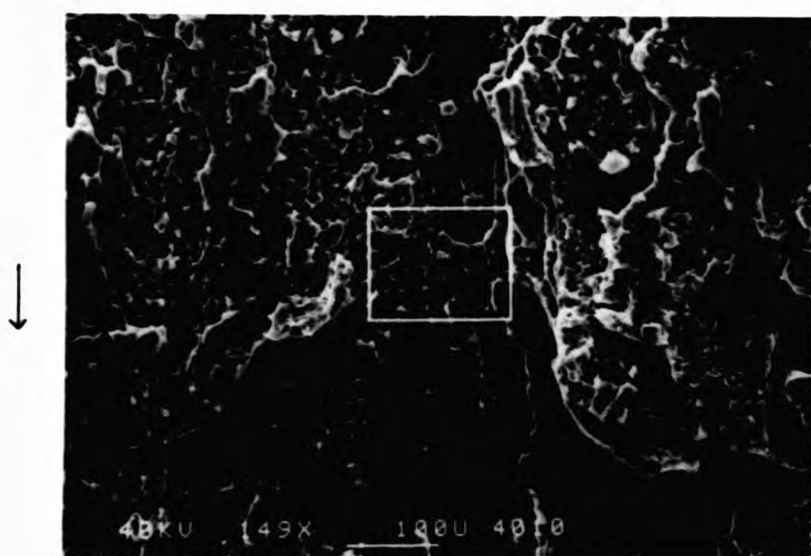


Fig 72 Specimen 28, regions of ductility within the SC crack at high stress intensities near the SC crack/overload fracture interface, (NaCl 70°C).

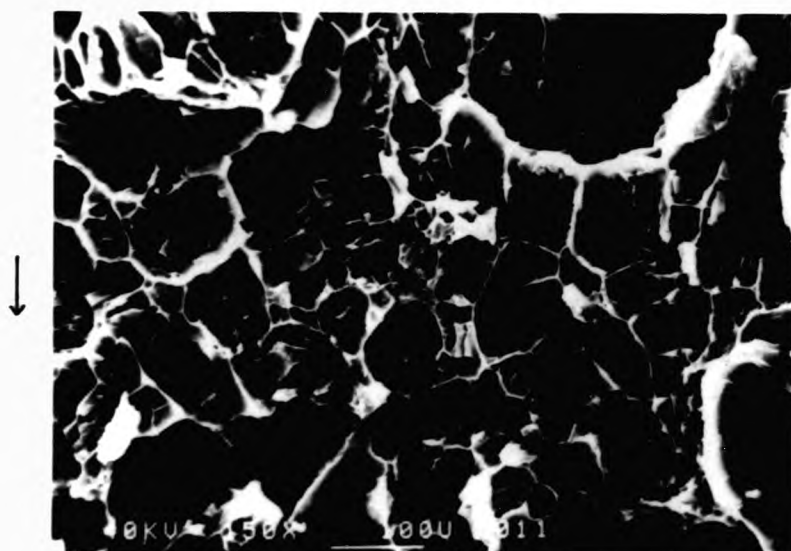


Fig 73 Specimen 28, detailed view of the region of microvoid coalescence shown in Fig 72, (NaCl, 70°C).

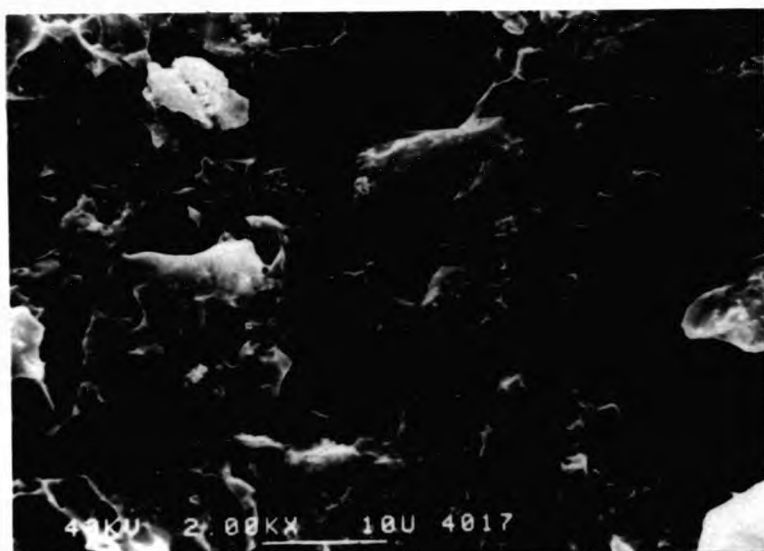


Fig 74 Specimen 28, high magnification view of the stress corrosion crack surface, (NaCl 70°C).

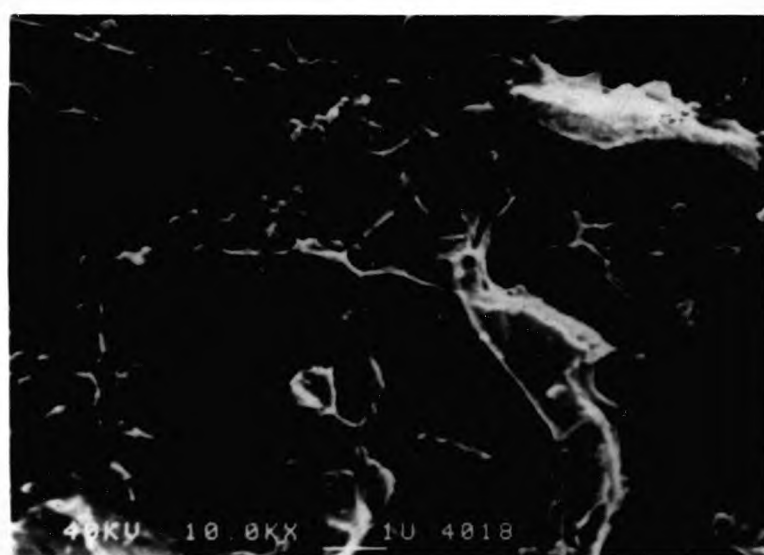


Fig 75 Specimen 28, high magnification view of the stress corrosion crack surface, (NaCl 70°C).

that hides any detail present of the fracture surface. Defilming the fracture surface by the application of cellulose acetate strips previously softened with acetone serves to remove the bulk corrosion product but will not allow resolution of fine detail on the fracture surface.

Figures 76 and 77 show the corrosion product on the surface of specimen 19 (H₂O, 50 C). As a result of the long exposure time of this specimen (77 hours), a fully developed hydrous oxide film is present on the fracture surface near the start of the SC crack (Fig.76). Further along the SC crack the hydrous oxide crystals are seen before their amalgamation into a continuous hydroxide film (Fig.77). Hydrous oxide film formation on AlZnMg alloys is discussed in greater detail in Section 4.5.2. Figure 78 shows the characteristic mud cracking of an extensive film of corrosion product and NaCl developed on specimen 31 (3% sodium chloride, 90 C) after the fracture surface has been allowed to dry.

Figure 79 shows the transition between intergranular stress corrosion crack growth and the overload failure which is ductile and predominantly microvoid coalescence. The region of extended SC crack growth on the CT specimen edge of specimen 23 (H₂O, 90 C) is shown in Figure 80 and the lip on specimen 11 (H₂O, 70 C) is shown in Figure 81, with a higher magnification of the SC crack in this region shown in Figure 82. The morphology of the SC crack in these regions is essentially the same as the



Fig 76 Specimen 19, fully developed aluminium hydroxide corrosion product film on the SC crack surface at high magnification, (water 50°C).



Fig 77 Specimen 19, start of aluminium hydroxide film growth on the fracture surface at the end of the SC crack, (water 50°C).



Fig 78 Specimen 31, mud cracking in the dried corrosion product film developed in 3% NaCl at 90°C during SC crack growth.

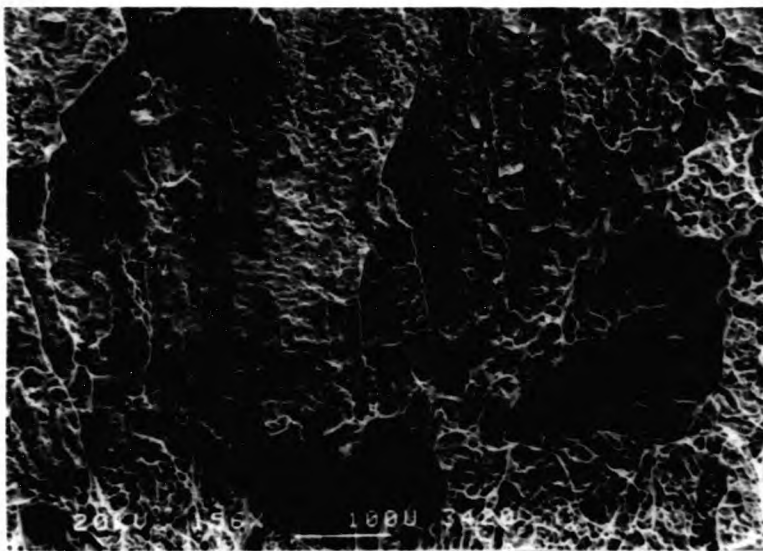


Fig 79 Specimen 26, the SC crack/overload fracture interface, (WSAV 70°C).



Fig 80 Specimen 23, extended SC crack growth on specimen edge, (H₂O, 90°C).

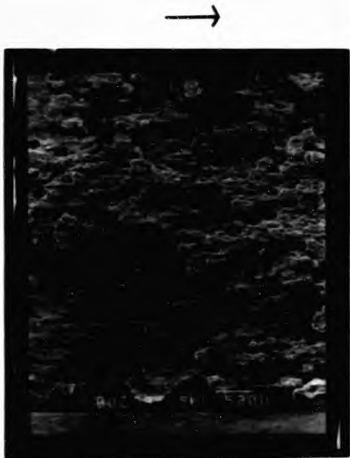
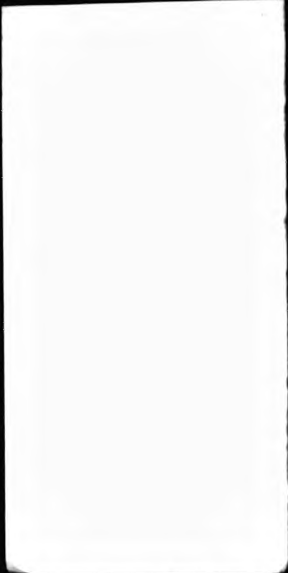


Fig 81 Specimen 11, extended crack growth on specimen edge, (H_2O , $70^{\circ}C$).



Fig 82 Specimen 11, higher magnification view of the region of extended SC crack growth, (H_2O , $70^{\circ}C$.)

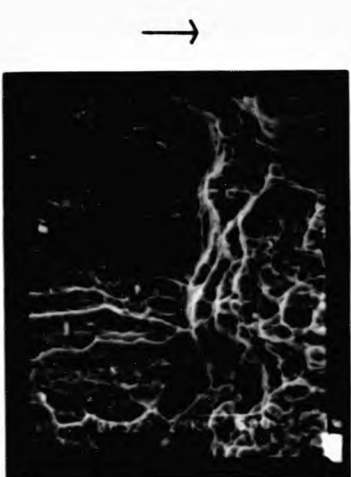


Fig 83 Specimen 23, SC crack/overload failure interface, (H_2O , $90^{\circ}C$).

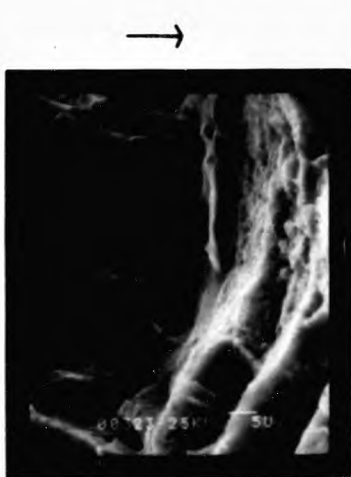


Fig 84 Specimen 23, SC crack/overload failure interface, (H_2O , $90^{\circ}C$).

bulk of the SC crack, with the exception that the shorter time interval over which these regions have been exposed to the environment has resulted in less corrosion product on the fracture surface.

Figures 83 and 84 show in detail the transition between the end of the SC crack and the overload fracture. At the point of fast, ductile fracture the crack path climbs a number of grains to develop within the most favourably oriented grain. These ledges are clearly seen on Figures 83 and 84. The fracture shown here is for specimen 23 (H₂O, 90 C).

Figures 85 and 86, specimen 21, (H₂O, 60 C) show the region of ductile overload failure. The failure mechanism is entirely by microvoid coalescence and the dimple rupture is clearly visible on the fracture surface. A large percentage of dimples contain second phase particles, some of which have fractured in a brittle manner during the overload failure as shown in Figure 86.

Figures 87 and 88 show the extended SC crack growth regions on the edge of specimen 21 (H₂O, 60 C). The high magnification view of the SC crack in this region, which has had a short exposure time and was tested at a lower temperature (60 C), shows some evidence of striations (arrowed) on the fracture surface, possibly indicating discontinuous crack growth (Fig.88).

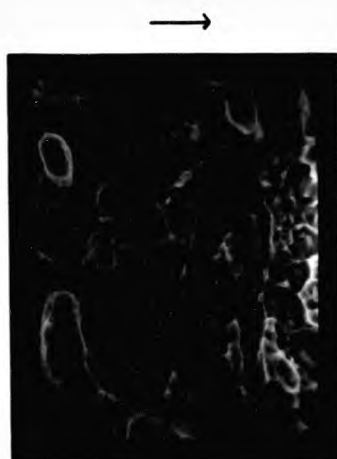


Fig 85 Specimen 21, overload fracture by microvoid coalescence, (H_2O , $60^\circ C$).



Fig 86 Specimen 21, overload fracture showing fractured second phase particles within dimples on the fracture surface, (H_2O , $60^\circ C$).



200 μ

Fig 87 Specimen 21, extended crack growth on specimen edge, (H_2O , 60°C).



5 μ

Fig 88 Specimen 21, high magnification view of the region of extended SC crack growth showing evidence of crack arrest markings, (H_2O , 60°C).

(x 2000)

Figures 89 and 90 show a similar sequence to that discussed previously but for specimen 19 (H_2O , $50^\circ C$). The higher magnification view shows possible evidence (arrowed) of discontinuous crack growth on the fracture surface (Fig.90). However, discontinuous crack growth is most clearly shown in a DCB specimen exposed to laboratory air at a relative humidity of 48-62% (see Section 4.3.4, Figures 129 and 130).

Figures 91 and 92 show respectively the secondary electron (SE) and back-scattered electron (BSE) images of the SC crack surface of specimen 20 (H_2O , $40^\circ C$). The secondary cracks oriented transverse to the principal crack growth directions are thought to be the start of SC crack growth at subgrain boundaries, a feature seen in DCB specimens and discussed further in Section 4.3.4, and which is more apparent in the BSE mode. Second phase particles embedded in the fracture surface are also clearly shown. This has been cited as evidence that the SC fracture is wholly brittle¹⁰¹. As expected the fracture surface of this specimen, where the SC crack was grown at $40^\circ C$, shows little evidence of corrosion product films near the SC crack tip which aids high resolution fracture surface examination. This point is discussed further in relation to DCB tests in water vapour and laboratory air.

Figures 93 and 94 show regions of ductile fracture (as in Figs. 72 and 73) at high stress intensities near the end of the SC crack tip. This feature in the SC crack morphology is general to all CT specimens. Figure 93 shows specimen 8 ($NaCl$, $20^\circ C$), 0.40

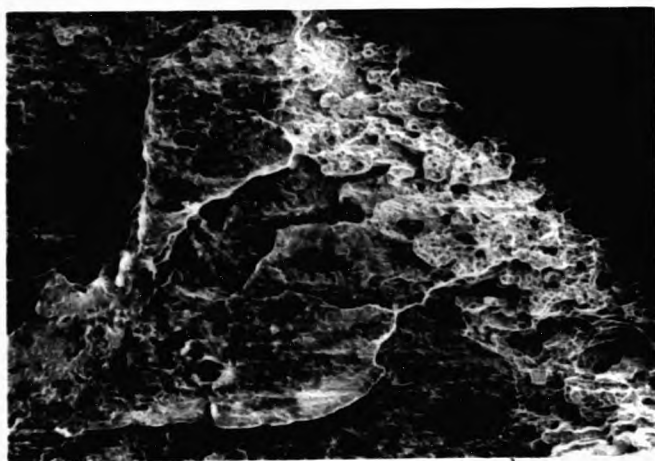


Fig 89 Specimen 19, extended crack growth on specimen edge, (H_2O , $50^{\circ}C$).

275 μ

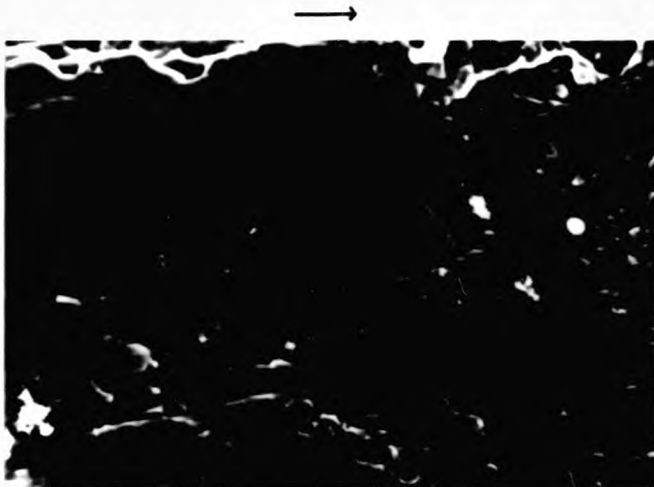
(x50)



Fig 90 Specimen 19, high magnification view of the region of extended SC crack growth showing evidence of crack arrest markings, (H_2O , $50^{\circ}C$).

5 μ

(x 5000)



5 μ
 Fig 91 Specimen 20, secondary electron image of the SC fracture surface near the SC crack/overload failure interface, (H₂O, 40°C).



5 μ
 Fig 92 Specimen 20, back-scattered electron image of the SC fracture surface near the SC crack/overload failure interface showing evidence of subgrain SC crack initiation and uncorroded second phase particles on the fracture surface, (H₂O, 40°C).
 (x 7000)

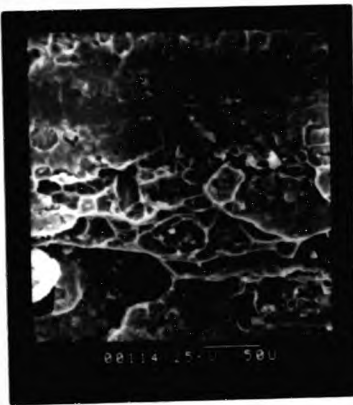


Fig 93 Specimen 8, regions of ductility within the SC crack at high stress intensities, (NaCl, 20°C).

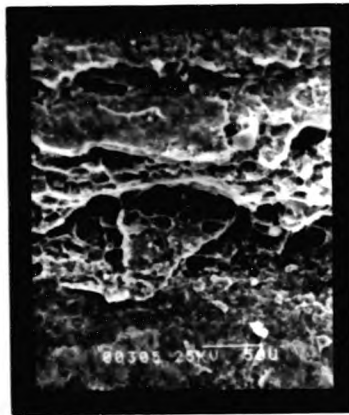


Fig 94 Specimen 26, regions of ductility within the SC crack at high stress intensities, (WSAV, 70°C).

mm back from the SC crack/overload fracture interface. Figure 94 shows specimen 28 (WSAV, 70 °C), 1.32 mm back from the SC crack/overload fracture interface.

4.1.2 Stress corrosion crack growth activation energy determinations in distilled water, WSAV and 3% NaCl for compact tension specimens.

The results of crack growth rate versus stress intensity experiments for double distilled water, WSAV and 3% NaCl environments have been reported and are shown in Figures 55 and 56 respectively. The effect of the chloride environment on the stage II crack growth rate is to increase the plateau velocity by just over half (0.6) an order of magnitude at 50 °C to just under two (1.7) orders of magnitude at 90 °C. The effect of stage I crack growth rate is not clear as the experimental technique employed, of progressively increasing the static load on the specimen if no crack growth is recorded after 1 hour, has resulted in the absence of stage I crack growth in CT specimens in double distilled water and WSAV at all temperatures employed except 60 and 40 °C (specimens 20 and 21).

The experimental crack growth rate data used for activation energy determination is given in Table 9 for double distilled water and 3% NaCl environments.

The data in Table 9 is presented as activation energy plots in Figure 95 for SC crack growth in double distilled water and Figure 96 for SC crack growth in 3% NaCl.

Specimen No.	Environment	Temperature (°C)	Basis	Crack growth rate (ms ⁻¹)
23	H ₂ O	90	Plateau	2.5 x 10 ⁻⁷
21	H ₂ O	60	1st Plateau	3.0 x 10 ⁻⁸
19	H ₂ O	50	1st Plateau	1.7 x 10 ⁻⁸
20	H ₂ O	40	Plateau	1.4 x 10 ⁻⁸
31	3%NaCl	90	Plateau	1.4 x 10 ⁻⁵
28	3%NaCl	70	Plateau	3.6 x 10 ⁻⁶
32	3%NaCl	50	Plateau	8.0 x 10 ⁻⁸
49	3%NaCl	20	Plateau	1.8 x 10 ⁻⁹
31	3%NaCl	90	Stage I at 6MNm ^{-3/2}	9.3 x 10 ⁻⁷
28	3%NaCl	70	Stage I at 6MNm ^{-3/2}	6.9 x 10 ⁻⁸
32	3%NaCl	50	Stage I at 6MNm ^{-3/2}	8.4 x 10 ⁻⁹

Table 9 Activation energy data for SC crack growth in double distilled water and 3%NaCl for CT specimens, based upon plateau and Stage I velocities.

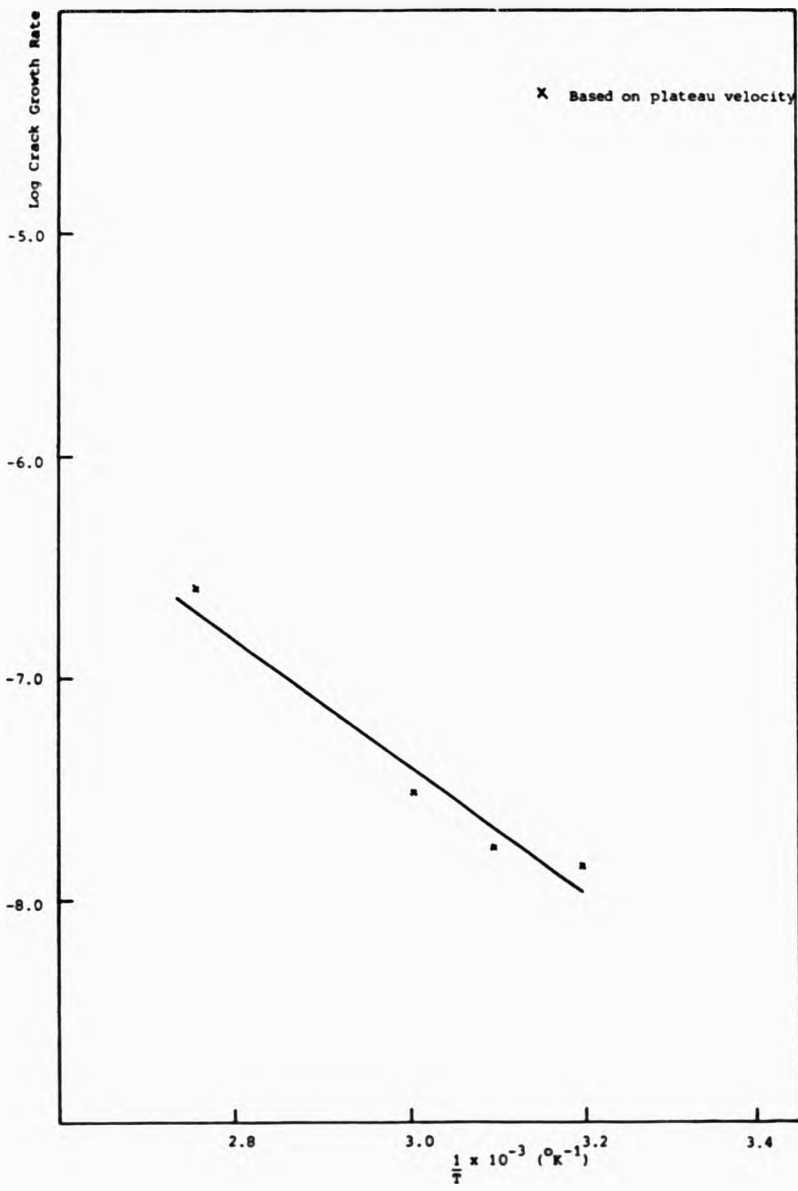


Fig.95 Activation energy plot for SC crack growth in double distilled water using CT specimens.

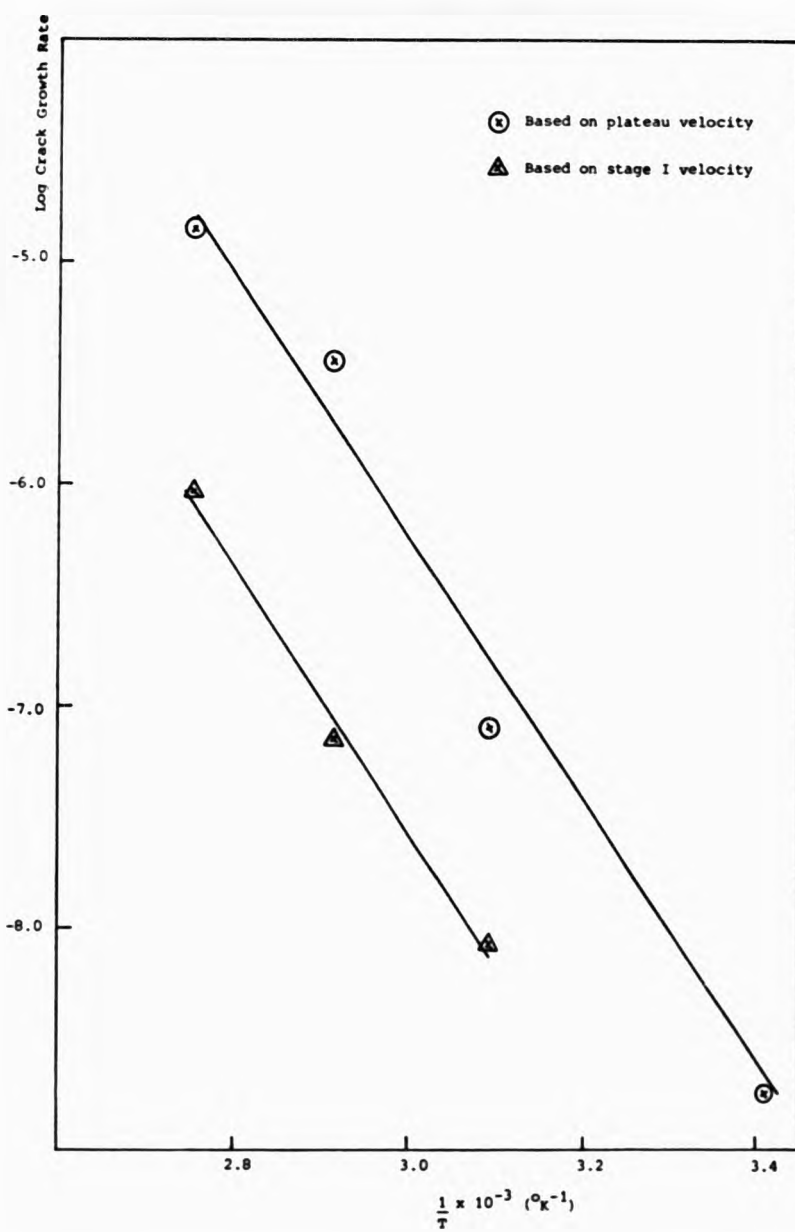


Fig.96 Activation energy plot for SC crack growth in 3%NaCl using CT specimens.

In the case of SC crack growth in double distilled water, the experiments at 50 and 60 C yielded double plateaus. The first plateau at the lower crack growth rate has been used for activation energy determination on the basis that a longer time, as a proportion of total specimen lifetime, is spent at this crack growth rate.

The activation energy plot for the 3% NaCl environment shows crack growth data based upon both plateau velocities and Stage I crack growth rates extrapolated to a constant stress intensity of $6\frac{3}{2}$ MN/m^{3/2}.

As discussed, activation energy data for Stage I crack growth in double distilled water is not available from the experimental results due to the absence of Stage I crack growth in most specimens.

The activation energies calculated from the log da/dt versus $1/T$ (K) graphs are presented in Table 10.

Activation energies for SC crack growth in DCB specimens are presented in Section 4.3.5 and the results of activation energy determinations for both CT and DCB specimens are discussed in Section 5.

Environment	Basis	Activation energy ⁻¹ (kJ mole)
H ₂ O	Plateau velocity	55.5
3%NaCl	Plateau velocity	104.6
3%NaCl	Stage I at $\dot{G}_{min}^{-3/2}$	114.3

Table 10 Activation energies for SC crack growth in double distilled water and 3%NaCl for CT specimens

4.2 THE INFLUENCE OF TEST CONDITIONS ON STRESS CORROSION CRACK GROWTH

A number of features of stress corrosion crack growth in the series of experiments performed with compact tension specimens required further investigation. These features included;

- a) The increased rate of SC crack growth at the specimen edges, noticed in particular at 70 °C, in double distilled water and water saturated air vapour environments. Generally SC crack growth in double distilled water or WSAV resulted in pronounced concave crack fronts at final fracture, whilst specimens tested in 3%NaCl showed convex SC crack fronts at final fracture.
- b) The anomalous crack growth at 70 °C in double distilled water and water saturated air vapour, where the SC crack velocity initially decreases from a high value and builds up again to form a "U" shaped crack growth rate versus stress intensity curve.

4.2.1 The effect of blanking-off compact tension specimen sides.

On CT specimen 39, the CT specimen sides were isolated from the environment by a "Lacomit" layer which prevented or considerably reduced the access of the environment to the SC crack tip at the specimen sides. The SC crack growth experiment was conducted in WSAV at 70 C. The crack growth rate versus stress intensity plot is shown in Figure 97.

SC crack growth has taken place over a range of velocities similar to that observed in other experiments in water or WSAV environments at 70 C, and the SC crack growth rate shows the same decrease in crack growth rate at low stress intensities. The increasing crack growth rate portion of the curve also shows a more characteristic plateau at a stress intensity of $16 \text{ MNm}^{-3/2}$.

The shape of the SC crack front at final fracture is shown on the macrophotograph of the fractured specimen (Figs. 98 and 99). Preventing access of the environment to the SC crack sides has stopped the increased rate of crack growth at the specimen sides. In all other respects the fracture surface is similar to that seen previously.

175
Van Leeuwen has suggested that if extension of a SC crack occurs by hydrogen embrittlement, it will be particularly affected by the triaxiality of the stress at the crack tip, since the diffusion of hydrogen is enhanced by a high triaxial (hydrostatic) stress. It follows from this that SC crack growth

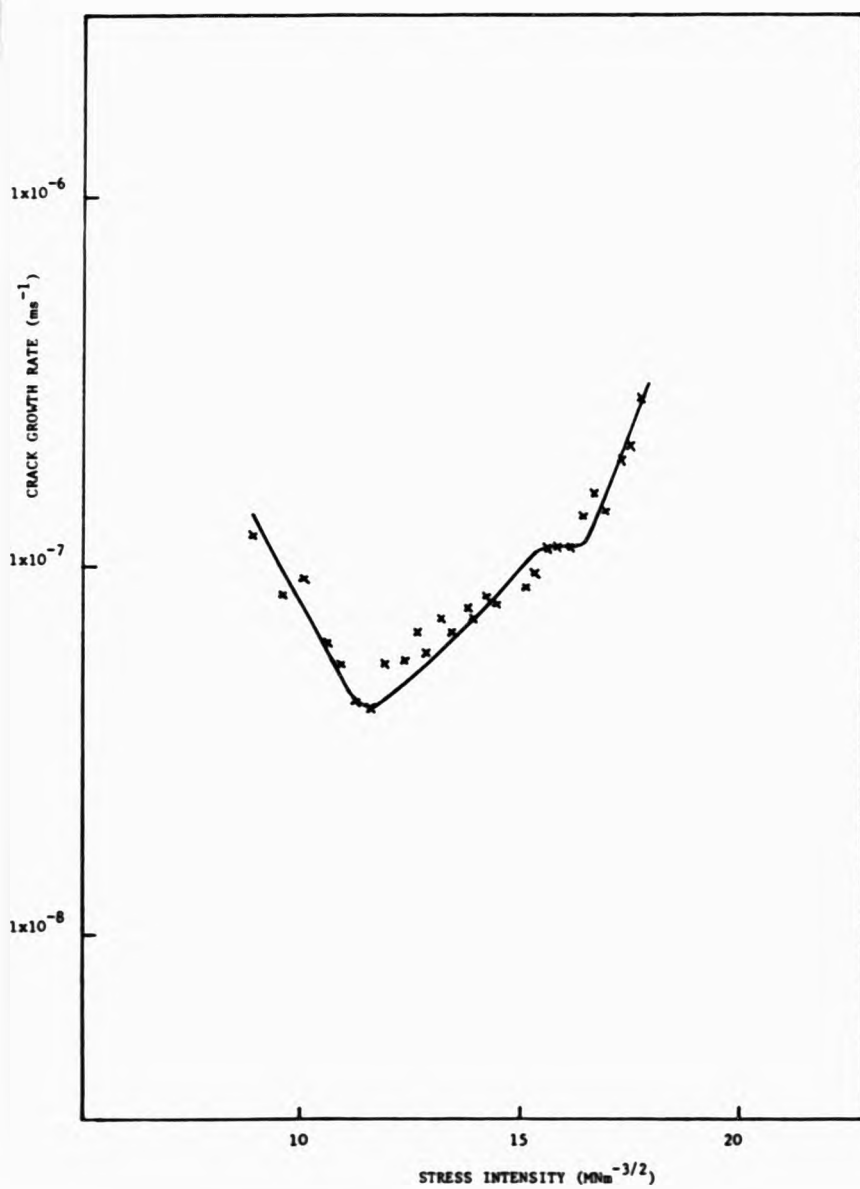


Fig 97 Crack growth rate versus stress intensity of 7017 type AlZnMg alloy, T651 condition at 70°C in WEAV with CT specimen sides blanked off.

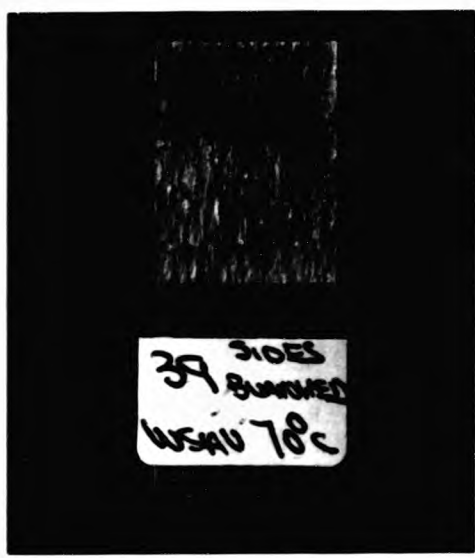
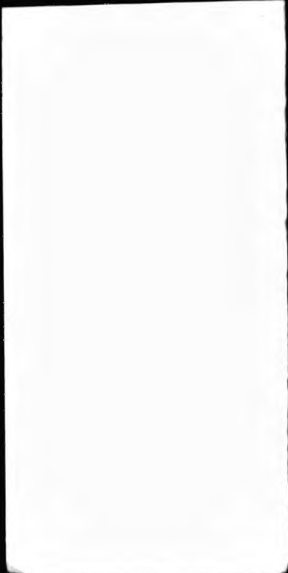


Fig 98 Specimen 39, specimen sides have been blanked off, note the absence of regions of extended SC crack growth, (WSAV, 70°C).

Magnification x 2.3

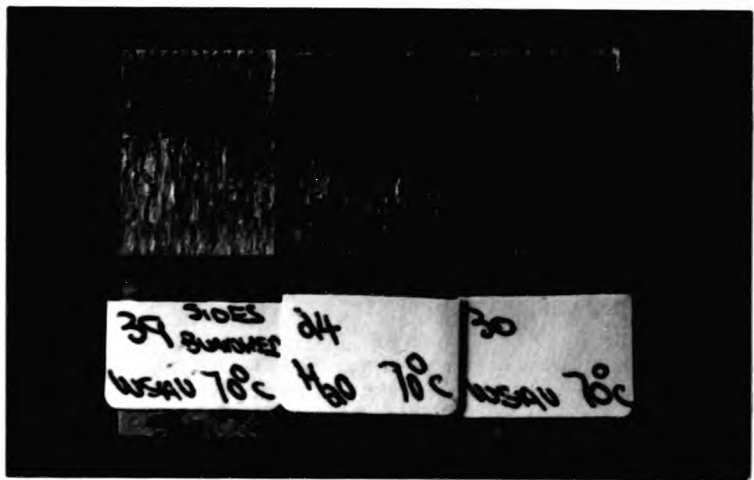


Fig 99 Comparison of SC crack growth in double distilled water and WSAV at 70° with access of the environment to the specimen sides prevented in specimen 39.

Magnification x 1.9

will be enhanced in the centre of the specimen resulting in a convex SC crack front at final fracture in SC experiments in which stress intensity increases with crack length. At the specimen edges the size of the crack tip plastic zone is a maximum as a result of the plane stress condition in this section of the specimen. Hartman⁸⁴ has suggested in connection with the stress corrosion of AlZnMg alloys that the plastic zone size will affect the oxide film rupture characteristics. The increased strain at the outer extremities of the crack will increase the rate at which film rupture takes place, increasing SC crack growth at the specimen sides. This will result in a concave SC crack front at final fracture where SC crack growth occurs by an anodic dissolution mechanism. This situation is illustrated in Figure 100.

Hartman gives a series of results for SC crack growth in 3%NaCl, in an AlZnMg 7075 type alloy which show concave crack fronts at potentials near to the pitting potential for this alloy and convex crack fronts at potentials around -0.95V vs SHE.

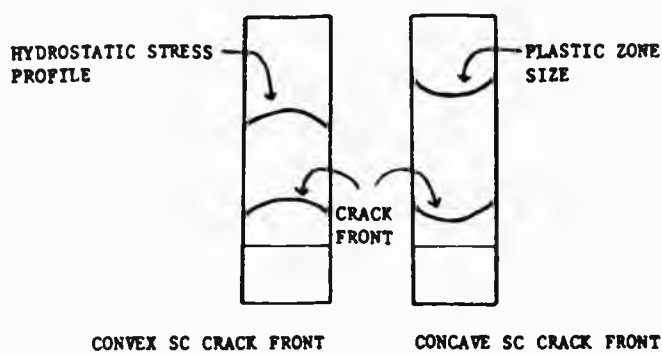


Fig 100 Schematic representation of the relationship between SC crack growth mechanism and the stress regime across the specimen width along the SC crack front.

84

The conclusion Hartman drew from these results was that a dual mechanism of crack growth was apparent, depending upon specimen potential, with anodic dissolution dominant at more positive potentials and a hydrogen embrittlement mechanism dominant at more negative potentials.

The work reported here is at the free corrosion potential of the 7017 type alloy, where for the 7075 alloy Hartman reported concave SC crack fronts at final fracture, (i.e. evidence for crack growth as a result of an anodic dissolution mechanism.) In the current work the important difference is the establishment of plane strain conditions over a larger section of the CT specimen width. Based upon a short transverse fracture toughness of $25 \text{ MNm}^{-3/2}$ for the 7017 alloy and a reported short transverse fracture toughness for the 7075 alloy of $30 \text{ MNm}^{-3/2}$,

the minimum specimen width to establish plane strain conditions in the specimen is given by equation 4.1, (B, K and r_y are as previously defined, Section 3.2.1)

$$B > 2.5 \left(\frac{K_{IC}}{r_y} \right)^2 \quad (4.1)$$

The yield stress of 7017 alloy is 435 MNm⁻² and the yield stress of 7075 alloy is 470 MNm⁻²(10). The minimum specimen thickness therefore for plane strain conditions should be 8.3 mm for the 7017 alloy and 10.2 mm for the 7075 alloy. The specimen used in the Hartman study was 6.5 mm thick while those used in the present work were 15 mm thick.

It is therefore proposed that the concave SC crack fronts seen in the current work in double distilled water and WSAV represent access of hydrogen generated at the specimen sides to the region ahead of the SC crack tip causing enhanced SC crack growth in these areas. Where access of hydrogen is prevented by restricting or preventing water diffusion to the crack tip at the specimen side, the SC crack front takes on a convex profile, more characteristic of a hydrogen embrittlement mechanism with all hydrogen generated on the crack surface and diffusing to the region ahead of the crack tip. In effect, in WSAV and double distilled water, the rate of production of hydrogen is the controlling factor for SC crack growth, whilst it is proposed that in chloride environments sufficient hydrogen is generated at the crack surface adjacent to the crack tip to maintain a

convex SC crack profile as seen in Figure 63. In the results presented by Hartman, significant plane stress conditions at the specimen sides due to the use of relatively thin specimens may not have allowed the effect of the development of a convex SC crack front at the pitting potential, due to hydrogen transport by a hydrostatic stress gradient, to become apparent. It is significant that, in the work reported here the concave SC crack fronts were only present in double distilled water or WSAV environments when the 3% NaCl environment might be expected to accentuate more the effects attributable to an anodic dissolution mechanism.

4.2.2 The influence of pre-exposure and electrochemical pre-charging.

The effect of pre-exposure to WSAV for 50 hours at 70 °C (specimen 34) and electrochemical pre-charging at 20 °C at a potential of -1.75 V vs SHE for 50 hours in 3% NaCl (specimen 35) was investigated, as pre-exposure and pre-charging effects are associated with hydrogen embrittlement mechanisms^{91, 193, 194}.

The average current density was 60 mA cm⁻² based upon a pre-charged area of 2 cm² around the fatigue crack tip and extending along the SC crack growth direction, the bulk of the unstressed CT specimen being blanked off. The results of pre-charging in WSAV are shown in Figure 101 and of pre-charging at -1.75 V vs SHE in Figure 102. SC crack growth in both cases was in WSAV at 70 °C.

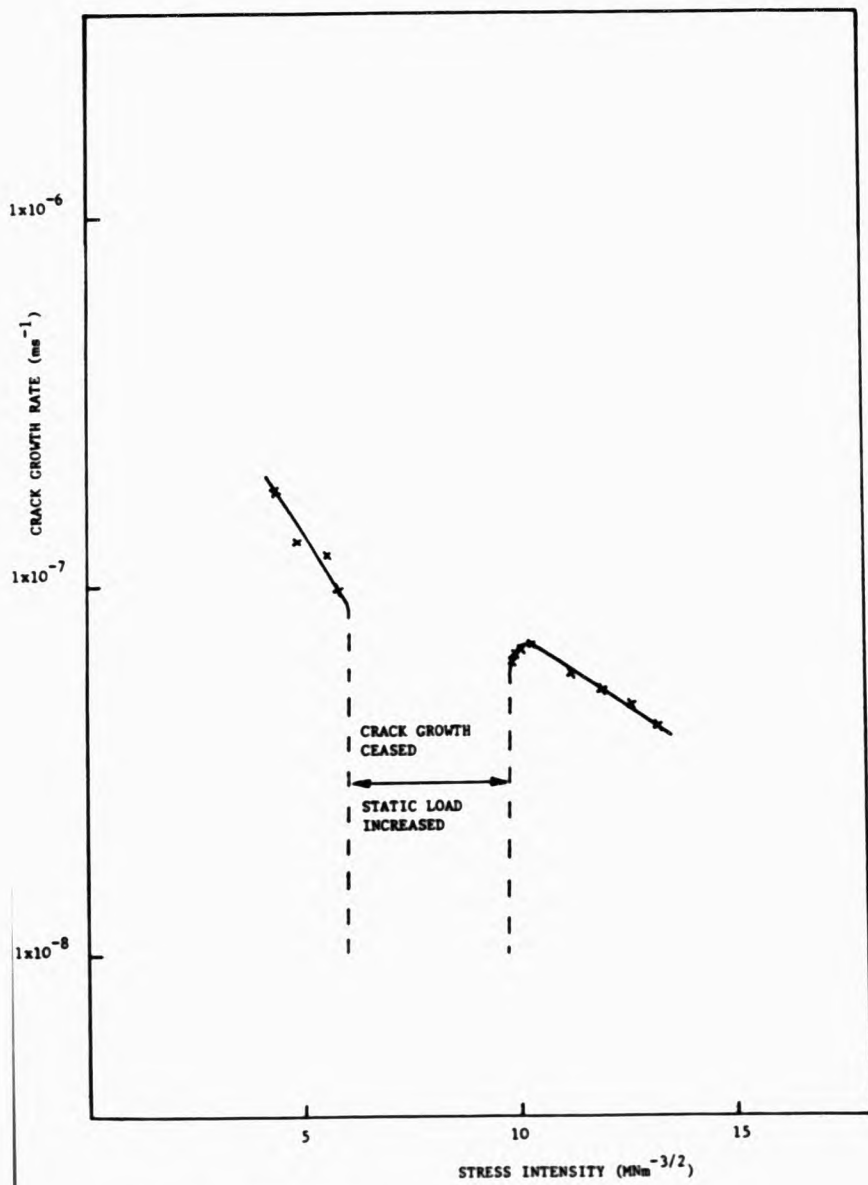


Fig 101 Crack growth rate versus stress intensity of 7017 type AlZnMg alloy, T651 condition pre-exposed to WSAV at 70°C for 50 hours followed by SC crack growth in WSAV AT 70°C.

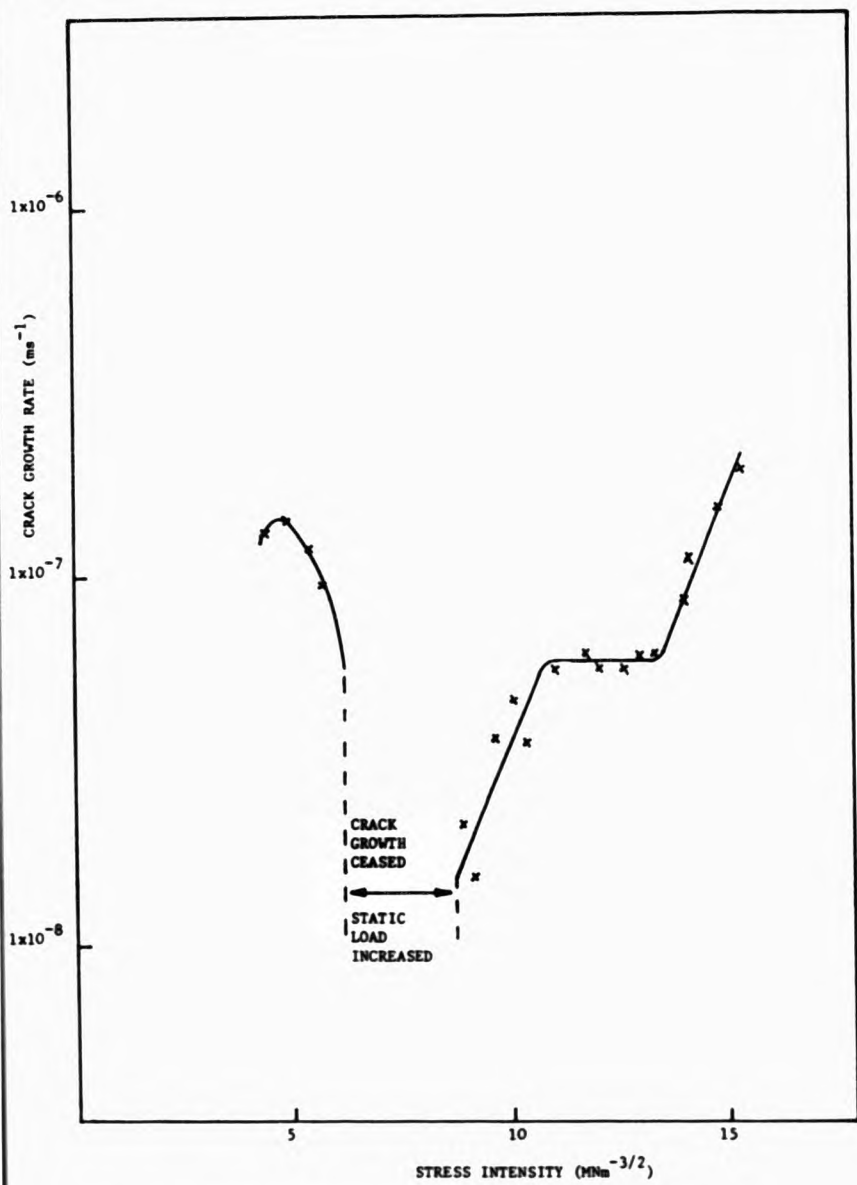


Fig 102 Crack growth rate versus stress intensity of 7017 type AlZnMg alloy, T651 condition pre-charged at -1.75 V vs SHE for 50 hours followed by SC crack growth in WSAV at 70°C.

Both curves show an initially decreasing crack growth rate with stress intensity and both show that the initial crack growth rate takes place at a stress intensity of just under $4.5 \text{ MNm}^{-3/2}$. This is substantially lower than the K_{ISOC} values seen in NSAV without pre-charging of around $9.5 \text{ MNm}^{-3/2}$ (K_{ISOC} in double distilled water at 70°C was in the range 8.8 to $10.8 \text{ MNm}^{-3/2}$). Crack growth ceased at intermediate stress intensities of around $6 \text{ MNm}^{-3/2}$ for both specimens and was only resumed by increased static load. Crack growth was re-established at $9 - 10 \text{ MNm}^{-3/2}$. Specimen 37 resulted in a more conventional crack growth rate versus stress intensity plot, while specimen 34 showed further decreases in crack growth rate until final fracture. Increased SC susceptibility as a result of pre-exposure to the environment is indicative of a hydrogen embrittlement mechanism. The presence of hydrogen in the specimen, as a result of either the reaction of water with the aluminium alloy surface (Section 2.5.6) or as a result of cathodically generated hydrogen, results in crack growth due to embrittlement at lower stress intensities than when crack growth and hydrogen generation are occurring simultaneously.

Enhanced crack growth at the specimen sides has taken place in the specimen pre-exposed to NSAV and to a much lesser extent in the electrochemically pre-charged specimen (Fig.103).

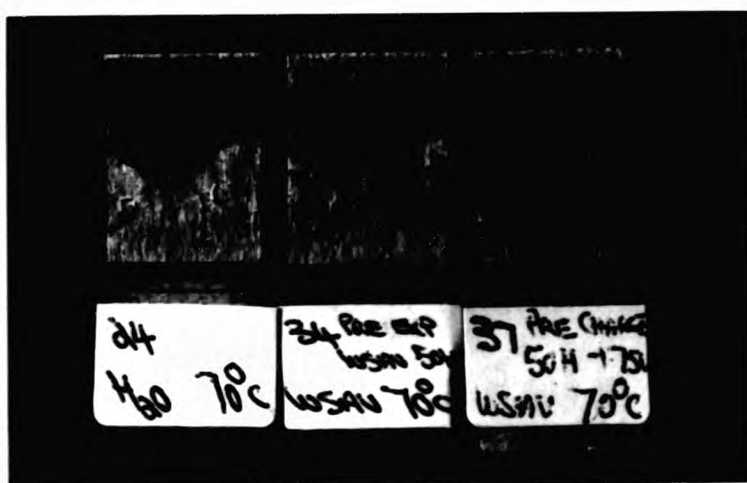


Fig 103 Comparison of SC fracture surfaces of specimen 34, pre-exposed to WSAV and specimen 37, pre-charged at -1.750 V vs SHE.

(Magnification x 2)

Figure 102 also serves to illustrate the effect of allowing a few mm of SC crack growth to take place, subsequently reloading the specimen at a higher static load (higher stress intensity) and performing the SC test with a short stress corrosion crack as opposed to a fatigue crack as the starter crack. The results of this experiment would tend to suggest that a more conventional crack growth rate versus stress intensity plot is obtained (see Section 4.2.3), with a plateau velocity in WSAV of $5.8 \times 10^{-8} \text{ ms}^{-1}$. The more conventional crack growth rate versus stress intensity plot is not repeated for specimen 34, pre-exposed to WSAV at 70 °C, after a few mm of SC crack growth. The plateau velocity in Figure 102 is slightly lower than that previously obtained in double distilled water at 60 °C ($6.3 \times 10^{-8} \text{ ms}^{-1}$). The halt in crack growth at intermediate stress intensities of around 6 MNm^{-3/2} indicates that "recovery" of the CT specimen has taken place, and that the environmental embrittlement sustained during the initial stages of crack growth was not sufficient to promote stress corrosion at intermediate stress intensities between 6 and 9 MNm^{-3/2}, after the volume of material embrittled by pre-exposure had fractured (for further discussion see Section 5.5).

Crack growth had taken place for 1.62 mm in the case of the specimen pre-exposed to WSAV and for 1.42 mm in the specimen pre-

charged at a potential of -1.75 V vs SHE before an increase in stress intensity was required to re-establish crack growth.

4.2.3 Anomalous crack growth rates at 70 C in water and MSAV.

A further experiment was conducted in MSAV at 70 C, where the stress corrosion crack growth was halted just after the increase in crack growth rate, in order to establish that SC crack growth was in fact taking place during the period of decreasing crack growth, and to examine the fracture surface of the specimen. The crack growth rate versus stress intensity plot is shown in Figure 104. It can be seen that crack growth has taken place over the same range of velocities as previous tests, although the K_{ISCC} is slightly lower at $6.7 \text{ MN}\sqrt{\text{m}}^{-3/2}$. The minimum velocity corresponds to a stress intensity of $7.6 \text{ MN}\sqrt{\text{m}}^{-3/2}$. The complete fracture surface is shown in Figure 105, after the specimen had been broken open. It is clear that between 2 and 3 mm of SC crack growth has taken place. The development of increased SC crack growth on one side of the specimen (arrowed "A") has taken place early in the life of the specimen.

The fracture surface of the SC crack formed in specimen 29 is shown in Figures 106-108. The SC fracture is similar to that seen previously and in particular the transition between the fatigue pre-crack and the SC crack is similar to that shown in Figures 69 and 70 for SC crack growth in double distilled water at 90 C, although the SC fracture surface of specimen 29 is less distinct due to the hydrous oxide present on the surface.

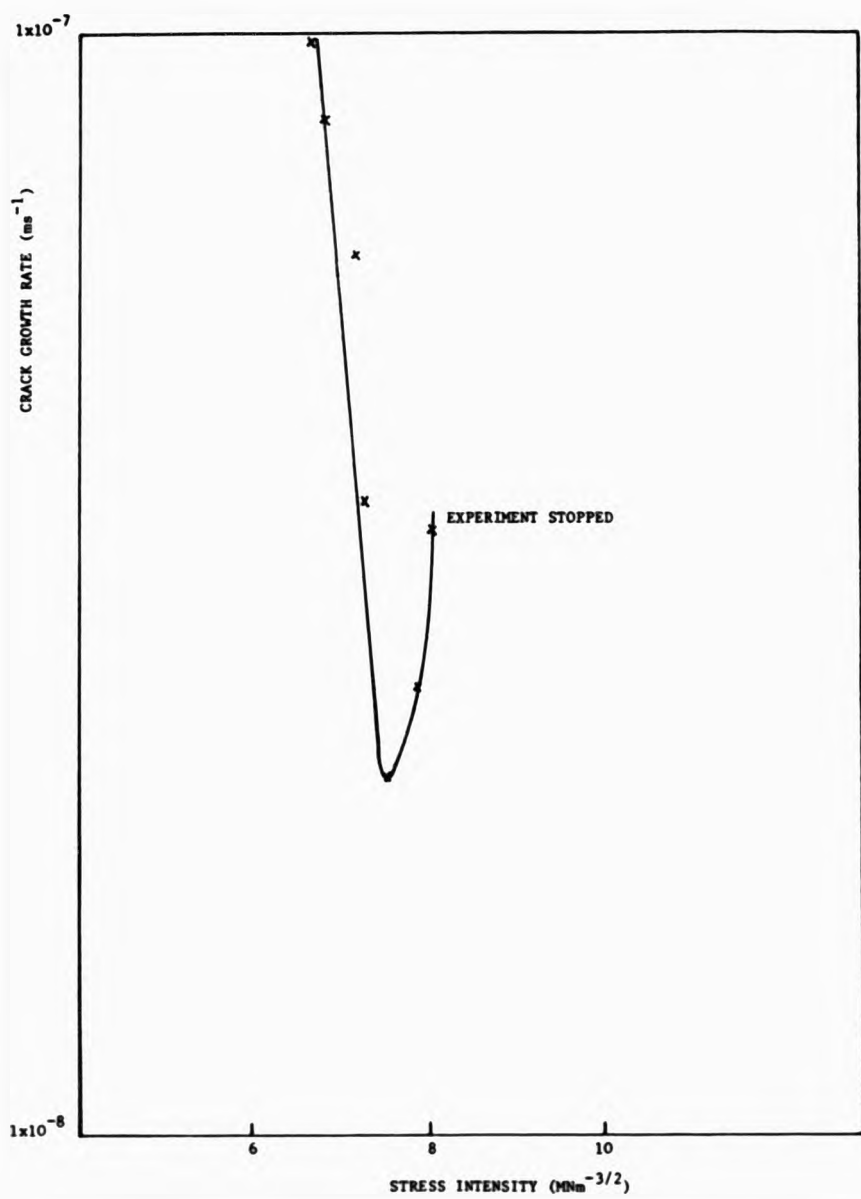


Fig 104 Crack growth rate versus stress intensity of 7017 type AlZnMg alloy, T651 condition. SC crack growth has been halted after the increase in SC crack growth rate was detected.

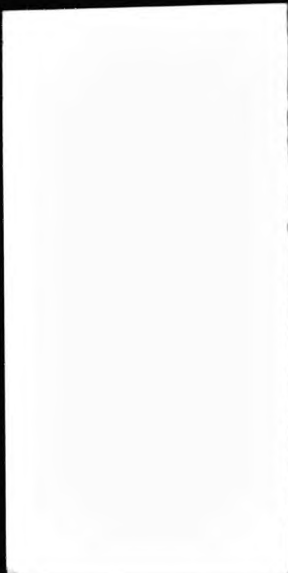


Fig 105 Specimen 29, SC crack growth in WSAV at 70°C has been halted after the period of decreasing crack growth rate.

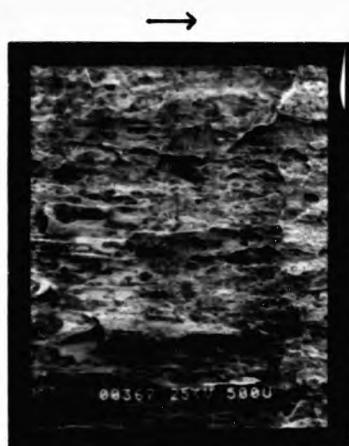


Fig 106 Specimen 29, general view of the short SC crack formed in WSAV at 70°C and stopped just after the observed decrease in crack growth rate.

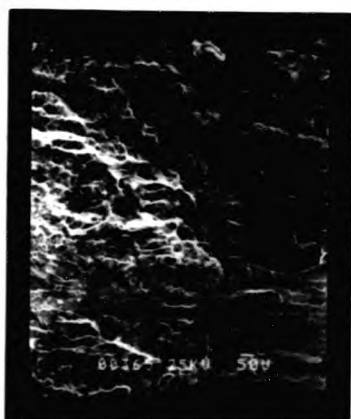


Fig 107 Specimen 29 showing the interface between the fatigue pre-crack and the SC crack. (WSAV, 70°C, SC crack growth halted).

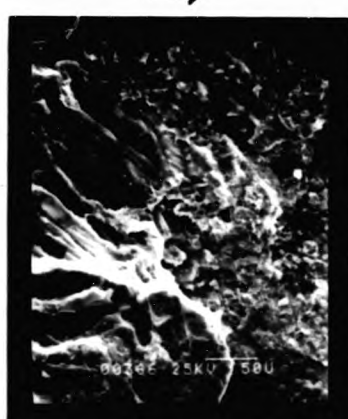


Fig 108 Specimen 29 showing a higher magnification view of Fig 107. Note the transition from fatigue to stress corrosion is very similar to that shown in Figs 69 and 70. (WSAV, 70°C, SC growth halted).

An experiment was performed in which the environment was absent, but the specimen was loaded to the same static load at 70 °C (2.059 kN) thus producing a dry air environment. Any change in voltage across the clip gauge would therefore indicate that creep of the specimen was taking place at 70 °C and not stress corrosion crack growth. No voltage change was observed over a period of 140 hours and it was therefore concluded that creep during the period of decreasing crack growth, instead of SC crack growth, was not a factor in the anomalous results obtained at 70 °C.

There are an additional number of possible mechanisms to account for the anomalous crack growth at 70 °C in double distilled water and MSAV. These are as follows:

- 1) The transition between the transgranular fatigue pre-crack and a completely intergranular stress corrosion crack proceeds at an initially fast crack growth rate at low stress intensities until the remaining transgranular ligaments in the crack path effectively pin the SC crack front resulting in a reduction in crack growth rate. This process occurs until, at higher stress intensities, the pinning of the SC crack front by transgranular ligaments is overcome and crack growth increases again from some intermediate stress intensity.
- 2) The alloy is undergoing additional ageing at 70 °C during the SCC experiment in which the additional grain boundary precipitate growth results in increased gettering of the available hydrogen, and thereby increases the critical

concentration of hydrogen necessary for further crack extension. This results in a decrease in the crack growth rate. This effect is overcome at intermediate stress intensities when the grain boundary precipitates become saturated, and/or cease growing after a period of time at 70 °C, with the effect that the SC crack growth rate increases as more hydrogen becomes available for grain boundary embrittlement. This proposed mechanism is based upon some of the proposals of Christodoulou and Flower⁷⁰, Scamans¹³⁷ and Tuck⁹⁸ discussed in Sections 2.4.1 and 2.5.4.2.

- 3) Local plastic deformation in the region ahead of the crack tip as a result of hydrogen induced delayed plasticity (HIDP) causes a reduction in the SC crack growth rate. This local plastic deformation occurs at low to intermediate stress intensities. HIDP has been observed by other workers²⁰¹ in DCB specimens of 7475 - T651 AlZnMgCu alloy tested in a chloride-chromate solution at 20 °C. Here crack growth rate during Stage II was observed to decrease and subsequently increase by over an order of magnitude.

The HIDP has been attributed to environmental or hydrogen interaction with dislocation nucleation processes and slip band formation. A reduction in crack growth rate is observed because plastic deformation processes are substituting for crack growth.

The three mechanisms summarised above are discussed in more detail in Section 5.

4.3 THE INFLUENCE OF ENVIRONMENT ON STRESS CORROSION CRACK GROWTH IN DOUBLE CANTILEVER BEAM SPECIMENS.

As discussed in Section 4.1, one of the objectives of this study has been to compare SC crack growth data generated by CT and DCB test specimens. It is thought that the loading history, in particular whether the crack tip stress intensity increases or decreases during the SCC test, may have an important effect on the accuracy of the data generated, and also may provide information on the mechanism of SC crack growth.

The results of a series of experiments on DCB specimens machined from 7017-T651 alloy are presented here for comparison with the CT results. The experiments have been conducted in the same environments as the CT specimen experiments and over the same temperature range, 20 - 90 C.

The majority of DCB specimens had starter cracks formed by bolt loading the specimens until an overload failure occurred. The resultant "pop-in" overload failure crack tip was the initiation point for further SC crack growth when placed in the SC environment. The results of the "pop-in" failures and the fatigue pre-cracking of the remaining DCB specimens are tabulated below (Tables 11 and 12). Fatigue pre-cracked specimens were also bolt loaded. One bolt was provided with a rounded end in order to equalize stresses on each side of the DCB specimen.

Specimen No.	Pop in crack on specimen sides(mm) From to Length		Pop in crack From to Length		Bow Length(mm) From load line		Bow Average Length (mm)	Displacement at load line V(mm)	Load line to notch distance L(mm)				
	(notch)	(A)	(B)	from load line(mm)	0.25b	0.50b				0.75b			
1 WSAV 70°C	5.48	8.67	3.19	5.94	8.71	2.77	8.69	12.90	14.30	14.19	5.11	0.165	5.71
2 JNMaCl 70°C	5.94	8.23	2.29	5.44	6.81	1.37	7.52	Surface Corroded		-	-	0.260	5.69
3 H ₂ O 70°C	5.94	9.20	3.26	5.46	9.09	3.63	9.15	14.92	15.18	14.56	5.74	0.445	5.70
4 WSAV 90°C	5.72	7.10	1.18	5.58	6.99	1.41	7.05	11.57	12.38	11.84	4.88	0.290	5.65
5 JNMaCl 90°C	6.35	8.91	2.56	5.89	8.73	2.84	8.82	Surface Corroded		-	-	0.105	6.12
6 H ₂ O 90°C	6.88	8.69	1.81	6.34	8.39	2.05	8.54	13.63	14.13	13.02	5.05	0.280	6.61
7 JNMaCl 10°C	6.13	10.83	4.70	6.38	10.84	4.46	10.84	Surface Corroded		-	-	0.290	6.26
8 JNMaCl 50°C	6.03	10.12	4.29	5.94	11.74	5.80	11.03	Surface Corroded		-	-	0.380	5.99
9 H ₂ O 10°C	5.81	8.98	3.17	5.73	9.78	4.05	9.38	Surface Corroded		-	-	0.250	5.77
10 H ₂ O 50°C	5.70	9.86	4.16	5.83	10.31	4.48	10.09	Surface Corroded		-	-	0.330	5.77
11 WSAV 10°C	5.51	9.72	4.19	6.69	9.81	3.12	9.77	14.76	15.42	14.41	5.09	0.360	6.11
12 WSAV 50°C	5.82	9.08	3.26	5.80	7.80	2.00	8.44	12.48	12.96	12.33	4.15	0.280	5.81
13 LAB AIR	5.64	14.08	8.44	5.62	12.95	7.33	13.52	18.00	18.12	15.51	4.36	0.410	5.63
14 JNMaCl 70°C	Fatigue Pre-cracked										-	0.220	5.76
15 H ₂ O 70°C	Fatigue Pre-cracked										-	0.235	5.71
16 WSAV 70°C	Fatigue Pre-cracked										-	0.230	5.48
17 JNMaCl 70°C	Fatigue Pre-cracked										-	0.224	5.68

Table 11. Summary of DCB specimen data for SCC experiments.

Specimen No.	Fatigue Pre-Crack Growth (mm)		Length (B)	Effective Length - a (mm)	Displacements			Loads (kN)			$\left(\frac{\Delta a}{w}\right)_{\text{MIN}}$ (%)	$K_{I,3/2}$ (MNm)	Fatigue Ratio R $\left(\frac{P_{\text{min}}}{P_{\text{max}}}\right)$	No of cycles		
	From to Length (notch) (A)	From to Length (notch) (B)			Max (mm)	Min (mm)	Ave (mm)	Max	Ave	Min						
14	5.80	14.18	8.38	5.72	12.16	6.44	13.17	0.45	0.11	0.916	0.478	0.091	4.12	0.192	0.099	244480
15	5.73	13.80	8.07	5.68	12.99	7.31	13.40	0.44	0.16	1.033	0.526	0.047	1.65	0.219	0.045	157880
16	5.23	13.96	8.73	5.72	13.88	8.16	13.92	0.70	0.50	1.058	0.454	0.062	0.16	0.231	0.059	123760
17	5.47	13.77	8.30	5.89	12.95	7.06	13.36	0.49	0.14	0.958	0.492	0.086	1.67	0.205	0.089	229320

Table 12. Summary of DCB specimen fatigue pre-cracking data for SCC experiments.

4.3.1 The influence of temperature.

The influence of temperature was studied in double distilled water, WSAV and 3% NaCl environments at four temperatures, 30, 50, 70 and 90 C. The data obtained for double distilled water is shown in Figure 109, for WSAV in Figure 110 and for 3% NaCl in Figure 111.

Again the macroscopic grain shape of the alloy can be seen in the microstructure of the DCB specimens after breaking the specimen open. It was evident from the crack growth determinations on the specimen sides that crack branching has been taking place to a greater extent than in the CT specimens. The macro surfaces of the SC cracks are shown in Figure 112 for the double distilled water environment, Figure 113 for the WSAV environments and Figure 114 for the 3% NaCl environment. The SC crack surface in WSAV at 90 C (Fig 113) in particular shows crack branching towards the end of the specimen. The SC crack surfaces in the 3%NaCl environment (Fig 114) show evidence of substantial corrosion product contamination which obliterates any fine detail of the fracture surface.

The bowed "pop-in" failure is shown clearly in the SC cracks grown in double distilled water and WSAV (Figs 112 and 113). Again plane strain conditions have been maintained throughout the SC test but small shear lips appear on the specimen sides where the specimen has been broken open to reveal the fracture surface.

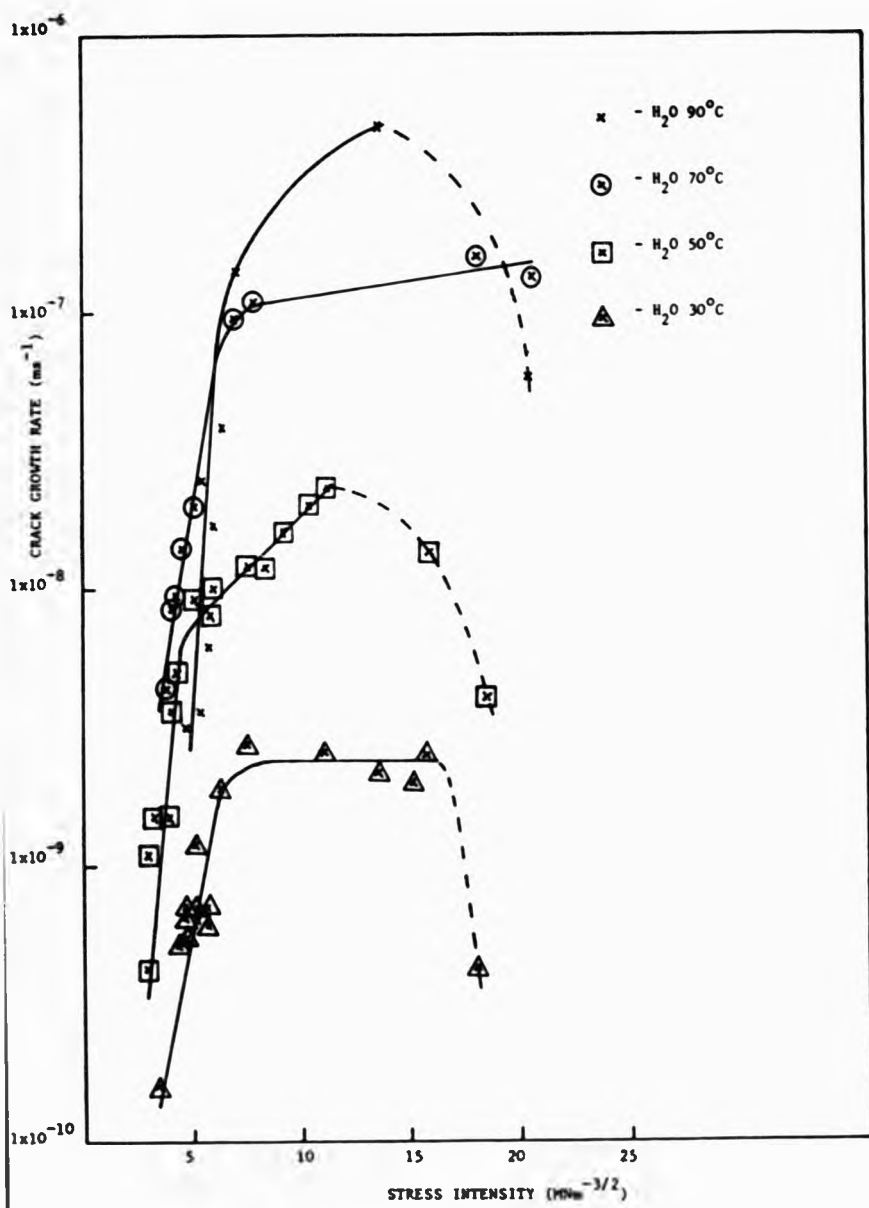


Fig 109 Crack growth rate versus stress intensity of 7017 type AlZnMg alloy DCB specimens, T651 condition at different temperatures in double distilled water.

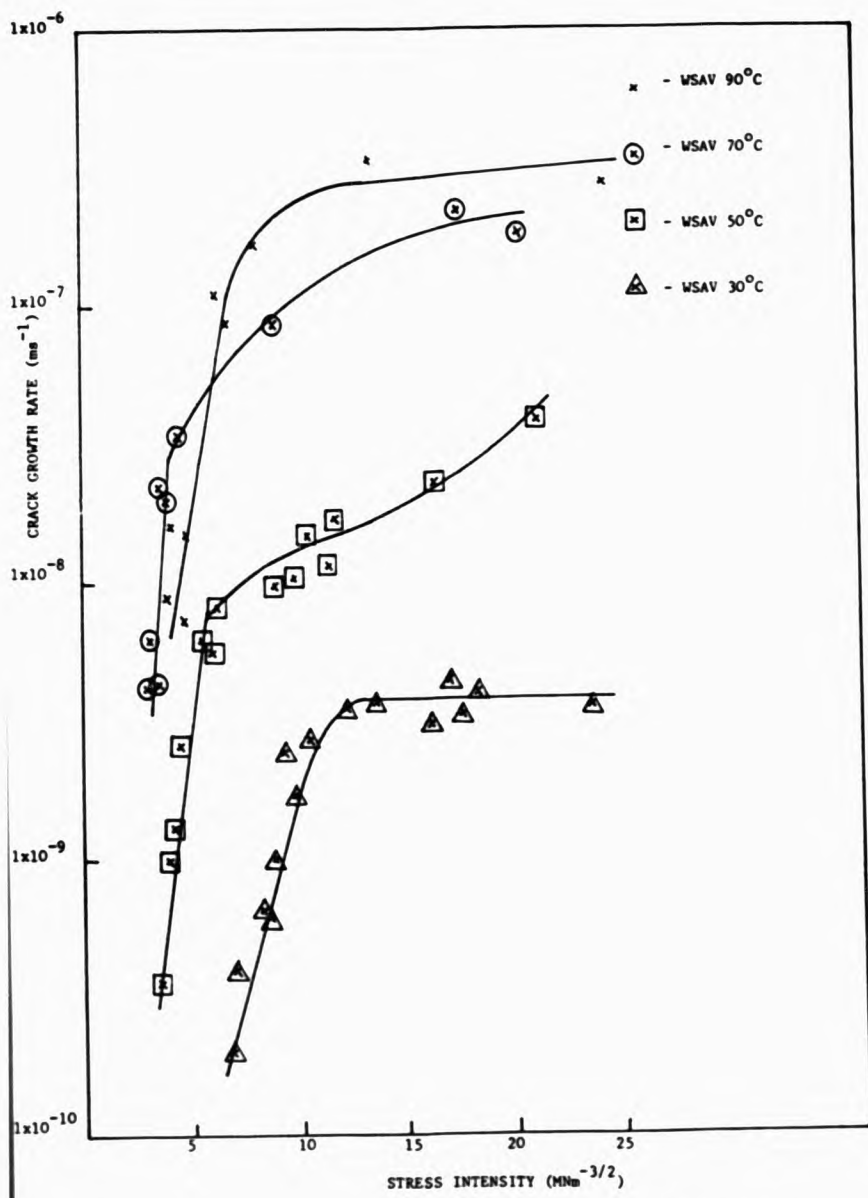


Fig 110 Crack growth rate versus stress intensity of 7017 type AlZnMg alloy DCB specimens, T651 condition at different temperatures in WSAV.

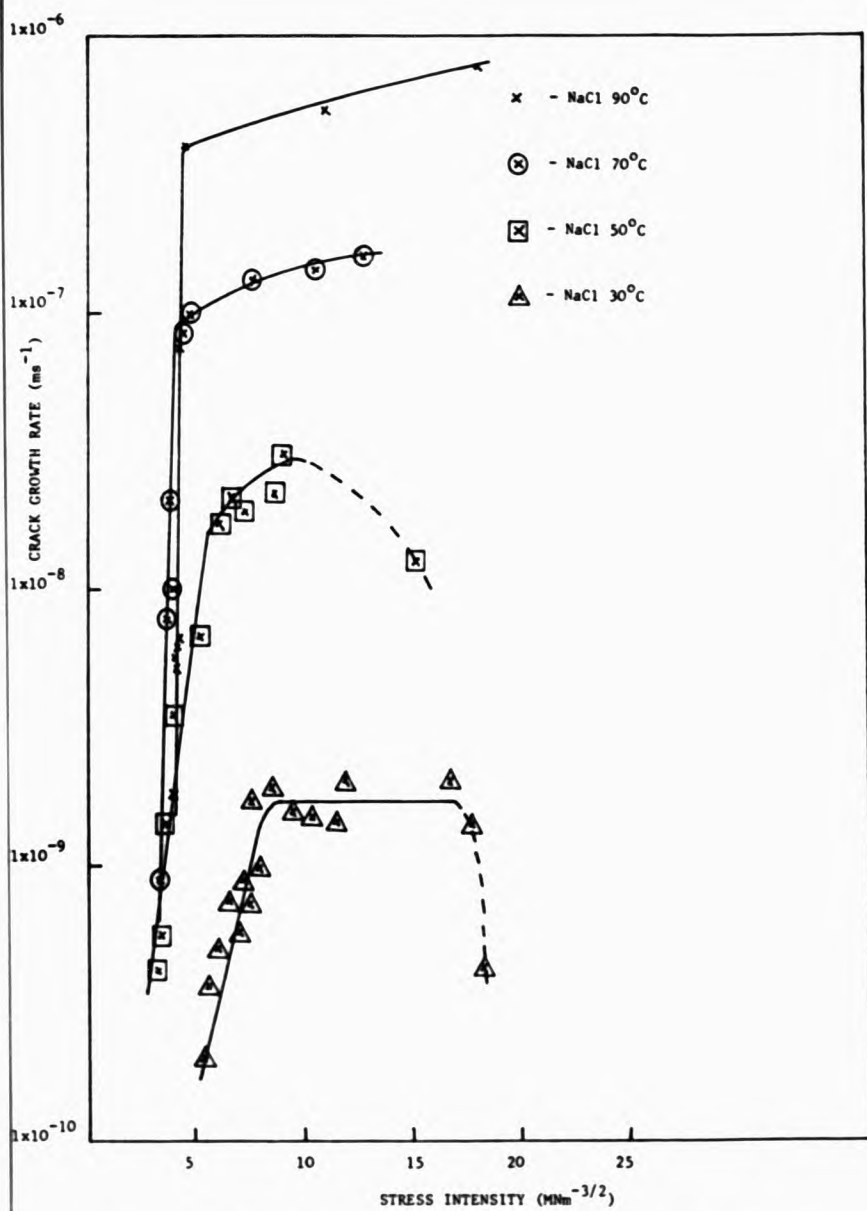


Fig 111 Crack growth rate versus stress intensity of 7017 type AlZnMg alloy DCB specimens, T651 condition at different temperatures in 3% sodium chloride.



Fig 112 Fracture surfaces of DCB specimens after crack growth in double distilled water at 30, 50, 70 and 90°C.
Magnification x 1.3

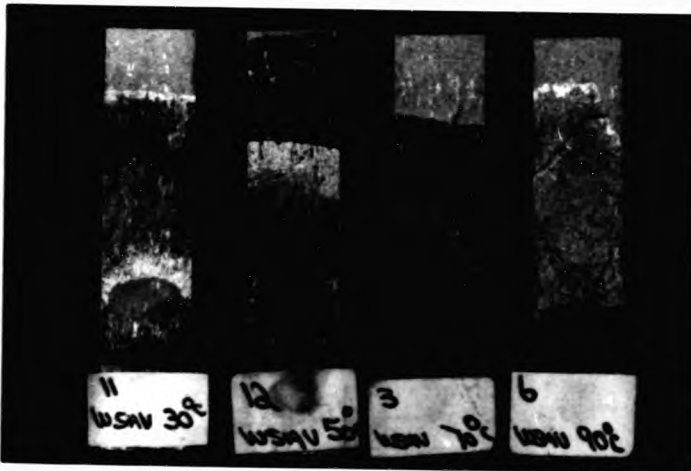


Fig 113 Fracture surfaces of DCB specimens after crack growth in WSAV at 30, 50, 70, 90°C.
Magnification x 1.3



Fig 114 Fracture surface of DCB specimens after crack growth in 3% NaCl at 30, 50, 70, 90°C. Magnification x 1.3



Fig 115 Fracture surface of DCB specimen after crack growth in laboratory air at 23 - 26°C, relative humidity 48 - 62%. Magnification x 1.7

The results of the SC crack growth rate versus stress intensity experiments indicate a number of features;

- 1) With the possible exception of the result for WSAV at 50 °C, no Stage III crack growth was detected. All tests showed a distinct Stage II plateau velocity followed by Stage I decelerating crack growth. The slope of the Stage I crack growth curve is generally much steeper than in the CT specimens.
- 2) Plateau region crack growth rates do not vary markedly between the different environments. The plateau velocities are shown in Table 13. The data obtained indicates that in DCB specimen tests with "pop-in" starter cracks there is a marked dependence of crack growth rate on temperature but very little dependence on environment.

Temperature ° (C)	Plateau Velocity (ms ⁻¹)		
	D D Water	WSAV	3% NaCl
30	2.4 x 10 ⁻⁹	3.9 x 10 ⁻⁹	1.7 x 10 ⁻⁹
50	1.0 x 10 ⁻⁸	1.5 x 10 ⁻⁸	2.2 x 10 ⁻⁸
70	1.25 x 10 ⁻⁷	1.5 x 10 ⁻⁷	1.5 x 10 ⁻⁷
90	3.0 x 10 ⁻⁷	2.5 x 10 ⁻⁷	5.0 x 10 ⁻⁷

Table 13 Comparison of SC crack growth rate plateau velocities for DCB specimens in double distilled water, WSAV and 3% NaCl over a range of temperatures.

The CT specimen tests showed an increase in plateau velocity of just under two orders of magnitude from 2.5 x 10⁻⁷ ms⁻¹ in double

distilled water at 90 °C to 1.4×10^{-5} ms⁻¹ in 3% NaCl at 90 °C. However, the plateau velocity for DCB specimens in 3% NaCl is approximately the same as that shown for double distilled water and MSAV and distinctly lower than the plateau velocities obtained in CT tests. The significantly lower crack growth rates in 3% NaCl in DCB specimens could result from;

- a) Corrosion product build-up in the 3% NaCl environment preventing access of the solution to the crack tip (see Section 4.3.3).
 - b) Significant crack branching in the specimen, where the presence of additional cracks adjacent to the main crack reduces the major crack tip stress intensity resulting in a lower crack growth rate.
 - c) The bowed overload (pop-in) failure which results in a transgranular pre-crack. The pre-crack experiences a difficult transition to an intergranular SC crack, resulting in an initially lower crack growth rate. Secondly, the pop-in failure results in effective crack blunting, the absence of a sharp pre-crack causing initially lower crack growth rates in Stage II (also reported by Spowls et al¹⁷⁶).
- 3) Initially slower crack growth rates (shown by the dashed portion of the V - k curve) were noted in the double distilled water experiments at 30, 50 and 90 °C and in the 3% NaCl experiments at 30 and 50 °C. This observation tends to

confirm the theory that initially slow crack growth rates are experienced at the start of crack growth in the plateau velocity region, and that the plateau velocity in the case of the 3% NaCl environment, never subsequently reaches the expected velocity indicated in the CT specimen results for the reasons outlined above.

- 4) Where direct comparisons can be made, the plateau velocity of CT and DCB specimens in double distilled water are similar.

$\overset{\circ}{\circ}$ - 90 C CT specimen $2.5 \times 10^{-7} \text{ ms}^{-1}$, DCB specimen $3.0 \times 10^{-7} \text{ ms}^{-1}$
 $\overset{\circ}{\circ}$ - 50 C CT specimen $1.7 \times 10^{-8} \text{ ms}^{-1}$, DCB specimen $1.0 \times 10^{-8} \text{ ms}^{-1}$
 and $3.3 \times 10^{-8} \text{ ms}^{-1}$

The CT specimen in double distilled water at 50 C showed a double plateau. In the double distilled water environment therefore, the initially slow crack growth rate does reach the expected plateau velocity indicated by the CT results. However, the plateau velocity at 90 C is only marginally higher than the corresponding velocities at 70 C for all three environments.

- 5) The region I stress intensities at 30, 50 and 70 C show a clear trend towards a higher K_{ISCC} as the test temperature decreases. However, the region I curves at 70 and 90 C are not clearly distinguished, the stress intensities at 90 C being marginally higher than those at 70 C.

4.3.2 Stress corrosion crack growth in DCB specimens from fatigue pre-cracked starter cracks.

A set of experiments were performed where the stress corrosion crack was grown from fatigue pre-cracks in DCB specimens exposed to double distilled water, NSAV and 3% NaCl at 70 °C. The results of using a fatigue pre-cracked starter crack are shown in Figure 116.

Crack growth rates in 3% NaCl at 70 °C have increased half an order of magnitude in the initial stages of crack growth. There is no clearly defined plateau velocity but the maximum average crack growth rate observed was $5.5 \times 10^{-7} \text{ ms}^{-1}$ compared with $3.6 \times 10^{-6} \text{ ms}^{-1}$ for the CT specimen in 3% NaCl at 70 °C with a pop-in starter crack. The provision of a fatigue pre-crack has also resulted in a distinct transition between Stage III crack growth, which was present in these tests, and the plateau velocity region in double distilled water and NSAV environments.

Fatigue pre-cracking the DCB specimens, which was also the technique used for the CT specimens, results in more comparable CT and DCB stress corrosion crack growth rates. However, in a 3% NaCl environment, the crack growth rate remains lower than those observed in constant load CT specimens.

No evidence of an initially lower crack growth rate than the observed plateau velocity was detected in the fatigue pre-cracked DCB specimens. The macro views of the fatigue pre-cracked DCB specimens are shown in Figure 117.

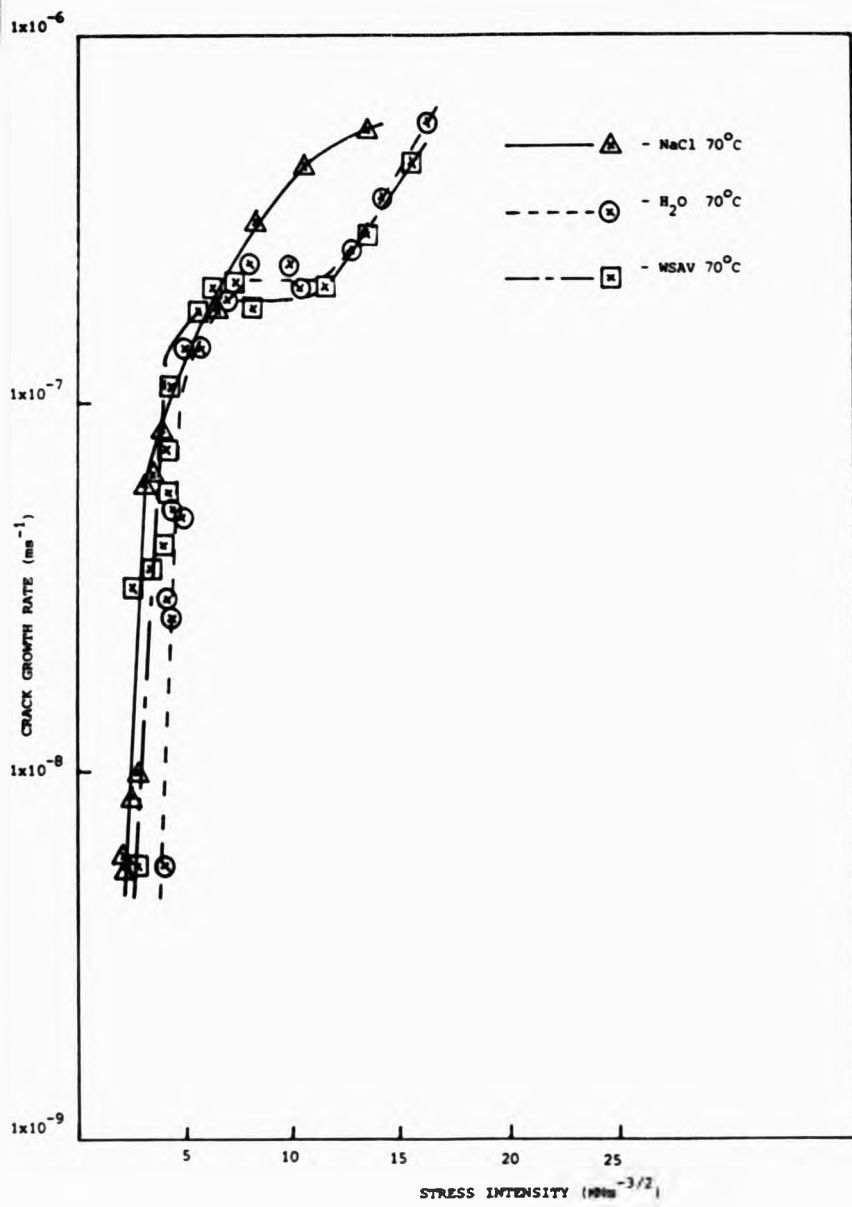


Fig 116 Crack growth rate versus stress intensity of 7017 type AlZnMg alloy DCB specimen, T651 condition at 70°C in environments indicated using a fatigue pre-crack as a starter crack.



Fig 117 Fracture surfaces of fatigue pre-cracked DCB specimens exposed to double distilled water, WSAV and 3% NaCl at 70°C.

Magnification x 1.3

4.3.3 Stress corrosion crack growth in 3% NaCl in DCB specimens from fatigue pre-cracked starter cracks and with regular solution replacement and DCB specimen cleaning.

An additional experiment was performed where the stress corrosion crack was grown from a fatigue pre-crack in the DCB specimen and where the 3% NaCl solution, in which crack growth took place, was replaced every 60 minutes for the first ten hours of crack growth. The experiment was performed at 70 C and each time the solution was replaced, or the stress corrosion crack length measured, the DCB specimen was thoroughly cleaned in an ultrasonic bath containing fresh 3% NaCl followed by two rinses in acetone and two rinses in double distilled water. In this way the crack tip and crack faces were kept free from corrosion product build-up, as evidenced by the absence of mud cracking and other corrosion products on the fracture surface after breaking the specimen open.

The result of this treatment on the crack growth rate versus stress intensity curve is shown in Figure 118, and the specimen after fracture is shown in Figure 120.

Crack growth rates in the Stage II region have increased to 1.8×10^{-6} ms⁻¹ which is in reasonable agreement with the results reported in the present work for CT specimens in a 3% NaCl environment at 70 C of 3.6×10^{-6} ms⁻¹. The results are also within the variation reported in crack growth rates for Stage II crack growth between constant load (CT) and constant displacement (DCB) specimens by other workers¹⁹⁵, of half an order of

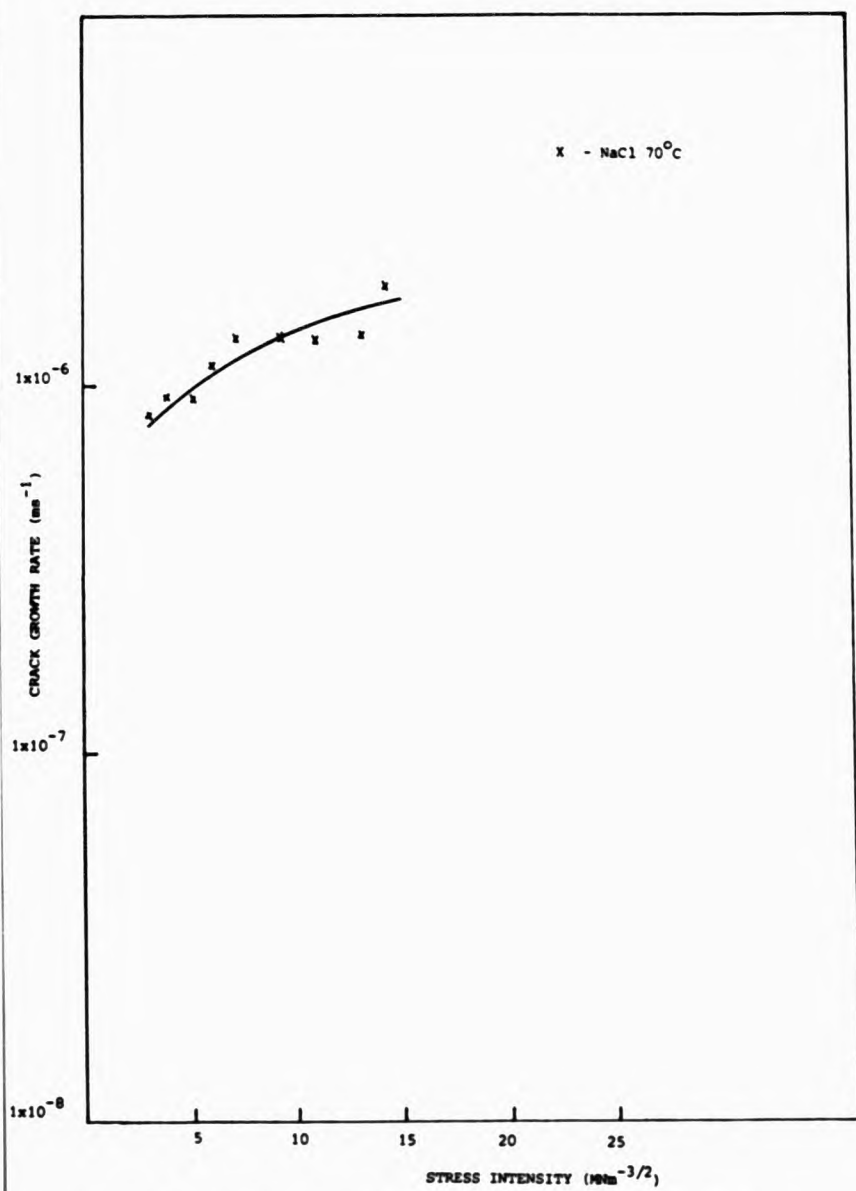


Fig 118 Crack growth rate versus stress intensity of 7017 type AlZnMg alloy DCB specimen, T651 condition at 70°C in 3%NaCl using a fatigue pre-crack, regular replacement of the 3%NaCl solution and cleaning of the DCB specimen.

magnitude (the DCB specimens gave a lower plateau velocity). These results were reported for 2024-T351 aluminium alloy (Al - 4.5%Cu - 1.1%Mg - 0.4%Mn - 0.3%Fe - 0.1%Si) tested in 3%NaCl at room temperature. In contrast, Doward and Hasse have reported differences in crack velocity of up to an order of magnitude with constant displacement specimen SC crack velocities faster than constant load tests in 7075-T651 alloy in synthetic sea water¹⁹⁶. Periodic changing of the 3%NaCl solution and cleaning of the DCB specimen therefore may be a contributory factor in obtaining accurate crack growth rate data in constant displacement tests (see Section 5.4).

4.3.4 Stress corrosion crack growth in laboratory air.

The result of crack growth rate versus stress intensity determinations for stress corrosion in laboratory air is shown in Figure 119. Crack growth took place at temperatures of 23-26 °C and at relative humidities of 48 - 62%. The stress corrosion crack growth under these conditions was essentially free from corrosion product build-up allowing detailed examination of the fracture surface. The macro surface of the specimen is shown in Figure 115.

The results of the SEM investigations of the fracture surfaces of the DCB specimen exposed to laboratory air (Specimen No 13) are presented here. The following SEM photographs have all been taken with a gold coated fracture surface, in order to improve the high resolution fractography, except where noted.

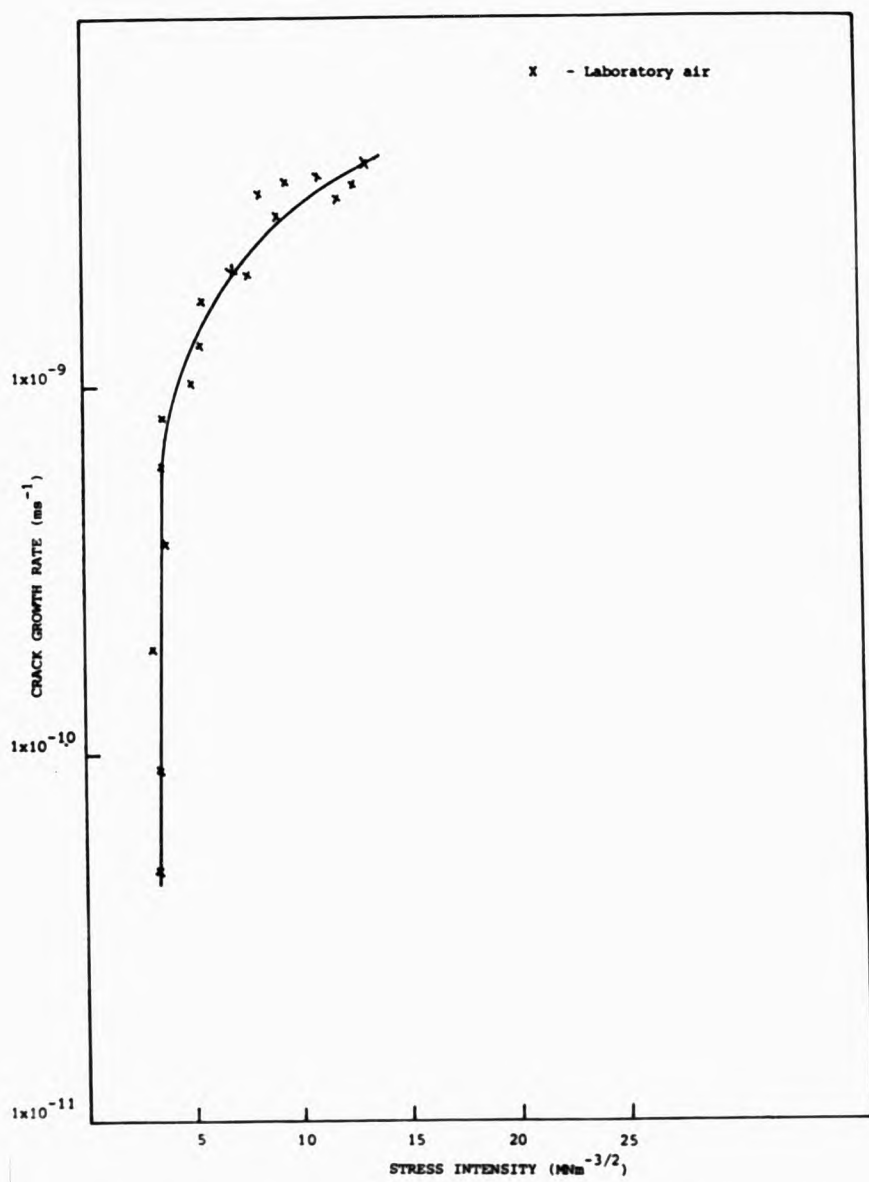


Fig 119 Crack growth rate versus stress intensity of 7017 type AlZnMg alloy DCB specimen, T651 condition at 23-26°C, 48-62%R.H. in laboratory air.



Figures 121 and 122 show the interface between the overload failure and the SC crack. The interface in Figure 122 shows the SC crack has initiated at grain boundaries below the main "pop-in" failure. Figures 123 - 126 show a sequence of higher magnification views of a region near the end of the SC crack, at the interface with the overload failure where the specimen was broken open. The main SC crack with flat pancake shape grains perpendicular to the ST direction is shown in Figure 123. Figures 125 and 126 are high magnification views showing brittle subgrain SC cracks on the main fracture surface. It is thought that the growth of the main SC crack through localised areas of subgrain boundaries gives rise to this type of brittle intergranular SC fracture surface. Figures 127 and 128 show clearly the very brittle nature of the SC failure, where the fracture surfaces are entirely matching and show no evidence of corrosion. Second phase grain boundary precipitate particles can be seen embedded in the main fracture surface. Figures 127 and 128 are of fracture surfaces without a spluttered gold coating.

Figures 129 and 130 show respectively the secondary electron and back scattered electron image of the SC fracture surface 4.64 mm back from the SOC/overload failure interface. The SC fracture surface shows evidence of striations lying perpendicular to the main SC crack growth direction. The striated fracture surface has been cited as evidence that SC crack growth is discontinuous and that this discontinuous crack growth is a feature of failure caused by hydrogen embrittlement and not anodic dissolution .

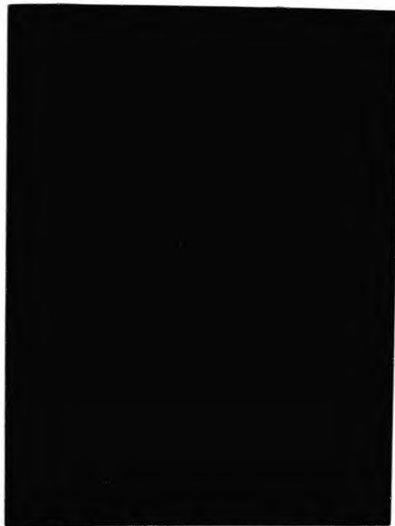


Fig 120 Fracture surface of DCB specimen after crack growth in 3% NaCl at 70°C in which the solution was regularly replaced and the DCB specimen cleaned of corrosion product.

Magnification x1.6



Fig 121 Specimen 13, "pop-in" failure/SC crack interface (lab air, 23-26°C, 48-62% RH).



Fig 122 Specimen 13, "pop-in" failure/SC crack interface.

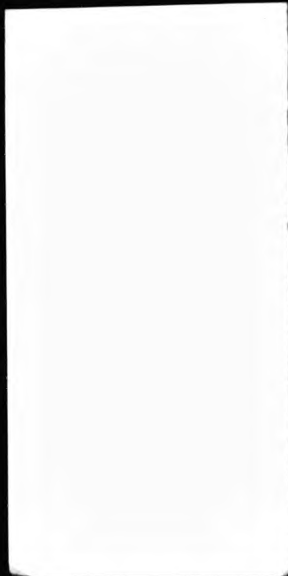


Fig 123 Specimen 13, SC crack/overload failure interface.

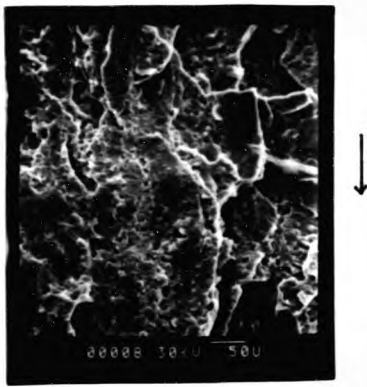


Fig 124 Specimen 13, stress corrosion crack fracture surface.



Fig 125 Specimen 13, brittle intergranular sub-grain boundary SC cracks.

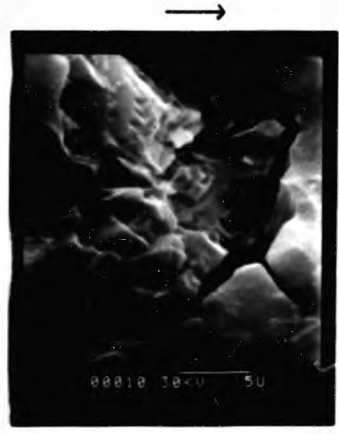


Fig 126 Specimen 13, brittle intergranular sub-grain boundary SC cracks.

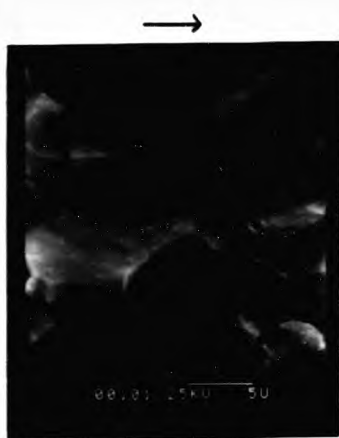


Fig 127 Specimen 13, brittle nature of SC crack in Al-Zn-Mg.



Fig 128 Specimen 13, brittle nature of SC crack in Al-Zn-Mg.

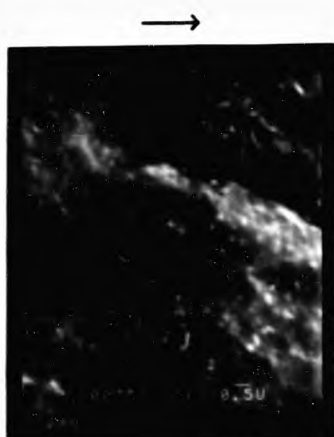


Fig 129 Specimen 13, high magnification view of view of SC fracture surface 4.64 mm from SC/overload fracture showing evidence of crack arrest markings (secondary electron image).

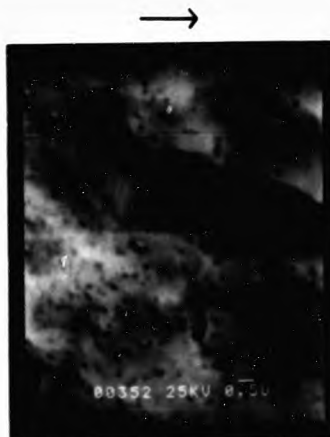


Fig 130 Specimen 13, same area as Figure 129 showing evidence of crack arrest markings, (backscattered electron image).

Second phase particles can also be seen embedded in the fracture surface. The striation spacing is approximately 2500 Å.

Figures 131 - 133 and 134 - 137 show two sequences of higher magnification views of the SC fracture surface near to the interface with final overload fracture. The higher magnification views, especially in Figures 136 and 137 clearly show the array of subgrains located on the main fracture surface, the brittle separation of the subgrains with no evidence of plastic deformation and the initiation of secondary stress corrosion cracks at the subgrain boundaries.

4.3.5 Stress corrosion crack growth activation energy determinations in distilled water, NSAV and 3% NaCl for double cantilever beam specimens.

The results of crack growth rate versus stress intensity determinations on DCB specimens for double distilled water, NSAV and 3% NaCl environments have been reported and are shown in Figures 109, 110, 111 respectively. It has been noted previously that, unless special precautions are taken with the experimental technique, the effect of a chloride environment on crack growth rate is only marginal in DCB specimens. However, in order to make comparisons under similar experimental conditions, the results of activation energy determinations presented here are for specimens with "pop-in" starter cracks.

The experimental crack growth rate data used for activation energy determination in the three environments is given in Table 14.

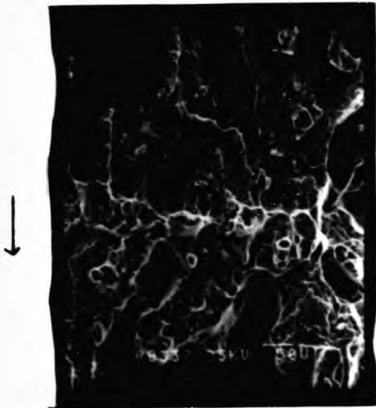


Fig 131 Specimen 13, SC crack/overload failure interface.



Fig 132 Specimen 13, subgrain SC cracking.



Fig 133 Specimen 13, brittle intergranular nature of subgrain SC cracking.

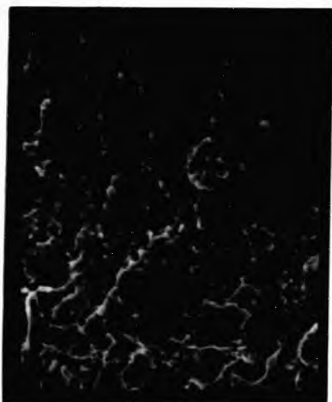


Fig 134 Specimen 13
crack/overload
failure interface.



Fig 135 Specimen 13 sub-
grain SC cracking.



Fig 136 Specimen 13,
brittle, inter-
granular nature of
subgrain SC cracking.



Fig 137 Specimen 13,
brittle nature of
subgrain SC crack-
ing.

Specimen No.	Environment	Temperature °C	Basis	Crack growth rate (ms ⁻¹)
9	H ₂ O	30	Plateau	2.4 x 10 ⁻⁹
10	H ₂ O	50	Plateau	1.0 x 10 ⁻⁸
3	H ₂ O	70	Plateau	1.25 x 10 ⁻⁷
6	H ₂ O	90	Plateau	3.0 x 10 ⁻⁷
11	WSAV	30	Plateau	3.9 x 10 ⁻⁹
12	WSAV	50	Plateau	1.5 x 10 ⁻⁸
1	WSAV	70	Plateau	1.5 x 10 ⁻⁷
4	WSAV	90	Plateau	2.5 x 10 ⁻⁷
7	3%NaCl	30	Plateau	1.7 x 10 ⁻⁹
8	3%NaCl	50	Plateau	2.2 x 10 ⁻⁸
2	3%NaCl	70	Plateau	1.5 x 10 ⁻⁷
5	3%NaCl	90	Plateau	5.0 x 10 ⁻⁷
9	H ₂ O	30	Stage I at 5KMNm ^{-3/2}	3.2 x 10 ⁻¹⁰
10	H ₂ O	50	Stage I at 5KMNm ^{-3/2}	4.5 x 10 ⁻⁹
3	H ₂ O	70	Stage I at 5KMNm ^{-3/2}	7.2 x 10 ⁻⁹
11	WSAV	30	Stage I at 6KMNm ^{-3/2}	3.0 x 10 ⁻¹⁰
12	WSAV	50	Stage I at 6KMNm ^{-3/2}	8.75 x 10 ⁻⁹
1	WSAV	70	Stage I at 6KMNm ^{-3/2}	6.65 x 10 ⁻⁸
7	3%NaCl	30	Stage I at 4KMNm ^{-3/2}	7.8 x 10 ⁻¹¹
8	3%NaCl	50	Stage I at 4KMNm ^{-3/2}	1.4 x 10 ⁻⁹
2	3%NaCl	70	Stage I at 4KMNm ^{-3/2}	8.0 x 10 ⁻⁸

Table 14 Activation energy data for SC crack growth in double distilled water. WSAV and 3%NaCl for DCB specimens, based upon plateau and Stage I velocities.

The data in Table 14 is presented as activation energy plots in Figure 138 for double distilled water, Figure 139 for WSAV and Figure 140 for 3% NaCl. Activation energies based upon both stage I crack growth rate at a constant stress intensity⁶³ and upon the plateau velocity have been calculated. The activation energies for SC crack growth for each environment during stage I and stage II are given in Table 15.

Crack growth rate data for region I of specimens tested at 90 °C have been omitted as the region I curves at 70 °C and 90 °C are not clearly distinguished in all three environments (see Section 4.3.1 (5)).

Environment	Basis	Activation energy ⁻¹ (kJ mole ⁻¹)
H ₂ O	Stage I at 5MPa ^{-3/2}	73.9
H ₂ O	Plateau velocity	74.8
WSAV	Stage I at 6.5MPa ^{-3/2}	114.7
WSAV	Plateau velocity	74.2
3%NaCl	Stage I at 4MPa ^{-3/2}	149.6
3%NaCl	Plateau velocity	89.0

Table 15. Activation energies for SC crack growth in double distilled water, WSAV and 3%NaCl for DCB specimens.

The results of activation energy determinations for both CT and DCB specimens are discussed in Section 5.

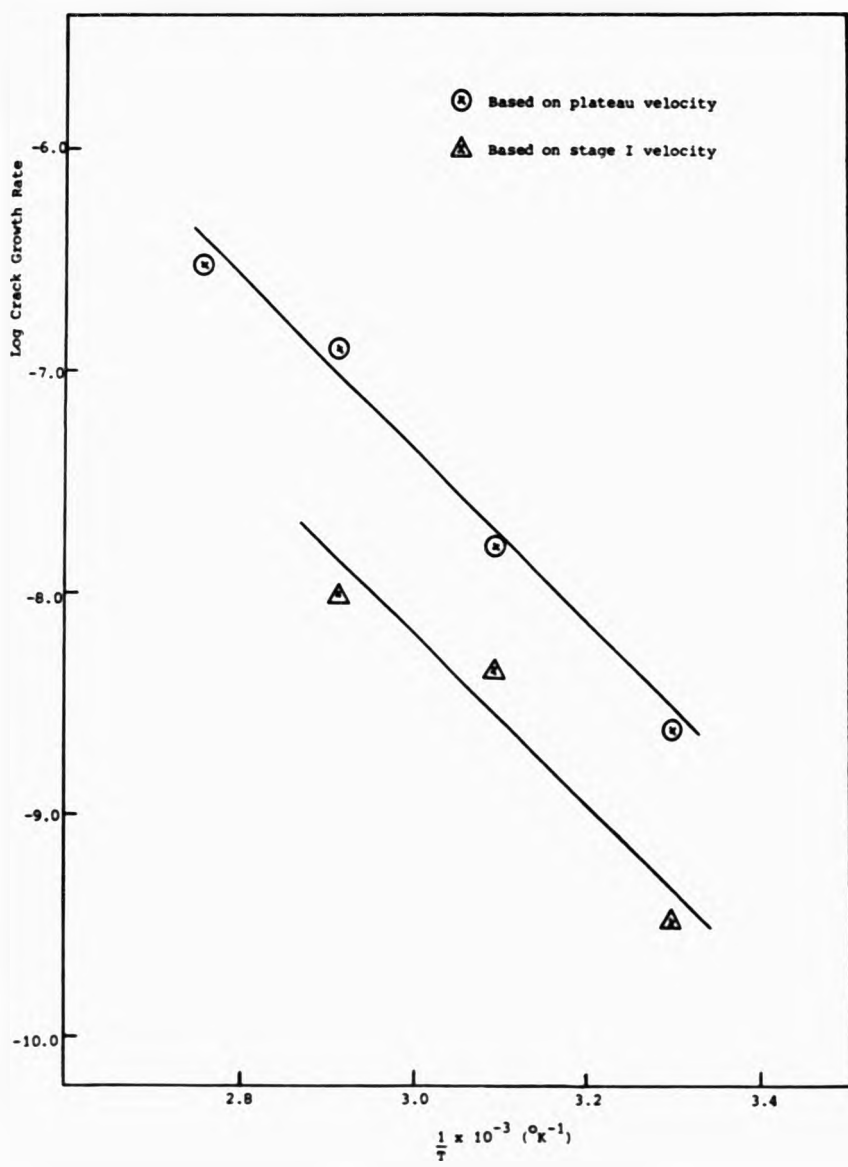


Fig 138 Activation energy plot for SC crack growth in double distilled water using DCB specimens.

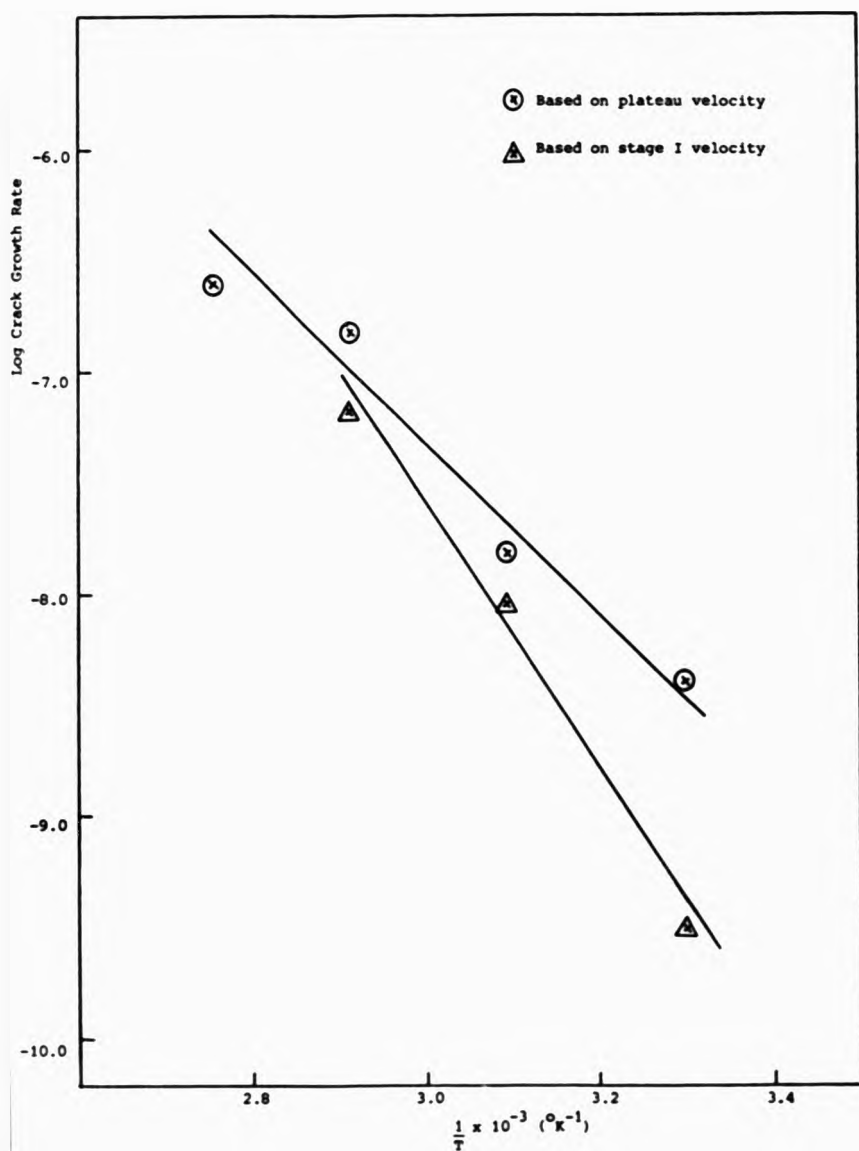


Fig 139 Activation energy plot for SC crack growth in WSAV using DCB specimens.

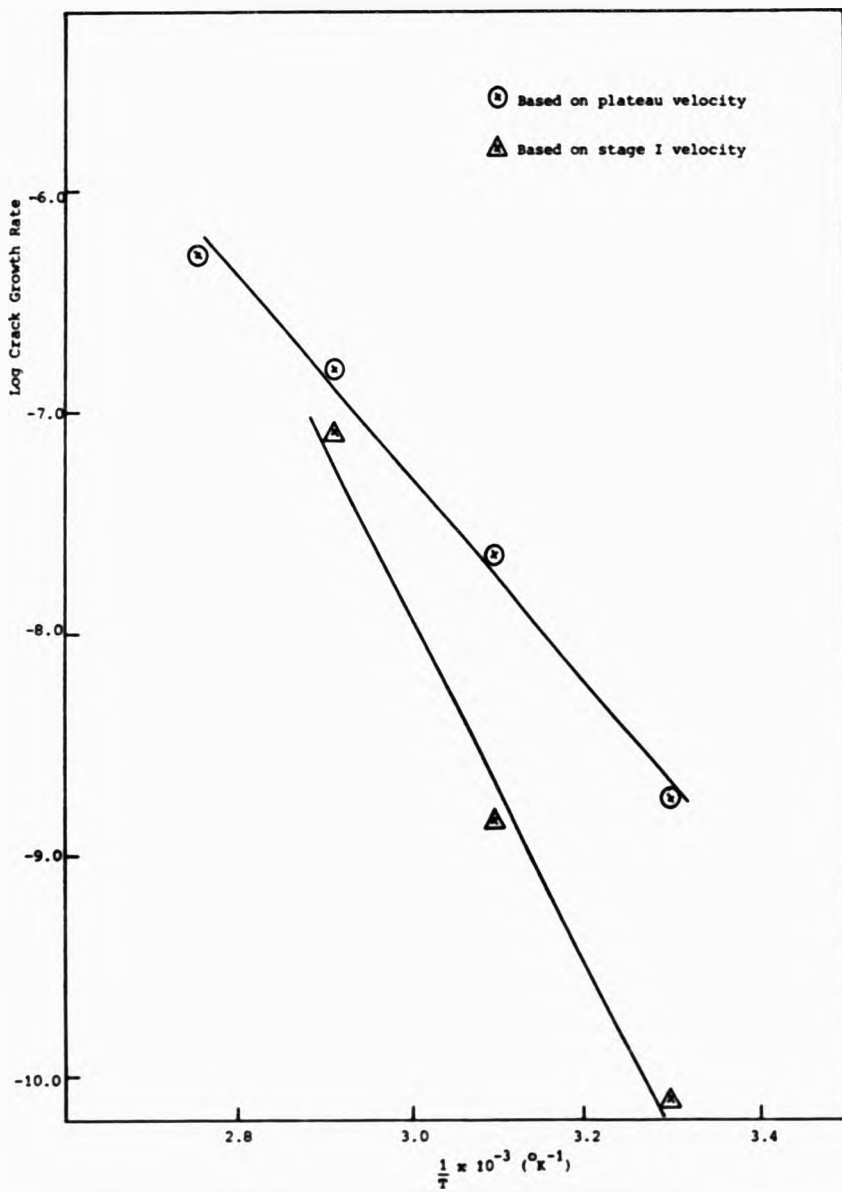


Fig 140 Activation energy plot for SC crack growth in 3%NaCl using DCB specimens.

4.4 HYDROGEN DIFFUSION EXPERIMENTS

4.4.1 Electrochemical hydrogen permeation experiments on EN8 steel - proving the technique.

As discussed previously (Section 3.2.3), it was thought necessary to validate the experimental equipment and technique developed for hydrogen diffusion experiments on steel coupons (made from EN8 steel; nominal composition Fe - 0.4%C - 0.25%Si - 0.80%Mn - 0.05%S - 0.05%P, and supplied in the normalised condition) prior to performing hydrogen diffusion experiments on AlZnMg coupons.

A series of experiments were performed on an EN8 coupon 0.13 mm thick over a range of cathodic charging current densities. Cathodic charging and the hydrogen permeation current analysis were both performed in pre-electrolysed 0.1M NaOH at room temperature. The anodic potential was held at +440 mV vs SHE during analysis as this corresponds to the plateau in the permeation current versus anodic potential curve¹⁷⁷, ensuring that all hydrogen atoms diffusing through the membrane are ionised and recorded as a permeation current. At higher anodic potentials (above + 850 mV) Sehmbhi¹⁷⁷ found that oxygen evolution on the membrane made a contribution to the total permeation current recorded. After plating palladium onto the analysis side of the mild steel membrane, the polarity of the membrane was reversed in order to reduce the hydrogen content of the membrane caused by the plating operation. Oxidation of residual hydrogen continued until the background current passing between the exposed surface area of the permeation specimen and the counter electrode in the potentiostatic analysis circuit had dropped to approximately 1 μamp (0.566 $\mu\text{A cm}^{-2}$).

The permeation transients are shown in Figure 141 and the results are presented in Table 16. Table 17 shows the diffusion coefficients calculated on the basis of breakthrough time, rise time and time lag, in accordance with equations 3.17, 3.18 and 3.15 respectively.

The background currents recorded in the potentiostatic analysis circuit ranged from 0.2 μ amps (0.113 mA cm⁻² charging current density experiment) to 2.8 μ amps (0.566 mA cm⁻² charging current density experiment).

As discussed in the experimental procedure (Section 3.3.5.4), the steel specimens were plated with a thin layer of palladium on the side of the specimen that would be in the anodic compartment of the permeation cell. This procedure is adopted in electrochemical permeation experiments in order to prevent anodic dissolution or passivation of the specimens without materially decreasing the permeation rate of hydrogen through the membrane.¹⁷⁷

It was intended that the electrochemical permeation experiments on AlZnMg coupons would be performed with a palladium coating thickness increased by a factor of either two or five (4 and 10 ml of 200 mg l⁻¹ palladium chloride, [1.128 x 10⁻³ M PdCl₂, and assuming that the increased plating times resulted in the deposition of the theoretical quantity of palladium] added to the anode compartment for plating onto the specimen prior to the permeation experiment). A further experiment on an EN8 steel

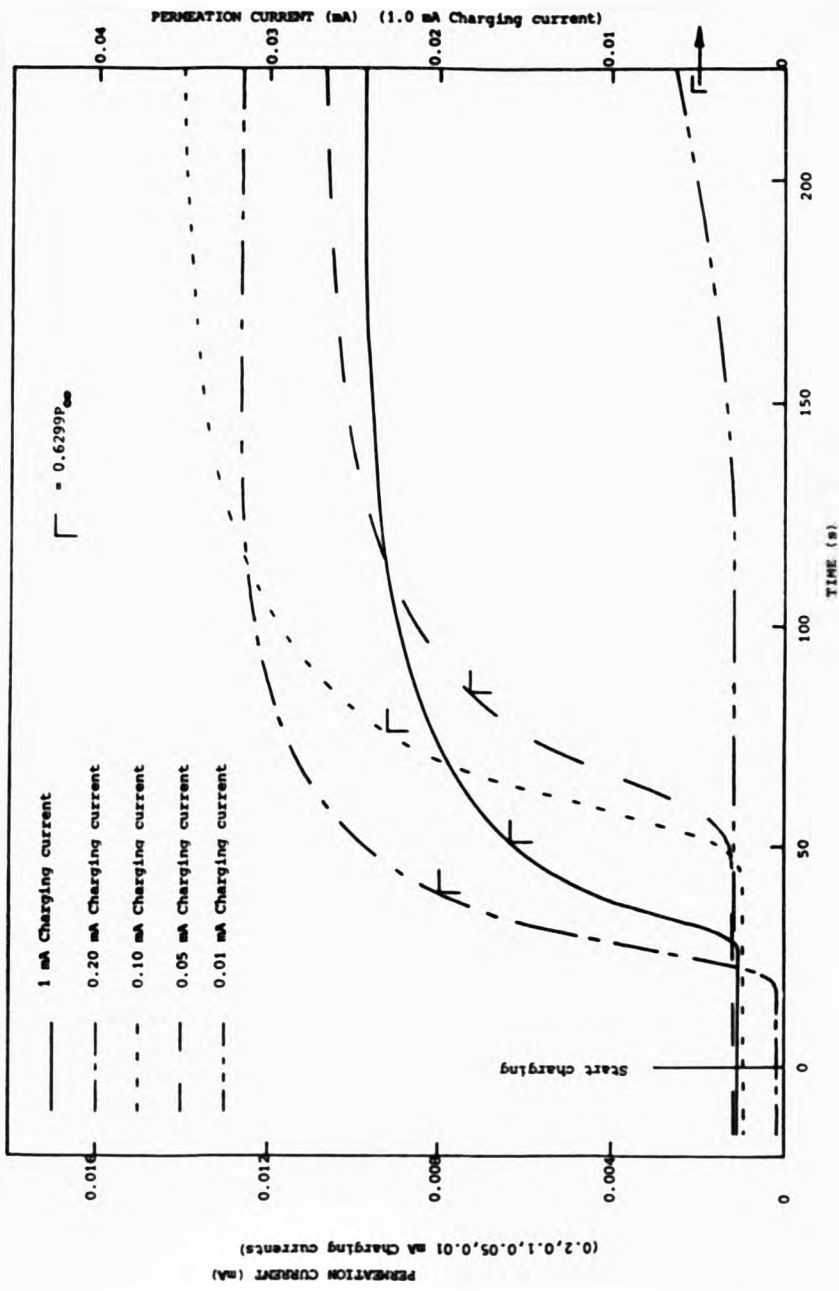


Fig 141 Permeation transients for hydrogen diffusion through an EN8 steel coupon over a range of charging current densities.

I_{charge} (mA)	Charging current density (mA cm ⁻²)	$T_{\text{breakthrough}}$ (S)	I_{max} (mA) (on 1.767 cm ² membrane)	$T_{\text{O, rise}}$ time (S)	T_{L} , time lag (= $T_{\text{D}} + T_{\text{O}}$) (S)
1	0.566	28	0.0234	23	51
0.2	0.113	18	0.0126	22	40
0.1	0.057	43	0.0130	34	77
0.05	0.028	50	0.0097	35	85
0.01	0.006	130	0.0030	134	264

Table 16 Results of hydrogen diffusion experiments on KNS steel using the electrochemical permeation technique.

I_{charge} (mA)	Charging current density (mA cm ⁻²)	Breakthrough time diffusion coefficient (cm ² s ⁻¹)	Rise time diffusion coefficient (cm ² s ⁻¹)	Time lag diffusion coefficient
1	0.566	3.945×10^{-7}	7.445×10^{-7}	5.523×10^{-7}
0.2	0.113	6.137×10^{-7}	7.783×10^{-7}	7.042×10^{-7}
0.1	0.057	2.569×10^{-7}	5.036×10^{-7}	3.658×10^{-7}
0.05	0.028	2.209×10^{-7}	4.892×10^{-7}	3.314×10^{-7}
0.01	0.006	0.850×10^{-7}	1.278×10^{-7}	1.067×10^{-7}

Table 17 Hydrogen diffusion coefficients calculated on the basis of breakthrough time, rise time and time lag for electrochemical permeation experiments on KNS steel.

Plating conditions	I_{charge} mA	Charging c.d. (mAcm ⁻²)	$T_{\text{breakthrough}}$ (s)	I_{max} (mA) (on 1.767 cm ² membrane)	$T_{\text{c, rise}}$ time (s)	T_{L} , time lag (= $T_{\text{b}} + T_{\text{o}}$) (s)
A) A further 2ml 1.128 x 10 ⁻³ M PdCl ₂ plated at 30mAcm ⁻² 1 minute then at 3mAcm ⁻² 3 minutes	0.205	0.116	112	0.0143	66	178
B) A further 6ml 1.128 x 10 ⁻³ M PdCl ₂ plated at 10mAcm ⁻² 1 minute then at 3mAcm ⁻² 10 minutes	0.190	0.107	139	0.0121	79	218

Table 18 Results of hydrogen diffusion experiments on EN8 steel with varying palladium plating thicknesses on the anodic side of the specimen.

Plating Condition	Breakthrough time diffusion coefficient (cm ² s ⁻¹)	Rise time diffusion coefficient (cm ² s ⁻¹)	Time lag diffusion coefficient (cm ² s ⁻¹)
A) 2ml 1.128 x 10 ⁻³ M PdCl ₂	0.986 x 10 ⁻⁷	2.594 x 10 ⁻⁷	1.582 x 10 ⁻⁷
B) 2 + 6ml 1.128 x 10 ⁻³ M PdCl ₂	0.795 x 10 ⁻⁷	2.168 x 10 ⁻⁷	1.292 x 10 ⁻⁷

Table 19 Hydrogen diffusion coefficients calculated on the basis of breakthrough time, rise time and time lag with varying palladium plating thickness on the anodic side of the specimen.

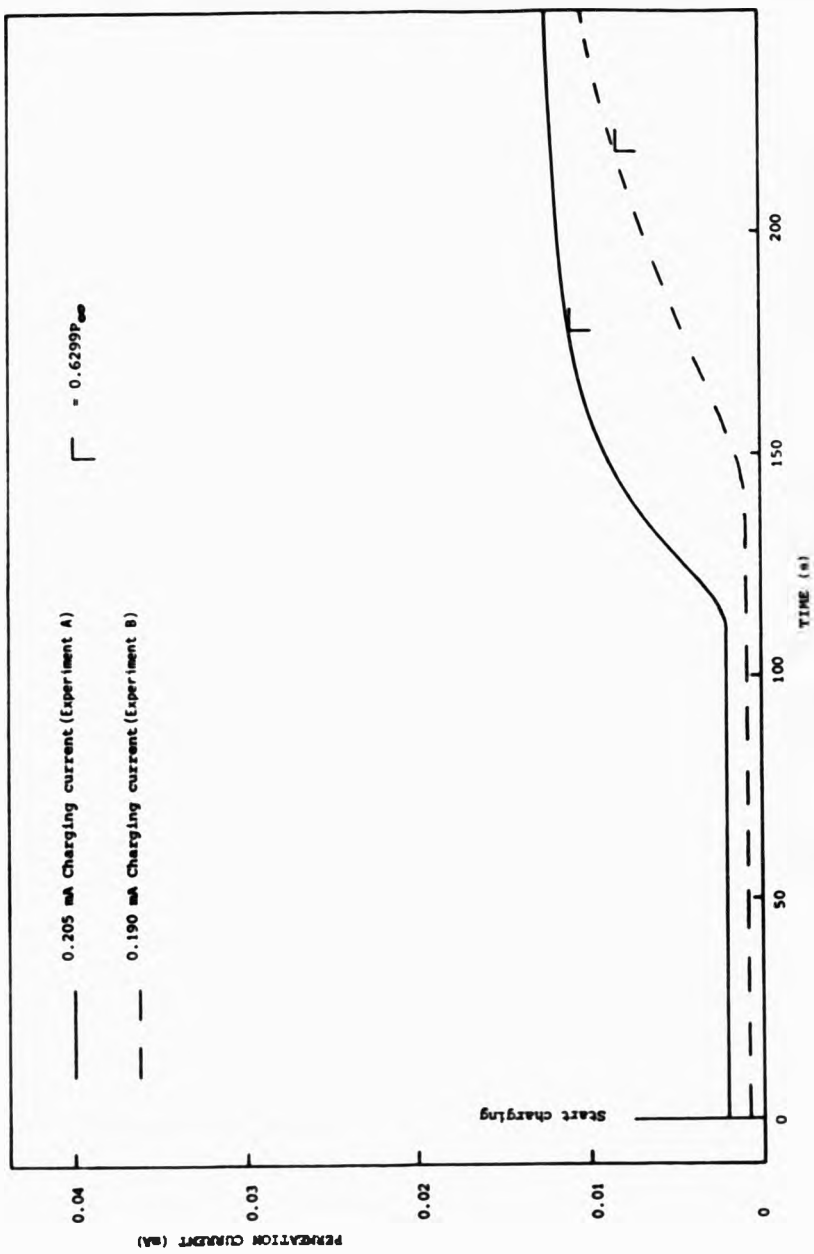


Fig 142 Permeation transients for hydrogen diffusion through an EN8 steel coupon with varying palladium plating thickness on the anodic side of the specimen.

specimen was therefore performed to assess the extent to which this increased palladium coating thickness affects the permeation rate.

The permeation transients are shown in Figure 142 and the results are presented in Table 18. Table 19 shows the diffusion coefficients calculated on the basis of breakthrough time, rise time and time lag.

The following results were obtained by Washash¹⁷⁸ on an EN2 steel specimen (nominal composition Fe - 0.15%C - 0.25%Si - 0.8%Mn - 0.05%S - 0.05%P and supplied in the normalised condition) where hydrogen charging and analysis were both performed in 0.1M NaOH (Table 20). These results show a good agreement with the current work.

Charging current (mA)	Charging current density (mA cm ⁻²)	Time lag diffusion coefficient (Washash ¹⁷⁹ , EN2 steel) (cm ² s ⁻¹)	Current work-time lag diffusion coefficient, EN2 steel (cm ² s ⁻¹)
1	0.566	4.23×10^{-7}	5.523×10^{-7}
0.1	0.057	2.27×10^{-7}	3.658×10^{-7}
0.01	0.006	1.19×10^{-7}	1.067×10^{-7}

Table 20 Comparison of hydrogen diffusion coefficients in mild steel obtained by electrochemical permeation.

The diffusion coefficients calculated from the permeation transients show an anomalously high value at a charging current

density of 0.113 mA cm^{-2} , and a slightly lower maximum permeation current I_{max} of 0.0126 mA , compared with I_{max} of 0.0130 mA at a charging current density of 0.057 mA cm^{-2} (see Tables 16 and 17).

The effect of increased palladium plate thickness is to reduce the measured diffusion coefficients from approximately $7.0 \times 10^{-7} \text{ cm}^2 \text{ s}^{-1}$ to approximately $1.6 \times 10^{-7} \text{ cm}^2 \text{ s}^{-1}$ for a two fold increase in thickness and $1.3 \times 10^{-7} \text{ cm}^2 \text{ s}^{-1}$ for a five fold increase in thickness, all based upon the time lag value. The reported²⁰⁴ diffusion coefficient of hydrogen in palladium is $1.3 \times 10^{-7} \text{ cm}^2 \text{ s}^{-1}$. It is clear that a measurable reduction in the hydrogen diffusion coefficient in steel has occurred which probably results from doubling the palladium plate thickness, however this reduction becomes smaller for a further 2.5 times increase in palladium thickness. However, for the purposes of electrochemical permeation of hydrogen in AlZnMg alloys where the expected diffusion coefficients, obtained by other techniques, lie in the range $2 \times 10^{-9} \text{ cm}^2 \text{ s}^{-1}$ to $5 \times 10^{-10} \text{ cm}^2 \text{ s}^{-1}$ (Section 2.5.7.3), a five fold increase in palladium thickness would not materially affect measured diffusion coefficients. As an increased palladium thickness would be expected to have a beneficial effect in reducing anodic dissolution of the AlZnMg specimen it was decided initially to increase the electroplated palladium thickness on AlZnMg specimens by a factor of five.

The results on the EN8 steel specimens demonstrated that the electrochemical hydrogen permeation equipment assembled was functioning correctly.

4.4.2 Electrochemical hydrogen permeation experiments on Al-Sn-Mg coupons.

There are two immediately apparent problems in attempting to measure electrochemical hydrogen permeation transients in aluminium based alloys.

157,158
Firstly, the reported diffusion coefficients in aluminium
86,160 and AlZnMg alloys of between 8×10^{-12} and 1×10^{-9} $\text{cm}^2 \text{s}^{-1}$
for pure aluminium at 70 C and of between 1×10^{-10} and
 2×10^{-9} $\text{cm}^2 \text{s}^{-1}$ for AlZnMg alloys at room temperature, would
indicate that diffusion experiments would take a long time and
that the permeation currents recorded due to hydrogen diffusion
would be low. This would necessitate a high sensitivity in the
potentiostatic analysis circuit, along with a background current
due to specimen corrosion at least an order of magnitude lower
than the expected hydrogen diffusion current.

Secondly, the length of time over which the AlZnMg membrane is anodically polarised would make the specimen prone to general dissolution or pitting corrosion before a hydrogen permeation current is recorded.

The following is a summary of the results obtained from the electrochemical hydrogen permeation experiments on AlZnMg alloy coupons. All potentials are with respect to the Standard Hydrogen Electrode (SHE).

Experiment No 1 - Summary

Membrane thickness - 0.10 mm
Hydrogen charging solution - Water Saturated Air Vapour at 70 °C
Anodic cell (analysis) solution - 0.1M Na₂SO₄
Anodic cell pH - 6.8
Temperature in analysis cell - 24 to 27 °C
Anodic potential in analysis cell - +230 mV
Anodic circuit background current - varying around 0.6 - 1.0 mA
(0.34 - 0.57 mA cm⁻²)
Duration of experiment - 114.33 hours

Results - pitting of the AlZnMg coupon from the anodic side of the membrane resulted in loss of solution to the cathodic compartment. The palladium electroplate prior to the diffusion experiment is shown in Figure 143. A streaky deposit was obtained because the plating conditions were outside the practical current density range. Stirring of the plating solution in later experiments improved the visual quality of the palladium electrodeposit by bringing the current density used into the practical current density range for the plating solution employed.

Pitting of the coupon was extensive, and from the anodic current versus time graph the coupon had been perforated for 2.7 hours prior to the coupon being retrieved. The increase in current observed when the pitting of the membrane allowed solution into

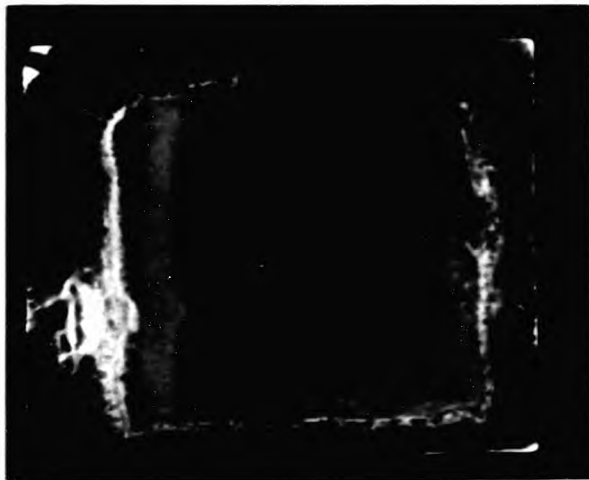


Fig 143 Palladium electroplate on AlZnMg alloy hydrogen permeation coupon No 1.

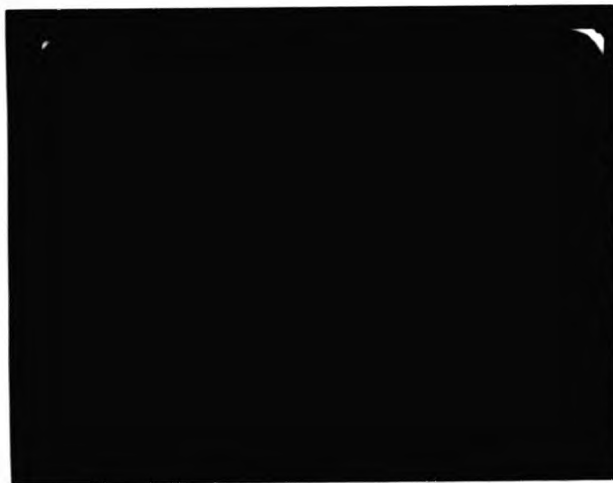


Fig 144 Palladium electroplate on AlZnMg alloy hydrogen permeation coupon No 2.

the charging cell (the charging cell has previously contained only a few cm³ of water to produce the NSAV environment) resulted from corrosion of the unplated side of the coupon in the charging cell as a result of ingress of solution from the analysis cell. The current transient that was obtained at the end of the experiment is shown in Appendix A, Figure 195.

For reasons discussed later (Section 4.4.2.1), the background current in the analysis cell is too high to measure a hydrogen permeation current. It was therefore decided to use a solution of 50 gl Boric Acid + 0.4 gl Ammonium Hydrogen Tetraborate in the anodic cell. This solution is used in barrier layer anodising of capacitor foils. When aluminium is anodically polarised in the above solution an anodic film thickness of the order of 10 - 14Å per volt is obtained¹⁹⁷. In the context of electrochemical hydrogen diffusion experiments on AlZnMg alloys, the use of a boric acid solution would enable a non porous oxide film to grow at defects in the palladium electroplate rather than corrosion of the AlZnMg coupon. This would reduce the background current in the analysis cell to a level where the current due to the hydrogen permeation transient could be detected above the background current. The solution pH was adjusted up to pH 6.3 with additions of 0.1 M NaOH in order to increase the conductivity of the solution from $4.7 \times 10^{-3} \text{ S m}^{-1}$ (Boric acid 50 gl + Ammonium Hydrogen Tetraborate 0.4 gl) to 0.65 S m^{-1} .

Experiment No 2 - Summary

Membrane thickness - 0.20 mm
Hydrogen charging solution - Water Saturated Air Vapour 70 C
Anodic cell (analysis) - Boric acid 50 gl + Ammonium Hydro-
solution gen Tetraborate 0.4 gl
Anodic cell pH - 6.3 (adjusted with 0.1 M NaOH)
Temperature in analysis cell - 22 - 24 C
Anodic potential in analysis cell - +90 mV
Anodic circuit background current - 2.0 - 4.7 μA
(1.13 - 2.66 $\mu\text{A cm}^{-2}$)
Duration of experiment - 380.75 hr

Results - The use of a boric acid solution in the analysis cell had reduced the background current by over two orders of magnitude, however after just over 380 hours, no permeation transient had been detected. No pitting of the membrane was visible to the naked eye.

Calculations of the expected breakthrough time and hydrogen permeation current (see Section 4.4.2.1) indicated that the expected breakthrough time based upon a time lag equation (3.15) and the reported diffusion coefficients would be between 9.4 and 185.2 hours and that after 22.5 days the expected permeation current due to hydrogen diffusion (at 70 C from the NSAV reaction) would be 0.01 μA for the size of permeation membrane employed (0.00566 $\mu\text{A cm}^{-2}$). It was clear therefore that the experimental conditions of the second permeation experiment would

not show a permeation transient with an anodic circuit background current of around 3.5 μA . The effect of attempting to increase the hydrogen fugacity on the charging side of the membrane by electrochemical charging with a current of 1 mA (current density 0.566 mA cm^{-2}) was investigated. However, whilst pitting of the membrane on the anodic side was not visible, the addition of 0.1 M H_2SO_4 to the cathodic cell and energising of the charging circuit resulted in an immediate increase in the background current in the analysis circuit and visible perforation of the membrane. This indicated that the membrane had been perforated in a number of locations and that the increase in current observed was due to solution interaction effects. Alternatively the increase in current observed indicated that the current density on the cathodic side of the membrane was not sufficient to cathodically protect the specimen and corrosion on the cathodic (charging) side of the membrane occurred. This corrosion combined with the presence of pits that had not perforated on the anodic (analysis) side of the membrane, resulted in rapid perforation and solution interaction effects.

The current transient that was obtained at the end of the experiment is shown in Appendix A, Figure 196. The palladium electroplate prior to the diffusion experiment is shown in Figure 144. Agitation of the plating solution has resulted in a deposit of more uniform appearance in the central section of the membrane.

A third experiment was performed in which the membrane was electrochemically charged at a current density of 0.566 mA cm^{-2} on the cathodic side from a solution of Boric acid (50 gl^{-1}) + Ammonium Hydrogen Tetraborate (0.4 gl^{-1}) + concentrated Sulphuric Acid (1 cm^3 in volume of charging cell - H_2SO_4 concentration 0.1 M). The experiment would show the effect of electrochemical charging with hydrogen over hydrogen charging of the membrane as a result of the AlZnMg reaction with NSAV at 70°C . The membrane thickness was increased to 0.25 mm and the charging cell was kept at room temperature.

Experiment No 3 - Summary

Membrane thickness	- 0.25 mm
Hydrogen charging solution	- Boric acid 50 gl^{-1} + Ammonium Hydrogen Tetraborate 0.4 gl^{-1} + conc H_2SO_4 1 cm^3 in volume of charging cell.
Charging current density	- 0.566 mA cm^{-2}
Anodic cell (analysis) solution	- Boric acid 50 gl^{-1} + Ammonium Hydrogen Tetraborate 0.4 gl^{-1}
Anodic cell pH	- 6.4 (adjusted with 0.1 M NaOH)
Temperature in analysis cell	- $19 - 21^\circ \text{C}$
Anodic potential in analysis cell	- $+100 \text{ mV}$
Anodic circuit background current	- $1.0 - 3.5 \text{ }\mu\text{A}$ ($0.57 - 1.98 \text{ }\mu\text{A cm}^{-2}$)
Duration of experiment	- 176.53 hr

Results - The addition of sulphuric acid to the cathodic charging cell made hydrogen evolution visible on the cathodic side of the membrane surface. Pitting corrosion of the membrane caused the current transient seen after 176.53 hrs. The current transient obtained is shown in Appendix A, Figure 197. The anodic current immediately before breakthrough was $3.5 \mu\text{A}$ ($2 \mu\text{A cm}^{-2}$), and this increased after 11.81 hr to $1850 \mu\text{A}$ ($1050 \mu\text{A cm}^{-2}$) when the experiment was terminated. A general view of the anodic side of the pitted membrane is shown in Figure 145. Pitting corrosion as seen from the cathodic side of the membrane by SEM is shown in Figures 146 and 147.

A fourth experiment was performed in which the membrane was electrochemically charged at a current density of 0.566 mA cm^{-2} on the cathodic side from a $0.1 \text{ M H}_2\text{SO}_4$ solution. In this experiment the analysis potential was increased to $+400 \text{ mV}$ and the membrane thickness reduced to 0.17 mm .

Experiment No 4 - Summary

Membrane thickness	- 0.17 mm
Hydrogen charging solution	- $0.1 \text{ M H}_2\text{SO}_4$
Charging current density	- 0.566 mA cm^{-2}
Anodic cell (analysis) solution	- Boric acid 50 gl^{-1} + Ammonium Hydrogen Tetraborate 0.4 gl^{-1}
Anodic cell pH	- 6.4 (adjusted with 0.1 M NaOH)
Temperature in analysis cell	- $19 - 21 \text{ }^\circ\text{C}$
Anodic potential in analysis cell	- $+400 \text{ mV}$

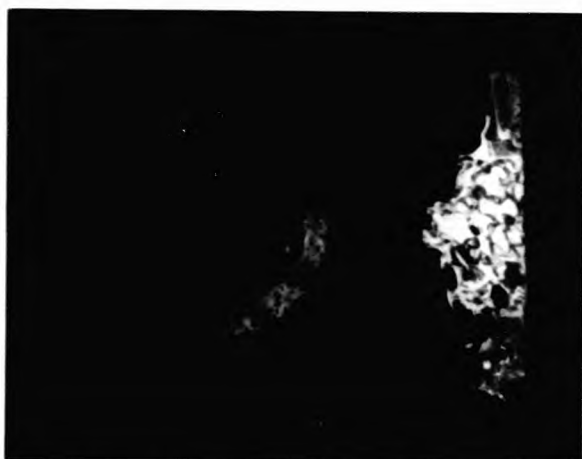


Fig 145 Electrochemical hydrogen diffusion AlZnMg coupon showing pitting corrosion through the membrane from the anodic side, experiment No 3.



Fig 146 Permeation experiment No 3 on AlZnMg, showing pitting corrosion as seen from the cathodic side of the membrane.

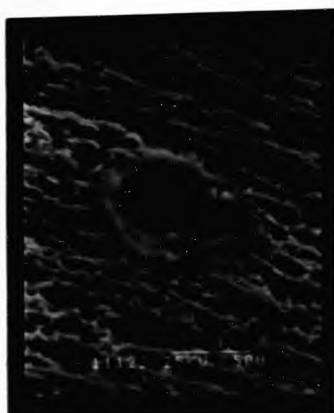


Fig 147 Permeation experiment No 3 on AlZnMg, showing a pit perforating the membrane as seen from the cathodic side of the membrane.

Anodic circuit background - 9 - 41 μA
current (5.09 - 23.20 $\mu\text{A cm}^{-2}$)
Duration of experiment - 5.93 hrs

Results - Increasing the potential of the analysis side of the membrane in the anodic direction increased the pitting corrosion rate from $1.4 \times 10^{-3} \text{ mm hr}^{-1}$ in experiment No 3 (anodic potential + 100 mV) to $2.9 \times 10^{-2} \text{ mm hr}^{-1}$ in this experiment (anodic potential + 400 mV). Pitting rates given here are the time to perforation of the membrane and therefore represent the fastest pitting rate observed.

The background current has also increased by just over an order of magnitude. The current transient obtained is shown in Appendix A, Figure 198. The anodic side of the membrane is shown in Figure 148 and the cathodic side of the membrane is shown in Figure 149. There is a tendency for the pitting corrosion reaction to take place preferentially around the edges of the specimen where a crevice forms between the specimen, the rubber "O" ring and the glass cell, or where the geometry at this point results in a specimen potential at the edge which is still in the active region resulting in an enhanced corrosion rate. SEM photographs of the anodic side of the membrane are shown in Figures 150 and 151 which show clearly the pits formed on the anodic side of the membrane. The experiment was terminated by the pitting corrosion of the coupon, but at the anodic potential employed, the background current was too high to record a permeation transient.

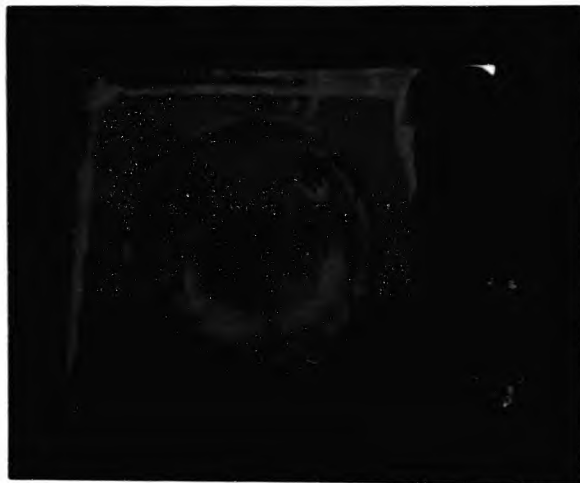


Fig 148 Electrochemical hydrogen diffusion AlZnMg coupon showing pitting corrosion through the membrane from the anodic side, experiment No 4.

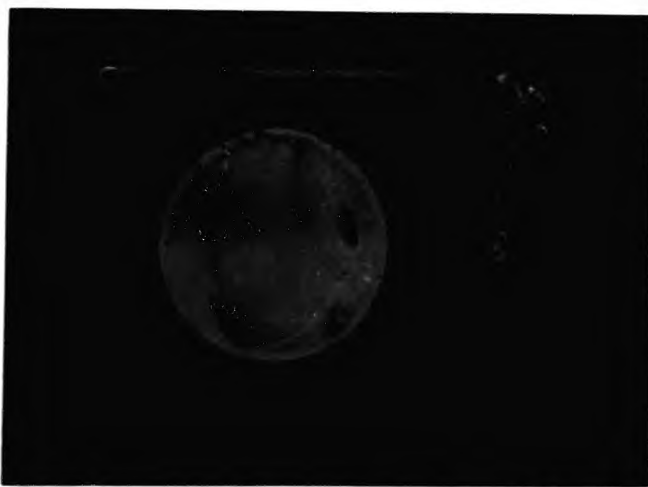


Fig 149 Electrochemical hydrogen diffusion AlZnMg coupon - cathodic side of membrane, experiment No 4.

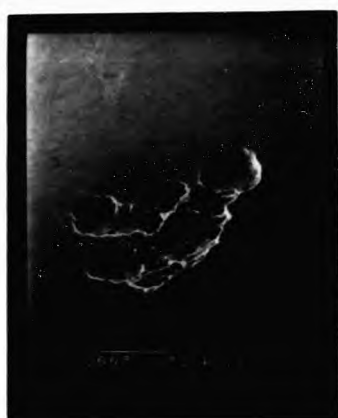


Fig 150 Permeation experiment No 4 on AlZnMg, showing pitting corrosion on the anodic side of the membrane.



Fig 151 Permeation experiment No 4 on AlZnMg, showing high magnification view of a pit formed on the anodic side of the membrane.



Fig 152 Electrochemical hydrogen diffusion AlZnMg coupon showing pitting corrosion that has not perforated the 0.85 mm thick membrane, experiment No 5.

A final experiment was performed in an enclosed container provided with heating elements to enable both cells of the electrochemical permeation apparatus to be maintained at 70 °C. Silver/silver chloride reference electrodes were used for this experiment as they provide a more accurate reference potential at elevated temperatures than mercury/mercurous sulphate reference electrodes¹⁹⁸. The objective of this experiment was to determine whether the hydrogen generated from the reaction of AlZnMg with 3% NaCl at 70 °C (see Section 4.5), whilst the whole membrane was kept at 70 °C to increase the diffusion rate and permeation of hydrogen in AlZnMg, would result in a detectable permeation transient. The anodic cell membrane potential was also made less positive, but kept above the hydrogen oxidation reaction potential by +500 mV at pH 7, in an attempt to further reduce corrosion of the membrane.

Experiment No 5 Summary

Membrane thickness	- 0.85 mm
Hydrogen charging solution	- 3% NaCl at 70 °C
Anodic cell (analysis) solution	- Boric acid 50 g ⁻¹ + Ammonium Hydrogen Tetraborate 0.4 g ⁻¹
Anodic cell pH	- 7.1 (adjusted with 0.1 M NaOH)
Temperature in analysis cell	- 70 °C
Anodic potential in analysis cell	- +100 mV
Anodic circuit background	- at 22 °C, 1.0 - 2.5 µA (0.57 - 1.41 µA cm ⁻²) at 70 °C, initially 180 µA (102 µA cm ⁻²) dropping to 70 µA (40 µA cm ⁻²)
Duration of experiment	- 48 hrs

Results - The background current at room temperature was lower than previously recorded, however on increasing the temperature to 70°C, the current increased to 180 μA (102 μA cm⁻²) and dropped during the course of the experiment to an approximately constant figure of 70 μA (40 μA cm⁻²). This level of background current would have swamped any effect due to hydrogen permeation where the expected current due to hydrogen is in the region of 0.01 μA (0.00566 μA cm⁻²). Pitting corrosion of the anodic side of the membrane took place but the 0.85 mm membrane did not perforate during the course of the experiment. The anodic side of the membrane is shown in Figure 152.

In conclusion therefore, whilst the rise in current observed during the permeation experiments may at first sight indicate the permeation of hydrogen through the membrane, a more detailed examination of the circumstances associated with the "permeation transients" indicates that the transient is explained by perforation or pitting of the specimen membranes. This results in a rise in current in the potentiostatic circuit as a consequence of the principal dissolution reaction;



and/or as a result of consequent solution contact effects, as a result of intermixing of the anolyte and catholyte.

A similar effect of pitting corrosion and solution contact effects during electrochemical hydrogen diffusion experiments on an 18%Ni maraging steel have been reported¹⁷⁹. In this study, if

the conclusion that the permeation transient was as a result of the dissolution reaction recorded in the potentiostatic circuit and not as a result of hydrogen permeation, Craig¹⁷⁹ concluded that the observations of electrochemical hydrogen permeation of Barth and Troiano¹⁸⁰ and Shively and Wild¹⁸², who also employed permeation techniques to demonstrate that absorption of hydrogen into high strength and austenitic stainless steels occurs during anodic polarisation, could be explained on the same grounds.

4.4.2.1 Analysis of theoretical hydrogen diffusion current levels from hydrogen diffusion coefficients and hydrogen solubilities reported for Al-Zn-Mg alloys.

The theoretical permeation current on the anodic side of the sample membrane in an electrochemical hydrogen diffusion experiment can be calculated from the following equation¹⁸³ ;

$$J_{\infty} = \frac{D(C_o - C_L)F}{L} \quad (4.2)$$

where;

J_{∞} = steady state current of permeating hydrogen (A cm⁻²)

D = diffusion coefficient (cm² s⁻¹)

L = membrane thickness (cm)

C_o = $C_{(o,t)}$ = concentration (mole cm⁻³) = $2C$ = a constant value

C_L = $C_{(L,t)}$ = concentration (mole cm⁻³) = 0

C = average concentration in the sample membrane, the solubility (mole cm⁻³).

F = Faraday's constant = 9.6487×10^4 (C mole⁻¹).

C_0 and C_L are defined with the following boundary conditions imposed on the system, i.e. $C_{(0,t)} = C_0$; $C_{(L,t)} = 0$ and $C_{(x,0)} = 0$. The theoretical permeation currents of hydrogen given here based upon solubility data are all for a membrane thickness, L , of 0.13 mm (0.013 cm), and an assumed diffusion coefficient, D , of $1 \times 10^{-10} \text{ cm}^2 \text{ s}^{-1}$. From the literature $1 \times 10^{-10} \text{ cm}^2 \text{ s}^{-1}$ is a reasonable value to use for the diffusion coefficient of hydrogen in AlZnMg type alloys at 70 C.

Tuck⁹⁸, using samples of Al-5%Mg and Al-4.5%Zn - 1.5%Mg alloy 0.5 mm thick, 6 mm in diameter and pre-exposed to WSAV at 70 C for 40 days on both sides of the sample in the case of the AlMg alloy and pre-exposed for 25 days on one side of the sample in the case of the AlZnMg alloy, obtained the following hydrogen contents.

The values are inferred from the magnesium hydride concentrations in the alloy samples as a result of pre-exposure using a differential scanning calorimetry technique.

- AlMg alloy sample - 0.005 ml H₂
- AlZnMg alloy sample - 0.001 ml H₂

Using these hydrogen solubilities, the following theoretical hydrogen permeation currents are obtained:

- AlMg alloy sample - 0.047 $\mu\text{A cm}^{-2}$
- AlZnMg alloy sample - 0.0094 $\mu\text{A cm}^{-2}$

In a separate experiment reported by Tuck⁹⁸ a sample coupon of Al - 5%Mg alloy was pre-exposed to WSAV at 70 C for 40 days (coupon size 60 x 5 x 0.5 mm), and subsequently heated at

temperatures between 400 and 500 C to evolve any hydrogen in the sample, the volume of hydrogen produced was 0.04 ml. This was taken as quantitative evidence that hydrogen produced in this temperature range is due to magnesium hydride decomposition. Using this solubility of hydrogen in an AlMg alloy, the theoretical hydrogen permeation current is $0.0353 \mu\text{A cm}^{-2}$.

For comparison, Edwards and Eichenauer¹¹⁹ have reported the following hydrogen solubilities in pure (99.999%) aluminium at 600 C, using a vacuum extraction technique. Solubilities were reported for samples before and after grain growth over a period of two months:

- solubility at 600 C, 1 mm grain size - 7.5×10^{-7} mole H per mole Al;
- solubility at 600 C, 5 mm grain size - 5.0×10^{-7} mole H per mole Al.

The decrease in solubility was attributed to the decrease in grain boundary area as a result of grain growth. The observations were explained by assuming that some of the hydrogen atoms are reversibly trapped at defects, the most likely defect being the grain boundary. The additional solubility is reduced in proportion to the decrease in defect density (grain boundary area) caused by continuous annealing at the test temperature during the course of the experiment. The true bulk solubility of hydrogen was calculated as 4.5×10^{-7} moles H per mole of aluminium by subtracting the grain boundary component.

For the 1 mm grain size material the theoretical hydrogen permeation current based upon bulk solubility at 600 C is 0.00011 $\mu\text{A cm}^{-2}$. An equivalent hydrogen permeation current can also be calculated from hydrogen diffusion experiments reported by Scamans and Tuck¹⁶⁰ in which the hydrogen content on the analysis side of the specimen membrane was measured by gas chromatography.

In the referenced experiment, hydrogen charging was by WSAV at 70 C, the specimen area was 56.25 cm^2 , the specimen thickness was 0.5 mm and the volume of the analysis side of the diffusion cell compartment was 168.75 cm^3 . The measured quantities of hydrogen permeating the membrane may be considered as equivalent hydrogen currents from the following equation:

$$J = \frac{QF}{t} \quad (4.3)$$

where;

J = equivalent current of hydrogen (amps)

Q = quantity of hydrogen detected on analysis side of membrane (moles)

F = Faraday's constant = 9.64870×10^4 (C mole⁻¹)

t = time to measure quantity of hydrogen, Q, (seconds)

The reported breakthrough time was 99.12 hours for a super pure base Al-4.3%Zn-1.5%Mg alloy aged to peak susceptibility to SCC. After 240 hours the hydrogen content in the analysis cell was 0.01% H. Based upon the average quantity of hydrogen diffusing through the membrane (4.665×10^{-14} moles H s⁻¹) and the area of

the membrane, the equivalent hydrogen permeation current is
 $0.0025 \mu\text{A cm}^{-2}$.

The equivalent hydrogen permeation current at a later stage in the same experiment (between 20 and 25 days), when the measured hydrogen content in the analysis cell rose from 0.04% H₂ to 0.06% H₂, is $0.006 \mu\text{A cm}^{-2}$ (1.095×10^{-13} moles H s⁻¹).

The equivalent hydrogen permeation current from cylindrical geometry hydrogen diffusion experiments, where hydrogen charging was by a 3% sodium chloride solution at 25°C, reported here (Section 4.4.3) and analysed on the same basis as above is $0.062 \mu\text{A cm}^{-2}$. In this experiment (No 6) the breakthrough time was 70 hours and the time to reach 4.81% H₂ within the cylinder of internal volume 2.20 cm³, internal surface area 5.34 cm² and wall thickness 0.5 mm, was 410 hours. The average quantity of hydrogen was 1.1306×10^{-12} moles H s⁻¹. This experiment, out of the six conducted, showed the highest permeation of hydrogen. The variability of the results is discussed in Section 4.4.3.

The expected current on the analysis side of an electrochemical hydrogen permeation experiment AlZnMg specimen membrane therefore is in the range from 0.0025 to $0.06 \mu\text{A cm}^{-2}$, (0.004 to 0.10 $\mu\text{A cm}^{-2}$ for an electrochemical permeation sample membrane of 1.767 cm²). This is between one and three orders of magnitude lower than the background current measured in the permeation experiments reported. It is concluded therefore that without reducing the

background current by between two and four orders of magnitude, it would not be possible to measure an electrochemical hydrogen permeation transient in an AlZnMg alloy. The lowest background currents measured of around 1 μ A, on AlZnMg alloy specimens in boric acid solutions are comparable with the level of background current obtained during the EN8 steel permeation experiments where the analysis solution was 0.1M NaOH.

Hydrogen diffusion coefficients for AlZnMg type alloys determined by an electrochemical hydrogen permeation technique have been reported in Section 2.4.7.3, reference number 86. The experiments, reported by Gest and Troiano, were for a 7075-T651 alloy with a composition Al-5.86%Zn-2.60%Mg-1.57%Cu. The experiments were performed in a hydrochloric acid solution (pH=1) without the provision of a palladium electroplate on the anodic side of the membrane since the reported objective of the experiments was to demonstrate evidence of hydrogen permeation rather than evaluate its precise level¹⁸⁴. The analysis side of the membrane was held at the zero charge potential for the alloy which is approximately -560 mV vs SHE.

Gest noted that under the experimental conditions three possible reactions could take place on the analysis side of the specimen membrane: the hydrogen oxidation reaction, the oxygen evolution reaction and the chlorine evolution reaction. Anodic dissolution of the AlZnMg membrane, which would make a significant contribution to the total current in the absence of a protective palladium electroplate, was omitted. It is likely that the

analysis potential is not sufficiently positive for oxygen evolution or chlorine evolution to make a significant or any contribution to the total current recorded. Furthermore, it is unlikely that hydrogen atoms will be oxidised to protons at this potential, which is the pre-requisite for demonstrating a hydrogen permeation current.

The results obtained by Gest are reproduced here for convenience (Figures 153 and 154) and show the reported permeation current due to hydrogen under galvanostatic charging conditions for a range of currents from 4 mA anodic to 9 mA cathodic, Figure 153, and the permeation due to hydrogen under potentiostatic charging conditions from 0 mV to -2,000 mV, vs SCE, Figure 154. Each point on the curve represents the permeation current reported by Gest for a single permeation experiment performed under the galvanostatic or potentiostatic conditions indicated on the current or applied potential axis, respectively, of the graphs.

Under constant charging conditions hydrogen permeation currents of up to $70 \mu\text{A}$ ($7.8 \mu\text{A cm}^{-2}$) were reported, irrespective of membrane thickness (at a charging current of 81 mA on a 9 cm^2 sample membrane - charging current density = 9 mA cm^{-2}). At a charging current density of 0.566 mA cm^{-2} on the 0.089 mm thick sample membrane, a hydrogen permeation current of approximately $5 \mu\text{A}$ ($0.56 \mu\text{A cm}^{-2}$) was reported. A charging current density of 0.566 mA cm^{-2} was the current density used in experiment No 3 of the present work performed under less aggressive conditions, with a sample membrane thickness of 0.25 mm. Cathodic charging at

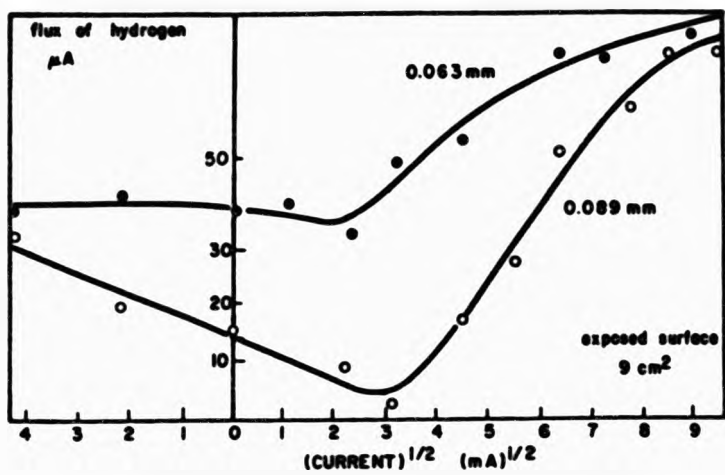


Fig 153 Hydrogen permeability under current control (After Gest). Charging current is plotted against hydrogen flux.

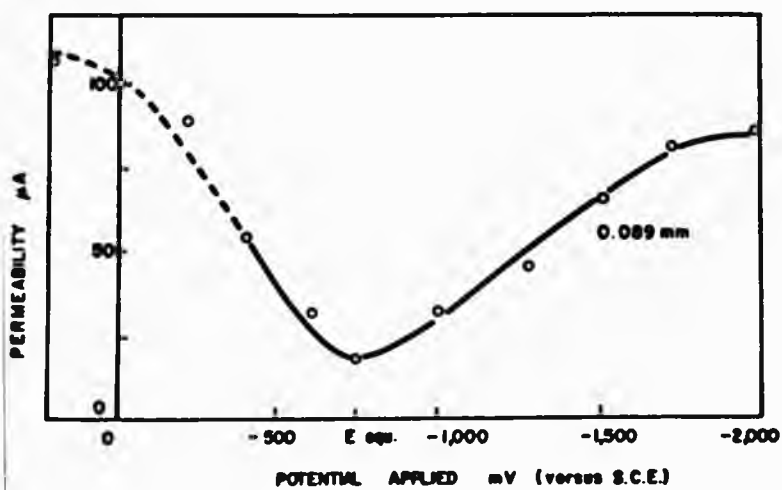


Fig 154 Hydrogen permeability under potential control (After Gest). Charging potential is plotted against hydrogen flux.

9 mA cm⁻² may effect a modest increase in the hydrogen fugacity and hence the hydrogen solubility above the levels reported by Tuck⁹⁸. This would indicate a theoretical hydrogen permeation current of 1.38 μA cm⁻² based upon a diffusion coefficient of $2 \times 10^{-9} \text{ cm}^2 \text{ s}^{-1}$ and a sample membrane thickness of 0.089 mm. Nevertheless, the hydrogen permeation current reported of 7.8 μA cm⁻² is between one and three orders of magnitude greater than would be expected. The hydrogen permeation currents are of a similar order of magnitude to that reported for an EN8 steel in Section 4.4.1 where for sample membranes 0.13 mm thick and charging current densities of 0.006 to 0.566 mA cm⁻², permeation currents of between 1.7 and 13.6 μA cm⁻² were recorded.

¹⁸⁴
Gest's original thesis does not report the actual permeation transients obtained nor the detailed condition of the samples after the permeation experiment, except to report that some pitting corrosion had taken place, and it is considered (along with the observations of Craig¹⁷⁹) that pitting corrosion of the sample membrane and solution interaction effects could have played a more significant role in his results. It is the view expressed here that the only published reference to the electrochemical permeation of hydrogen in an AlZnMg alloy should be more thoroughly investigated. This is both because of the doubt surrounding the validity of hydrogen permeation measurement using the electrochemical technique on AlZnMg alloys, and because a substantial number of published papers^{101,106,201} quote the results of Gest and Troiano by reference to their published

papers, without an in depth discussion of the thesis presenting the original results.

4.4.3 Gas chromatography hydrogen diffusion experiments using cylindrical geometry specimens.

The following experiments reported here use a cylindrical geometry to measure the amount of hydrogen diffusing from the outside surface of a hollow aluminium cylinder to the inside surface. The volume of the inside of the cylinder is sampled with a syringe and analysed by gas chromatography as discussed in Section 3.3.6. Environmental charging is by a 3% (0.5 M)NaCl solution at 25, 50 and 70 C.

The analysis of permeation transients in cylindrical geometry requires the solution of the Bessel function eigenvalue problem to obtain α_n (see equations 4.15 and 4.16). The solutions are not available in a closed form as are the solutions to diffusion in planar geometry specimens (see equations 3.15, 3.17 and 3.18), and therefore have to be evaluated numerically for any particular cylindrical geometry used. The solution to the diffusion equation in cylindrical geometry to give a value for the diffusion coefficient as a function of the breakthrough time (t_b) is therefore given here (Section 4.4.3.1).

4.4.3.1 Solution of the diffusion equation for cylindrical geometry.

For a hollow cylinder with the following boundary conditions, at the surface $r = a$ (cylinder inside radius) is maintained at concentration C_1 , $r = b$ (cylinder outside radius) at C_2 and the

concentration in the wall of the cylinder, $a \leq r \leq b$, is initially at C_0 , the concentration approaches a steady state distribution according to the expression¹⁸⁵:

$$C = \frac{C_1 \ln(b/r) + C_2 \ln(r/a) + \pi C_0 \sum_{n=1}^{\infty} \frac{J_0(a\alpha_n) U_0(r\alpha_n)}{J_0(a\alpha_n) + J_0(b\alpha_n)} e^{-D\alpha_n^2 t}}{\ln(b/a)} - \pi \sum_{n=1}^{\infty} \frac{[C_2 J_0(a\alpha_n) - C_1 J_0(b\alpha_n)] J_0(a\alpha_n) U_0(r\alpha_n)}{J_0^2(a\alpha_n) - J_0^2(b\alpha_n)} e^{-D\alpha_n^2 t} \quad (4.4)$$

In equation 4.4, α_n 's are the positive roots of the equation;

$$U_0(r\alpha_n) = J_0(r\alpha_n) Y_0(b\alpha_n) - J_0(b\alpha_n) Y_0(r\alpha_n) = 0 \quad (4.5)$$

also;

D = Diffusion coefficient ($\text{cm}^2 \text{s}^{-1}$)

t = time (s)

In equation 4.5, J_0 and Y_0 are Bessel functions of the first and second kind respectively of order zero. Setting $C_1 = C_0 = 0$, initially, for the case of diffusion into the cylinder, then:

$$C = \frac{C_2 \ln(r/a) - \pi C_0 \sum_{n=1}^{\infty} \frac{J_0(a\alpha_n) U_0(r\alpha_n)}{J_0^2(a\alpha_n) - J_0^2(b\alpha_n)} e^{-D\alpha_n^2 t}}{\ln(b/a)} \quad (4.6)$$

$$\text{Let } c' = \frac{c}{c_2} \quad (4.7)$$

$$\frac{r}{\delta r} \frac{\delta c'}{\delta r} = \frac{1}{\ln(b/a)} \cdot \frac{1}{r/a} \cdot \frac{1}{a} - \pi r \sum_{n=1}^{\infty} \frac{J_0(\alpha_n a) U_0'(\alpha_n r)}{J_0^2(\alpha_n a) - J_0^2(\alpha_n b)} e^{-D\alpha_n^2 t} \quad (4.8)$$

From Barrer¹⁸⁶:

$$\left[\frac{r}{\delta r} \frac{\delta U_0(\alpha_n r)}{\delta r} \right]_{r=0} = - \frac{2i \cdot J_0(\alpha_n b)}{\pi J_0(\alpha_n a)} \quad (4.9)$$

therefore:

$$\left[\frac{2\pi D r \delta c'}{\delta r} \right]_{r=a} = \frac{2\pi D}{\ln(b/a)} + 4D\pi \sum_{n=1}^{\infty} \frac{J_0(\alpha_n a) J_0(\alpha_n b)}{J_0^2(\alpha_n a) - J_0^2(\alpha_n b)} e^{-D\alpha_n^2 t} \quad (4.10)$$

Let Q = the amount of material diffusing into unit length of the walls of the cylindrical tube as a function of time, t .

$$\frac{Q}{2\pi c_2} = \int_a^b \left(\frac{Dr}{\delta r} \frac{\delta c'}{\delta r} \right)_{r=a} \delta t = \frac{Dt}{\ln(b/a)} + 2D \sum_{n=1}^{\infty} \frac{J_0(\alpha_n a) J_0(\alpha_n b)}{J_0^2(\alpha_n a) - J_0^2(\alpha_n b)} \frac{e^{-D\alpha_n^2 t} + K}{-D\alpha_n^2} \quad (4.11)$$

At time, $t = 0$, $Q = 0$, therefore:

$$K = 2 \sum_{n=1}^{\infty} \frac{1}{\alpha_n^2} \frac{J_0(\alpha_n a) J_0(\alpha_n b)}{J_0^2(\alpha_n a) - J_0^2(\alpha_n b)} \quad (4.12)$$

and;

$$\frac{Q}{2\pi C_2} = \frac{Dt}{\ln(b/a)} + 2 \sum_{n=1}^{\infty} \frac{1}{\alpha_n^2} \cdot \frac{J_0(\alpha_n a) J_0(\alpha_n b)}{J_0^2(\alpha_n a) - J_0^2(\alpha_n b)} \cdot (1 - e^{-D\alpha_n^2 t}) \quad (4.13)$$

The straight line asymptote of $\frac{Q}{2\pi C_2}$ is

$$\frac{Q}{2\pi C_2} = \frac{Dt}{\ln(b/a)} + 2 \sum_{n=1}^{\infty} \frac{1}{\alpha_n^2} \cdot \frac{J_0(\alpha_n a) J_0(\alpha_n b)}{J_0^2(\alpha_n a) - J_0^2(\alpha_n b)} \quad (4.14)$$

The intercept, $t = L$ on the time axis is then given by:

$$L = \frac{2 \ln(b/a)}{D} \sum_{n=1}^{\infty} \frac{1}{\alpha_n^2} \cdot \frac{J_0(\alpha_n a) J_0(\alpha_n b)}{J_0^2(\alpha_n b) - J_0^2(\alpha_n a)} \quad (4.15)$$

α_n can be computed from ¹⁸⁶;

$$\alpha_n = \frac{n\pi}{(\mu-1)} - \frac{(\mu-1)}{8\mu(n\pi)} + \left[\frac{100(\mu^3-1)}{3(8\mu)^3(\mu-1)} + \frac{1}{(8\mu)^2} \right] \frac{(\mu-1)^3}{(n\pi)^3} + \left[\frac{-32(1073)(\mu^5-1)}{5(8\mu)^5(\mu-1)} + \frac{50(\mu^3-1)}{3\mu(8\mu)^3(\mu-1)} - \frac{2}{(8\mu)^3} \right] \frac{(\mu-1)^5}{(n\pi)^5} + \dots \quad (4.16)$$

where;

$$\mu = b/a \quad (4.17)$$

$J_0(a_nb)$ and $J_0(a_na)$ are found by computer program since standard tables do not exceed numerical solutions of $J_0(x)$ for $x > 16.00$. The technique used was to determine $J_n(x)$ by generating trial values, T_k , through the use of recurrence relations¹⁸⁷. The recurrence is begun at an index m given by:

$$m = 2 \text{ INT} \left[\frac{6 + \max(n, Z) + \frac{9Z}{Z+2}}{2} \right] \quad (4.18)$$

where;

$$Z = \frac{3x}{2} \quad (4.19)$$

The initial values selected for recurrence are $T_{m+1} = 10^{-9}$, $T_{m+2} = 0$. For the function $J_n(x)$, each term T_k ($0 \leq k \leq m$) is computed by the relation,

$$T_k(x) = \frac{2(k+1)}{x} \cdot T_{k+1}(x) - T_{k+2}(x) \quad (4.20)$$

beginning with $k = m$.

$J_n(x)$ is then found by dividing the term $T_n(x)$ by the normalising constant:

$$K = T_0(x) + 2 \sum_{k=1}^{m/2} T_{2k}(x) \quad (4.21)$$

The dimensions of the cylinder used in the experiments reported here (Section 4.4.3.2) are radius $a = 0.25$ cm, radius $b = 0.30$ cm wall thickness 0.10 cm, length of cylinder 8.0 cm, thickness of base 0.10 cm, and $\rho = \frac{b}{a} = 1.2$.

The following term from equation 4.15 was evaluated numerically for $n = 1$ to 5.

$$\sum_{n=1}^{n=5} \frac{1}{\alpha_n^2} \frac{J_0(\alpha_n a) J_0(\alpha_n b)}{J_0^2(\alpha_n b) - J_0^2(\alpha_n a)} \quad (4.22)$$

n	$\frac{1}{\alpha_n^2} \frac{J_0(\alpha_n a) J_0(\alpha_n b)}{J_0^2(\alpha_n b) - J_0^2(\alpha_n a)}$
1	1.393×10^{-3}
2	-3.470×10^{-4}
3	1.548×10^{-5}
4	-8.634×10^{-5}
5	5.478×10^{-4}

$$\sum_{n=1}^{n=5} = 1.169 \times 10^{-3}$$

The value 1.169×10^{-3} is therefore a constant numerical factor for the particular cylindrical geometry given above.

The equation for the breakthrough time, t_b , for the cylindrical geometry given above is therefore:

$$t_b = \frac{2 \ln(b/a)}{D} \cdot 1.169 \times 10^{-3} \quad (4.23)$$

where;

- t_b = Breakthrough time (s)
- b = Outside radius of the hollow cylinder = 0.30 cm
- a = Inside radius of the hollow cylinder = 0.25 cm
- D = Diffusion coefficient ($\text{cm}^2 \text{s}^{-1}$)

4.4.3.2 Results of the hydrogen diffusion experiments using cylindrical geometry specimens and gas chromatography analysis.

Two sets of experiments were performed, one at ambient temperature (25 °C) and one at elevated temperatures (50 °C and 70 °C). The experimental method was as discussed in Section 3. The ambient temperature experiments were performed with a charging solution of 3% NaCl on the outside of the cylinder. The elevated temperature experiments at 50 and 70 °C were also performed with a 3% NaCl charging solution. In all experiments a control experiment was run in which an identical 7017-T651 AlZnMg cylinder was sampled through the septum and the gas analysed for hydrogen content. In the control experiment the charging solution was replaced with anhydrous magnesium perchlorate to ensure that no water or water vapour was present to react with the outside surface of the AlZnMg cylinder. Any hydrogen therefore in the gas sampled from the control cylinder is as a result of reaction between water vapour in the control cylinder

and the internal surface of the cylinder. In order to reduce to a minimum the hydrogen produced as a result of action inside the cylinder, a small quantity of anhydrous magnesium perchlorate was placed in the bottom of each cylinder.

Unlike an electrochemical hydrogen diffusion experiment, hydrogen is not continuously removed from the exit surface, but remains in the inner volume of the sample cylinder, and, secondly, measurement of hydrogen content is not continuous but is at discrete times when the internal volume of the cylinder is sampled.

The cylindrical samples for the ambient temperature experiments were machined from a block of rolled AlZnMg alloy in two principal orientations, namely short transverse and longitudinal as shown in Figure 44(ii). As hydrogen diffusion in AlZnMg alloys is thought to be grain boundary diffusion^{98,104,136}, the ambient temperature experiments, with two sets of sample cylinders machined with their principal axis in two different orientations, were designed to establish whether an effect was present in the hydrogen diffusion characteristics that was due to grain boundary orientation. The control cylinder was machined in the short transverse direction and both experiments were conducted simultaneously.

The results of the ambient temperature experiment using short transverse oriented sample cylinders are shown in Figure 155, and

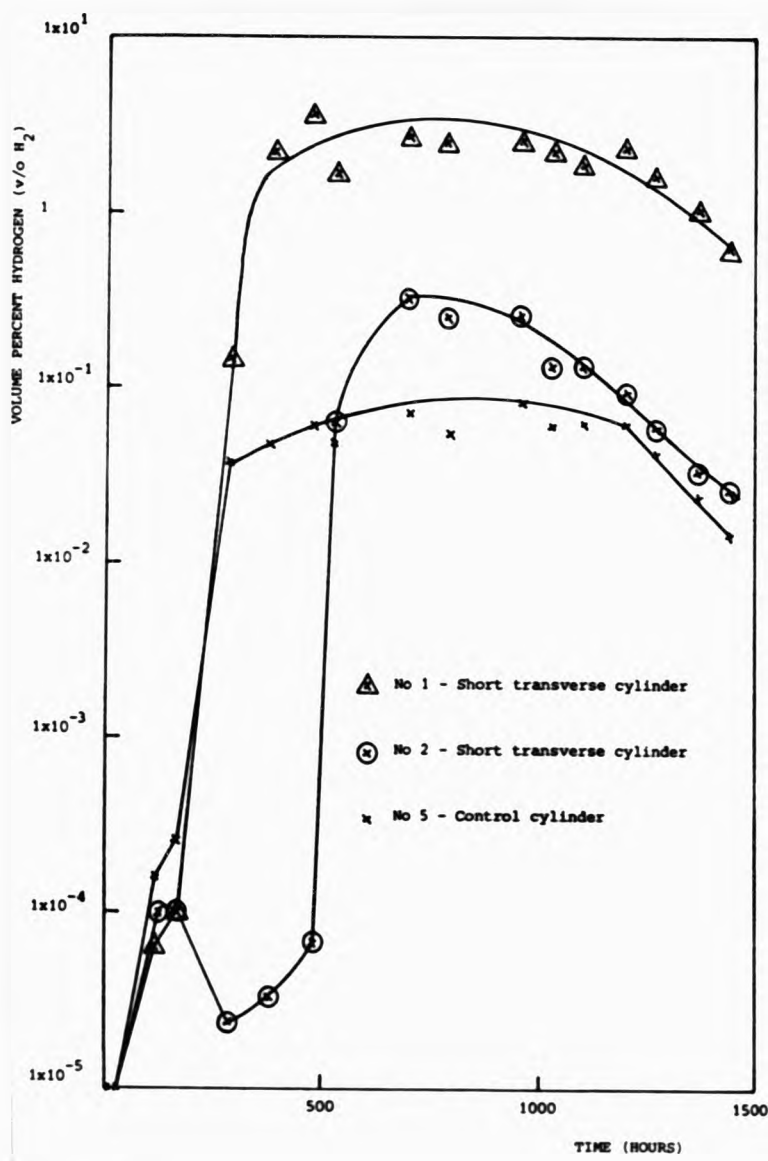


Fig 155 Results of the cylindrical geometry hydrogen diffusion experiment at 25°C using a 3% NaCl charging solution and short transverse oriented sample cylinders.



Figure 156 shows the results of the ambient temperature experiment using longitudinally oriented sample cylinders.

The breakthrough time, T_b , is not as clearly defined in these experiments as it is in electrochemical hydrogen diffusion experiments. The results of the control experiment show that some hydrogen is generated inside the control sample cylinder, probably as a result of air containing water vapour diffusing back into the cylinder as a result of the partial vacuum formed when the 1 ml analysis sample is withdrawn by syringe from the internal volume of the cylinder. This aspect of the experimental technique is discussed later.

For the purpose of calculating the hydrogen diffusion coefficient, the breakthrough time has been defined as the time at which the amount of hydrogen in the sample cylinder exceeds the hydrogen content of the control sample cylinder. The following breakthrough times are therefore reported (Table 21).

Experiment	Sample cylinder orientation	Breakthrough time, T_b (hours)
1	Short transverse	270
2	Short transverse	540
3	Longitudinal	140
4	Longitudinal	300

Table 21 Summary of the breakthrough times obtained from the cylindrical geometry hydrogen diffusion experiments.

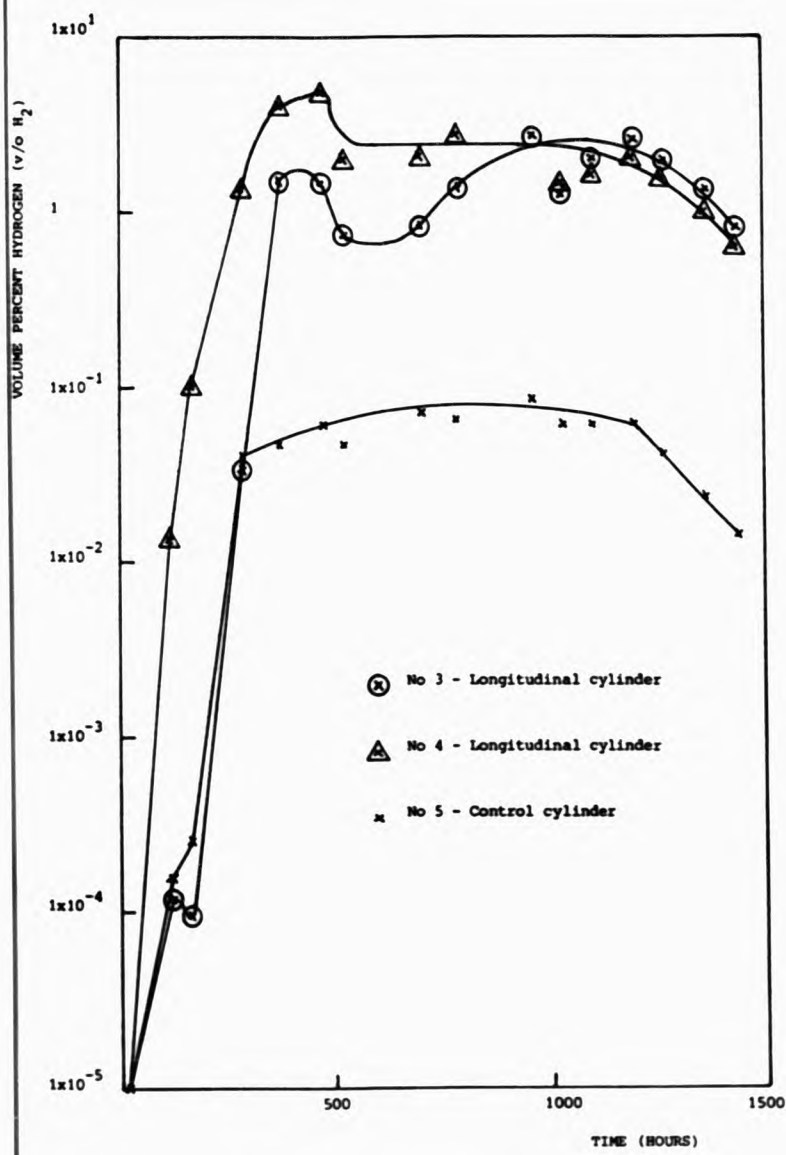


Fig 156 Results of the cylindrical geometry hydrogen diffusion experiment at 25°C using a 3% NaCl charging solution and longitudinal oriented sample cylinders.

The shape of the permeation curve differs from that of an electrochemical hydrogen diffusion experiment in that the measured hydrogen content inside the cylinder reaches a plateau level but then decreases after 1000 to 1200 hours. The decrease in hydrogen content is noted when charging solution is still present in the reaction cell. This decrease in hydrogen content in the cylinder is thought to be either as a result of leakage from the gas fitting and septum mounted on the cylinder or as a result of stifling of the corrosion reaction generating hydrogen on the outer cylinder surface or a combination of the two mechanisms. A further experiment reported later indicates that hydrogen does not leak out of the cylinder at ambient temperatures except that when a 1 ml syringe sample is withdrawn for analysis the hydrogen content of the cylinder is reduced. It is proposed therefore that the rate of the corrosion reaction that generates hydrogen decreases after 1000 to 1200 hours and that this reduction in reaction rate, along with the effect of removing hydrogen from the cylinder for analysis, results in a reduction in hydrogen content in the cylinder towards the end of the experiment.

The results of the experiments at 50 and 70 °C using short transverse oriented sample cylinders are shown in Figure 157. The breakthrough times are 22 hours at 50 °C and 9 hours at 70 °C.

The following diffusion coefficients for hydrogen in AlZnMg, 7017 - T651 alloy are obtained using equation 4.23, (Table 22).

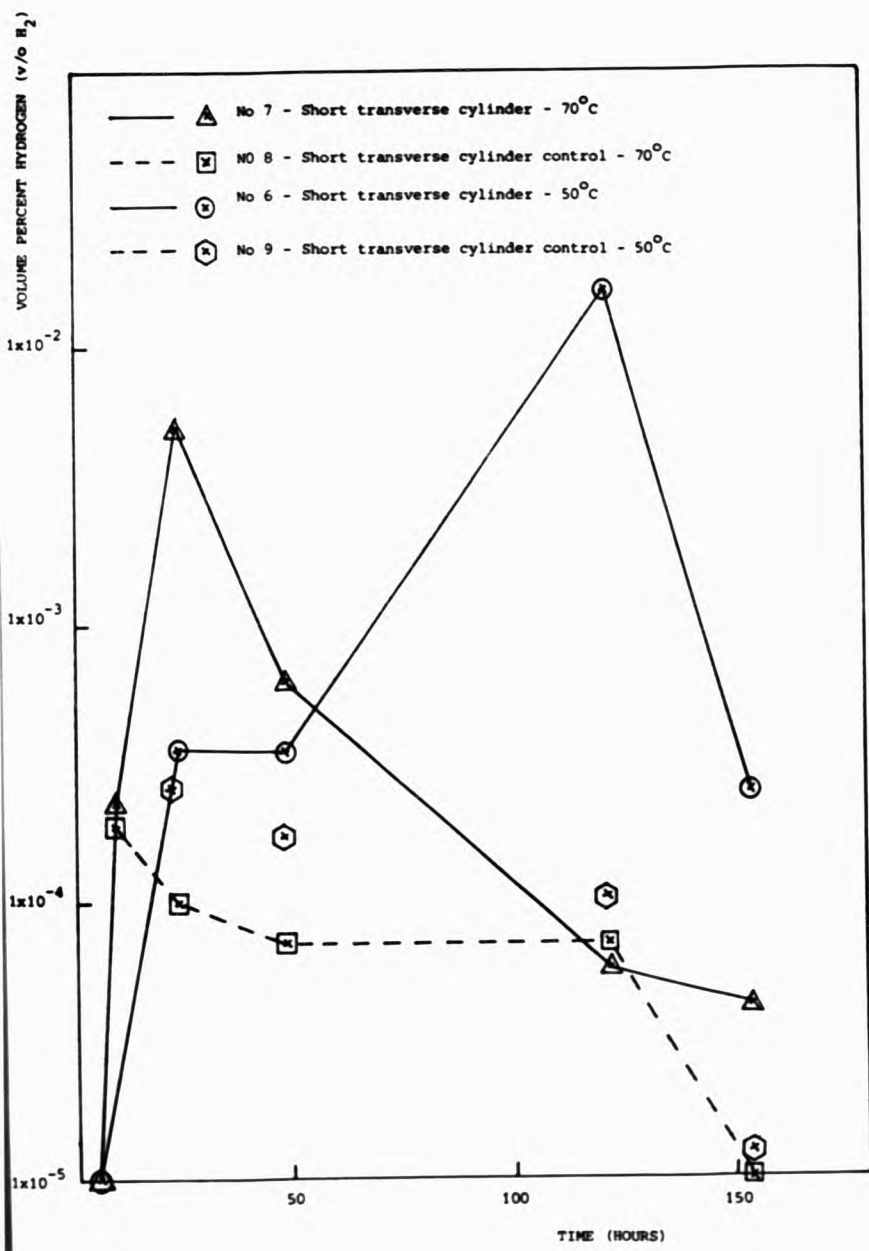


Fig 157 Results of cylindrical geometry hydrogen diffusion experiments at 50°C and 70°C using a 3%NaCl charging solution.

Experiment	Sample cylinder orientation	Temperature ° (C)	Breakthrough time (hours)	Diffusion Coefficient 2^{-1} (cm s^{-1})
1	Short transverse	25	270	4.39×10^{-10}
2	Short transverse	25	540	2.19×10^{-10}
3	Longitudinal	25	140	8.46×10^{-10}
4	Longitudinal	25	300	3.95×10^{-10}
5	Short transverse	50	22	5.38×10^{-9}
6	Short transverse	70	9	1.32×10^{-8}

Table 22 Hydrogen diffusion coefficients obtained from cylindrical geometry hydrogen diffusion experiments.

From the above results there are on average shorter breakthrough times and faster hydrogen diffusion coefficients for the longitudinally oriented sample cylinders compared with the short transverse cylinder. However, there is significant variation in the diffusion coefficient obtained from samples with the same orientation. All the hydrogen diffusion coefficients for experiments performed at 25 C are within an order of magnitude, ranging from $2.19 \times 10^{-10} \text{ cm s}^{-1}$ to $8.43 \times 10^{-10} \text{ cm s}^{-1}$. The measured diffusion coefficient increases with increasing temperature as would be expected from a thermally activated process. The diffusion coefficients obtained are comparable with those obtained by other workers using different diffusion techniques and reported earlier ^{86,160}. The activation energy for diffusion calculated from the above results is approximately 60 kJ mole^{-1} .

An average value has been taken for the diffusion coefficient at ⁰ 25 C when calculating the activation energy.

Figure 158 shows schematically the grain orientation in the sample cylinders. It is clear that a grain boundary diffusion path exists from the outer surface of the cylinder to the inner surface for both cylinder orientations. Whilst it was proposed that, if stress corrosion in AlZnMg type alloys is as a result of hydrogen embrittlement, the orientation of hydrogen diffusion specimens may correlate with the SC susceptible orientations of the alloy, i.e. that short transverse oriented hydrogen diffusion sample specimens would show shorter breakthrough times and faster hydrogen diffusion coefficients than longitudinally or long transverse oriented specimens. This would correlate with the increased susceptibility to stress corrosion and increased crack growth rates observed in the short transverse direction in these alloys ^{10,63}. Any effect on the hydrogen diffusion coefficient would be more readily distinguished in diffusion specimens with planar geometry which was the original intention of the diffusion experiments on AlZnMg alloy samples. The ratio of grain boundary lengths exposed to the charging solutions for short transverse and longitudinal sample cylinders is approximately 1.6:1. It is proposed that this difference in grain boundary length, but similar diffusion path length, between cylinders of different orientation is not sufficient to have a significant effect on the measured diffusion coefficient. This is because other factors, such as differences in grain boundary susceptibility to reaction ^{98,145} with aqueous solutions, differences in grain boundary

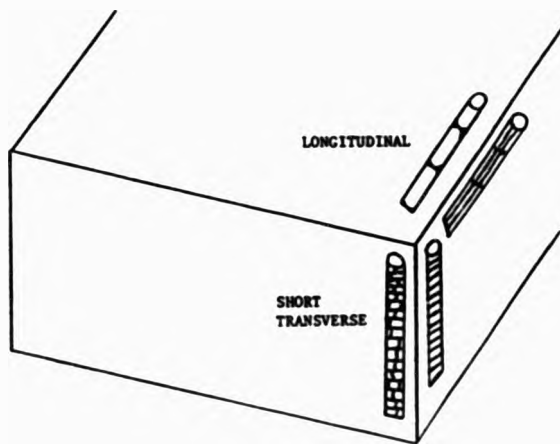
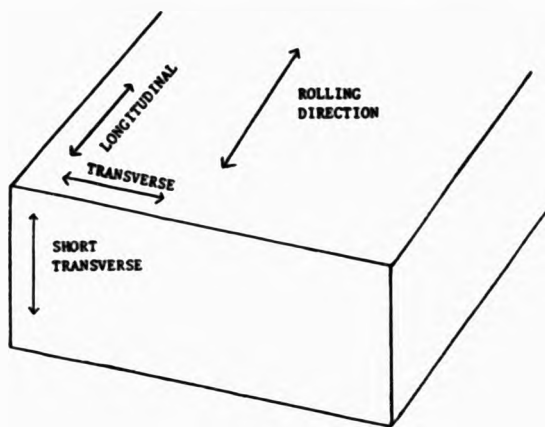


Fig 158 Schematic representation of the grain orientations on the sides of longitudinally and short transverse hydrogen diffusion experiment specimen cylinders.

hydrogen diffusion rates and experimental differences due to different sampling times, specimen location in the original rolled plate and effectiveness of the septum and sampling arrangement, also contribute to the variability between results.

In order to determine whether the partial vacuum formed when a 1 ml sample is withdrawn from the cylinder results in 1 ml of surrounding air being drawn back into the cylinder via the gas fittings or septum on the top of the cylinder, the following experiment was performed.

After the hydrogen diffusion experiment had been terminated, the cylinders from experiments 2 and 3 with the highest hydrogen contents inside the cylinder were sampled every twenty minutes and the composition of the gas inside the cylinder analysed. Analysis was performed on 1 ml samples in the same manner as for the diffusion experiments, except that the cylinders were removed from the charging environment.

Assuming that the hydrogen inside the cylinder is diluted by air intake of 1 ml after a 1 ml sample has been withdrawn then the following applies:

let the system volume = V ml and the
initial concentration = $[conc]_1$ ppm.

After the first dilution the system contains [conc]₁ in (V_o - 1) ml.

$$[\text{conc}] = [\text{conc}]_1 \times \frac{(V_o - 1)}{V_o} \quad (4.24)$$

$$[\text{conc}] = [\text{conc}]_2 \times \frac{(V_o - 1)}{V_o} \quad (4.25)$$

$$\text{Therefore } [\text{conc}]_n = [\text{conc}]_1 \left(\frac{V_o - 1}{V_o} \right)^{n-1} \quad (4.26)$$

and a graph of log [conc]_n vs n is a straight line with a slope

$$\text{of } \log \left(\frac{V_o - 1}{V_o} \right).$$

The graphs of log [concentration (ppm)] versus n, the number of 1 ml samples withdrawn, are shown in Figure 159. The approach to a straight line graph indicates that air diffuses back into the cylinder to equalise the pressure inside the cylinder and secondly that hydrogen, in the case of these experiments at room temperature, is not lost from the system except by removal via the syringe when a sample is taken for analysis.

It is assumed that the hydrogen levels recorded in the control experiment cylinders are generated as a result of the reaction between water vapour in the surrounding air and the inner walls of the control experiment cylinder. Because hydrogen is removed from the cylinder for analysis during the course of the experiment, the hydrogen concentrations recorded with time do not reflect the total hydrogen that has diffused through the cylinder wall.

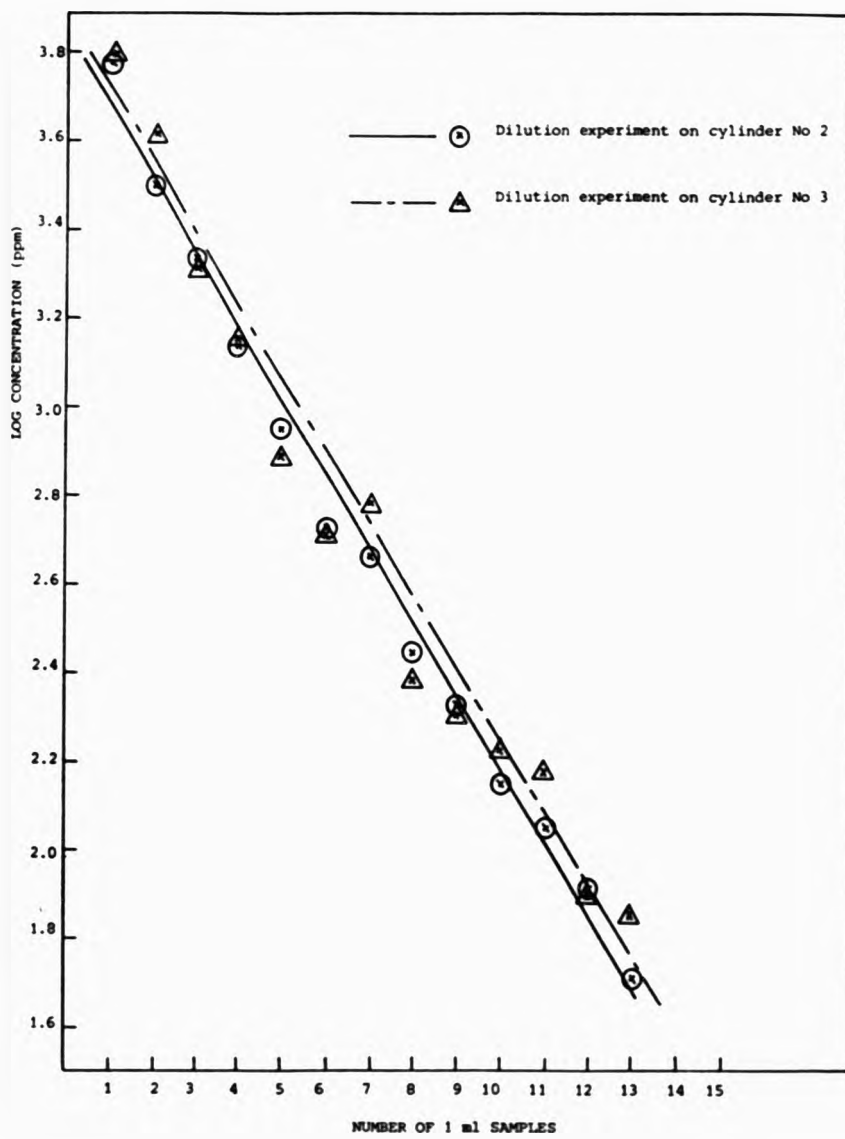


Fig 159 Graph of log [concentration (ppm)] versus number of 1 ml samples withdrawn from cylindrical hydrogen diffusion experiment specimens.

From the slope of the log [concentration] versus n line, the theoretical internal volume of the cylinder including the gas fitting is 3.15 cm^3 . The measured volume of the cylinder is 2.20 cm^3 . This result indicates that the gradient of the line should be shallower if the assumption upon which the equation for the gradient is based is correct. A steeper gradient indicates that the concentration of hydrogen remaining in the cylinder falls to a given level in fewer dilutions, whilst the experiment shows that the hydrogen concentration falls to a given level with a greater number of dilutions. Therefore the pressure inside the cylinder is not completely equalised as less than 1 ml of air returns to dilute the hydrogen remaining in the cylinder, while the hydrogen diffusing through the cylinder wall during the hydrogen diffusion experiment remains inside the cylinder unless withdrawn by the syringe for analysis.

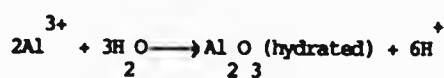
In the case of the elevated temperature cylindrical geometry diffusion experiments, the graphs at 50 and 70 C show a decrease in the hydrogen content of the cylinder after 124 hours and 24 hours respectively. Here it is thought that the increased mobility of hydrogen with increased temperature prevents hydrogen that has diffused into the internal volume of the cylinder from remaining there at elevated temperatures for any length of time, a similar effect being observed when measuring hydrogen production rates on 7017 type AlZnMg alloy surfaces at elevated temperatures (see Section 4.5.1).

After the completion of the diffusion experiments, the cylinders were sectioned and polished to establish whether stress corrosion of the cylinder had led to the charging solution seeping into the cylinder and thereby generating hydrogen by reaction with the inner wall of the cylinder. No evidence of stress corrosion cracking was found, and a typical section of cylinder wall is shown in Figure 160.

Whilst the experimental results presented do not enable a distinctly defined breakthrough time to be obtained as in an electrochemical hydrogen permeation experiment, it is proposed that the results do demonstrate diffusion of hydrogen through 7017 AlZnMg alloy membranes. In addition, solution of the diffusion equation for cylindrical geometry allows the calculation of the hydrogen diffusion coefficient for the alloy.

4.5 SURFACE REACTIONS ON Al-Zn-Mg ALLOYS IN WATER, NEAR AND 3% SODIUM CHLORIDE.

It is well known that aluminium reacts with water vapour according to the following summary reaction ⁹⁶ ;



This reaction may occur at the vapour/oxide interface or at some point within the surface oxide film depending on the relative mobilities of the Al^{3+} ions and hydroxyl ions through the surface oxide. In either case the ionisation of the aluminium results in electron discharge by a number of mechanisms, but the most

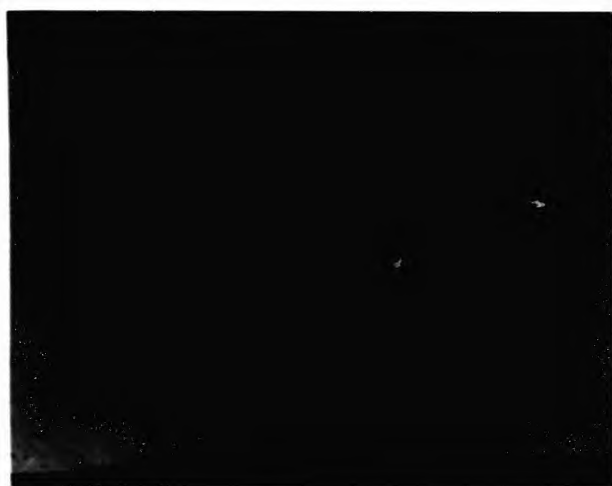
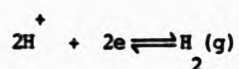


Fig 160 Section of 7017 alloy hydrogen diffusion sample cylinder polished, showing no evidence of stress corrosion cracking.

(Magnification x 146)

important in relation to hydrogen entry would be the discharge of protons;



The intention of these studies is twofold:

- a) To determine the rate of hydrogen production on 7017 AlZnMg alloy surfaces exposed to WSAV, water and 3% NaCl all at 70 °C. These environments were chosen as they correspond with the environments employed during SC crack growth rate experiments. Exposure to water and 3% NaCl was conducted with the alloy surface fully submerged in the environment.
- b) To examine the products of the reaction with WSAV at 70 °C of a high purity variant of 7017, and of the commercial alloy 7017, using high resolution SEM and TEMSCAN. TEMSCAN allows TEM samples to be examined either in the transmission mode using SE (secondary electron) or STE (scanning transmission electron) imaging respectively. Thus, reaction sites could be examined in detail together with the underlying microstructure.

4.5.1 Hydrogen production rates of Al-Zn-Mg alloys in water, WSAV and 3% sodium chloride.

The quantity of hydrogen detected as a result of the reaction of the 1/4 micron polished 7017 alloy sample in each of the environments studied, namely, double distilled water, WSAV and 3% NaCl at 70 °C is shown in Figures 161, 162 and 163 respectively. The quantity of hydrogen, in mm³ per cm² of surface, shows a rapid increase within the first 100 minutes to a peak value after

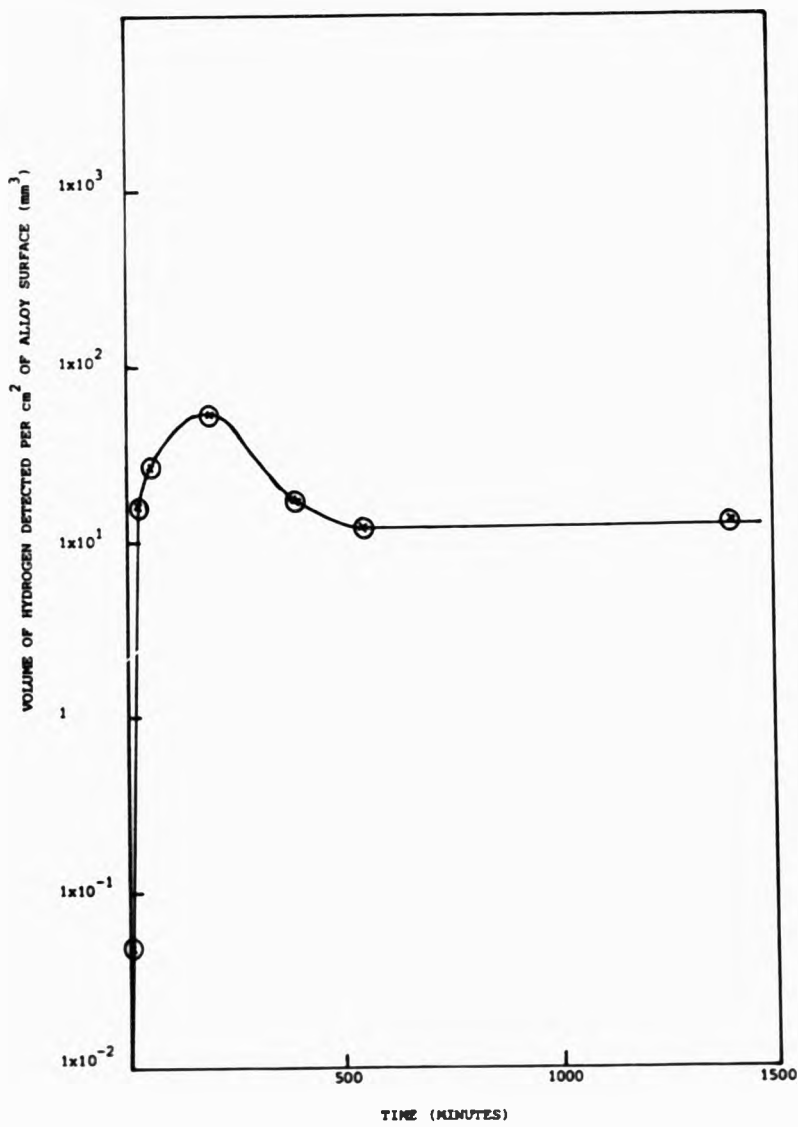


Fig 161 Quantity of hydrogen detected as a result of the reaction between 7017-T651 alloy and double distilled water at 70°C.

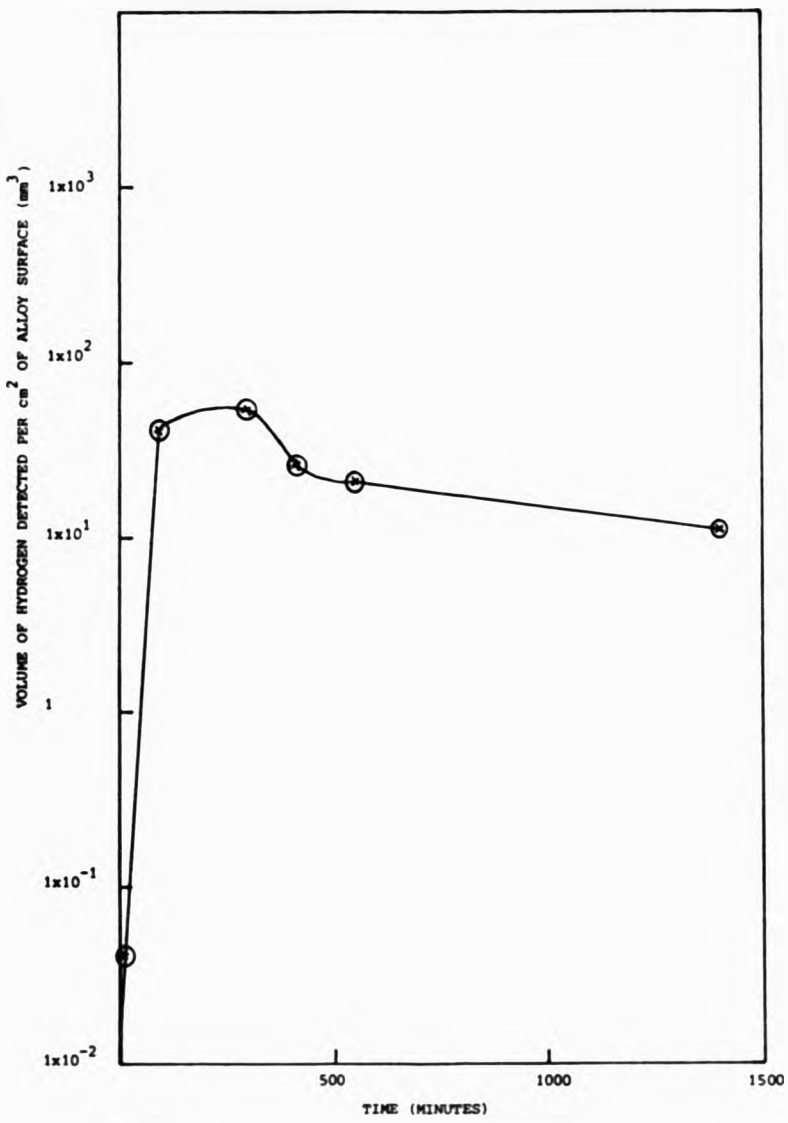


Fig 162 Quantity of hydrogen detected as a result of the reaction between 7017-T651 alloy and WSAV at 70°C.

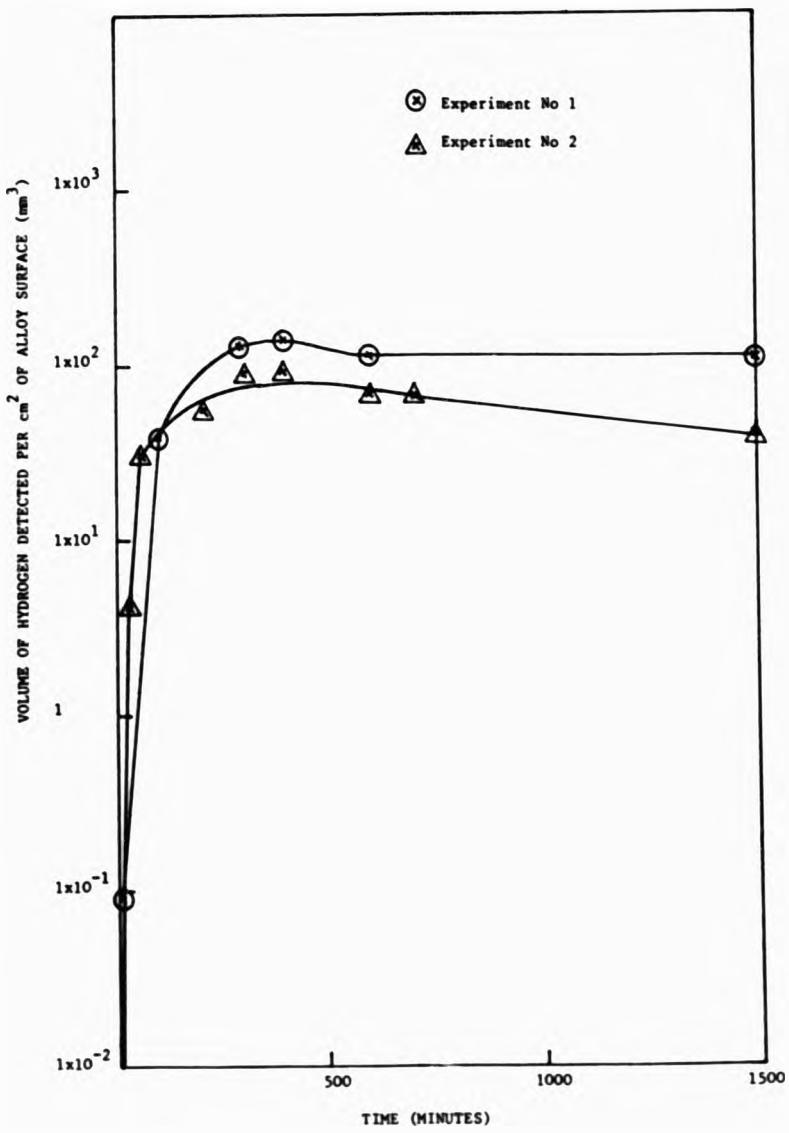


Fig 163 Quantity of hydrogen detected as a result of the reaction between 7017-T651 alloy and 3%NaCl at 70°C.

300 minutes which then falls to a steady or slightly declining level for the duration of the experiment, 1700 minutes.

The peak hydrogen production in water and WSAV at 70 °C is 53.7 and 54.4 $\frac{\text{mm}^3 \text{H}_2}{\text{cm}^2}$ per cm² of surface.

Hydrogen is a highly mobile species at 70 °C and it is probable that some hydrogen escapes from the reaction cell through the PTFE seals. The reaction is also probably stifled by thickening of the hydrous oxide film and this is discussed in more detail in Section 4.5.2. It is proposed that stifling of the reaction combined with loss of hydrogen from the reaction cell accounts for the decrease in the total quantity of hydrogen detected with time.

However, as the three experiments were performed under the same conditions, it is clear that the reaction in the presence of chloride ions results in two and a half times the total quantity of hydrogen being produced, compared with distilled water or WSAV.

The bulk pH in the 3% NaCl solution remained constant at pH 6.2 for the duration of the experiment. This is expected as acid hydrolysis, leading to a decreased pH around 3.5, is only thought to occur in the crevice conditions found in a stress corrosion crack.

Anodic dissolution mechanisms of stress corrosion crack growth attribute the increased velocity of SC cracks in chloride environments to the role of the chloride ion in destroying the immunity of the air formed oxide film, and thus allowing access of the environment to the crack tip. Chloride, bromide and iodide anions are unique pitting agents for aluminium alloys and as such influence both the rate of crack growth and the initiation of SCC in smooth specimens by the formation of pits that act as stress raisers. Subsequent anodic dissolution mechanisms have been discussed in detail in the literature survey (Section 2.3.2).

If hydrogen embrittlement is the dominant mechanism of crack extension in these alloys, an alternative view of the specific role of the chloride ion is that the pitting corrosion reaction on susceptible aluminium alloys increases the environmental fugacity of hydrogen. These reactions occur by exposing fresh aluminium surface as a result of pitting reactions, and because the chloride ions enhance removal of corrosion product from the crack tip and crack sides, allowing access of the environment to the crack tip area. Removal of corrosion product probably involves the formation of soluble aluminium chloride from the insoluble aluminium hydroxides present on the alloy surface. Hence anodic dissolution plays an important role, not in the dissolution of a section of the precipitate free zone adjacent to the grain boundary, but in the general chemical reaction with aluminium to generate hydrogen. Hydrogen is generated as a result of the reduction in pH at the crack tip to around pH 3.5, due to

o

pseudoboehmite is heated in air at 300 C it is dehydrated to a poorly crystallised γ -Al₂O₃¹⁴. Protons produced at the barrier layer are attracted to the metal-oxide interface which is negatively charged due to the aluminium ions in excess in the adjacent oxide. At the metal-oxide interface they can be readily discharged and combined to form molecular hydrogen. This process effectively decoheres the interface and surface film blistering is initiated. Blister growth is depicted schematically in Figure 40, and further discussed in relation to the commercial AlZnMg alloy 7017 in Section 4.5.2.

As discussed the role of the chloride ion may then be to undermine the barrier layer and to remove corrosion products thus exposing new aluminium directly to the aqueous environment. This process would result in the generation of the greater quantities of hydrogen seen in the surface reaction rate experiments. The increased hydrogen fugacity may then be the determining factor in the increased crack growth rates seen in aqueous chloride environments, where for compact tension specimens increases in the plateau velocity of just under two orders of magnitude at 90 C and just under one order of magnitude at 50 C were observed in the current work over crack growth rates obtained in water and NSAV (Table 9).

4.5.2 WEAV reaction and examination on Al-Zn-Mg alloy surfaces.

The results of the reaction of NSAV with samples of an alloy similar to 7017 cast from high purity materials was studied first. The alloy had the following percentage composition (as

reported in Section 3.1), Al-4.9%Zn-1.84%Mg-0.11%Fe-0.05%Si. Samples of the alloy in the form of 3 mm diameter transmission electron microscope disks were prepared as described in Section 3.5.3.

Exposure to WSAV was for periods of 10, 20 and 100 minutes, and was achieved by placing the specimens horizontally on a Perspex holder in a humidity chamber at 100% relative humidity under conditions where condensation of water on the specimen surface was observed. After exposure the specimens were examined immediately in the electron microscope in the secondary electron imaging mode (SEI) using a liquid nitrogen cold trap at the specimen location to minimise surface contamination. The general area of a number of reaction sites is shown in Figure 164 after 10 minutes exposure to WSAV. Exposure has resulted in the random nucleation of circular areas of an aluminium hydroxide. Close examination shows that these reaction sites are areas where the surface has been effectively defilmed by the formation of a blister. That blister formation has taken place is more readily seen in Figure 165 after 20 minutes exposure to WSAV. After a number of blisters have fractured, the blister wall then becomes readily apparent (arrowed "A" and "B"). The area of the reaction site, where the air formed surface oxide film has thickened by forming hydroxide and where blister formation has taken place, is initially seen in dark contrast (arrowed "A"). After the blister wall has fractured, the remaining wall is seen in light contrast, while the interior of the blister where the remains of the

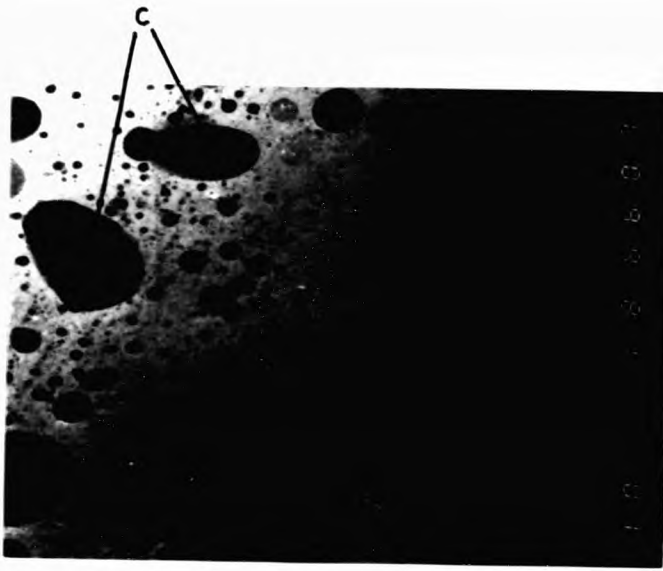


Fig 164 SEI image of WSAV reaction sites on AlZnMg virgin alloy after 10 minutes exposure.
Magnification x1000

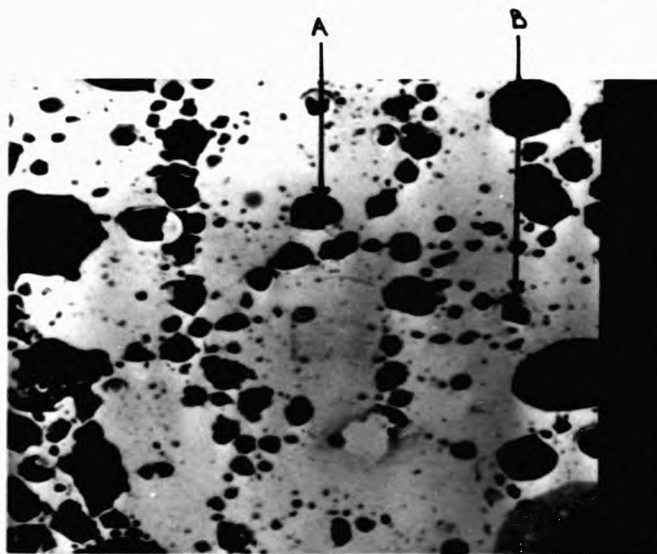
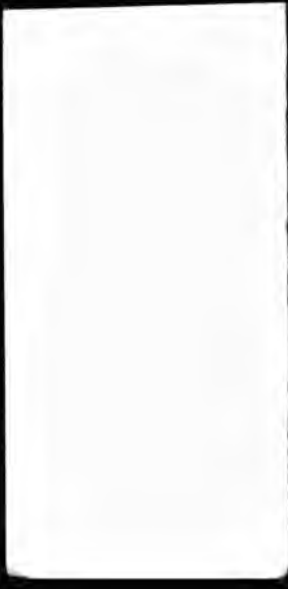


Fig 165 SEI image of WSAV reaction sites on AlZnMg virgin alloy after 20 minutes showing blistered reaction sites.
Magnification x 5000



surface film debris has collapsed onto the circular reaction site is again seen in dark contrast (arrowed "B"). The blister formation is attributed to decohesion of the amorphous oxide-metal interface by hydrogen generated at the reaction site¹⁴⁵. At the circumference of the reaction sites, the surface film shows a region of dark contrast between adjacent reaction sites (arrowed "C"). This feature, which is often noted, is also attributed to decohesion of the amorphous oxide-metal interface by hydrogen generated at the reaction site.

In a number of areas on the specimen surface, preferential reaction at grain boundary-surface intersections was noted (arrowed "E"). Here the reaction sites are lined up along the grain boundary-surface intersection (Figures 166 and 167).

The reaction sites are shown in detail after 100 minutes exposure to WSAV in Figures 168-171. The higher magnification view in Figure 169 and 170 shows that at this stage the reaction site is completely covered in a pseudoboehmite layer which is readily identified from its characteristic morphology appearing as platelets, fibrils or needles¹⁴⁵. Figure 171 shows another example of a region of dark contrast around the circumference of a reaction site, attributed to decohesion but not blistering of the metal-oxide interface as a result of hydrogen generation (arrowed "D").

Figures 172 and 173 show conventional transmission electron microscope images of WSAV-AlZnMg alloy reaction sites, again for

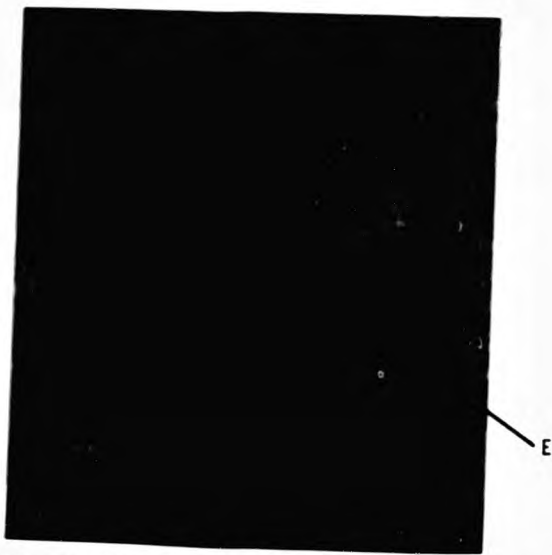


Fig 166 SEI image of WSAV reaction sites on AlZnMg virgin alloy after 10 minutes exposure, showing localisation of reaction at the grain boundary.
Magnification x2000

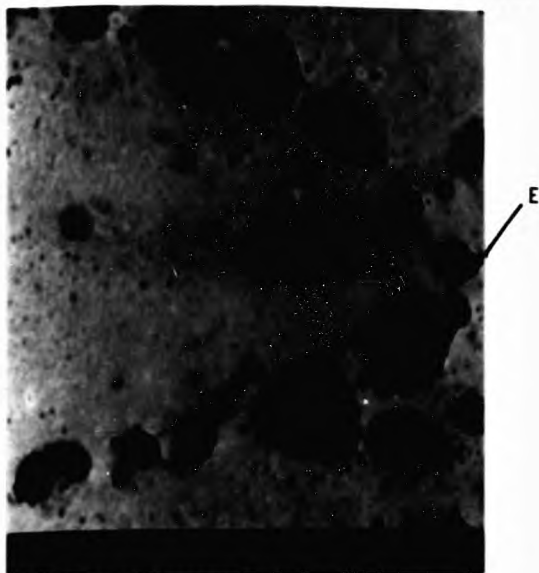


Fig 167 Higher magnification of the grain boundary reaction site shown in Figure 166.
Magnification x8000



Fig 168 SEI image of WSAV reaction sites on AlZnMg virgin alloy after 100 minutes exposure.
Magnification x2000



Fig 169 SEI image of area shown in Figure 168 showing characteristic platelet morphology of pseudoboehmite inside the reaction site.
Magnification x5000



Fig 170 SEI image of pseudoboehmite inside the reaction site shown in Figure 168 at high magnification.
Magnification x 10000



Fig 171 SEI image of de-cohered region around the circumference of a blister reaction site on virgin AlZnMg alloy after 100 minutes exposure to WSAV at 70°C.
Magnification x5000



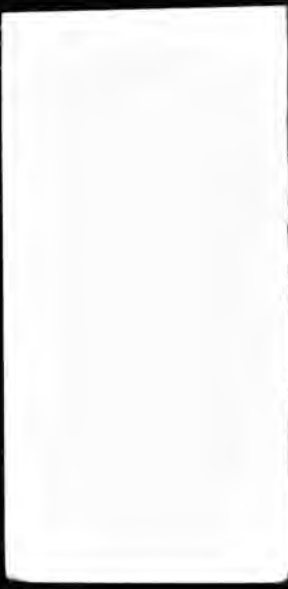
Fig 172 TEM image of WSAV reaction with AlZnMg virgin alloy after 100 minutes exposure to WSAV showing surface reaction sites and the underlying MgZn₂ precipitate structure in the alloy matrix.

Magnification x33000



Fig 173 TEM image of pseudoboehmite after WSAV reaction with AlZnMg virgin alloy for 100 minutes. Note the characteristic fibril or needle morphology.

Magnification x15000



the virgin alloy after 100 minutes exposure to WSAV. Figure 172 shows the reaction sites in an electron transparent area of the specimen near to the hole formed by the jet impingement polishing equipment. The overlapping reaction sites shown (arrowed "F") may be as a result of reaction sites on both sides of the specimen. Figure 173 shows the characteristic fibril or needle like morphology of pseudoboehmite where it has grown adjacent to the central jet impingement polishing hole in the specimen.

Figures 174 and 175 show the result of exposure of 7017 alloy in the T651 condition to WSAV for 10 minutes. The reaction sites are similar to those described for virgin alloy specimens of AlZnMg alloy. However, it was noted that there was no evidence for grain boundary specificity in the reaction of the commercial alloy with WSAV.

Scamans and Rehal¹⁴⁵ noted the growth of small ($< 0.5 \mu\text{m}$) bayerite crystals on specimens after 1400 minutes exposure to WSAV at 70 C. Bayerite is also identified by its characteristic morphology, appearing as wedges, rods and hour-glass figures and these diverse shapes have been given the general classification of somatoids¹⁴. Bayerite was not identified in these studies for exposures up to 1000 minutes. However, the growth of small areas of more compact pseudoboehmite identified after 1000 minutes exposure to WSAV (Figures 176 and 177) may be the precursor to bayerite growth.

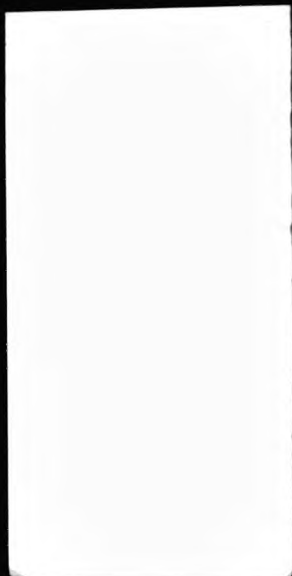


Fig 174 SEI image of WSAV reaction sites on a 7017-T651 commercial alloy surface after 10 minutes exposure at 70°C.
Magnification x15000



Fig 175 Higher magnification SEI image of reaction sites after WSAV exposure of commercial 7017-T651 for 10 minutes.
Magnification x30000



Fig 176 SEI image of WSAV reaction site after 1000 minutes exposure at 70°C of a commercial 7017-T651 alloy surface.

Magnification x2000

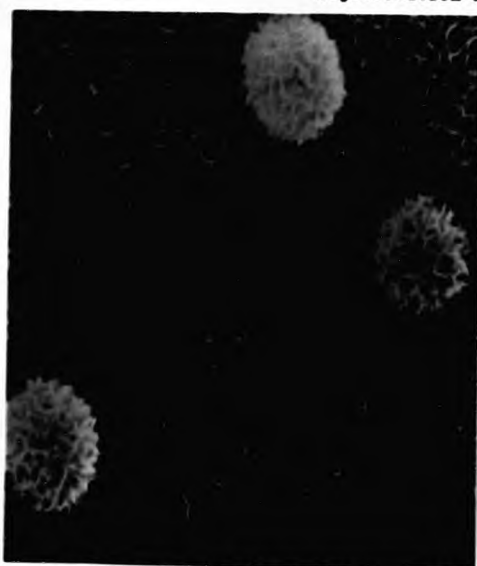


Fig 177 Higher magnification SEI image of reaction site shown in Figure 176 showing light contrast crystals still with a characteristic pseudoboehmite morphology.

Magnification x8000

Bayerite crystals were observed at high magnification on the fracture surfaces of CT specimens during SCC growth. The development of a duplex hydroxide film (bayerite and pseudoboehmite) was noted both under conditions of total immersion in double distilled water at 70 C and where the environment was NSAV at 70 C. It is likely that water condenses on the SC crack surface in the NSAV environment and that conditions here are akin to those found under total immersion. The following conventional SEM images show the development of the duplex hydroxide film on the crack surface with increasing exposure time in the environment. The SEM images are all from specimen 26 (NSAV, 70 C).

The SC crack growth was for a period of approximately 1400 minutes, which is the maximum period that the fracture surface at the start of the SC crack was exposed to the environment. Crack sides adjacent to the final position of the crack tip before fast fracture will have only been exposed to the environment for a number of minutes. The fracture surface 0.78 mm back from the SCC - overload fracture interface is shown in Figure 178, the high magnification view of this area, Figure 179 shows the characteristic morphology of pseudoboehmite on the fracture surface. Figures 180, 181 and 182 show a similar sequence 4.7 mm back from the SCC-overload fracture interface. At this location a duplex hydroxide film has started to develop with bayerite ~~scantoids~~ present. It is not clear whether these are growing from the pseudoboehmite film or from the underlying metal surface. Finally, Figures 183 and 184 show the same sequence



Fig 178 Fracture surface 0.78 mm back from SC-overload fracture interface (specimen 26, WSAV 70°C).



Fig 179 High magnification of fracture surface shown in Figure 178. The surface film is entirely pseudoboehmite.



Fig 180 Fracture surface 4.7 mm back from SC-overload fracture interface (specimen 26, WSAV 70°C).



Fig 181 High magnification of fracture surface shown in Figure 180. The surface film is now a duplex hydroxide film with the growth of bayerite somatoids evident.



Fig 182 Higher magnification view of bayerite somatoids embedded in the fracture surface. It is not clear whether growth of bayerite is from the alloy surface or from the pseudoboehmite layer.

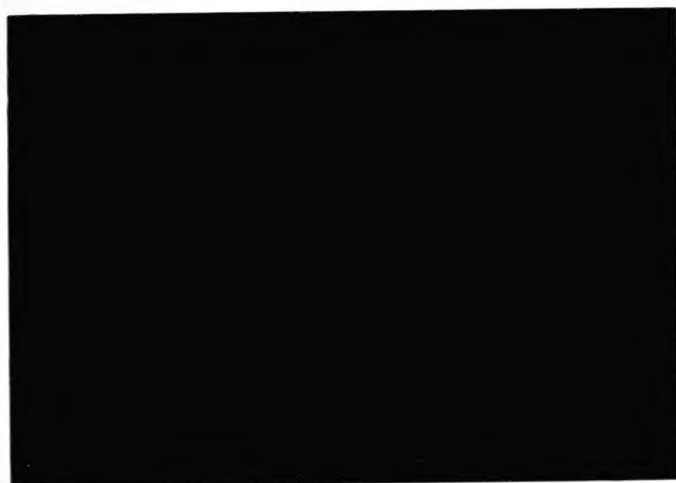


Fig 183 Fracture surface 9.6 mm back from the SC-overload fracture interface (specimen 26, VSAV 70°C).



Fig 184 High magnification of fracture surface shown in Figure 183. The SC crack sides now show a fully developed duplex hydroxide film of pseudoboehmite and bayerite.



Fig 185 SEM image of commercial 7017-T651 alloy surface exposed to WSAV at 70°C for 1400 minutes. Note the almost complete blister wall in the centre of the photomicrograph. Magnification x215

9.6 mm back from the SC-overload fracture interface. The high magnification image in Figure 184 shows a fully developed duplex hydroxide film of pseudoboehmite and bayerite. The period of exposure to the environment at this location is similar to that of the disk specimens shown in Figures 176 and 177 after exposure to WSAV at 70 C for 1000 minutes. The development of the duplex hydroxide film therefore appears to be faster under conditions of total immersion, although the results presented in Section 4.5.1 indicate that the rates of hydrogen production in WSAV and under conditions of total immersion are similar.

The blister formation in WSAV at 70 C is shown more clearly in a conventional scanning electron microscope image in Figure 185. The blister walls are seen in light contrast, and the blister wall debris is seen in dark contrast on the reaction site. The blisters shown in Figures 185, 186 and 187 have developed after 1400 minutes exposure to WSAV at 70 C on a plain surface of AlZnMg 7017-T651 commercial alloy used in the hydrogen production rate experiments reported in Section 4.5.1. Blisters are 30 to 150 μm in diameter. Figures 186 and 187 show a second area of reaction sites on the same specimen where the blister wall appears to have a cellular structure, evidenced both by the structure of the blister wall itself and the cellular debris on the reaction sites.

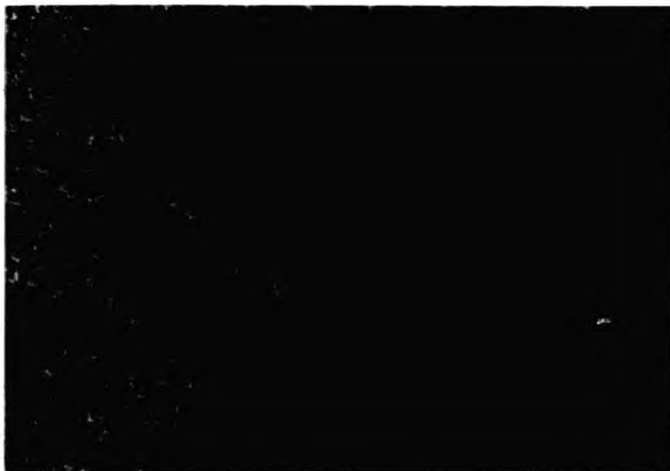
Figures 188 and 189 show the distinctly different results of the reaction of a commercial 7017-T651 alloy surface totally immersed



Fig 186 SEM image of commercial 7017-T651 alloy surface exposed to WSAV at 70°C for 1400 minutes.

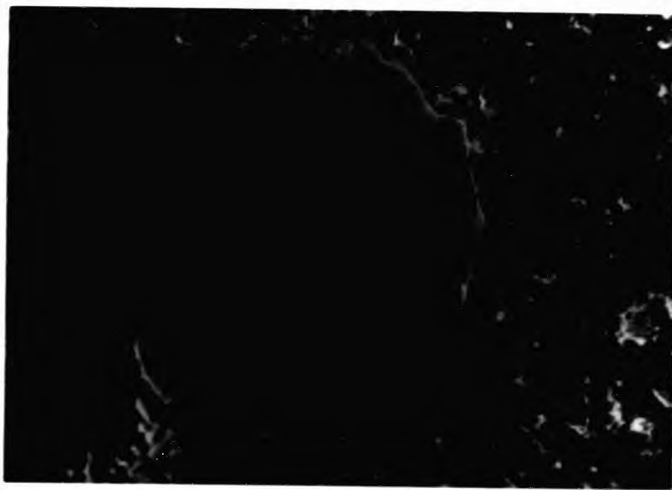


Fig 187 SEM image of commercial 7017-T651 alloy surface shown in Figure 186 but at a higher magnification showing cellular nature of blister wall and blister wall debris.



70 μ

Fig 188 SEM image of commercial 7017-T651 alloy exposed to 3% NaCl at 70°C for 1700 minutes.



20 μ

Fig 189 Higher magnification SEM image of area shown in Figure 188. Note the deep pitting attack of the alloy surface.

in a 3% NaCl solution after 1700 minutes exposure. Again these SEM images are of the specimen used in the hydrogen production rate experiments. Here the surface reaction is characterised by general pitting corrosion and has been discussed in Section 4.5.1.

The reactions taking place on exposure of pure aluminium and aluminium alloys has been discussed in detail elsewhere and is reported in the literature survey (Section 2.5.6). However, a number of conclusions have been made from the studies reported here.

The reaction on specimens prepared for transmission electron microscopy, which may have perchlorate ions incorporated in the initial oxide film as a result of the use of a perchlorate based electro-polishing solution, is in fact similar to the reaction seen on the surface of bulk specimens prepared by abrasive grinding and polishing.

In the work reported by Scamans and Rehal¹⁴⁵ the grain boundary specificity of the WSAV reaction on virgin AlZnMg and AlMg alloy surfaces was cited as being in a convenient location for hydrogen to enter the grain boundary to cause embrittlement. It was also noted that in high purity alloys the specificity of the reaction with respect to the grain boundary was a strong function of the solution heat treatment temperature. In the AlMg binary alloy, solution treated at 550 C, random attack nucleation had occurred, whereas at solution treatment temperatures of 350 and 450 C there

was a very strong selectivity of the attack at grain boundary-surface intersections. However, in the specimens solution treated at 350/450 °C not all the grain boundaries were attacked and it was not possible to identify the boundary type which provided this immunity. The observed effect of magnesium additions, both singly (AlMg) and in combination with zinc (AlZnMg), causing preferential grain boundary reaction was attributed to magnesium segregation to grain boundaries. Although magnesium segregation was not detected by Scamans and Rehal, because the X-ray microanalysis technique they used had an analysis beam size too large to discern the narrow band over which the magnesium segregation is thought to occur, more recent work by Green et.al.⁹³ has demonstrated such magnesium enrichment.

Green et. al. used electron spectroscopy to show a magnesium enriched zone, less than 10Å wide, at grain boundaries in AlZnMg alloys at a level of segregation that would be beyond the resolution of X-ray microanalysis. This work did not look at the effect of solution heat treatment temperature on magnesium segregation. However, Taylor and Edgar¹⁹¹ have shown from studies on anodic films that magnesium segregation in AlZnMg alloys decreases as the solution heat treatment temperature is raised, and that the SC cracking susceptibility is correspondingly diminished. Barrier layer anodic oxidation is affected by underlying alloy composition and regions of high magnesium segregation produce a thinner final oxide layer. This leads to grain boundary grooves on the surfaces of AlZnMg alloys

after solution heat treatment at low temperatures. Tuck and Scamans proposed that the enrichment of magnesium at grain boundaries must lead to its incorporation in the initial surface oxide film above the boundary sites, and that this must stimulate hydration and blistering on exposure to WSAV, as a result of the more active electrode potential of magnesium .

In the commercial 7017 alloy, the non-specificity of the WSAV reaction is also probably due to reduced segregation of magnesium to the grain boundary. The solution heat treatment temperature used to produce the T651 temper is in the range 400 - 430 °C which would be expected to result in magnesium segregation. However, it is proposed that it is the effect of the alloying additions made to the commercial alloy that result in reduced or non-segregation of magnesium to the grain boundary and hence the absence of grain boundary specificity in the WSAV surface reaction. Iron, silicon and nickel in particular could reduce the extent of magnesium segregation in commercial 7017 alloys by the following mechanism. Iron, silicon and nickel have a low solubility in aluminium and are precipitated during casting as intermetallic particles. These precipitates, along with grain boundaries, will act as sinks for vacancies, and during quenching from solution heat treatment the magnesium atom/vacancy pairs will travel both to the grain boundaries and to the segregate particles. Thus, magnesium segregation at the grain boundaries of AlZnMg alloys with iron, silicon and nickel additions (iron 0.45%, silicon 0.35%, nickel 0.10% in the 7017 alloy) would be less than that in pure AlZnMg, causing the observed reduced

reactivity of the commercial alloy grain boundaries with WSAV. There is also evidence that, as would be expected, commercial alloys have a reduced SCC susceptibility than their corresponding high purity alloy versions, particularly on smooth specimens such as those used in slow strain rate tensile testing ¹⁹².

Tuck and Scamans ¹⁹² have shown that high purity alloy versions of Al-4.5%Zn-1.5%Mg with either single alloying additions of iron, nickel, silicon, copper or iron and nickel additions in combination show reduced but not zero specificity of the WSAV reaction with the grain boundary. These results are summarised in Table 23.

Alloy (weight percent)	% of grain boundaries attacked in WSAV reaction
Al-4.5%Zn-1.5%Mg	95
Al-5%Mg	95
Al-4.5%Zn-1.5%Mg + Fe(0.11%)	10
+ Ni (0.05%)	50
+ Si	50
+ Cu	80
+ Fe(0.11%) + Cr(0.10%)	90

Table 23 The percentage of grain boundaries attacked by the WSAV reaction at 70°C as a function of alloying additions made to the base alloy.

It is however proposed that the lack of any grain boundary specificity in the WSAV reaction of commercial AlZnMg alloys is

not significant in the stress corrosion of pre-cracked CT or DCB specimens. In a pre-cracked specimen the specific grain boundary (or grain boundaries) along which the SC crack will grow have been determined by the geometry of the specimen. As the WSAV reaction (or reaction with water or 3% NaCl etc.) will take place randomly on any alloy surface, including the two crack surfaces exposed after fracture, hydrogen is being generated in the region of the SC crack tip. This hydrogen is available for transport by mechanisms such as dislocation transport, or diffusion to the region of maximum hydrostatic stress, to the area immediately in front of the advancing crack. The specimen sides are in fact the only areas where grain boundary - surface intersections are present and where the specificity of the reaction with WSAV may be a significant factor in stress corrosion. The bulk of the reaction with the environment takes place on the grain boundary already exposed by intergranular fracture. Blanking off the specimen sides (specimen No 39, Section 4.2.1) has shown that the entry of hydrogen at this point is not a significant factor in contributing to the SC crack growth rate. As bayerite growth on the alloy surface only takes place after periods of exposure greater than approximately 1000 minutes, it is the reaction with aluminium to produce boehmite or pseudoboehmite (depending on temperature, boehmite is the reaction product at temperatures below 70 °C) and hydrogen, probably small distances away from the crack tip, that is responsible for crack growth by a hydrogen embrittlement mechanism. The significant distances in this case are unlikely to be greater than the observed striation widths on the fracture surfaces.

It is possible that the specificity of the WSAV - grain boundary reaction is a more important factor in the stress corrosion of (initially) smooth surface specimens, eg. slow strain rate tensile specimens. Here entry of hydrogen at the grain boundary-surface intersection, rather than at random reaction sites, may play an important role in determining the extent of stress corrosion susceptibility.

5.0 DISCUSSION

Most of the results have already been discussed in detail under the appropriate results sections. Consequently it is proposed here to briefly summarise the results, to bring together and discuss the main points that have emerged from this work, and to indicate the contribution of these points to the understanding of the mechanism of stress corrosion cracking in AlZnMg alloys.

5.1 SUMMARY OF RESULTS

1) The variation in crack growth rate with temperature for fatigue pre-cracked compact tension geometry specimens in double distilled water results in an activation energy for crack growth based upon plateau velocity of $55.5 \text{ kJ mole}^{-1}$ and in 3% sodium chloride the activation energy based upon plateau velocity is $104.6 \text{ kJ mole}^{-1}$. In 3% NaCl it was also possible to obtain a value for the activation energy for stage I crack growth which was $114.3 \text{ kJ mole}^{-1}$.

2) In CT specimens evidence of ductility was seen in the SEM photomicrographs of the stress corrosion crack surface at high levels of stress intensity, towards the end of crack growth. This ductility, indicated by areas of microvoid coalescence on the fracture surface, was observed both in specimens where crack growth had taken place in water and in 3% NaCl environments. The regions of ductility were surrounded by areas of stress corrosion crack surface where brittle separation of the crack faces had taken place with no evidence of ductility.

3) The effect of preventing access of a distilled water environment to the crack tip where it intersects the specimen side was investigated in CT specimens. If access is prevented the resultant SC crack profile is convex whereas the normal SC crack profile is concave in distilled water environments. In 3% NaCl the normal SC profile is convex. This observation was interpreted in terms of a hydrogen embrittlement mechanism for crack growth (see Section 4.2.1).

4) The effect of pre-exposure to WSAV and pre-charging with cathodic hydrogen were investigated and it was shown that, for subsequent crack growth in WSAV at 70 °C, the effect of pre-exposure and pre-charging was to reduce the stress intensity required for the initiation of SC crack growth to around $4.5 \text{ MNm}^{-3/2}$ compared with a K_{ISCC} of between 8.8 and $10.8 \text{ MNm}^{-3/2}$ for specimens that had not been pre-exposed in an environment where hydrogen generation takes place, or where electrochemical pre-charging with hydrogen has not occurred. After the establishment of crack growth, at intermediate stress intensities of approximately $6 \text{ MNm}^{-3/2}$ crack growth ceases and is only re-established when the stress intensity is increased to a value between 9 and $10 \text{ MNm}^{-3/2}$. This is interpreted in terms of a hydrogen embrittlement mechanism whereby the stress corrosion crack grows out of the region of the specimen where an initially high hydrogen concentration had been established by pre-exposure or pre-charging. The extent of crack growth in the region embrittled by pre-exposure or pre-charging is between 1.4

and 1.6 mm. Whilst this is not strictly a recovery process, the specimen as a whole "recovers" from the initial embrittlement suffered as a result of initially higher hydrogen levels ahead of the pre-existing fatigue pre-crack.

5) Anomalous crack growth rate versus stress intensity curves were obtained for the specific case of crack growth in water or WSAV at 70 °C. Here, crack growth rates were seen to decrease by just under an order of magnitude from their value at K_{ISCC} to an intermediate stress intensity of between 11 and 16 $MNm^{-3/2}$. This was then followed by an increase in crack growth rate at higher stress intensities until final fracture of the specimen, resulting in a "U" shaped plot of stress intensity versus crack growth rate. Three possible mechanisms are proposed to account for the anomalous behaviour and these are discussed further in Section 5.3.

6) The variation in crack growth rate with temperature for double cantilever beam geometry specimens in three environments, water, WSAV and 3% NaCl was investigated for specimens that had "pop-in" type pre-cracks. The following activation energy results were obtained, (Table 24).

Environment	Basis of activation energy determination	Activation energy ⁻¹ (kJ mole ⁻¹)
H ₂ O	Stage I at 5 MNm ^{-3/2}	73.9
H ₂ O	Plateau velocity	74.8
WSAV	Stage I at 6.5 MNm ^{-3/2}	114.7
WSAV	Plateau velocity	74.2
3%NaCl	Stage I at 4 MNm ^{-3/2}	149.6
3%NaCl	Plateau velocity	89.0

Table 24 Activation energies for SC crack growth in double distilled water, WSAV and 3%NaCl for DCB specimens.

Activation energies for both CT and DCB specimens are discussed in Section 5.4.

7) A comparison of crack growth rates obtained in both CT and DCB specimens in the three environments and over the temperature range studied has been made and the results further discussed in Section 5.2. The principal discrepancy in the DCB specimen results was the low crack rates obtained for the plateau velocity of cracks grown in a 3% NaCl environment over a temperature range from 30 to 90 °C. Here crack growth rates from the "pop-in" type starter cracks were comparable with those obtained from water and WSAV environments (Table 13). Further experiments using fatigue pre-cracked specimens, and employing a technique involving regular replacement of the 3%NaCl solution, and cleaning the specimen by washing in an ultrasonic bath, demonstrated an increase in the plateau crack growth rate velocity to a level comparable with the equivalent CT test result.

8) In DCB specimens a number of observations were made during the SEM examination of the fracture surfaces. The principal observations were;

- The presence of crack arrest markings on the fracture surface which was interpreted as evidence that the stress corrosion crack growth was discontinuous.

- Clear photomicrographic evidence of totally brittle separation between the crack faces which was interpreted in terms of a hydrogen embrittlement crack growth mechanism.

- Sub-grain boundary cracking in the DCB specimens near to the SC/overload failure interface which again involved a totally brittle separation between the two crack faces.

9) Hydrogen diffusion experiment results on AlZnMg alloys are reported for two experimental techniques, namely electrochemical hydrogen permeation through a flat membrane and gas chromatographic analysis of hydrogen diffusion into a hollow cylindrical geometry specimen. The electrochemical hydrogen permeation technique was initially validated on steel specimens and comparable results with those published by other workers were obtained.

10) Electrochemical hydrogen permeation experiments were performed on AlZnMg specimens and the results indicated the following:

- Under the experimental conditions employed and using a palladium electroplate on the anodic side of the specimen, pitting of the specimen and consequent solution interaction effects occurred before a permeation transient could be detected.

- From a theoretical analysis of the hydrogen solubilities reported in AlZnMg alloys, and the electrochemical transient characteristics, it was shown that the theoretical hydrogen permeation current would be in the range 0.0025 to $0.06 \mu\text{A cm}^{-2}$ depending upon hydrogen solubility. This theoretical permeation current was between one and three orders of magnitude lower than the lowest background current obtained in the electrochemical permeation experiments.

- The results of a previously reported electrochemical hydrogen permeation experiment on an AlZnMg alloy⁸⁶ were evaluated. The permeation currents reported in these experiments of between 0.56 and $7.8 \mu\text{A cm}^{-2}$, depended upon charging current density and sample thickness. They were between one and three orders of magnitude greater than expected, and were in fact comparable with results obtained during hydrogen diffusion experiments on plain carbon steels. The possibility of pitting corrosion and solution interaction effects playing a greater role in these results⁸⁶ was suggested as a contributory factor. Attention was drawn to the importance of demonstrating electrochemical permeation of hydrogen through AlZnMg membranes. This is due in part to the accepted importance of the technique in hydrogen embrittlement research^{121,163,200} and also the substantial number

of published papers ^{101,106,201} which quote this published ⁸⁶ reference to electrochemical permeation .

11) Hydrogen diffusion through AlZnMg alloy specimens was demonstrated by a technique involving generation of hydrogen as a result of the aluminium-water reaction on the outside surface of a hollow AlZnMg cylinder and measuring the diffused hydrogen using gas chromatography. A numerical solution to the Bessel function equations that describes diffusion in cylindrical geometries was developed in order that a time-lag equation could be employed to determine the hydrogen diffusion coefficient. The following results were obtained;

- Average diffusion coefficient obtained at 25 C in short transverse oriented cylinders was $3.29 \times 10^{-10} \text{ cm}^2 \text{ s}^{-1}$.

- Average diffusion coefficient obtained at 25 C in longitudinal oriented cylinders was $6.20 \times 10^{-10} \text{ cm}^2 \text{ s}^{-1}$.

- Diffusion coefficient obtained at 50 C in a short transverse oriented cylinder was $5.38 \times 10^{-9} \text{ cm}^2 \text{ s}^{-1}$.

- Diffusion coefficient obtained at 70 C in a short transverse oriented cylinder was $1.32 \times 10^{-8} \text{ cm}^2 \text{ s}^{-1}$.

- The activation energy for hydrogen diffusion based upon the above results was $56.7 \text{ kJ mole}^{-1}$.

A further experiment was performed to show that, with the experimental technique employed of withdrawing the gas sample for analysis by syringe through a septum, at room temperature,

hydrogen diffusing into the cylinder is not lost but the partial vacuum formed in the cylinder causes air to diffuse back into the cylinder after sampling. It was proposed that the water vapour contained in this air is responsible for the generation of the small quantities of hydrogen detected in the control cylinder.

12) The reaction rate of water, WSAV or 3% NaCl aqueous solution on a polished 7017 AlZnMg alloy surface at 70 °C was studied in order to determine the rate of hydrogen production in different environments. It was shown that the rate of hydrogen production in water and WSAV environments was similar, but that exposure to 3% NaCl solution resulted in just under a threefold increase in the volume of hydrogen produced per cm² of alloy surface.

It was proposed that the pitting corrosion reaction in a chloride containing solution plays an important role in the stress corrosion cracking of these alloys, not in terms of dissolution of a section of the precipitate free zone as in the anodic dissolution mechanisms of SC crack growth, but in that the anodic dissolution reaction in a chloride solution results in an increased environmental hydrogen fugacity where crack extension is by a hydrogen embrittlement mechanism. The relationship between activation energy for SC crack growth, hydrogen diffusion in AlZnMg alloys, and the mechanism of crack growth is discussed in Sections 5.4 and 5.5.

13) The surface reactions occurring during the exposure of AlZnMg alloy surfaces to water, WSAV and 3% NaCl were studied using conventional SEM imaging and in the SEI imaging mode on a

scanning-transmission electron microscope. Blister formation and growth as a result of hydrogen production as previously reported for high purity alloy AlZnMg compositions ¹⁴⁵ was noted. However, preferential surface reaction at locations where grain boundaries intersected the sample surface was only observed in isolated instances in the commercial 7017-T651 alloy studied here. This observation was related to other work ¹⁹² which showed that single or double impurity alloying additions to a high purity alloy sample of AlZnMg did reduce the specificity of the grain boundary reaction, expressed as a percentage of the total number of grain boundaries attacked, from 95% in the case of the virgin alloy to 10% in the case of a single iron addition.

14) High resolution SEM microscopy was employed to study the surface of stress corrosion cracks grown in WSAV at ^o70 C. The development of a duplex hydroxide film of pseudoboehmite and bayerite, as identified by their characteristic morphologies, was demonstrated on the fracture surface as a function of the length of exposure to the WSAV environment of different regions of the crack surface after fracture. It was proposed that the absence of grain boundary specificity in the reaction between a commercial AlZnMg alloy and WSAV was probably not significant in the stress corrosion of pre-cracked CT or DCB specimens since the WSAV reaction (or reaction with other aqueous environments) takes place on the crack surface already established. It was noted however that grain boundary specificity may be more significant in the initiation of crack growth in (initially) smooth specimens, such as slow strain rate tensile specimens.

5.2 DISCUSSION OF CT AND DCB CRACK GROWTH RATE EXPERIMENTS.

It is clear that the general form of the crack growth rate versus stress intensity curves for the DCB specimens is similar for all environments investigated, with Stage I crack growth rate decreasing by up to two orders of magnitude over a stress intensity range of up to $5 \text{ MNm}^{-3/2}$. Plateau velocities measured at 30, 50 and 70 C vary by just under an order of magnitude for each 20 C increase in temperature. This is in contrast to results reported by Speidel^{63,72} which show a form of curve (see for example Figure 13 for a 7079 alloy in Section 2.3.1) in which the plateau velocity over a test temperature range from -11 C to 105 C varies by just over one order of magnitude.

In contrast, the CT specimen results with the exception of the initially decreasing crack growth rates observed in water and WSAV at 70 C, exhibit a number of different forms of crack growth rate curve including double plateaus (H₂O at 50 and 60 C, Fig 55), pronounced stage I crack growth over 10 - 15 $\text{MNm}^{-3/2}$ (3%NaCl at 90 C, Fig 56), and crack growth up to stress intensities greater than the fracture toughness of the alloy, 25 $\text{MNm}^{-3/2}$, (3%NaCl at 70 and 90 C, Fig 56).

Crack growth under conditions of increasing stress intensity, as found in a CT specimen experiment, is more realistic in terms of the normal mode of failure of engineering structures. The apparent consistency and characteristic form of a set of DCB specimen results, where the geometry of the specimen precludes crack growth above K_{IC} , should therefore be regarded with caution,

if the results are to be applied to the assessment of an engineering structure.

The initial period of slow crack growth observed in a number of DCB results (H_2O at $30^\circ C$, $50^\circ C$ and $90^\circ C$, $3\frac{1}{2}\%NaCl$ at $30^\circ C$ and $50^\circ C$, Figs 109 and 111) may be as a result of a slow transition process by which the stress corrosion crack develops from the mechanical "pop-in" pre-crack. This hypothesis is supported by the SEM photomicrograph presented in Figure 122. Large vertical discontinuities are evident in the region where the "pop-in" pre-crack transforms into a stress corrosion crack. The former crack is primarily transgranular, whereas the latter is intergranular. For a stress corrosion crack to initiate, therefore, it must "find" an intergranular crack plane. This requires either transgranular stress corrosion (a very slow process) or a mixed mode of intergranular stress corrosion and mechanical rupturing of the remaining ligaments. In this case mechanical rupturing of remaining ligaments in the short transverse direction is the probable mechanism, assisted by transgranular stress corrosion. The transition to stress corrosion from a fatigue pre-crack is more uniform as shown in Figures 69 and 70 for a CT specimen, where the initial stress intensity is lower, as evidenced by the DCB results obtained when fatigue pre-cracking is employed. Indeed, Figure 116 shows no evidence of a period of decreased SC crack growth. There is also evidence of stage III crack growth in the fatigue pre-cracked DCB specimens.

It is proposed that, for DCB specimens, the combination of fatigue pre-cracking procedures, promoting a more rapid transition to stress corrosion crack growth from the fatigue pre-crack, and regular cleaning of DCB specimens undergoing stress corrosion crack growth in an aqueous chloride environment, allowing access of the chloride ion to the crack tip, both act to increase the observed plateau SC crack growth velocity to a value comparable to that obtained in CT specimen tests.

An additional feature of the "pop-in" pre-cracked DCB specimens is the pronounced bow that is formed during stress corrosion. As crack growth rates are based on measurements taken at the same time for tests conducted at any one temperature, and secondly as crack lengths have been measured on the specimen sides, and the average stress corrosion crack lengths calculated assuming that the bow disappears linearly as the stress corrosion crack grows, in accordance with the procedure outlined in Section 3.3.4, all stress corrosion crack lengths are calculated on an equivalent basis. The bowed stress corrosion crack may be expected to show an initially fast and decreasing crack growth rate as the crack assumes a straighter profile. The observed increase in crack growth rate, to attain the plateau velocity, seen in some tests is therefore a separate feature associated with the time taken for mechanical rupturing and stress corrosion of transgranular ligaments.

The feature observed in CT specimens of regions of ductility at high stress intensities has been noted by other workers⁸⁴, where at high values of K and at high crack growth rates, the mechanical factor becomes dominant and the fracture surface displays features of stress corrosion (intergranular fracture) and of overload fracture (microvoid coalescence). A possible mechanism may involve bursts of unstable fracture which are subsequently arrested in higher toughness regions where (relatively) fast stress corrosion is re-established. Higher toughness in these regions may result from a reduced susceptibility to hydrogen embrittlement, e.g. due to the extent of magnesium segregation in this region of grain boundary, if a HE mechanism is dominant. Alternatively, it may result from regions of tougher material due to the physical metallurgy of these areas in the alloy, e.g. second phase particle size and distribution, if stress corrosion is as a result of an anodic dissolution mechanism.

DCB specimens that had been fatigue pre-cracked exhibited a dramatic reduction in the extent of secondary cracking as shown in Figures 190 and 191. The lower values of crack growth rate obtained in the tests performed under constant displacement from a "pop-in" failure in 3%NaCl could also result from secondary cracking reducing the effective stress intensity operating at the crack tip, K_{eff} , from that calculated simply from the applied stress, the specimen geometry and the crack length. It has been proposed⁶³ that macroscopic crack branching occurs only for $K_{app} > 1.4 K_{pl}$, where K_{app} is the stress intensity calculated from

MAJOR STRESS CORROSION CRACK SURFACE

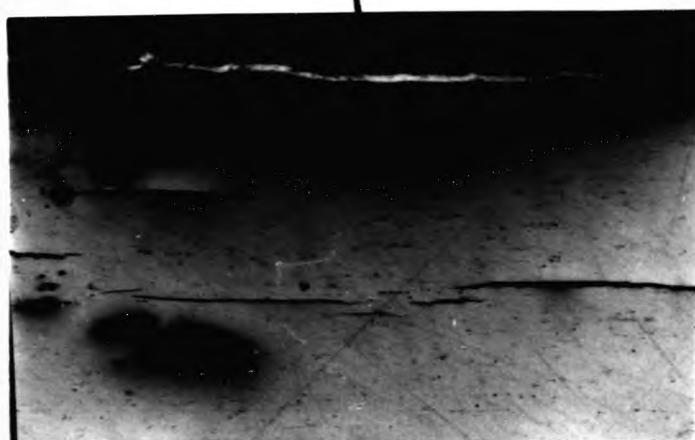


Fig.190 Metallographic section taken perpendicular to the stress corrosion crack direction showing extensive crack branching with a pop-in starter crack (No 8, 3%NaCl 50°C).
(Mag x 100)



Fig.191 Metallographic section taken perpendicular to the stress corrosion crack direction showing no crack branching in a fatigue pre-cracked specimen (No 14, 3%NaCl 70°C).
(Mag x 120)

the applied stress, the specimen geometry and the crack length and K_{pl} is the stress intensity factor at which the independent stage II plateau velocity begins. In a constant displacement test typically started at a high K_{app} value, crack branching effects can be expected to be present from the start of testing; while with an increasing K test procedure, crack branching effects should only be present towards the end of the test, where in particular they could cause stage II crack growth to appear longer than it really is. The present results indicate that a stress corrosion crack grown from an overload "pop-in" pre-cracking procedure tends to transform into a multitude of closely spaced parallel stress corrosion cracks rather than into a single crack. Although strictly speaking not a crack blunting effect, this phenomenon can be considered to cause blunting of the major SC crack as a result of tearing or cracking in the short transverse direction between the individual microscopic cracks, which are oriented perpendicular to this direction and which individually have sharp crack tips.

A fatigue pre-cracking procedure, (provided the maximum stress intensity during the fatigue crack growth does not exceed $0.7 K_{IC}$ resulting in a large plastic zone at the crack tip) can reduce the effects of crack branching by reducing the discontinuity between the starter crack and the subsequent stress corrosion crack grown from it. In the DCB results reported here the maximum stress intensity during fatigue crack growth was 0.23

-3/2
MHe .

The bolt loaded DCB specimen is a more practical specimen than the constant load CT specimen. However, it is necessary to minimise the effects tending to cause $K_{app} \neq K_{eff}$. The principal effect discussed above is the tendency of crack branching to cause K_{eff} to be less than K_{app} . Other effects tending to cause $K_{app} \neq K_{eff}$ include residual stresses in the vicinity of the crack tip and oxide wedging which can in particular influence stage I crack growth when the crack velocity is highly sensitive to K_{eff} and the low SC crack velocities can favour the build up of significant thicknesses of corrosion product. However, the high gradients for stage I recorded for DCB tests in the present work, which were steeper than those recorded in the CT specimen results, indicate that there was no significant influence of corrosion product wedging effects.

It is thought preferable that results obtained in constant displacement tests be checked by performing a limited number of tests involving an increasing stress intensity procedure. Results obtained on constant displacement samples which do not show a well defined plateau, or which show crack growth rates passing through a maximum at an intermediate stress intensity value should be regarded as suspect and such results should be verified.

0

5.3 ANOMALOUS CRACK GROWTH AT 70 C IN WATER AND WSAV.

The three mechanisms proposed in Section 4.2.3 to account for the anomalous crack growth in water and WSAV are repeated below and critically discussed.

1) The transition between the transgranular fatigue pre-crack and a completely intergranular stress corrosion crack proceeds at an initially fast crack growth rate at low stress intensities until the remaining transgranular ligaments in the crack path effectively pin the SC crack front, resulting in a reduction in crack growth rate. This process occurs until, at high stress intensities, the pinning of the SC crack front by transgranular ligaments is overcome and crack growth increases again at some intermediate stress intensity.

No evidence was found of transgranular ligaments that were either fractured by a tearing mechanism or were subject to dissolution or transgranular stress corrosion in the SEM fractography that was performed. The transition between the transgranular fatigue pre-crack and the stress corrosion crack was similar to that observed in other environments (e.g. Figs 69 and 70 for stress corrosion in water at 90 C) where no period of decreasing crack growth rate was observed.

The transition itself, as discussed in Section 5.2, may indeed involve slow transgranular stress corrosion in order to establish stress corrosion crack growth on the most favourably oriented grain boundary. However, the process is accomplished probably

within a distance of some 60 μm as indicated on Figure 69 and not the 2-3 mm of stress corrosion crack growth observed in specimen 29, where the CT test was halted immediately after the period of decreasing crack growth rate in WSAV at 70 C. This situation is different from that pertaining in some DCB tests where at high initial stress intensities a rapid increase in crack growth rate is noted until the plateau crack growth rate velocity is reached. Here the SEM photomicrograph shown in Figure 122 shows evidence of mechanical rupturing of transgranular ligaments in a direction normal to the stress corrosion crack growth direction.

2) The second mechanism assumes that the alloy is undergoing additional ageing at 70 C during the SCC experiment and that the additional grain boundary precipitate growth results in increased gettering of the available hydrogen, assuming that a hydrogen embrittlement mechanism is operating. This process, of tying up hydrogen in overaged grain boundary precipitates, and thereby increasing the critical concentration of hydrogen necessary for further crack extension results in a decrease in crack growth rate if the availability of hydrogen is not increased. The process is overcome at intermediate stress intensities when the grain boundary precipitates become saturated and/or cease growing after a period of time at 70 C, with the effect that the SC crack growth rate increases as more hydrogen becomes available for grain boundary embrittlement. The proposal of this mechanism is based upon some of the research discussed by Christodoulou and Flower⁷⁰, Tuck⁹⁸ and Scamans¹³⁷ and reviewed earlier (Section 2.4.1).

They propose that the grain boundary precipitate in AlZnMg alloys acts as a sink for hydrogen and that a layer of magnesium, preferentially diffused to the grain boundary, forms a planar layer of magnesium hydride which is responsible for the observed embrittlement. In addition, the overaged grain boundary precipitate acts as a better sink for hydrogen than under or peak aged grain boundary precipitates.

Thus a dynamic process can be postulated where the hydrogen available for embrittlement varies during the course of the stress corrosion test on a CT specimen as a function of changes in the physical metallurgy of the alloy. This mechanism could explain the temperature specificity of the observed decreasing crack growth rate, in that sufficient ageing of the grain boundary precipitates does not take place below 70 °C, and at temperatures above 70 °C sufficient hydrogen is generated to overcome the gettering effect of the grain boundary precipitates. In addition, the environmental specificity could be explained in a similar manner, in that the hydrogen production rate experiments on smooth AlZnMg alloy surfaces show that three times the quantity of hydrogen is generated in a chloride environment at the same temperature when compared with water or NSAV environments.

However, measurement of grain boundary precipitate size in 7017-T651 alloy before and after a period of 24 hours at 70 °C failed to show any increase in the grain boundary precipitate size above

a range of 200 - 300 Å in length x 120 - 160 Å wide, see Figures 192 and 193, nor any decrease in hardness of the alloy after 24 hours at 70 °C below a range of 154 - 160 HV₂₀ as a result of overageing. It was therefore concluded that this mechanism could not explain the observed decreasing crack growth rate at low to intermediate stress intensities, followed by an increase in the crack growth rate at intermediate to high stress intensities.

3) The third and most probable mechanism involves local plastic deformation in the region ahead of the crack tip as a result of hydrogen induced delayed plasticity (HIDP) which causes a reduction in the SC crack growth rate. This local plastic deformation occurs at low to intermediate stress intensities. HIDP has been observed by other workers¹⁹⁹ in DCB specimens of 7475-T651 AlZnMgCu alloy tested in a chloride-chromate solution at 20 °C. Here crack growth rate during Stage II was observed to decrease and subsequently increase by over an order of magnitude.

The HIDP has been attributed to environmental or hydrogen interaction with dislocation nucleation processes and slip band formation. A reduction in crack growth rate is observed because plastic deformation processes are substituting for crack growth.

The above results were obtained as a result of employing a shadow optical caustic technique which enables stress intensity factors to be determined independent of their calculation from a knowledge of load, crack length and specimen geometry. The shadow optical caustic enables an optical measurement of the



Fig.192 TEM photomicrograph of grain boundary precipitates in 7017-T651 alloy, as-received plate. Electron beam 100 kV. Mag. 100,000 X

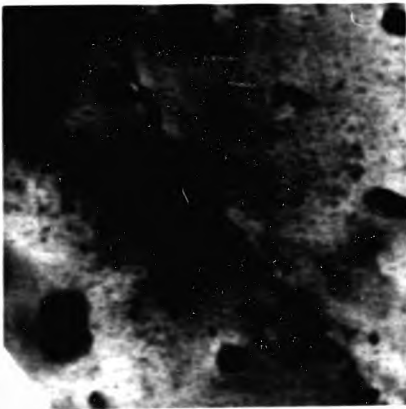


Fig.193 TEM photomicrograph of grain boundary precipitates in 7017-T651 alloy after ageing at 70°C for 24 hours. SC test duration in water or WSAV at 70°C is between 14.7 and 24.5 hours. Electron beam 100 kV. Mag. 120,000 X

stress intensification at the crack tip to be made, and details of the experimental technique and procedure are given elsewhere ²⁰² .

The use of a shadow optical caustic technique requires that the stress intensity value obtained by this technique, K_{opt} , is not affected by environmental effects at the crack tip. However, during the progress of the stress corrosion tests, the authors reported ¹⁹⁹ swelling of the caustic diameter, indicating an apparent increase in stress intensity, and an associated decrease in SC crack velocity was observed. This effect was fully reproducible. The authors of this work suggested ¹⁹⁹ that the so-called stage II crack velocity plateau is not constant but fluctuates and that this process may well be responsible for the scatter reported during stage II cracking for pre-cracked stress corrosion experiments ¹⁹⁹ .

It is recommended that a continued development of the shadow optical caustic technique includes its application to CT geometry specimens in order to demonstrate whether an apparent increase in stress intensity, as measured by the shadow caustic size, occurs during the period of decreasing stress corrosion crack growth rate, and secondly whether the caustic swelling is attributable to local plastic deformation at the crack tip. In addition the technique may be employed to investigate the nature of the environmental and temperature specificity of the phenomenon.

5.4 ACTIVATION ENERGY EXPERIMENTS ON CRACK GROWTH RATES IN CT AND DCB GEOMETRY SPECIMENS.

The activation energies obtained for crack growth between 20 C and 90 C for CT and DCB specimens in water, NSAV and 3%NaCl environments have been summarised in Section 5.1. It is apparent that in general the results obtained are significantly higher than those reported by Speidel⁶³ for crack growth in short transverse DCB specimens of 7079-T651 alloy exposed to 3M KI solution. The specimens in the work reported by Speidel were held at a potential of -450mV vs SHE in a solution of pH6 and crack growth rate experiments were conducted between -11 C and 105 C, see Figure 13. Speidel obtained activation energies of 112.7 kJ mole⁻¹ for stage I crack growth and 15.9 kJ mole⁻¹ for stage II crack growth. A clear inference was made on the basis of these results that different processes were rate controlling in each of these regions of the crack growth rate curve. Possible rate limiting processes proposed¹⁰ were mass transport in the solution filling the crack for stage II with a low activation energy and chemical reaction (anodic dissolution) for stage I with a high activation energy. However, other results reported by Speidel⁷² for the crack growth of a 7039 AlZnMg alloy in distilled water showed an activation energy of 37.6 kJ mole⁻¹ for stage II crack growth. On the basis of similar activation energies for crack growth in distilled water shown by the 7039 alloy and Nimonic 105 alloy, 300M steel and a 12% chromium steel, where hydrogen embrittlement is thought to be the mechanism of stress corrosion crack growth, it was proposed that similar rate

controlling steps for hydrogen entry are involved in all four alloys in a distilled water environment.

In the current work, in particular for DCB specimens at the free corrosion potential with "pop-in" type starter cracks, there are important differences in the characteristics of the crack growth rate versus stress intensity curves which are responsible for the differences in activation energy obtained. The crack growth rate curves reported by Speidel (Fig.13) show a range of plateau velocities differing by just over one order of magnitude for a temperature range of 116 C (between -11 and 105 C), and clearly separated region I plots for each temperature, each with an approximately constant gradient. The present work shows plateau velocities differing by over two orders of magnitude for a temperature range of 60 C (between 30 C and 90 C) for all three environments studied. This leads to higher activation energies than those reported by Speidel. In addition the stage I crack growth is less clearly defined than in Figure 13, with the stage I stress intensity curve at 70 and 90 C crossing in all three environments, and with the gradient of the stage I curve showing a greater variation than in Figure 13.

The results of the activation energy determinations for stage I crack growth are not strictly comparable between environments as the curves obtained prevent comparison of crack growth rates at the same stress intensity, the stress intensity used for the 3%NaCl environment being lower than that used for distilled water or WSAV. However, comparisons of the stage II activation energy-

-3/2

ies are over similar stress intensity ranges of 5 to 20 $\text{MNm}^{-3/2}$. The clear difference between stage I and stage II activation energy determinations on DCB specimens is not apparent with the results for distilled water being very similar (Stage I-73.9 kJ mole^{-1} , stage II-74.8 kJ mole^{-1}) and with the results for WSAV and 3%NaCl showing a trend to higher activation energies for stage I but the stage I activation energy is only a factor of 1.5 greater for WSAV (stage I-114.7 kJ mole^{-1} , stage II-74.2 kJ mole^{-1}) and a factor of 1.7 greater for 3%NaCl (stage I-149.6 kJ mole^{-1} , stage II-89.0 kJ mole^{-1}). This is in contrast to the results presented by Speidel¹⁰ where the stage I activation energy is a factor of 7 higher than the plateau velocity activation energy.

The results of the activation energy determinations on CT specimens, again at the free corrosion potential, show a similar trend in that the stage I and II activation energies in 3%NaCl are similar (stage I activation energy is a factor of 1.1 higher, stage I-114.3 kJ mole^{-1} , stage II-104.6 kJ mole^{-1}). It was only possible to determine the plateau velocity activation energy in distilled water for increasing stress intensity CT specimens (stage II activation energy 55.5 kJ mole^{-1}).

It is proposed therefore, that at the free corrosion potential in 7017-T651 alloy, similar rate controlling processes are responsible for crack growth both during stage I and stage II of the specimen life. The activation energy for hydrogen diffusion

-1

in the current work was found to be approximately 60 kJ mole⁻¹ which is lower than the activation energy for crack growth (with the exception of distilled water in CT specimens). It is likely therefore that some other process, possibly the aluminium-water reaction to generate hydrogen or hydrogen entry into the material, is rate controlling. Bernard and Randall¹⁴² have proposed that inward diffusion of water through the oxide film is the rate controlling process in the reaction between aluminium and water.

There is a second trend apparent of increased activation energy for crack growth in 3%NaCl, and it is recommended that further work takes place to determine the activation energy for the AlZnMg - water reaction in a chloride environment and that this is compared with the activation energy for AlZnMg - water reactions and AlZnMg - WSAV reactions in the absence of chloride ions.

As discussed earlier, (Section 4.5.1), the increased hydrogen fugacity as a result of the reaction between water and a 7017 AlZnMg alloy surface in the presence of chloride ions may account for the increased crack growth velocities observed. Increased hydrogen fugacity, as a result of chloride ion activity, is probably due to chloride ions undermining the barrier layer formed on aluminium alloy surfaces and removing corrosion product from the metal surface. This results in the exposure of a fresh metal surface, and allows access of the environment to the crack tip, with a consequent increase in the hydrogen evolution

reaction rate. Removal of corrosion product from the crack tip probably involves the formation of soluble aluminium chloride from the insoluble aluminium hydroxides present in the SC crack, followed by acid hydrolysis of the aluminium chloride and a subsequent decrease in the pH to around pH 3.5. The reduction in pH increases the hydrogen ion concentration and favours increased nascent hydrogen generation as discussed in Section 4.5.1.

In DCB specimens, where SC crack growth is in 3%NaCl, the corrosion product forms an adherent, compact film on the SC crack surfaces. An additional measure of regular cleaning of the DCB specimen is required to allow solution access to the region of the crack tip.

The similarity of the SC crack growth mechanism and therefore possibly the rate controlling processes in both region I and II during the stress corrosion of AlZnMg alloys has been proposed by Scamans¹⁰⁴. This is on the basis of studies of crack arrest markings in different AlZnMg alloys and over different regions of the stress corrosion crack surface, corresponding to low - region I and high - region II stress intensities. The spacing between crack arrest markings is constant for a given alloy composition and independent of applied stress intensity. The accelerated crack growth in region II is therefore due to an increased frequency of crack jump, but the mechanism of crack advance remains the same.

5.5 STRESS CORROSION CRACK PROPAGATION IN AlZnMg ALLOYS.

The literature survey has shown that there is support in the literature for mechanisms of crack growth in AlZnMg alloys which are primarily based upon anodic dissolution or hydrogen embrittlement. A major limitation that plagues all studies of hydrogen embrittlement, and which has not been resolved in the present work, involves the inability to quantitatively analyze for the critical concentration of damaging hydrogen. There is substantial evidence that the major portion of hydrogen in a material is not available for damage and therefore, in order to correlate the effects of damaging hydrogen with other environmental or metallurgical attributes, the concentration of damaging hydrogen must be determined. However, the determination of mechanism proceeds by the proposal of hypotheses and establishing whether the hypotheses or any deductive consequences correspond to reality. It is therefore proposed here to discuss a mechanism for crack growth in AlZnMg alloys and to indicate the contribution of the present work to this task.

It is proposed that environmentally assisted crack growth occurs by a combination of anodic dissolution and hydrogen embrittlement. Anodic dissolution plays a role in the generation of the hydrogen necessary to cause embrittlement. Using as an example the growth of an established stress corrosion crack in an AlZnMg alloy in NSAV, the growth of the crack is illustrated in Figure 194. Starting with "clean" grain boundary surfaces shown in (I) and a region of uncracked grain boundary to the right, filming of the grain boundary surface occurs with the

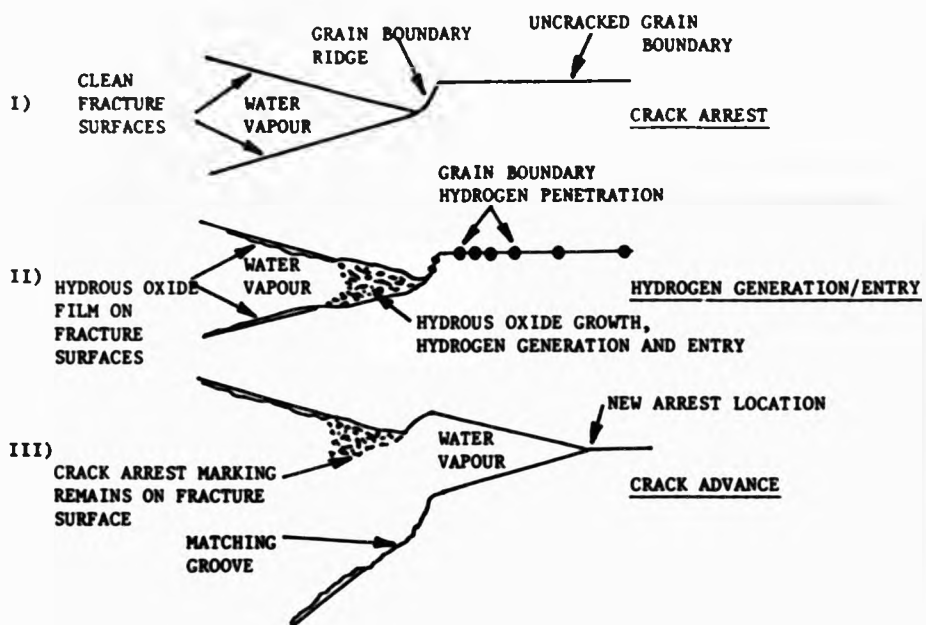


Fig.194 Schematic representation of stress corrosion crack growth in an AlZnMg alloy.

formation of a hydrous oxide film as a result of reaction with water vapour as discussed in Section 4.5.2. At the crack tip, reaction with water vapour on both faces of the parted grain boundary surfaces results in the formation of a volume of boehmite/pseudoboehmite²⁰³ depending upon temperature (II). The low secondary electron emissivity of these hydrous oxides is responsible for the contrast observed in the fracture morphology. The observation of a striated fracture surface has been reported in Section 4.3.4 (and see reference 102). The striations observed on the fracture surfaces in Figures 129 and 130 were observed where crack growth had taken place in laboratory air at a relative humidity of 48-62%, where the relatively non-corrosive nature of the environment has assisted in making the striations visible on the fracture surface and not obscured by corrosion product.

The reaction with water vapour at the crack tip generates hydrogen at the crack tip and additionally on the crack faces as discussed in Section 4.5.1 and 4.5.2. The necessary volume of boehmite/pseudoboehmite to form a striation is probably generated without significant penetration of the crack walls or ahead of the arrested crack tip by corrosion. The fibrilous nature of the product, its inherent low density and the presence of up to 45% of bound water¹⁴⁴ make a significant consumption of aluminium (or magnesium) ions unnecessary.

Hence anodic dissolution plays an important role, not in the dissolution of a section of the precipitate free zone adjacent to the grain boundary, but in the general chemical reaction with aluminium (or magnesium) to generate hydrogen which subsequently embrittles the grain boundary.

Diffusion of atomic hydrogen then takes place along the grain boundary. Diffusion of hydrogen in AlZnMg has been demonstrated, see Section 4.4.3, although this is not direct evidence of the involvement of hydrogen in SC crack growth. Embrittlement as a result of magnesium hydride formation on the grain boundary plane, where preferential magnesium segregation has taken place, has been proposed by Tuck⁹⁸ as previously reported. It seems highly probable that previous reports of the observation of hydrogen permeation through thin membranes of AlZnMg alloy when subject to cathodic polarisation to generate hydrogen on one side of the membrane, and anodic polarisation to detect permeating hydrogen on the reverse side of the membrane, as in the electrochemical hydrogen permeation technique, may be a consequence of perforation of the membranes as discussed in Section 4.4.2.1.

It is suggested that the rate determining step in the process may be the inward diffusion of water through the surface oxide film, after the work of Bernard and Randall¹⁴² in their study of the reaction between aluminium and water.

It has been proposed here (Section 4.5.2) that the absence of grain boundary specificity in the water vapour reaction with plain surfaces of the commercial 7017 AlZnMg alloy is probably not significant with respect to stress corrosion crack growth in pre-cracked specimens, as the reaction site has already been localised at the crack tip by the existing specimen geometry. However, in (initially) smooth surface specimens, e.g. slow strain rate specimens, the specificity of the reaction and the degree of its localisation at grain boundary/surface intersections may be an important factor in the initiation of stress corrosion cracks.

Under the action of the applied stress, the embrittled grain boundary separates (III), leaving the striation formed by the boehmite/pseudoboehmite on the fracture surface. The striation is at the location of crack arrest. The crack remains arrested until sufficient reaction has taken place to generate the hydrogen necessary to cause further embrittlement. The striated fracture surface is therefore evidence of discontinuous crack propagation which is associated with hydrogen embrittlement mechanisms. Scamans¹⁰³ has shown that the striation spacing is not a strong function of the applied stress intensity, being approximately constant at 3700Å per crack jump for the 7017 alloy in the T651 condition, where SC crack growth is in water vapour at 95% relative humidity at 40°C. The crack jump frequency is probably therefore the parameter that changes with stress intensity to give the observed velocity in different regions of the crack growth rate versus stress intensity curve. During

region I the jump frequency would have to be one every 72 seconds (corresponding to a crack growth rate of $5 \times 10^{-9} \text{ ms}^{-1}$) and in region II the jump frequency would have to increase to one every 7.2 seconds (corresponding to a crack growth rate of $5 \times 10^{-8} \text{ ms}^{-1}$). The effect of stress intensity may then be regarded as increasing the hydrogen diffusion velocity or decreasing the amount of hydrogen to cause embrittlement or a combination of both mechanisms. The stress assisted diffusion of hydrogen or the lowering of the critical hydrogen concentration then reduces the time interval between constant lengths of crack jump. In the plateau region the increase in stress assisted hydrogen diffusion may become constant but at a faster, limiting rate, resulting in the observed constant plateau SC crack velocity with a constant crack jump length.

A major advance in understanding the detailed mechanism of hydrogen embrittlement in this alloy system would be achieved by attributing numerical values to the critical hydrogen concentration as a function of stress intensity and the associated hydrogen diffusion coefficients.

Other aspects of the work presented here which give good grounds for a hydrogen embrittlement mechanism, and which have been discussed elsewhere are;

- The stress corrosion crack profile in CT specimens which is normally concave in distilled water environments but is convex when access of the environment to the specimen sides is

prevented. The absence of extended crack growth at the specimen sides when access of the environment to the specimen sides is prevented results from preventing hydrogen access at these locations. The normal SC crack profile in 3%NaCl is convex (see discussion in Section 4.2.1) and the association is made of a convex SC crack profile, where maximum crack growth is at the centre of the specimen, with a hydrogen embrittlement mechanism, where hydrogen is transported as a function of the hydrostatic stress gradient which is also convex. In water vapour or distilled water environments it is proposed that insufficient hydrogen is generated to maintain a convex SC crack profile. Additionally it was noted therefore that;

a) hydrogen entry from the specimen sides plays an important role in the SC crack profile in water and NSAV environments where enhanced SC crack growth takes place at the specimen sides,

and;

b) the concave crack profile associated with an anodic dissolution mechanism, where significant plane stress conditions at the specimen sides leads to increased film rupture and consequent dissolution, might be expected to be more pronounced in a chloride environment which is not the case in the results presented here (Section 4.2.1).

- Secondly, the effect of pre-exposure and pre-charging on SC crack growth in NSAV at 70 °C in CT specimens also gives support to a hydrogen embrittlement mechanism. In these specimens, crack

growth at stress intensities lower than those found in the absence of pre-exposure or pre-charging, and "recovery" effects, were observed as a result of pre-exposure (to NSAV at 70 °C for 50 hours) or pre-charging (at -1.75 V vs SHE for 50 hours in 3% NaCl). Recovery is of the specimen as a whole and is probably as a result of the establishment of an initially higher hydrogen concentration in the region around the fatigue pre-crack tip. Subsequently, after a period of crack growth at a lower stress intensity, the stress corrosion crack tip growth reaches a region of the specimen which has not been exposed to the effects of pre-exposure or pre-charging, and crack growth ceases. As indicated earlier, there is a critical hydrogen concentration associated with a given level of stress intensity and when this critical hydrogen concentration is exceeded crack growth can take place at a lower stress intensity. When SC crack growth takes the SC crack tip into a region where the hydrogen concentration is below the critical level for the new stress intensity, crack growth ceases until the stress intensity is increased. Whilst the halt in crack growth after 1.4 to 1.6 mm is strictly not a recovery process, the specimen recovers from the initial embrittlement as a result of the SC crack having grown through the embrittled region. Such a halt in SC crack growth would not be apparent if anodic dissolution mechanisms were operative as no other changes in the specimen's environment or stress pattern have taken place. The initial embrittlement suffered is probably therefore as a result of the increased hydrogen generated ahead of the fatigue pre-crack by pre-exposure or pre-charging the CT specimen.

6.0 CONCLUSIONS

The principal conclusions of the work carried out are as follows;

- 1) Activation energy determinations indicate that the rate controlling processes for stress corrosion crack growth at the free corrosion potential in 7017-T651 alloy are the same during region I and region II crack growth.
- 2) The observations of pre-exposure and pre-charging effects on stress corrosion crack growth in this alloy are indicative of a hydrogen embrittlement mechanism.
- 3) In addition, other observations of the stress corrosion crack including, the stress corrosion crack profile in different environments, the presence of striations indicating crack arrest on the fracture surface and the observation of otherwise totally brittle fracture, are indicative of a hydrogen embrittlement mechanism.
- 4) Providing care is exercised in the experimental technique, including provision of fatigue pre-cracked starter cracks in DCB specimens, regular replacement of the solution in which crack growth is occurring and regular cleaning of the DCB specimen, similar SC crack growth plateau velocities can be obtained for DCB and CT specimen geometries. This is particularly important in a 3%NaCl environment as opposed to distilled water or NSAV environments, where it is thought that corrosion product prevents access of chloride ions to the DCB specimen crack tip.

5) Measurement of hydrogen permeation through flat specimens of 7017-T651 AlZnMg alloy by the electrochemical permeation technique was shown to be impractical as the theoretical hydrogen permeation current is smaller than the experimentally achievable background current recorded on the anodic side of the permeation membrane.

6) Hydrogen diffusion in the 7017 AlZnMg alloy was demonstrated by a procedure involving generating hydrogen by chemical reaction with an aqueous environment on the outside surface of a hollow cylinder machined from 7017-T651 alloy, and measuring hydrogen diffusing into the cylinder using a gas chromatographic technique. The numerical solution to the Bessel function describing diffusion in cylindrical geometry was derived and the hydrogen diffusion coefficient obtained by a time-lag method. The average diffusion coefficient, D , at 25 C was $3.29 \times 10^{-10} \text{ cm}^2 \text{ s}^{-1}$ for short transverse oriented cylinders.

7) Hydrogen is generated in greater quantities when a 7017-T651 alloy surface reacts with water in a chloride (3%NaCl) solution than the reaction of a 7017-T651 alloy surface with either distilled water or WSAV. The hydrogen produced in a chloride environment is increased by a factor of 2.5. The increased hydrogen fugacity in chloride environments may account for the increased crack growth rates observed in this environment. Anodic dissolution plays an important role in the hydrogen embrittlement of this alloy system in generating the hydrogen on

the alloy surface which subsequently causes embrittlement. However, the dissolution reaction is not specific to a section of the grain boundary or the precipitate free zone.

8) The commercial alloy 7017 in the T651 condition does not exhibit the grain boundary specificity in the reaction with WSAV^o at 70 C which is observed in high purity alloy versions of 7017. However, it is proposed that whilst grain boundary specificity may be important in the initiation of stress corrosion cracking on smooth surfaces, the specificity of the reaction is not important when SC crack growth has been established.

7.0 RECOMMENDATIONS FOR FURTHER WORK

The following recommendations are made for areas where further research is considered to be necessary.

1) Investigation of anomalous crack growth rate versus stress intensity curves in distilled water and NSAV at 70 C with the shadow optical caustic technique to determine whether local plastic deformation is occurring at the stress corrosion crack tip during the period of decreasing crack growth rate.

2) Continued development of the electrochemical hydrogen permeation technique and its application to hydrogen diffusion research in AlZnMg and AlMg alloys. In particular research should address the sensitivity of the anodic circuit by attempting to reduce the anodic background current to a level where it is possible to detect a permeation transient due to diffusing hydrogen. An initial exercise would be an investigation of alternative barriers to anodic dissolution of the permeation membrane other than electroplated palladium. It is suggested that a technique which does not involve electrochemical plating such as ion plating or chemical vapour deposition of palladium onto the AlZnMg alloy substrate, with suitable cooling of the substrate to prevent microstructural changes due to heating, is investigated in the first instance. In addition, the use of alternative anodic cell solutions such as organic electrolytes, e.g. glycol borate should be investigated.

3) As diffusion of hydrogen in AlZnMg alloys is thought to be primarily grain boundary diffusion^{104,136,160,203}, an electrochemical hydrogen permeation technique could then be employed to look at the effect of membrane specimen orientation with respect to the principal working direction of rolled plate, and heat treatment, on the hydrogen diffusion coefficient. In addition, the effect of stress on the hydrogen diffusion coefficient is an important factor in hydrogen embrittlement studies to establish whether stress assisted diffusion of hydrogen is occurring¹⁷⁷ in order to account for the high stress corrosion crack growth rates observed in a number of AlZnMg alloys^{103,104}. The use of stressed electrochemical permeation membranes is a technique that has been employed in the study of hydrogen embrittlement of high strength steels¹⁷⁷.

4) Development of the gas chromatographic and cylindrical specimen geometry hydrogen diffusion technique should take place to determine the effect of different environments, including distilled water and WSAV, and the effect of electrochemical charging and pH on the hydrogen diffusion coefficient. In addition, the effect of heat treatment on the hydrogen diffusion coefficient should be incorporated.

5) The activation energy for the reactions between AlZnMg alloy surfaces and distilled water, WSAV and 3%NaCl should be investigated in order to reconcile the increased activation energy for SC crack growth in chloride environments with the chemical reactions that generate hydrogen in these environments.

REFERENCES

1. Polmear, I.J., *Light Alloys*, Edward Arnold, 1981.
2. Hahn, G.T. and Rosenfield, A.R., *Met.Trans.*, 6A, p.653, 1975.
3. Staley, J.T., *A.S.T.M. S.T.P.* 605, p.71, 1976.
4. Speidel, M.O., *Conference Proceedings 8th I.C.A.F.*, Lausanne, June 2, 1975.
5. Van Horn, K.R., *Aluminium Vol.1*, A.S.M., 1967.
6. Van Lancker, M., *Metallurgy of Aluminium Alloys*, Chapman and Hall, 1967.
7. Pelletier, J.M., Vigier, G. and Guyot, P., *Acta Met.*, 29, p.1335, 1981.
8. Kelly, A. and Nicholson, R.B., *Progress in Mat.Sci.*, Vol.10, p.151, Pergamon Press, 1960.
9. Lorimer, G.W. and Nicholson, R.B., *The Mechanism of Phase Transformations in Crystalline Solids*. Inst.of Metals, London, 1969.
10. Speidel, M.O., *Met.Trans.*, 6A, p.631, 1975.
11. Thomas, G. and Nutting, J., *J.Inst.Metals*, 88, p.81, 1959.
12. Cochran, C.N., *J. Electrochem.Soc.*, 108, 4, p.317, 1961.
13. Viswanadham, R.K., Sun, T.S. and Green, J.A.S., *Corrosion N.A.C.E.*, 36, p.275, 1980.
14. Alwitt, R.S., *Oxide and Oxide Films*, Vol.4, p.169, Marcel Dekker, New York, 1976.
15. Hart, R.K., *Trans.Paraday Soc.*, 53, p.1020, 1957.
16. Ailor, W.H., *Handbook on Corrosion Testing and Evaluation*, John Wiley and Sons, New York, 1971.
17. Raicheff, R.C., Despica, A.R., and Bockris, J.O'M., *J.Chem.Phys.*, 49, p.926, 1969.
18. Champion, F.A., *Symposium on Internal Stresses in Metals and Alloys*, Inst.of Metals, p.468, 1948.
19. Logan, H.L., *J.Res.Natn.Bur.Stand.*, 48, p.99, 1952.
20. Forty, A.J and Humble, P., *Phil.Mag.* 8, p.247, 1963.

21. McBvily, A.J. and Bond, A.P., *J.Electrochem.Soc.*, 112, p.141, 1965.
22. Pinchback, S.P., Clough, S.P. and Heldt, L.A., *Met.Trans.A*, 6A, p.1479, 1975.
23. Pugh, E.N., S.C.C and H.E. of Iron-Base Alloys, *Conf.Proc. N.A.C.E.*, Houston, p.1019, 1977.
24. Swann, P.R. and Pickering, H.W., *Corrosion N.A.C.E.*, 19, p.373, 1963.
25. Harston, J.D. and Scully, J.C., *Corrosion N.A.C.E.*, 25, p.493, 1969.
26. Zapffe, C.A. and Sims, C.E., *Metals and Alloys*, 11, No.5, p.245, No.6, p.177, 1940 and 12, No.1, p.44 and No.2, p.145, 1941.
27. Zapffe, C.A. and Sims, C.E., *Trans.Am.Inst.Mining and Met. Eng.*, 145, p.225, 1941.
28. Van Leeuwen, H.P., *J.Eng.Frac.Mech.*, 6, p.141, 1974.
29. Van Leeuwen, H.P., *Corrosion N.A.C.E.*, 29, p.197, 1973.
30. Troiano, A.R., *Trans.A.S.M.*, 52, p.54, 1960.
31. Troiano, A.R., *Corrosion N.A.C.E.*, 15, p.207, 1959.
32. Troiano, A.R., *Hydrogen in Metals*, A.S.M. Metals Park, Ohio, 1974.
33. John, C.S., *Scripta Met.*, 9, p.141, 1975.
34. Gerberich, W.W. and Chen, Y.T., *Scripta Met.*, 8, p.243, 1974.
35. Gerberich, W.W., *Hydrogen in Metals*, A.S.M., Metals Park, Ohio, 1974.
36. Oriani, R.A. and Josephic, P.H., *Scripta Met.*, 6, p.681, 1972.
37. Oriani, R.A., *Corrosion N.A.C.E.*, 32, p.18, 1976.
38. Oriani, R.A. and Josephic, P.H., *Acta Met.*, 25, p.979, 1977.
39. Oriani, R.A. and Josephic, P.H., *Acta Met.*, 22, p.1065, 1974.
40. Dix, E.H.Jr., *Edward de Mille Memorial Lecture 1949*, *Trans.A.S.M.*, 42, p.1057, 1950.

41. Mears, R.B., Brown, R.H. and Dix, E.H., Jr., Symposium on Stress Corrosion Cracking of Metals, p.329, published jointly by A.S.T.M. and A.I.M.E., 1944.
42. Dix, E.H., Jr., Trans.A.I.M.E., 132, p.11, 1940.
43. Cornish, A.J. and Day, M.R.B., J.Inst.Metals, 99, p.337, 1971.
44. Sedriks, A.J., Green, J.A. and Novak, D.L., Met.Trans., 4, p.1992, 1973.
45. Kent, K.G., J.Aust.Inst.Metals, 15, p.171, 1970.
46. Uswin, P.N.T. and Nicholson, R.B., Acta Met., 17, p.1379, 1969.
47. Petch, N.J., Phil.Mag., 1, p.331, 1956.
48. Foulouse, P.K., Morral, J.E. and McEvily, A.J., Met.Trans., 5, p.1393, 1974.
49. Peel, C.J., PhD thesis, Southampton University, 1977.
50. Peel, C.J., and Poole, P., Mechanisms of Environment Sensitive Cracking of Materials, Conf. Proc Univ. of Surrey, p.147, 4-7 April 1977.
51. Doig, P. and Bington, J.W., Corrosion N.A.C.E., 31, p.347, 1975.
52. Raghavan, M., Met.Trans., 11A, p.993, 1980.
53. Ward, D.E. and Lorimer, G.M., Proc.3rd Int.Conf.on Strength of Metals and Alloys. Inst.of Metals, Vol.1, p.488, 1973.
54. Griffith, A.A., Phil.Trans.Royal Soc., A221, p.163, 1924.
55. Logan, H.L., The Stress Corrosion of Metals, John Wiley, New York, 1966.
56. Parkins, R.N., Met.Review, 9, p.201, 1964.
57. McEvily, A.J., Clark, J.B. and Bond, A.P., Trans.A.S.M., 60, p.661, 1967.
58. Speidel, M.O., Proc.Air Force Materials Laboratory 50th Anniv. Technical Conf. on Corrosion of Military and Aerospace Equipment, Denver, Colorado, (AFML-TR-67-329), F.H. Meyer, Ed., 1967.
59. Holl, H.A., Corrosion N.A.C.E., 23, p.173, 1967.

60. Speidel, M.O., *Phys. Stat. Sol.*, 22, K71, 1967.
61. Scully, J.C., *The Metals Society Int.Conf. on Mechanisms of Environment Sensitive Cracking of Materials*, Univ.of Surrey, April 1977.
62. Scully, J.C., *Corrosion Science*, 20, p.997, 1980.
63. Speidel, M.O., *The Theory of SCC in Alloys* (Ed. Scully, J.C.) N.A.T.O, Brussels, p.289, 1971.
64. Moon, D.H., *Scripta Met.*, 8, p.1436, 1974.
65. Walter, R.J. and Chandler, W.T., *Reports of N.A.S.A. Contract NAS 8-19*, 1969.
66. Wei, R.P., *Int.J.Fracture Mechanics*, 4, p.159, 1968.
67. Nelson, H.G., *N.A.S.A. Technical Note*, D-6691, 1972.
68. Koch, G.H., *Corrosion N.A.C.E.*, 35, p.73, 1979.
69. Wiederhorn, S.M., *J.Am.Ceramic.Soc.*, 50, p.407, 1967.
70. Christodoulou, L. and Flower, H.M., *Acta Met.*, 28, p.481, 1980.
71. Ford, F.P., *Mechanisms of Environment Sensitive Cracking of Materials*, *Conf.Proc.Univ.of Surrey*, p.125, 4-7 April 1977.
72. Speidel, M.O., *Hydrogen in Metals*, *Am.Soc. of Metals*, 1974.
73. Poole, P. and Greenfield, D.C.L., R.A.E., Farnborough, *Technical Report 80117*, 1980.
74. Speidel, M.O. et.al., *Corrosion Fatigue Conf.Proc.*, N.A.C.E., Houston, p.324, 1972.
75. Speidel, M.O., *First Int.Congress on H in Metals. Editions Science et Industrie*, Paris, 1972.
76. Speidel, M.O. and Hyatt, M.V., *Advances in Corr.Sci. & Tech.*, 2, Plenum Press, p.115, 1972.
77. Oriani, R.A., *Berichte Bunsen-Gesellschaft für Physik.Chemie*, 76, p.848, 1972.
78. Oriani, R.A., *SCC and HE of Fe base alloys. Conf.Proc.*, N.A.C.E, Houston, 1974.
79. Brown, B.F., Fujii, C.T. and Dahlberg, E.P., *J.Electrochem. Soc.*, 116, p.218, 1969.
80. Evans, U.R., *J.Electrochem.Soc.*, 103, p.73, 1956.

81. Hoar, T.P., *Trans.Faraday Soc.*, 45, p.683, 1949.
82. Sedriks, A.J., Green, J.A.S., and Novak, D.L., *Localised Corrosion, Conf.Proc., N.A.C.E., Houston*, p.569, 1971.
83. Nguyen, T.H., Brown, B.F. and Foley, R.T., *Corrosion N.A.C.E.*, 38, p.319, 1982.
84. Hartman, A., National Aerospace Laboratory - The Netherlands. Report No. NLR TR 76042 U part III, *Study of the Growth of Stress Corrosion Cracks in Aluminium Alloy 7075*, 1976.
85. Brown, B.F., *Theory of SCC in Alloys (Ed., Scully, J.C.)*, p.186, N.A.T.O., Brussels, 1971.
86. Gest, R.J. and Troiano, A.R., *First Int. Congress on H in Metals, Paris. Editions Science et Industrie*, p.427, 1972.
87. Berggreen, J. PhD Thesis, Univ.of Erlangen-Nürnberg, 1973.
88. West, J.M., *Electrodeposition and Corrosion Processes, Van Nostrand Reinhold*, 1971.
89. Green, J.A.S., Hayden, H.W. and Montague, W.G., *Effect of Hydrogen on Behaviour of Materials. The Metallurgical Soc. of A.I.M.E., New York*, p.200, 1976.
90. Wilde, B.E. and Kim, C.E., *Corrosion N.A.C.E.*, 28, p.530, 1972.
91. Hardie, D., Holroyd, N.J.H., and Parkins, R.N., *Metal Science*, p.603, November 1979.
92. Green, J.A.S. and Montague, W.G., *Corrosion N.A.C.E.*, 31, p.209, 1975.
93. Chen, J.M., Sun, T.S., Viswanadham, R.K. and Green, J.A.S., *Met.Trans.A*, 8A, p.1935, 1977.
94. Viswanadham, R.K., Sun, T.S. and Green, J.A.S., *Met.Trans.A*, 11A, p.85, 1980.
95. Viswanadham, T.K., Sun, T.S. and Green, J.A.S., *Martin Marietta Laboratories Research Report MML TR 78-37C, Grain Boundary Segregation in Al-Zn-Mg alloys - Implications to Stress Corrosion Cracking*, 1978.
96. Scamans, G.M., Alani, R., and Swann, P.R., *Corr.Sci.*, 16, p.443, 1976.
97. Alani, R. and Swann, P.R., *Br.Corr.J.*, 12, p.80, 1977.

98. Tuck, C.D.S., Conf.Proc., Third Int.Conf. on the Effect of Hydrogen on the Behaviour of Materials, Jackson, Wyoming, 1980.
99. Chaturvedi, M.C. and Malis, T., J. Mat. Sci., 17, p.1479, 1982.
100. Montgrain, L. and Swann, P.R., In Hydrogen in Metals, Eds. Bernstein, I.M. and Thompson, A.W., A.S.M., p.575, 1974.
101. Scamans, G.M., Scripta Met., 13, p.245, 1979.
102. Scamans, G.M., Met.Trans., 11A, p.846, 1980.
103. Scamans, G.M., Conf.Proc. Third Int.Conf. on the Effect of Hydrogen on the Behaviour of Materials, Jackson, Wyoming., p.467, 1980.
104. Scamans, G.M., Alcan Laboratories Report - Stress Intensity and Heat Treatment Effects on Stress-Corrosion Crack Propagation in AlZnMg Alloys.
105. Holroyd, N.J.H. and Hardie, D., Conf.Proc. Third Int.Conf. on Effect of Hydrogen on the Behaviour of Materials, Jackson, Wyoming, p.449, 1980.
106. Holroyd, N.J.H. and Hardie, D., Corrosion Science, 21, p.129, 1980.
107. Holroyd, N.J.H. and Hardie, D., Conf.Proc. Third Int. Congress on Hydrogen in Metals, Editions Science et Industrie, Paris, 1982.
108. Green, J.A.S. and Hayden, H.W., Hydrogen in Metals (Bernstein, I.M. and Thompson, A.W. Eds.) A.S.M., Metals Park, Ohio, p.235, 1974.
109. St John, C. and Gerberich, W.W., Met.Trans., 4, p.589, 1973.
110. Pickens, J.R., Gordon, J.R. and Christodoulou, L. Stress Corrosion and Hydrogen Embrittlement in P/M x7091 and I/M 7075, Martin Marietta Laboratories, Baltimore, USA, 1982.
111. Cailletet, L., Compt.Rend., 58, p.327, 1864.
112. Graham, T., Phil.Trans.Roy.Soc., p.136, p.156, p.349, p.415, p.573, 1866.
113. Sieverts, A., Z.Physik.Chem., 60, p.169, 1907.
114. Sieverts, A., Krumphar, W., Z.Physik.Chem., 74, p.277, 1910.

115. Sieverts, A., Zape, G. and Moritz, H., *Z.Physik.Chem.*, A183, p.19, 1938.
116. Heyen, E., *Stahl U. Eisen*, 21, p.913, 1901.
117. Heyen, E., *Metallographist*, 6, p.39, 1903.
118. Melnick, L.M., Lewis, L.L. and Holt, B.D. (Eds), *Determination of Gaseous Elements in Metals*, Chemical Analysis Monographs, 40, John Wiley & Sons, London.
119. Edwards, R.A.H. and Eichenauer, W., *Scripta Met.*, 14, p.971, 1980.
120. Bodenstein, M., *Z.Electrochem.*, 28, p.517, 1922.
121. Wach, S.P. and Miodownik, A.P., *Trans.Faraday Soc.*, 66, p.2334, 1970.
122. de Kaczincy, F., *Jerncotorets Ann.*, 139, p.466, 1955.
123. Barrer, B.M., *Discussions of the Faraday Soc.*, 4, p.68, 1948.
124. Smialowski, M., *Neu Hutte*, 2, p.621, 1957.
125. Bastien, P.G., *Arch.Huttniewa*, 4, p.93, 1959.
126. Oriani, R.A., *Proceedings of Conference on Fundamental Aspects of Stress Corrosion Cracking*, Ohio State University, 1967, p.32. Published by N.A.C.E, 1969.
127. Gest, R.J., and Troiano, A.R., *Corrosion N.A.C.E.*, 30, p.274, 1974.
128. Hattori et.al., *J.Iron & Steel Inst.*, Japan, 58, 59, p.567, p.132, 1972, 1973.
129. Borisova, N.S., and Amosova, L.M., *Fiz-Khim Mekh.Mater.*, 12, p.10, 1976.
130. Darken, L.S. and Smith, R.P., *Corrosion N.A.C.E.*, 5, p.1, 1949.
131. Shigeru Asano, Kazuhisa Hara, Yoichi Nakai and Nanio Ohtani, *J.Japan. Inst.Metals*, 38, p.626, 1974.
132. Hill, M.L. and Johnson, E.W., *Trans.A.I.M.E.*, 215, p.717, 1959.
133. Vaughan, H.G. and de Morton, M.E., *Brit.Weld.J.*, 4, p.40, 1957.
134. Newman, J.F. and Shreir, L.L., *J.Iron and Steel Inst.*, 207, p.1369, 1969.

135. Tetleman, A.S. and Robertson, W.D., *Acta Met.*, 11, p.415, 1963.
136. Edwards, R.A.H. Conf.Proc. Third Int. Congress on Hydrogen and Materials, Editions Science et Industrie, Paris, 1962.
137. Scamans, G.M., *J.Materials Sci.*, 13, p.27, 1978.
138. Peterson, J.A., Gibala, R. and Troiano, A.R., *J.Iron and Steel Inst.*, Jan, p.86, 1969.
139. Whiteman, M.B. and Troiano, A.R., *Physica Status Solidi*, 2, p.7, 1964.
140. McBreen, J. and Genshaw, M.A., Conf.Proc. Fundamental Aspects of Stress Corrosion Cracking, Ohio State University, 1967, p.51. Published by N.A.C.E. 1969.
141. Bye, G.C. and Robinson, J.G., *Chem. and Ind.*, p.687, 1963.
142. Bernard, W.J. and Randall, J.J., *J.Electrochem Soc.*, 107, p.483, 1960.
143. Alwitt, R.S. and Archibald, L.C., *Corr.Sci.*, 13, p.687, 1973.
144. Vedder, W. and Vernilyea, D.A., *Trans.Faraday Soc.*, 65, p.561, 1969.
145. Scamans, G.M. and Rehal, A.S., *J.Mat.Sci.*, 14, p.2459, 1979.
146. Langmuir, I., *J.American Chem.Soc.*, 40, p.1361, 1918.
147. Taylor, H.S., *J.American Chem.Soc.*, 53, p.578, 1931.
148. Schertz, A.E. and Robertson, W.D., *Corrosion N.A.C.E.*, 13, p.437, 1957.
149. West, C. and Zener, C., *Phys.Review*, 67, p.1169, 1949.
150. Johnson, E.W. and Hill, M.L., *Trans. A.I.M.E.*, 218, p.1104, 1960.
151. Kass, W.J., Effect of Hydrogen on the Behaviour of Materials, p.327, 1976.
152. Louthan, W.R. et.al., Effect of Hydrogen on the Behaviour of Materials, p.337, 1976.
153. Oriani, R.A., *Acta Met.*, 18, p.147, 1970.
154. McNabb, A. and Foster, P.K., *Trans.T.M.S.-A.I.M.E.*, 227, p.618, 1963.

155. Foster, P.K., McNabb, A. and Payne, C.M., *Trans.T.M.S.-A.I.M.E.*, 233, p.1022, 1965.
156. Caskey, G.R. and Pillinger, W.L., *Met.Trans.A*, 6A, p.467, 1975.
157. Papp, K. and Kovacs-Csetényi, E., *Scripta Met.*, 11, p.921, 1977.
158. Eichenauer, W. and Pebler, A., *Z.Metallk.*, 48, p.373, 1973.
159. Ransley, C.E. and Talbot, D.E.J., *J.Inst.Metals*, 86, p.212, 1958.
160. Scamans, G.M. and Tuck, C.D.S., *Second Int.Congress on Hydrogen in Metals*, Editions Science et Industrie, Paris, 1977.
161. Holroyd, N.J.H. and Hardie, D., *Corrosion Science*, 23, p.527, 1983.
162. Radhakrishnan, T.P. and Shreir, L.L., *Electrochimica Acta*, 12, p.889, 1967 and 11, p.1007, 1966.
163. Devenathan, M.A.V. and Stachurski, Z.O.J., *J.Electrochem.Soc.*, 111, p.619, 1964.
164. McBreen, J., Nanis, L. and Beck, W., *J.Electrochem.Soc.*, 113, p.1218, 1966.
165. Methods of Test for Plane Strain Fracture Toughness (K_{IC}) of Metallic Materials, British Standards Institution, B.S.5447, 1977.
166. International Standards Organisation Document No.156/WG2N45. Recommendation for Making and Using Pre-cracked Specimens for Stress Corrosion Tests, 1980.
167. Smith, H.R. and Piper, D.E., *Boeing Report*, D6-24872, 1970.
168. Mostovsky, S., Crosky, P.B. and Ripling, E.J., *J.of Materials*, 2, p.661, 1967.
169. Peel, C.J. and Poole, P., R.A.E., Farnborough, Technical Report 80046, 1980.
170. Devanathan, M.A.V. and Stachurski, Z.O.J., *Proc.Royal Society*, A270, 90, 1962.
171. Ives, D.J.G. and Janz, G.J., *Reference Electrodes, Theory and Practice*, Academic Press, London, p.403, 1961.
172. Scrawley, J.E., *Int.J. of Fracture*, 12, p.475, 1976.
173. Devanathan, M.A.V., O.N.R. Technical Report No.4, 1961.

174. Holroyd, N.J.H., Alcan International Laboratories, Banbury, private communications.
175. Van Leeuwen, H.P., Corrosion N.A.C.E., 31, p.42, 1975.
176. Sprowls, D.O., Coursen, J.W. and Walsh, J.D., A.S.T.M.- S.T.P. 610, p.143, A.S.T.M., Philadelphia, 1976.
177. Seimbhi, T.S., PhD thesis, Effect of Structure and Tensile Stress on Hydrogen Permeation Through High Strength Steels., City of London Polytechnic, 1977.
178. Ibrahim, I.W., MSc thesis, The Effect of Polarisation Conditions on the Transport of Hydrogen through Mild Steel Membranes, City of London Polytechnic, 1979.
179. Craig, I.H., PhD thesis, Some Mechanistic Aspects of the Environmental Sensitive Cracking of an 18Ni Maraging Steel., University of Newcastle, 1977.
180. Barth, C.F., Steigerwald, E.A., and Troiano, A.R., Corrosion N.A.C.E., 25, p.353, 1969.
181. Shively, J., Corrosion N.A.C.E., 23, p.215, 1967.
182. Wild, B.E., Corrosion N.A.C.E., 27, p.326, 1971.
183. Gileadi, E., Fullenwider, M.A. and Bockris, J.O'M., J. Electrochem.Soc., 113, p.926, Sept.1966.
184. Gest, R., PhD thesis, Environmental Induced Failure of a High Strength Aluminium Alloy, Case Western Reserve University, 1972.
185. Crank, J., The Mathematics of Diffusion, 2nd Ed., Clarendon Press, Oxford, 1975.
186. Barrer, R.M., Diffusion in and Through Solids, Cambridge University Press, 1941.
187. Hewlett-Packard HP-41, Users Library Solutions, High Level Maths, Revision D, November 1982.
188. Irwin, G.R., Fracture Dynamics, Fracturing of Metals, A.S.M., 1948.
189. Balluffi, R.W., Met.Trans.B, 13B, p.527, 1982.
190. Pryor, M.J., J.Oxid.Metals, 3, p.271, 1971.
191. Taylor, I.T., and Edgar, R.L., Met.Trans., 2, p.833, 1970.

192. Tuck, C.D.S. and Scamans, G.M. Third International Congress on Hydrogen and Materials, p.665, Editions Science et Industrie, Paris, 1982.
193. Mueller, M., Bernstein, I.M. and Thompson, A.W., Scripta Met., 17, p.1039, 1983.
194. Albrecht, J., McTierman, B.J., Bernstein, I.M. and Thompson, A.W., Scripta Met., 11, p.893, 1977.
195. Blain, J., Mascunave, J. and Dickson, J.I., Corrosion Science, 24, p.1, 1984.
196. Dorward, R.C. and Hasse, K.R., Int.J.Fracture, 14, p.R31, 1978.
197. Hunter, M.S. and Fowle, P., J.Electrochem.Soc., 101, p.481, 1954.
198. Ives, D.J.G. and Janz, G.J., Reference Electrodes, Theory and Practice, Academic Press, London, p.226, 1961.
199. Holroyd, N.J.H., Scamans, G.M. and Hermann, R., T.M.S.-A.I.M.E., Conf.Proc. Embrittlement by the Localised Crack Environment, Philadelphia, Pa., USA, p.327, Oct.1983.
200. Van Gelder, K., Simon-Thomas, M.J.J. and Kroese, C.J., Corrosion N.A.C.E., 42, p.36, 1986.
201. Albrecht, J., Bernstein, J.M. and Thompson, A.W., Met. Trans.A, 13A, p.811, 1982.
202. Hermann, R. and Holroyd, N.J.H., Materials Science and Engineering, 76, p.119, 1985.
203. Scamans, G.M., 2nd Int.Conf.on Environmental Degradation of Engineering Materials, Virginia, USA, p.153, 1981.
204. Smithells, C.J.(Ed), Metals Reference Book, Second Edition, Vol II, Butterworth, London, p.533, 1955.
205. Godard, H.P., Materials Performance - N.A.C.E., p.9, July 1981.
206. Pourbaix, M., et. al., Atlas of Electrochemical Equilibria in Aqueous Solutions. Pub. Pergamon Press and Cebelcor, 1966.

APPENDIX A

The following actual anodic current transients obtained during the electrochemical permeation experiments on 7017-T651 alloy specimen membranes are presented.

Figure 195 - Current transient for permeation experiment No.1.

Experimental conditions:

Membrane thickness - 0.10 mm
Charging cell solution - water saturated air vapour, 70 °C
Analysis cell solution - 0.1M Na₂SO₄
Anodic cell potential - + 230 mV vs. SHE

Figure 196 - Current transient for permeation experiment No.2.

Experimental conditions:

Membrane thickness - 0.20 mm
Charging cell solution - water saturated air vapour, 70 °C
Analysis cell solution - Boric acid, 50 gm l⁻¹ + Ammonium
Hydrogen Tetraborate, 0.4 gm l⁻¹
Anodic cell potential - + 90 mV vs. SHE

Figure 197 - Current transient for permeation experiment No.3.

Experimental conditions:

Membrane thickness - 0.25 mm
Charging cell solution - Boric acid, 50 gm l⁻¹ + Ammonium
Hydrogen Tetraborate. 0.4 gm l⁻¹
+ conc H₂SO₄, 1 cm³ in volume
of charging cell.
Charging current density - 0.566 mA cm⁻²
Analysis cell solution - Boric acid, 50 gm l⁻¹ + Ammonium
Hydrogen Tetraborate, 0.4 gm l⁻¹
Anodic cell potential - + 100 mV vs. SHE

Fig 198 - Current transient for permeation experiment No.4.

Experimental conditions:

Membrane thickness - 0.17 mm
Charging cell solution - 0.1 M sulphuric acid
Charging current density - 0.566 mA cm⁻²
Analysis cell solution - Boric acid, 50 gm l⁻¹ + Ammonium
Hydrogen Tetraborate 0.4 gm l⁻¹
Anodic cell potential - + 400 mV vs. SHE

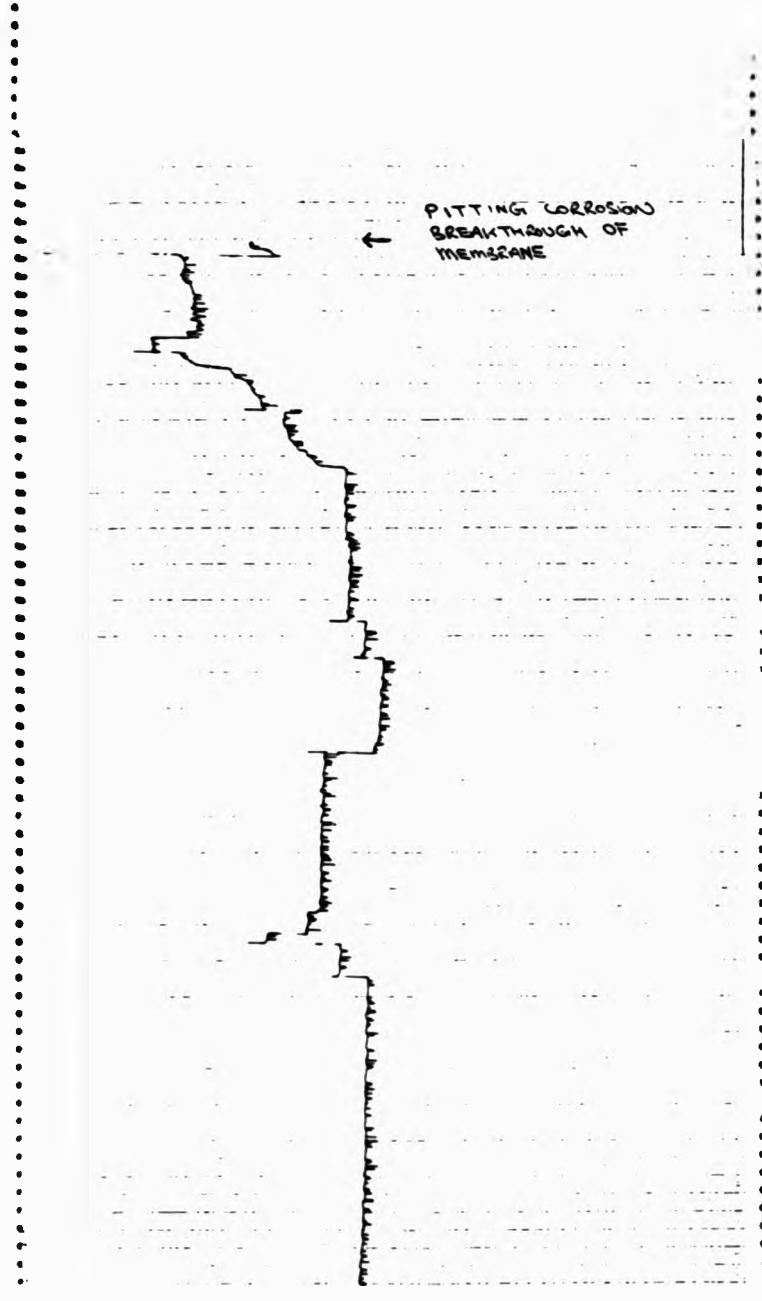


Fig.195 Current transient for permeation experiment No 1. Chart speed-10 minutes
cm, current axis - full scale deflection 1.0 mA.

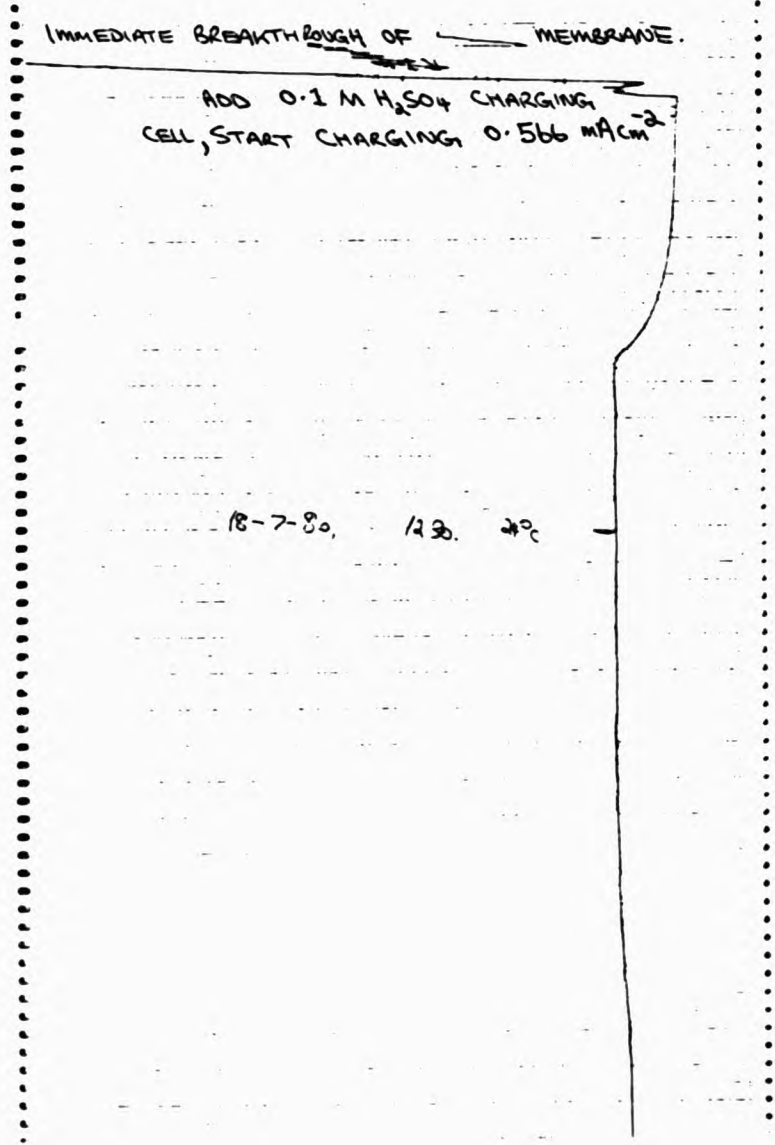


Fig.196 Current transient for permeation experiment No 2. Chart speed-10 minutes cm⁻¹, current axis - full scale deflection 0.02 mA.

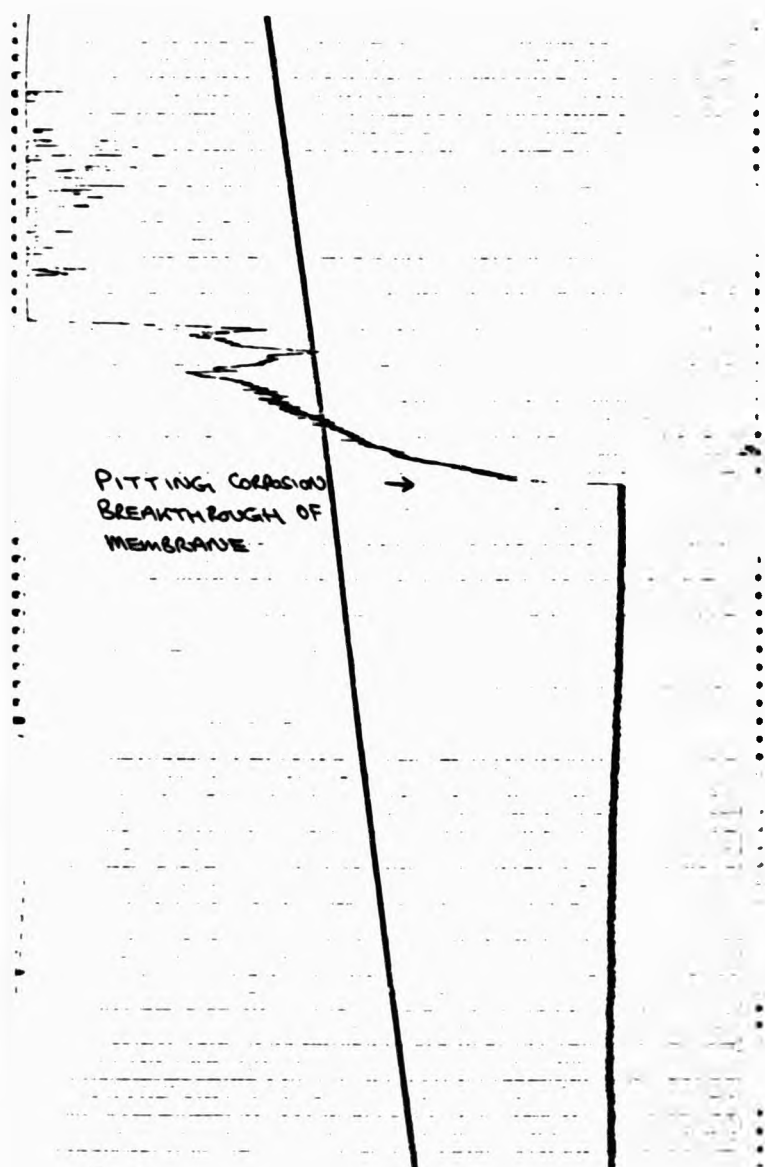


Fig.197 Current transient for permeation experiment No 3. Chart speed-10 minutes cm^{-1} , current axis - full scale deflection 0.02 mA.

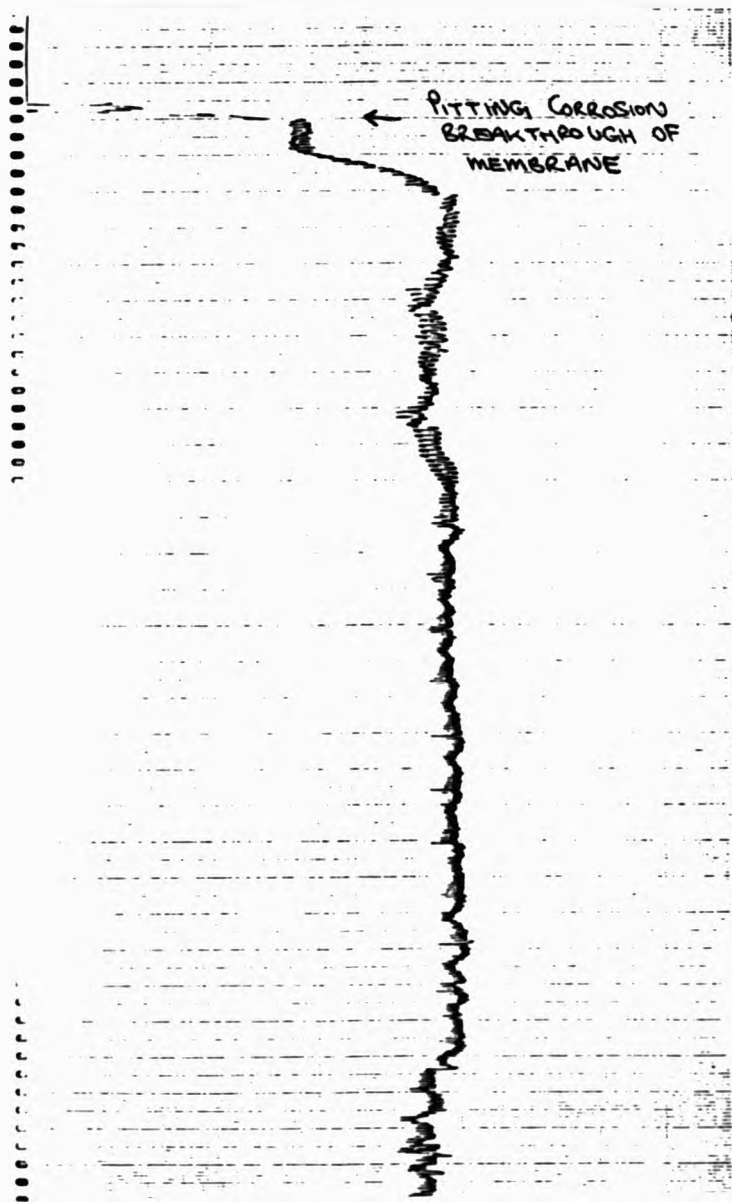


Fig.198 Current transient for permeation experiment No 4. Chart speed-10 minutes
 cm⁻¹, current axis - full scale deflection 0.01 mA.

THE BRITISH LIBRARY DOCUMENT SUPPLY CENTRE

TITLE HYDROGEN EMBRITTLEMENT OF AN Al-4.5Zn-2.5Mg ALLOY

AUTHOR EDWARD JOHN BCRAN

INSTITUTION CITY OF LONDON POLYTECHNIC.
and DATE C N A A 1989

Attention is drawn to the fact that the copyright of this thesis rests with its author.

This copy of the thesis has been supplied on condition that anyone who consults it is understood to recognise that its copyright rests with its author and that no information derived from it may be published without the author's prior written consent.



THE BRITISH LIBRARY
DOCUMENT SUPPLY CENTRE
Boston Spa, Wetherby
West Yorkshire
United Kingdom

REDUCTION X 21

CAM. 1



DX



89312

